THREE-DIMENSIONAL ANALYSIS OF CREEP VOID FORMATION IN STEAM-METHANE REFORMER TUBES

A thesis
submitted in partial fulfillment
of the requirements for the Degree
of

DOCTOR OF PHILOSOPHY IN MECHANICAL ENGINEERING
IN THE
UNIVERSITY OF CANTERBURY

by

AZMI ABDUL WAHAB

University of Canterbury
2007

Preface

This thesis is submitted as a partial requirement for the degree of Doctor of Philosophy in Mechanical Engineering in the University of Canterbury. This research was conducted under the supervision of Associate Professor Milo V Kral in the Mechanical Engineering Department, University of Canterbury, between March 2003 and December 2006.

Part of this work has been published in the following publications:

Azmi Abdul Wahab, Milo V. Kral, "*Three-Dimensional Analysis of Creep Voids*", Microscopy and Microanalysis 11 (2005) 224-225.

Azmi Abdul Wahab, Milo V. Kral, "*3D Analysis of creep voids in hydrogen reformer tubes*", Materials Science and Engineering A 412 (2005) 222-229.

Azmi Abdul Wahab, Christopher R. Hutchinson, Milo V. Kral, "*A three-dimensional characterization of creep void formation in hydrogen reformer tubes*", Scripta Materialia 55 (2006) 69-73.

Acknowledgements

I would like to acknowledge the following people and organizations that have made this research work possible:

- Associate Professor Milo V. Kral for supervision of this thesis, and also for his enthusiasm, optimism, knowledge, and friendship;

- Universiti Teknologi Petronas for the Staff Development Program Scholarship allowing me to pursue this work in New Zealand;

- Methanex (NZ) Ltd. and Schmidt-Clemens Spain S.A. for funding of this research; Peter Tait (Methanex) and Pedro Imizcoz Goni (Schmidt-Clemens) for the many useful information and communications;

- members of the University of Canterbury Materials Engineering Group (MEG), namely Dr. John Smaill, Dr. Mark Staiger, Emeritus Professor Les Erasmus, Frank Fahy, Mike Flaws, and Kevin Stobbs; MEG visitors, specifically George Vander Voort, Dr. George Spanos, and Dr. Chris Hutchinson; as well as fellow MEG students; for all their help, questions, comments, and critique;

- Administrative and technical staffs of Mechanical Engineering Department, the late Jill Porter, Margot Beck, Elizabeth Sands, Paul Southward, Julian Murphy, Julian Philips, Scott Amies, and Adam Latham, for all their kind assistance.

Most importantly, I dedicate this thesis to my wife Rosmawati, my children Sarah Hana and Luqman Ilyas, and to my parents.

Contents

Preface i
Acknowledgements ii
Contents iii
List of Figures vii
List of Tables xi
Nomenclature and Abbreviations xiii
Variables xiii
Chemical Abbreviations xv
Miscellaneous Abbreviations xvi
Abstract xvii

Chapter 1
INTRODUCTION 1
1.1 Research Objectives 1
1.2 Research Overview 3
1.3 Scope of Research 5
1.4 Format of Thesis 6

Chapter 2
LITERATURE REVIEW 9
2.1 Methanol Production Basics and the Role of the Steam-Methane Reformer 9
2.2 Reformer Tube Metallurgy 14
2.3 Overview of Creep Deformation in Metals 18
2.4 Brief Discussions on Void Growth Models 25
2.5 Three-Dimensional Analysis of Materials 26

Chapter 3

MATERIALS CHARACTERIZATION 31
3.1 Reformer Tube Samples 31
3.2 Optical and Scanning Electron Microscopy of Precipitates 33
3.3 X-ray Diffraction of Precipitates 38
3.4 Characterization of Precipitates Using EBSD 39
3.5 Transmission Electron Microscopy of Fine Precipitates 41
3.6 Summary of Precipitates in Ex-service Reformer Tube 44

Chapter 4

SERIAL SECTIONING AND 3D RECONSTRUCTION 45
4.1 Serial Sectioning Process 45
4.2 Image processing and 3D Reconstruction 50
4.3 3D Reconstruction of an As-Cast Reformer Tube Material 56

Chapter 5

ANALYSIS OF CREEP VOIDS IN A FAILED REFORMER TUBE 63
5.1 Serial Sectioning and 3D Reconstruction Methods 63
5.2 3D Characterization of Creep Voids 65
5.3 EBSD of Creep Void Precipitates 71
5.4 Conclusions 78

Chapter 6

CREEP VOIDS AT VARIOUS STAGES OF CREEP 79
6.1 Experimental Details 79
6.2 3D Reconstructions and Characterization of Voids 83
6.3 Results and Observations 90
6.4 Summary 102

Chapter 7

MODELING THE GROWTH OF CREEP VOIDS 105
7.1 Void Growth Model 105
7.2 Results and Discussions 113

7.3 Final Thoughts 122

Chapter 8

SUMMARY AND CONCLUDING REMARKS 125

8.1 Summary 125

8.2 Future Work 129

REFERENCES 131

Appendix I

SELECTED PROPERTIES OF CENTRALLOY CA4852-MICRO 139

Appendix II

CALCULATION OF STRESSES IN THE REFORMER TUBE 143

II.1 Thermal Stresses 143

II.2 Stresses Due to Internal Pressure 145

II.3 Stresses Due to Tube Weight 145

II.4 Calculation of Effective Stress 146

Appendix III

CALCULATION OF TIME-TO-RUPTURE 147

III.1 Code for Void Geometry Factors 147

III.2 Code for Integrating the Term $1/f(A)$ 148

III.3 Spreadsheet Layout to Calculate Time-to-Rupture 149

Appendix IV

PUBLICATIONS 153

Appendix V

ANIMATED 3D MOVIES 167

List of Figures

1.1: Microstructure of reformer tube material 3

1.2: Picturesque view of Methanex Kitimat Plant in British Columbia, Canada 4

1.3: Schematic of experimental process..... 5

2.1: Schematic of the methanol production process 10

2.2: Aerial view of Methanex (NZ) Waitara Valley methanol plant 11

2.3: Steam-methane reformer in action..... 14

2.4: Comparison of creep resistance of several reformer alloys..... 17

2.5: Typical macrostructure of a centrifugal cast reformer tube showing both the equiaxed and columnar grains..... 18

2.6: Three stages of creep typical of creep test performed under constant load..... 19

2.7: Presentation of creep-rupture and stress-rupture test data 21

2.8: Graphical representation of the Larson Miller parameter and the determination of the constant *C* 21

2.9: Diffusional flow creep deformation resulting from motion of atoms and vacancies..... 23

3.1: Cross-section of reformer tube wall showing the typical macrostructure 32

3.2: Preparation of metallography samples..... 34

3.3: Microstructure of ex-service reformer tube 35

3.4: Backscatter electron (BSE) image of ex-service reformer tube and the corresponding EDS spectra 36

3.5: XRD spectrum of reformer tube precipitates..... 39

3.6: Electron backscattered diffraction pattern of reformer tube precipitates 40

3.7: TEM bright field image and corresponding indexed SAD patterns of the fine intragranular precipitate 43

3.8: High resolution TEM image of a Cr-rich fine intragranular precipitate 44

4.1: Microhardness tester used for placement of fiducial marks 47

4.2: Buehler Minimet® 1000 polisher (left) and the older model Buehler Minimet® polisher 48

4.3: A sequence of nine serial section images showing the placement of fiducial marks and the reduction of their sizes due to polishing 49

4.4: Overlayed pair of serial section images showing the manual image registration process 51

4.5: Example of a 3D view of ex-service reformer tube microstructure 53

4.6: Detailed 3D reconstruction of a void and surrounding features 55

4.7: Microstructure of as-cast reformer tube 56

4.8: Backscatter electron (BSE) image of ex-service reformer tube and the corresponding EDS spectra 57

4.9: 3D reconstruction of an equiaxed region of the as-cast reformer tube 59

4.10: 3D reconstruction of a columnar region of the as-cast reformer tube 60

4.11: Detailed 3D reconstruction of a subvolume in the equiaxed region of the as-cast tube 62

5.1: 3D reconstruction of a 403×204×32-µm volume 66

5.2: Classification of creep void shapes 67

5.3: Schematic representations of void location classification 68

5.4: Characteristics of creep void obtained from 3D reconstruction of reformer tube material 70

5.5: EBSD mapping of reformer tube microstructure 72

5.6: Differences in microstructure between the tube samples 73

5.7: Phase identification procedure for precipitates near creep voids 75

5.8: Comparison of orientation relationships and misorientation angles between ex-service material and laboratory-aged sample 77

6.1: Temperature and pressure profiles of the Kitimat ex-service reformer tube 80

6.2: Diametral strain of the Kitimat ex-service reformer tube 81

6.3: Macrostructure of the reformer tube wall showing the approximate locations of where the volumes were obtained for 3D reconstructions 82

6.4: 3D reconstructions of the equiaxed microstructure at the inner wall of the tube 84

6.5: 3D reconstructions of the columnar microstructure at the outer wall of the tube 85

6.6: Transparent views of the 3D reconstructions of the equiaxed microstructure 86

6.7: Transparent views of the 3D reconstructions of the columnar microstructure 87

6.8: Type A, B and C classification of void types 89

6.9: Comparison of characteristics of grain boundary voids between the three samples taken at various positions along the reformer tube and at three wall positions 91

6.10: Correlation of void location with: (a) void size, and (b) void density 94

6.11: Correlation of contact precipitates with: (a) void size, and (b) void density 96

6.12: Correlation of void type with: (a) void size, and (b) void density 98

6.13: Correlation of void shape with: (a) void size, and (b) void density 99

6.14: Comparison of “minimum” and “mean” void-to-void distances 101

6.15: Mean angle of grain boundaries containing voids 101

7.1: Schematic of void array on a grain boundary and the associated parameters 111

7.2: Geometry factor of void configuration on the grain boundary F_B 112

7.3: Plot of time-to-rupture versus the reciprocal of absolute temperature for the ex-service samples with their existing level of creep damage 114

7.4: Comparison of Tresca stress distributions for various positions along the length of the idealized reformer tube 116

7.5: Time-to-rupture behavior for various sample locations on the idealized reformer tube 118

7.6: Adjusted time-to-rupture behavior for various sample locations on the idealized reformer tube 119

7.7: Effect of variations in void-to-void distance on the time-to-rupture computations for samples at the inner wall of the idealized reformer tube 120

7.8: Effect of tube wall temperature variations on the time-to-rupture computations 121

8.1: Void shapes and microstructures of tube material subjected to creep 127

I.1: Tensile properties for Schmidt-Clemens Centralloy CA4852-Micro 140

I.2: Parametric stress rupture strength for Schmidt-Clemens Centralloy CA4852-Micro 141

I.3: Coefficient of linear thermal expansion for Schmidt-Clemens Centralloy CA4852-Micro 141

I.4: Modulus of Elasticity for Schmidt-Clemens Centralloy CA4852-Micro 142

II.1: Schematic of a long thick-walled cylinder and its reference axes 143

List of Tables

I: Main alloying elements (in wt%) present in Schmidt-Clemens Centralloy® CA4852-Micro 32

II: List of candidate compounds used to determine the unknown precipitates 37

III: Summary of precipitates characterized 44

IV: Summary of operating conditions for the obtained samples 81

V: Particulars of reconstructed volumes 88

VI: Material constants for Fe (as the diffusing atom) at a grain boundary interface 109

VII: Summary of ex-service sample parameters used in the model 113

VIII: Summary of modeling parameters for the idealized tube 116

IX: Percent change (average) in time-to-rupture t_r due to variations in various modeling parameters 122

X: Layout of Microsoft Excel spreadsheet used in calculating time-to-rupture for the void growth model 150

Nomenclature and Abbreviations

Variables

α_1, α_2, α_3	corner angles of unit cell
α_F	void interface angle for two-grain junction, type A, and type B voids
α_T	coefficient of thermal expansion
β	constant for primary (transient) creep
β_F	void interface angle for three-grain junction voids
γ	surface free energy of the void
δ	grain boundary thickness
ε	strain
ε_o	instantaneous initial extension during creep loading
θ_F	void interface angle for four-grain junction void
θ_M	misorientation angle
κ	minimum creep rate constant
ν	Poisson's ratio
ρ_t	density of tube
σ	stress
σ_∞	remote applied stress
σ_1, σ_2, σ_3	principal stresses
σ_{aT}	axial stress due to temperature
σ_{ap}	radial stress due to internal pressure
σ_{aW}	axial stress due to weight of tube
σ_{hT}	hoop stress due to temperature
σ_{hp}	hoop stress due to internal pressure
σ_{rT}	radial stress due to temperature
σ_{rp}	radial stress due to internal pressure
σ_{TS}	Tresca stress
Ω	atomic volume

$1/f(A)$	simplified integral term of void growth model
a_1, a_2, a_3	lattice parameters
A	area projection of void
A_{max}	upper integration limit
A_{min}	lower integration limit
A_t	cross-sectional area of tube
[$\boldsymbol{A}$], [$\boldsymbol{B}$]	orientation matrices of arbitrary locations A and B
C	constant in Larson-Miller parameter equation
$(D_B)_0$	grain boundary diffusion coefficient
$D_B\,\delta$	grain boundary diffusivity
E	modulus of elasticity
F_B	geometry function of void configuration on the grain boundary
g	gravitational acceleration = 9.81 m/s^2
k	Boltzman's constant = 1.381×10^{-23} J K^{-1}
k_T	thermal conductivity
l	½ void-to-void spacing
l_{mean}	½ mean void-to-void spacing
l_{min}	½ minimum void-to-void spacing
l_t	vertical distance from tube's top flange to point of interest.
LMP	Larson-Miller parameter
m_{ij}	misorientation matrix elements (i, j are the indices)
$\boldsymbol{M}$, [$\boldsymbol{M}$]	misorientation, misorientation matrix
p	tube internal pressure
p_v	internal gas pressure inside voids
Q_B	grain boundary activation energy
r	tube radius
r_B	radius of curvature of void projection on the grain boundary
r_i	tube inside radius
r_o	tube outside radius
r_v	radius of void surface
r_c	critical radius for void nucleation
R	universal gas constant = 8.314 J mol^{-1} K^{-1}

t	time
t_r	time to rupture
T	temperature
T_i	inside wall temperature
T_o	outside wall temperature
$T(r)$	temperature as a function of tube radius
[u v w]	misorientation axis
W_t	weight of tube

Chemical Abbreviations

Bi	bismuth
C	carbon
Ce	cerium
CH_3OH	methanol
CH_4	methane
CO	carbon monoxide
CO_2	carbon dioxide
Cr	chromium
Fe	iron
HCl	hydrochloric acid
HNO_3	nitric acid
H_2	hydrogen
H_2O	water (steam)
M_7C_3	Cr-rich carbide (also noted as Cr_7C_3)
$M_{23}C_6$	Cr-rich carbide (also noted as $Cr_{23}C_6$)
Mn	manganese
MTBE	methyl tertiary butyl ether
Ni	nickel
Nb	niobium
NbC	niobium carbide
Pb	lead
Si	silicon
SiC	silicon carbide

Sn	tin
Ti	titanium
TiC	titanium carbide
W	tungsten
Zr	zirconium

Miscellaneous Abbreviations

2D	two-dimension
3D	three-dimension
AVI	audio-video interleave
BSE	backscatter electron
CAD/CAM	computer-aided design/computer-aided manufacturing
CATIA	computer aided three-dimensional interactive application
CDROM	compact disc read-only memory
DDR RAM	double-data rate random access memory
EBSD	electron backscattered diffraction
EBSP	EBSD patterns
EDS	energy dispersive spectroscopy
FIB	focused ion beam
FO	forescatter orientation
FZ	forescatter Z-contrast (atomic number contrast)
GIMP	GNU image manipulation program
HK, HP	designation of two types of high temperature cast stainless steels
OM	optical microscopy
OR	orientation relationship
RGB	red-green-blue
SAD	selective area diffraction
SEM	scanning electron microscopy
TEM	transmission electron microscopy
TIFF	tagged image file format
wt%	weight percent
XRD	x-ray diffraction

Abstract

In methanol processing plants, steam-methane reformers consist of hundreds of vertical tubes operating at temperatures up to 1000°C. These reformer tubes fail by creep through the formation of creep voids during service. Preliminary research showed that the occurrence of these voids was not random and may be related to certain microstructural features of the material.

In the present research, the technique of serial sectioning was used to generate three-dimensional reconstructions of voids in several steam-methane reformer tube samples with creep damage. The serial sectioning method and subsequent 3D reconstruction revealed creep void information such as size, density, location, and shape in three-dimensions, information that cannot be obtained from two-dimensional micrographs alone. Samples were obtained at various locations along the length of an ex-service reformer tube to investigate the effects of service conditions on the characteristics of creep voids. In addition, samples were taken from various positions along the wall thickness where there were differences in temperature, stress, and microstructure. Additionally, the identity and crystallographic orientations of the phases adjacent to creep voids were studied by electron backscatter diffraction (EBSD) to determine the crystallographic trends in creep void locations.

Three dimensional observations revealed that creep voids were indeed not uniformly distributed through the volume in terms of their size, shape, and location. All voids appeared next to carbides and these voids came into contact with $M_{23}C_6$ precipitates somewhere along their perimeter. Most of the voids were found on austenite (γ) grain facets (the interface between two γ grains) but the larger voids were generally found at grain edges and corners. The grain boundaries where voids were located were generally oriented at 45 degrees with respect to the hoop stress direction. Here, the effective stress due to a combination of loading and temperature were highest.

EBSD results showed that 80% of the $M_{23}C_6$ precipitates surrounding these voids have an irrational crystallographic orientation relationship (OR) with the austenite matrix. In contrast, grain boundary precipitates in an aged sample always show a rational OR with respect to one adjacent grain. This implied that the preferred sites for creep voids are low registry boundaries between $M_{23}C_6$ precipitates and austenite.

The data obtained from 3D observations were applied to a classic void growth model. Various permutations of the parameters obtained from this work were applied to the model to simulate conditions that may be beneficial to extending the service lives of reformer tubes. It was shown that the void growth model required accurate and representative materials constants for good estimation of life. Furthermore, the model revealed that more work was required in terms of observations of void nucleation in 3D, in order to fully utilize the model. Finally, it was shown that void density measurements are the most critical item for accurate prediction of growth of voids.

Chapter 1

INTRODUCTION

When metals are subjected to stress at a high temperature, a type of plastic deformation known as creep occurs. This deformation takes place over an extended period of time and failure is due to either excessive deformation of the components or physical separation of the affected parts. These failures are however not accurately predictable, and data scatter with regard to component lives is a paramount concern. Microstructural examinations of a failed part typically reveal small voids dispersed throughout the material. These voids are not completely random in occurrence, and their formation is due to certain material characteristics and service conditions. In the present research, creep voids occurring in ex-service steam-methane reformer tubes were studied by reconstructing their appearance in 3D. A database of information was collected and the results were applied to a creep void model. It is anticipated that the knowledge gained will be used to create tubes with longer and more predictable service lives.

1.1 Research Objectives

One engineering component which typically fails by creep is the steam-methane reformer tube. In methanol processing plants, steam-methane reformers consisting of hundreds of vertically oriented straight tubes are filled with catalyst, while gases pass over the catalyst at extremely high temperatures. The tube material is commonly centrifugally cast austenitic stainless steel, and these tubes typically fail via creep void formation and coalescence during service. The life expectancy of these tubes is 100,000 hours (11.4 years), however the actual lives achieved can be significantly shorter than the target. With the price of each tube exceeding US$7000, the cost of replacing these tubes and the associated cost of a plant shutdown is a major concern for plant operators.

Reformer tube materials usually undergo some sort of accelerated tests where test specimens are subjected to either a higher load and/or temperature (than the service conditions) such that the test samples will fail in a relatively short period of time. These results are then extrapolated to determine the suitable operating conditions for the tubes. Since the test parameters may not completely replicate the service conditions, unexpected tube failures are not uncommon. Microstructural studies of reformer after long term high-temperature service are usually performed to shed further light into the problem of creep. Cross-sections of failed tubes are metallographically prepared and creep void numbers and densities are determined from two-dimensional micrographs. Models based on these measurements are then generated and the results of the models are then used to further enhance the tube lives.

As mentioned, creep failures in steam-methane reformer tubes developed from void formation during service. Preliminary research showed that these voids may not be randomly occurring but rather forming preferentially at certain grain corners [1]. The exact locations of these voids are influenced by various inter-related parameters including material characteristics, crystallography, local geometry, and stress. A typical microstructure of an ex-service reformer tube is shown in Figure 1. Notice the creep voids which appeared as dark spots in the low magnification image of Figure 1(a). In Figure 1(b), the microstructure of the reformer tube surrounding the voids is further revealed.

In the present research, reformer tubes with various levels of creep damage were studied. Instead of the usual examination of the microstructure from two-dimensional micrographs, the study will be carried out on three-dimensional reconstruction of the reformer tube microstructure. Thus, the objectives of this research were as follows:

- characterize the microstructure of reformer tubes with creep damage and reconstruct the microstructure in 3D;
- obtain statistical measurement characteristics of creep voids and their relation to the surrounding microstructure;
- correlate the information obtained to various service conditions and levels of creep damage;
- apply data obtained into a void growth model to establish microstructure characteristics prone to creep damage.

It was anticipated that this thesis would present a novel way of studying material deformation or failure by viewing the defects and associated microstructural features in 3D, and from these unique observations, the knowledge of the high temperature creep deformation and void formation in steam-methane reformer tubes is further enhanced. It was also expected that the knowledge obtained could then be utilized to recommend microstructural characteristics least inclined to creep damage which can presumably be obtained through adjustments of tube processing parameters.

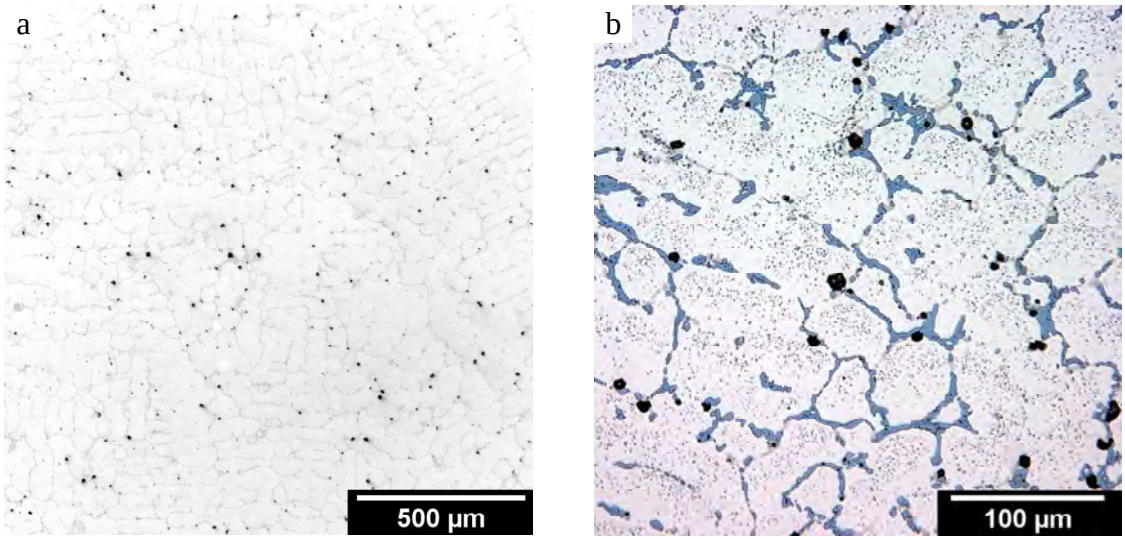

Figure 1.1: Microstructure of reformer tube material. (a) Low magnification as-polished micrograph showing creep voids as dark spots, (b) higher magnification etched image revealing the various precipitates near the voids (Murukami's tint etch).

1.2 Research Overview

The steam-methane reformer tube samples studied in this work were supplied by Methanex (NZ) Ltd., which is one of the sponsors for this project The centrifugally cast austenitic stainless steel tubes were manufactured by Schmidt-Clemens Spain S.A. which is the other sponsor for this project. The ex-service tubes used for the 3D reconstructions and analyses had been in service between six and ten years at the Methanex Kitimat plant in British Columbia, Canada (see Figure 1.2). Tube segments with known service histories were removed from the original 13.5-m length of the tubes and shipped to the Metallurgical Laboratories at the University of Canterbury for analysis.

Figure 1.2: Picturesque view of Methanex Kitimat Plant in British Columbia, Canada. The red arrow points to the building housing the steam-methane reformer.

The experimental process for this project is schematically summarized in Figure 1.3. Metallographic samples were first prepared from the tube segments received. The samples were then fully characterized with various laboratory techniques available. This step is vital in order to properly reconstruct the microstructure in 3D. The samples then underwent the serial sectioning process in which a set depth of material was removed by mechanically polishing the samples. Micrographs were obtained after each polishing and etching step. During the serial sectioning process, electron backscattered diffraction (EBSD) scans were obtained at 10 to 20 section intervals. This step was taken so that the crystallographic orientations of the various microstructural features in the vicinity of the voids were recorded. The set of micrographs obtained were then reconstructed into a 3D image using a computer software package. The reconstructions revealed various characteristics of the creep voids such as their sizes, shapes, locations, adjoining precipitates, and orientation in three-dimensions, information that cannot be obtained from two-dimensional micrographs alone. A database of information obtained from 3D observations was created and the results were then applied to a void growth model.

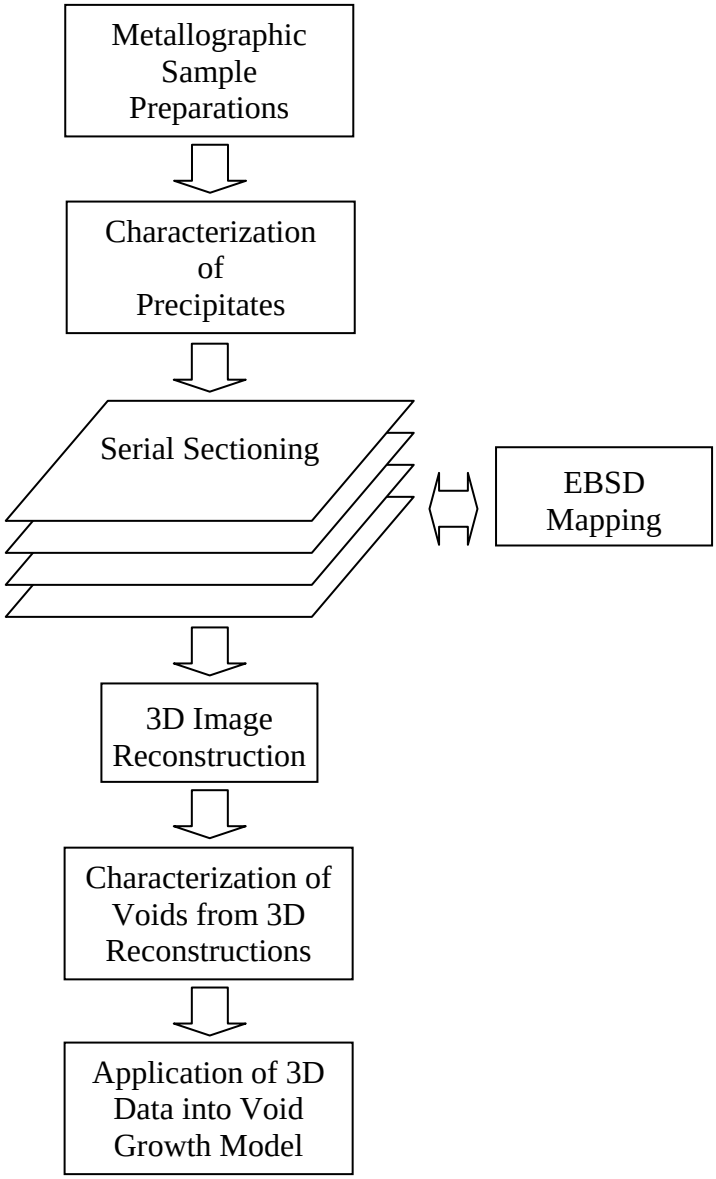

Figure 1.3: Schematic of experimental process.

1.3 Scope of Research

The initial plan of the research was threefold: study microstructures of ex-service tubes, study microstructures of interrupted accelerated creep tests, and modeling of data. However, preliminary work on the interrupted creep tests showed that the test samples and conditions could not faithfully replicate the ex-service material. Firstly, it was impossible to obtain a test piece from the reformer tube to be tested in such a way that the same

microstructural orientation and features aligned with the stress directions of the reformer tube in service. Attempts at performing an accelerated pressurized tube test in the presence of hydrogen gas were also not successful. Furthermore it was discovered that the characteristics of the microstructure and the creep voids of the accelerated test samples were completely different from the ex-service samples even though the respective Larson-Miller parameters were identical. The decision was then made to only study ex-service reformer tubes at various stages of creep. The ideal case would be to obtain tube samples after different periods of service. In reality however, it is impossible to request these samples because it involved interruptions in plant operations and also necessitated the removal of tubes that are still capable of service. Therefore, only a retired, unruptured ex-service tube was obtained for this study. By taking samples at different positions along the tube, different levels of creep damage can be studied. Thus the scope of this research can be represented by three phases as follows:

- Phase I: 3D characterizations of a failed reformer tube;
- Phase II: 3D characterizations of a retired reformer tube at various levels of creep damage;
- Phase III: Modeling of creep void growth.

This work is limited to only one alloy composition of tube material. In addition, a general conjecture was made throughout the work that all the characteristics observed were assumed to be the results of creep deformation mechanisms during high temperature service.

1.4 Format of Thesis

This thesis will be presented in eight chapters and five appendices as follows:

- Chapter 1 (this chapter) briefly discussed the objectives, overview, and scope of this research.

- Chapter 2 is a literature review chapter which addresses five topics pertinent to this research work, namely methanol production basics, metallurgy of reformer tube material, creep deformation in metals, void growth models, and three dimensional analysis of materials.

- Chapter 3 explains the characterization process used to identify various precipitates observed in the material. Use of various techniques such as optical microscopy (OM), scanning electron microscopy (SEM), energy dispersive spectroscopy (EDS), x-ray diffraction (XRD), electron backscattered diffraction (EBSD), and transmission electron microscopy (TEM) will be described.

- Chapter 4 provides the details of the serial sectioning and 3D reconstruction process used in this research. A 3D reconstruction of an as-cast reformer tube material will be shown.

- Chapter 5 presents the analysis of creep voids in a failed reformer tube. Serial sectioning and 3D reconstruction techniques are applied to study characteristics such as shapes, sizes, locations, and adjacent precipitates of creep voids. In addition, a crystallographic study of precipitates found adjacent to voids is also presented.

- Chapter 6 investigates the effects of service conditions on the characteristics of creep voids by studying samples obtained at three positions along an ex-service reformer tube. Samples were also obtained from various positions along the wall thickness where there are differences in temperature, stress, and microstructure.

- Chapter 7 describes the application of 3D data from Chapters 5 and 6 into a void growth model. Various combinations of parameters will be applied to the model to simulate conditions that may be beneficial to extending the service lives of reformer tubes.

- Chapter 8 is presents the summary and conclusions to the current work, and also possible future research work that expand on the current research.

- Appendix I lists selected properties of the reformer tube alloy.

- Appendix II shows the calculation of stresses in the reformer tube.

- Appendix III list the software code and spreadsheet layout used in the void growth model.

- Appendix IV contains a copy of each journal paper that was published during the course of this research.

- Appendix V contains a CDROM which contains movies of the serial sections and 3D volumes presented in this thesis.

Chapter 2

LITERATURE REVIEW

This chapter presents a general narrative on the subject matters contained within the research work; specifically this chapter will discuss the basics of methanol production, the metallurgy of the materials used in the reformer tubes, a general overview of creep deformation and void formation in metals, and three-dimensional methods in materials science.

2.1 Methanol Production Basics and the Role of the Steam-Methane Reformer

Methanex sole primary product is methanol (CH_3OH). At all the Methanex plants, the production of methanol can be broadly classified into four main sections: feed gas preparation, steam-methane reforming, compression and synthesis, and distillation* [2, 3]. The process flow for methanol production is shown schematically in Figure 2.1 and some of the respective features of the methanol process are indicated on an aerial view of a typical methanol plant in Figure 2.2.

Feed gas preparation is the first stage of the methanol process where natural gas (methane) is readied for use as fuel and also as raw material for the reforming process. Methane gas goes through an initial preheating stage after which a small portion of the gas is diverted to be used as fuel, while the remainder of the gas is heated further in the presence of cobalt-molybdenum or nickel-cobalt-molybdenum catalyst to convert any sulphur in the natural gas into sulphur dioxide. The gas then flows through a zinc oxide bed in the sulphur guard to remove the sulphur dioxide. This step is needed to prevent sulphur from contaminating the catalyst used in the reforming stage.

* The contents of this section are adapted from refs [2, 3] and the figures in this section are adapted and used with permission from Methanex (NZ).

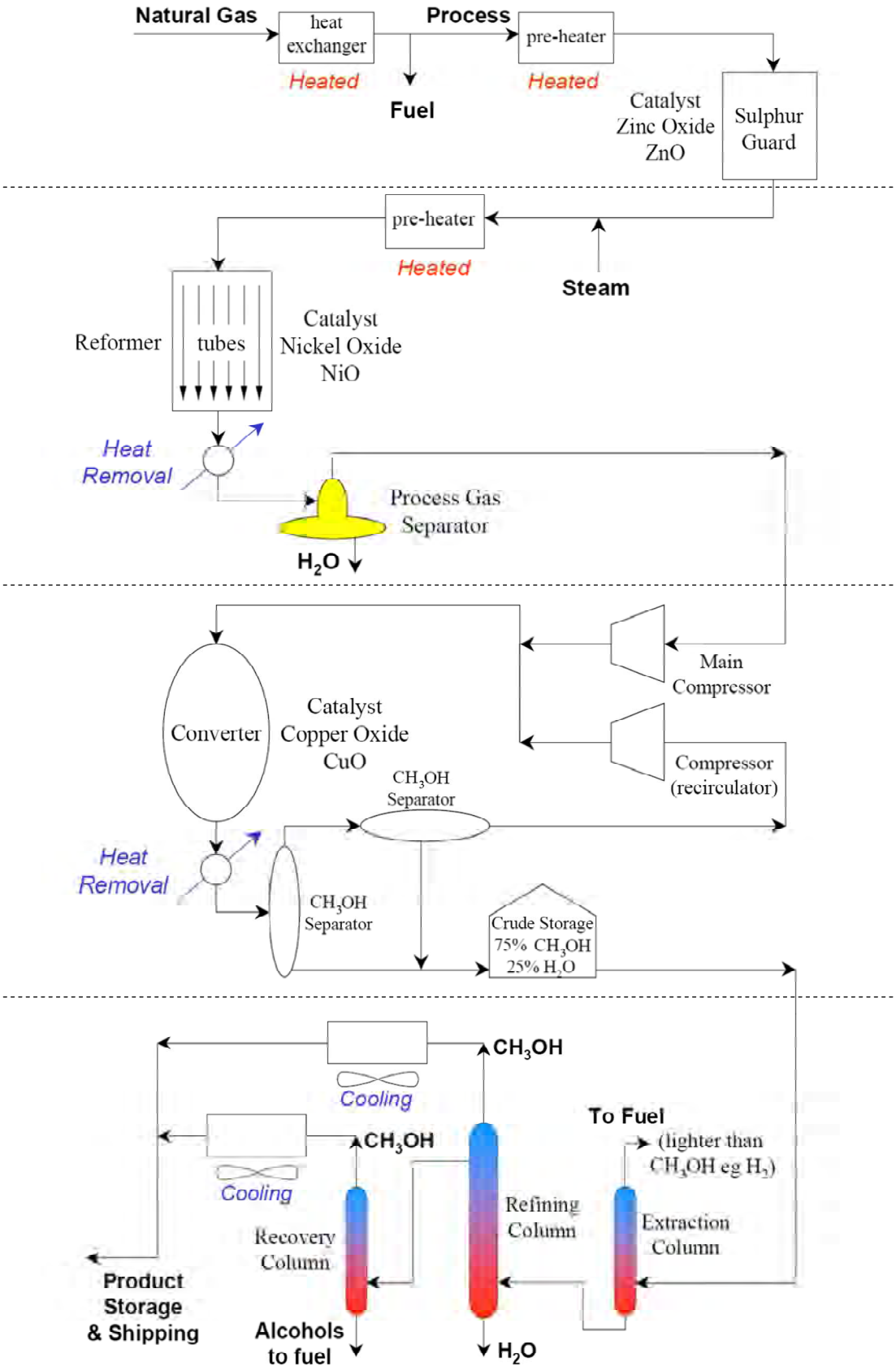

Figure 2.1: Schematic of the methanol production process. Dashed lines separate the four stages of the process: feed gas preparation, steam-methane reforming, compression and synthesis, and distillation [2, 3].

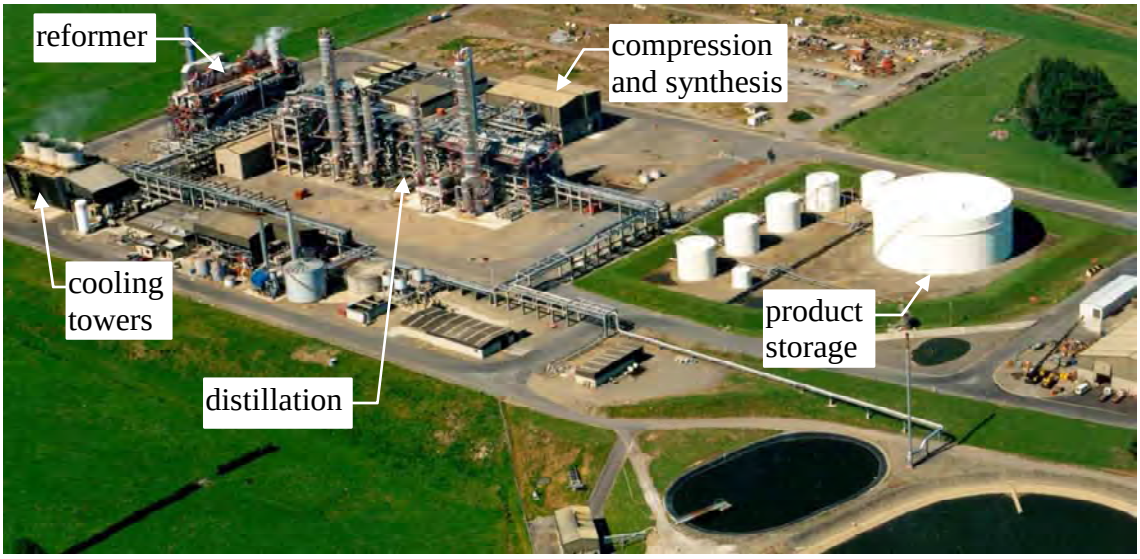

Figure 2.2: Aerial view of Methanex (NZ) Waitara Valley methanol plant showing some of the main features of the methanol production.

In general, reforming is a chemical process where gases are reacted to form other new gases. During steam-methane reforming (also known as hydrogen reforming), steam is added to the methane gas stream and this steam-methane mixture is further preheated before entering the reformer. A steam-methane reformer consists of hundreds of vertically oriented catalyst-filled tubes contained in a large furnace operating at a temperature around 900ºC. These tubes have an internal diameter and wall thickness of about 125mm and 10mm respectively, and are typically expected to sustain service for 100,000 hours (11.4 years). Methane and steam enters from the top of the tubes at an internal pressure of approximately 2MPa. In these tubes, the gas mixture reacts in the presence of nickel oxide catalyst to produce hydrogen, carbon monoxide, and carbon dioxide according to the following reaction equations:

$$CH_4 + H_2O \rightarrow CO + 3H_2$$

$$CO + H_2O \rightarrow CO_2 + H_2$$

The mixture of gases produced during steam-methane reforming is called synthesis gas and this gas mixture exits the tubes at the bottom of the furnace and cooled down to about 30°C.

In the next stage of the methanol process, the synthesis gas goes through a compressor raising the gas pressure from 1.5MPa to 8.6MPa. The compressed gas then enters the methanol converter containing a copper catalyst, and a chemical reaction ensues to form methanol and water. The products of the converter unit go through a methanol separator where unreacted synthesis gas is separated from the methanol, to be recompressed and recirculated back to the converter inlet. The methanol produced at this stage is referred to as crude methanol at approximately 75% purity.

The final stage of the methanol process is distillation. Two or more distillation columns sequentially separate the crude methanol into "light ends" (dissolved unreacted gases), water, and heavier alcohols. Light ends products such as hydrogen gas and heavier alcohols such as propanol are reused as fuel for combustion, while water is send to the sewer system. The resulting methanol is temporarily stored in shift tanks for quality checking before being sent to final product storage tanks. The methanol at this stage is 99.85% pure. The methanol produced is mainly used to produce formaldehyde, acetic acid, methyl tertiary butyl ether (MTBE), and various other chemical products

It would be fair to say that the steam-methane reformer is the heart of the methanol production plant. The reformer is probably the most expensive part of a methanol plant, and it is also the main energy user. The complex chemical and physical processes taking place in the hostile environment of the reformer also make it prone to various problems, and more often than not, the reformer is the cause of plant shutdowns or productions delays. It is thus not surprising that a lot of attention is paid to the "well-being" of the reformer components, especially the tubes. Tube wall and furnace combustion temperatures are regularly recorded in addition to many other process variables such as temperatures, pressures, and flow rates of the reacting gases. Whenever possible, the tubes themselves undergo diametrical measurement inspections or other nondestructive tests to determine any tube abnormalities so that catastrophic failures may be anticipated. It is also not uncommon for plant operators to obtain metallographic samples for evaluation of microstructural evidence of damage.

In general, reformer tubes fail due to creep. Although the tubes are designed to last at least 100,000 hours (11.4 years) of operation, some of the tubes in the furnace fail prematurely. A few of the possible causes of early failure of reformer tubes are listed below [4]:

1. Improper metallurgical properties of the tubes. This is by far the most difficult factor to pinpoint. The tubes are typically Fe-Cr-Ni cast austenitic stainless steel alloy with additions of elements such as Si, Nb, Ti, and Mn. The actual behavior of these alloys and the interactions between the various elements and precipitates at the high service temperatures and long service period are not fully understood and impossible to replicate in laboratory tests. The data scatter commonly present in laboratory creep tests is frequently attributed to material and test condition variations and this data scatter may be amplified in actual service conditions.
2. Thermal fatigue due to cycling of the tubes. This problem occurs during startup and shutdown of the plant and is sometimes identified as one of the main contributor to premature failures.
3. Poor heat distribution in the furnace. The large size of the reformer furnace almost guarantees some temperature variations between the many rows of tubes. Some of these tubes may experience extreme temperature conditions (overheat).
4. Different temperature profiles due to different tube sizes. In furnaces containing tubes of different sizes, the tube wall temperature profiles will be different, and thus create variations in expected lives. Furthermore, in some cases, eccentric tube bores can make part of the tube wall thinner than the minimum safe wall thickness and thus lead to early failure.
5. Catalyst induced temperature profile. Certain catalyst shapes or arrangements within the tubes are known to create hot spots which may accelerate untimely failure.

It is thus vital for plant operators to correctly identify the causes of early failures in their reformer tubes. Actions such as using reformer tubes with different alloy content or employing better monitoring methods of operational parameters may be implemented to prevent untimely failure of these tubes.

2.2 Reformer Tube Metallurgy

At Methanex plants, steam-methane reformers typically contain hundreds of vertical tubes which are expected to operate at about 900°C and 2MPa for 100,000 hours (11.4 years). Figure 2.3a shows a steam-methane reformer and Figure 2.3b shows reformer tubes in service. In addition to the high temperature and the internal pressure, the tube material must also be able to withstand high temperature corrosion from the chemical processes occurring within the tubes.

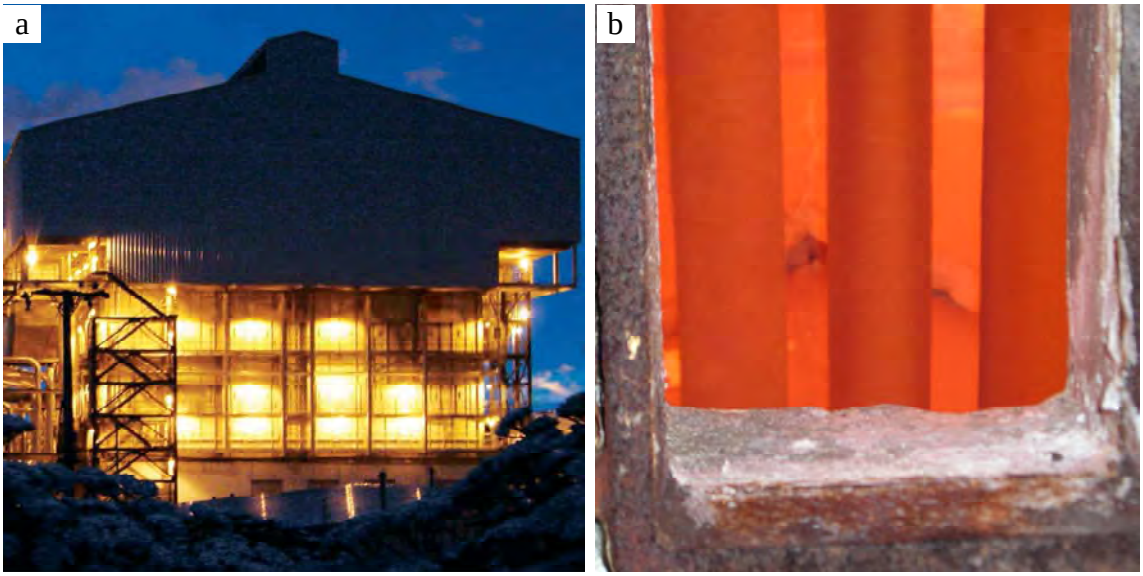

Figure 2.3: Steam-methane reformer in action. (a) Steam-methane reformer building at Methanex Chile II plant, (b) reformer tubes in service as seen through a viewing port.

Up to the early 1960s, reformer tubes were made from expensive wrought austenitic ferrous superalloy containing 18% (by weight) Cr and 37% Ni in order to withstand the service requirements of a steam-methane reformer [5]. To reduce the costs of the reformers, cast stainless steel tubes were introduced in the early 1960s. These early cast tubes have similar alloy content as the expensive wrought superalloy tubes. Subsequent research on creep of reformer tubes and development of reformer tube alloys found a cheaper alternative in HK40 alloy† containing 0.4% C, 25% Cr and 20% Ni, which has similar creep-rupture strength as the 18Cr-37Ni superalloy and better creep-rupture

† Designation system of the Alloy Casting Institute (ACI) which is now replaced by the High Alloy Product Group of the Steel Founders' Society of America.

strength than alloys with lower C content [5]. The higher C content in HK40 forms Cr-rich eutectic carbides (M_7C_3[‡]) along the cell and grain boundaries in the microstructure which improves creep resistance in the alloy [6, 7]. However, after high temperature exposure, M_7C_3 carbides transforms to $M_{23}C_6$ which is a more stable Cr-rich carbide. The in-situ transformation, first proposed by Shaw and Quarrell [8], leads to Cr being further depleted from the austenite matrix along the boundaries M_7C_3 carbides transforms to $M_{23}C_6$ precipitates. As a result, the cell and grain boundaries would be more susceptible to corrosion. Nevertheless, the HK40 alloy has become the basis of subsequent reformer alloy development.

A variation of the HK40 alloy used for reformer applications is the HP grade alloy, which contains higher Ni content than Cr (35% Ni vs. 25% Cr) that results in a very stable austenite structure, as opposed to HK40 alloy containing lower Ni content than Cr (20% Ni vs. 25% Cr). The stable austenite structure prevents any occurrence of ferrite in the microstructure which can transform into the brittle σ-phase at high temperature. The as-cast microstructure of the HP grade alloy also contains M_7C_3 carbides which convert to $M_{23}C_6$ after high temperature ageing. Common versions of the HP grade are the HP40 (0.4% C) and HP50 (0.5% C) which have improved high temperature strengths, and thus better resistance to thermal stresses and thermal cycling, plus superior performance in oxidizing and reducing environments [6]. Similar to HK40, the composition of the HP grade alloys also became the basis for further improvements of the reformer alloy.

The next significant development of the HK40 alloy was performed by International Nickel Ltd. which produced an alloy designated as IN519 which has 0.3% C, 24% Cr, 24% Ni, and 1% Nb. As in HP alloys, the microstructure is fully austenite due to the high Ni content, thus preventing the formation of brittle σ-phase from ferrite [6]. Furthermore, the slight decrease in the Cr and C content coupled with the addition of Nb reduces the volume fraction of $M_{23}C_6$ and forms NbC due to the greater affinity of Nb to C [9, 10]. These microstructural changes improve the creep strength and ductility of the material making it superior to both HK40 and HP40 alloys, as shown in Figure 2.4.

[‡] The “M” in the precipitate designation usually represents more than one metallic element.

When Nb was added to the HP grade alloys, numerous commercial variations were spawned that have been grouped under the “HP-Nb” or “HP-Nb mod” grade. Due to the greater affinity of Nb to C than Cr, it was found that higher Nb additions changes the stoichiometry of the chromium carbides from M_7C_3 to $M_{23}C_6$ as a result of having less available C to combine with Cr [11]. As in the IN519 alloy, the Nb additions resulted in NbC precipitates, which partially replace $M_{23}C_6$ precipitates [12]. The NbC precipitates form along the cell and grain boundaries in conjunction with the $M_{23}C_6$ precipitates causing fragmentation of the carbide network which is believed reduce creep failures at the carbide-matrix interface [13, 14]. Furthermore, the addition of Nb is believed to change the composition of the intragranular austenite matrix by reducing the amount of C present, and as a result, finer secondary precipitates of $M_{23}C_6$ during high temperature application was reported [15]. By and large, the presence of Nb in the HP-Nb grade alloy produced reformer tubes with superior creep rupture strength than IN519 [9, 15], as indicated in Figure 2.4.

The present development of reformer alloys is a progression of work done by Wen-Tai and Honeycombe [5, 14]. In their work, small additions of Zr and Ti produced more complicated eutectic microstructures which further improved the creep rupture strength of the material. Currently, reformer tube manufacturers perform what is referred to as “micro-alloying” by adding small amounts of Ti, Zr, W, Ce, or other proprietary combinations of elements to further enhance the high temperature properties of the reformer alloy. The improved high temperature properties achieved by micro-alloying additions is believed to be due to either or a combination of the following effects [10, 14, 15]: solid solution strengthening; formation of new MC carbides such as TiC or complex MC carbides such as (NbTiZr)C to further fragment the $M_{23}C_6$ carbide network; and prevention of precipitate coarsening during service. Figure 2.4 compares the average 100,000 hours creep resistance of several reformer alloys [9].

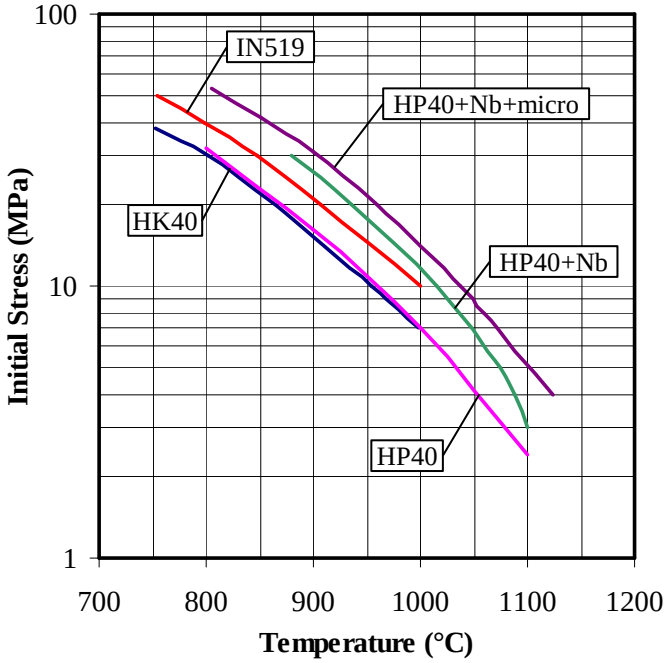

Figure 2.4: Comparison of creep resistance of several reformer alloys (redrawn from [9]).

Improvements to the high temperature properties of the reformer tube alloys were not confined to modifications of alloying features alone. Changes in manufacturing methods also contributed to the enhancement of reformer tube properties. Most of these changes are closely guarded industry secrets, but two of the common manufacturing advancements are the reduction of casting voids by centrifugal casting, and the control of the tube wall microstructure via adjustment of the cooling rates of the casting moulds. In centrifugal casting, molten metal is poured into a spinning horizontal tube mould. The centrifugal forces acting on the solidifying metal constrained any casting voids to the inner wall of the tube, which can then be removed by inside machining. On the other hand, controlling the temperature of the casting mould will influence the solidification process and thus the grain structure of the tube wall. Manufacturers typically desire to produce a reformer tube wall having 30% equiaxed structure along the inside wall where creep damage usually originates, and the presence of the equiaxed structure is believed to be a hindrance to creep crack propagation [9]. Together with centrifugal casting and inside machining processes, it is believed that tube failures due to internal pressure will be reduced [9]. Figure 2.5 shows a typical macrostructure of a reformer tube with a mixture of equiaxed and columnar structures.

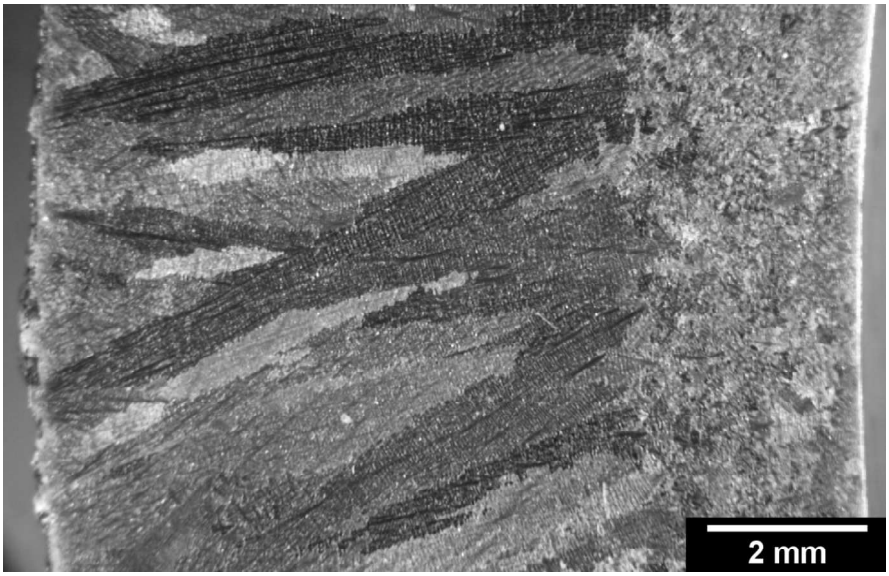

Figure 2.5: Typical macrostructure of a centrifugal cast reformer tube showing both the equiaxed and columnar grains. Alloy is an HP-Nb modified grade produced by Schmidt-Clemens Spain S.A.

It should be noted that development of reformer tube materials is actively ongoing and not confined to the methods discussed here. Various alloying combinations are being actively pursued and changes in manufacturing methods incorporating heat treatments are also being tested to further extend the service life of reformer tubes [9].

2.3 Overview of Creep Deformation in Metals

Creep is a permanent deformation that occurs more prominently in materials stressed at high temperature over an extended period of time. In metals, creep deformation usually becomes a significant issue when the metal is subjected to temperatures about 40 percent of its absolute melting temperature. Creep failure is said to have happened when a component exhibits excessive deformation that interferes with its function, or when the component fractures as a result of the creep process (creep rupture). A more detailed discussion on creep and its related topics can be found in various texts and papers (see for example [6, 16-18]). The discussion presented here is simply a brief overview of creep and will cover mainly basic concepts pertinent to the research work.

In a recent overview paper, Nabarro [18] classified creep in commercially pure polycrystalline metals subjected to constant stress into four stages: immediate extension occurring during loading, decelerating creep region called Andrade β creep, steady state creep region labeled Andrade κ creep, and accelerating creep region that leads to failure. These regions are shown schematically in Figure 2.6 and are typical of laboratory tests conducted under constant loads. The initial instantaneous extension occurs during loading and this strain ε_o is usually elastic but may also contain a plastic component if the initial stress is greater than the yield strength of the material. The next stage is the Andrade β creep, also referred to as primary creep or transient creep. In this stage, the strain rate is initially high but decreases as time and total strain increases, and this behavior is often described by the equation $\varepsilon = \beta t^{1/3}$, where β is a constant and t is time. As the strain rate decreases to a constant value, creep deformation enters the Andrade κ creep stage, otherwise known as secondary or steady state creep. The secondary stage persists for much longer than the other stages and therefore is more important in terms of engineering significance. This region is described by the relation $\varepsilon = \kappa t$, where κ is the material constant called the minimum creep rate. As time and total strain increases further, creep deformation enters a final phase where creep rate increases until rupture occurs. This regime of structural damage is commonly referred to as tertiary creep.

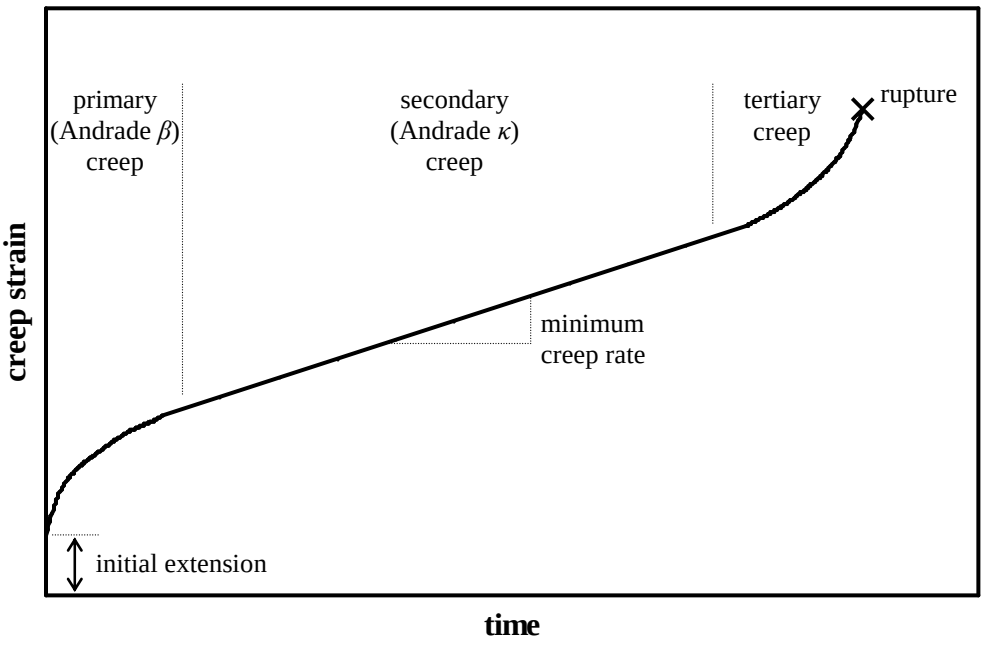

Figure 2.6: Three stages of creep typical of creep test performed under constant load.

Various types of creep tests can be set up to obtain useful creep properties for design. Creep-rupture tests performed on samples under constant uniaxial loading produce creep curves such as the ones shown in Figures 2.6 and 2.7a. This type of test requires strain measurement to be carried out during the duration of the test until failure occurs. The creep-rupture test measures creep deformation as a function of time until failure occurs for a given stress level. For example, the curves in Figure 2.7a shows the effect of stress and temperature on creep properties of a eutectic bismuth-tin solder alloy [19]. An assortment of information can be gathered from creep-rupture tests including time-to-rupture, strain-at-rupture, amount of primary and secondary creep, time to onset of secondary and tertiary creep, steady-state creep rate, and so forth [6]. In some instances, the test would be stopped prior to sample failure, and in this case the test is simply referred to as interrupted creep tests. A simpler type of creep test can also be carried out without strain measurements where samples are placed under a constant load until rupture occurs. In this case only the time-to-rupture and strain-at-rupture data would be obtained. These tests are referred to as stress-rupture tests and produce stress-rupture creep curves such as the ones shown in Figure 2.7 for eutectic bismuth-tin solder alloy [19].

Creep tests are usually performed for up to 1000 hours (41.7 days) and are rarely done for longer lifetimes. In order for the short-life test data to be useful in engineering applications, extrapolations to actual service conditions are required and typically involve the so-called time-temperature parameters. Various approaches for the time-temperature parameters have been proposed such as the Sherby-Dorn, Larson-Miller, and the Manson-Haferd parameters (see [17]). For reformer tube materials, the Larson-Miller parameter approach (commonly referred as *LMP*) is most common. The Larson-Miller parameter is given by the equation $LMP = T(\log t_r + C)$, where T is absolute temperature (K), t_r is the time-to-rupture (hours), and C is a constant. Figure 2.8 graphically shows the determination of the constant C from a plot of time to rupture vs. the inverse of absolute temperature for various stress levels. The value of C is usually close to 20. Once the constant C is obtained, a plot of stress σ vs. *LMP* can be created (for example see Figure I.2 in Appendix I) where time-to-rupture can be estimated for any given temperature and stress level. Similarly for any given stress level and rupture life, the maximum application temperature can be determined.

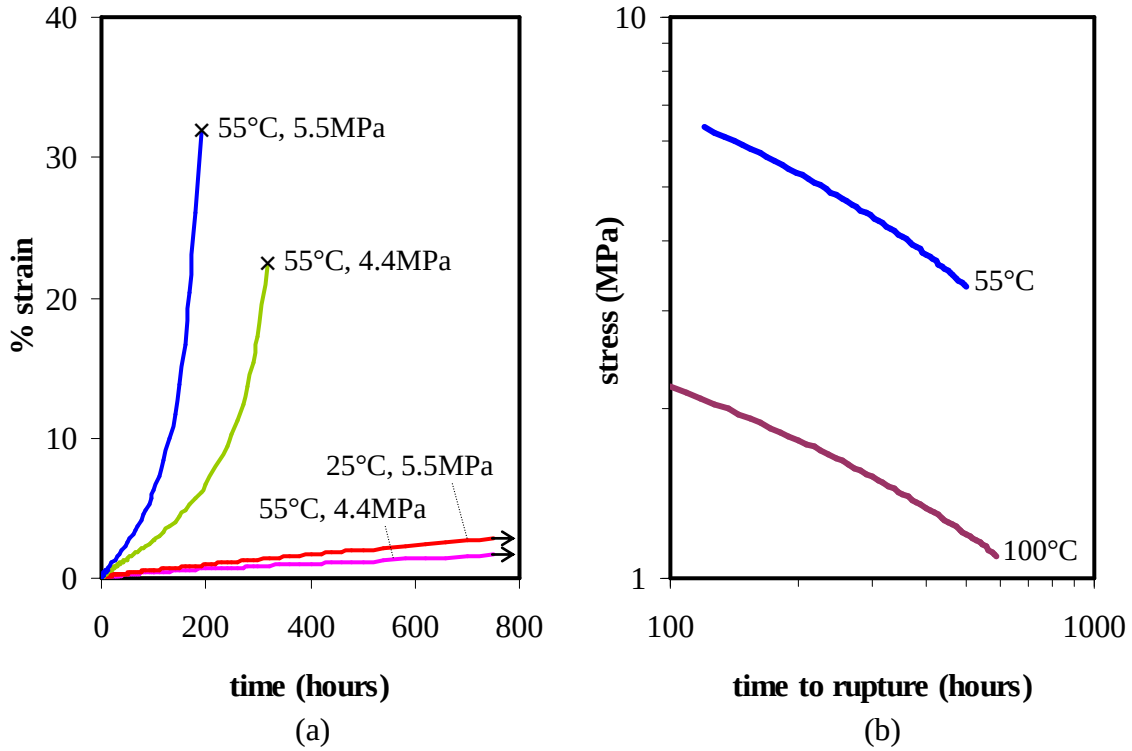

Figure 2.7: Presentation of creep-rupture and stress-rupture test data in (a) and (b) respectively. Data is for eutectic Bi-Sn solder alloy. Note in (a), an "×" indicates a ruptured sample while an arrow specifies an interrupted creep test.

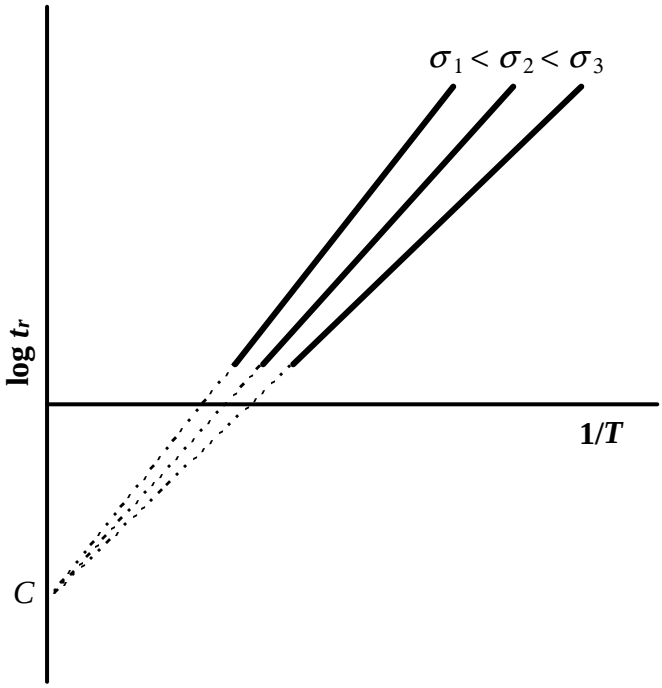

Figure 2.8: Graphical representation of the Larson Miller parameter and the determination of the constant *C*.

The physical mechanisms by which materials deform due to creep are dependent on the various combinations of stress and temperature. In various metallurgy textbooks, creep mechanisms occurring in metals are usually categorized into two general classes called diffusional flow creep and dislocation creep [16, 17]. Diffusional flow creep occurs at low stresses and high temperatures, and this mechanism requires the motion of vacancies. Conversely, dislocation creep, as the name implies, involves the movement of dislocations and requires much higher stresses. Under the two classes listed above, various creep mechanisms are described and given names such as Nabarro-Herring creep and Coble creep which are diffusional flow creep, dislocation glide creep and dislocation climb creep which are dislocation creep, and Harper-Dorn creep and grain boundary sliding which in general are a combination of both diffusional flow and dislocation creep. In reformer applications, the reformer tubes are subjected to temperatures approaching 75% of the absolute melting temperature of the material, while having to withstand service for 100,000 hours at relatively low stress levels. Assuming a maximum allowable creep strain of 3% during the life of the tube, the creep rates are on the order of 8×10^{-11} s^{-1} where the typical creep mechanisms can be classified as diffusional flow creep, Harper-Dorn creep, or grain boundary sliding [20, 21].

As previously mentioned, diffusional flow creep may happen at low stress levels but requires fairly high temperatures to allow for motion of vacancies in the lattice. Grain boundaries can be generally viewed as areas of lattice mismatch, and thus would contain a high concentration of vacancies. Under an applied tensile stress, grain boundaries perpendicular to the stress direction will be in tension and this would assist in the formation of more vacancies at these boundaries. Meanwhile the boundaries parallel to the applied stress will be in compression and would inhibit vacancy formation. This process is shown schematically in Figure 2.9. As a consequence, there will be a net migration of atoms near the boundaries in compression to the grain boundaries in tension, which also results in the migration of vacancies in the opposite direction (Figure 2.9a). Continuous motion of atoms and vacancies would eventually lead to permanent deformation of the grains in the direction of the applied stress (Figure 2.9b).

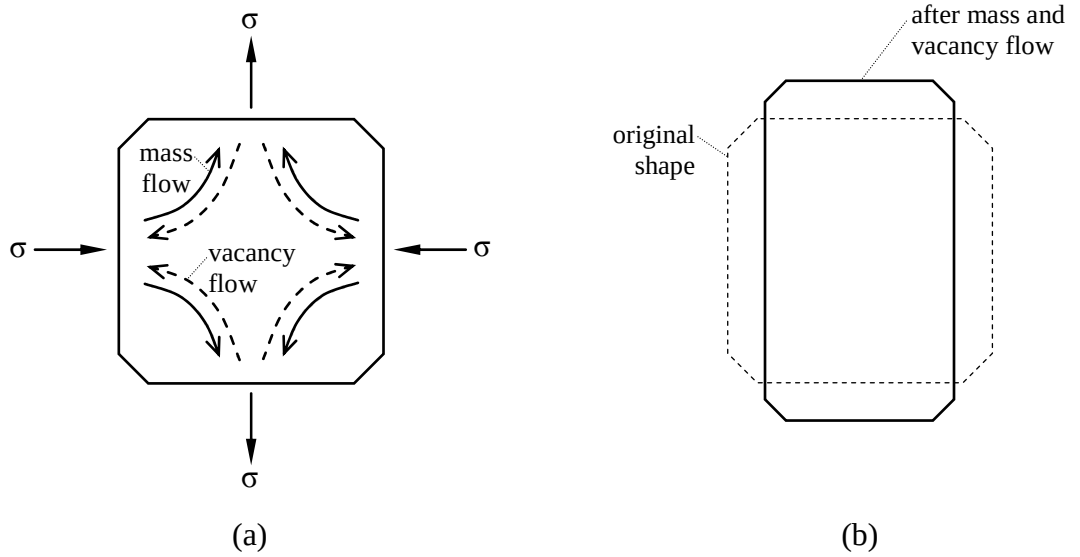

Figure 2.9: Diffusional flow creep deformation resulting from motion of atoms and vacancies. (a) Atoms migrate from boundaries in compression to boundaries in tension while vacancies move in the opposite direction; (b) over time, a net change in grain dimension will occur.

Creep deformation resulting from motion of atoms and vacancies through the crystal lattice (transgranularly) is called Nabarro-Herring creep, while deformation due to motion along grain boundaries is referred to as Coble creep. Creep-strain rates of both Nabarro-Herring and Coble creep are proportional to stress; however Nabarro-Herring creep is inversely proportional to the square of the grain size while Coble creep is inversely proportional to the cube of the grain size. Coble creep appears to be the more probable deformation process in many applications involving polycrystalline materials because the temperature may not be high enough for transgranular atomic and vacancy migration, and hence these migrations only occur along grain boundaries [22].

The description of the mechanism of Harper-Dorn creep and its occurrence in crystalline materials is somewhat more ambiguous due to some disagreement between various researchers [20, 23, 24]. However, the generally accepted characteristics of the Harper-Dorn creep are that it occurs at very low stresses, and although its creep-strain rate is proportional to stress as in Nabarro-Herring and Coble creep, the rate is independent of the grain size. Furthermore, the creep rate is higher than Nabarro-Herring creep by a factor of two or more and is proportional to the dislocation density [20, 24]. Nabarro [21] describes the mechanism of Harper-Dorn creep as a migration of vacancies from dislocations with

their Burgers vector parallel to the tensile axis to dislocations with Burgers vectors perpendicular to the stress axis. It is also believed that Harper-Dorn creep is a unique mechanism occurring under certain low stress conditions and this mechanism cannot be explained either by diffusional flow creep or the dislocation glide and climb mechanisms [20, 23].

During high temperature creep, the deformation of individual grains may also lead to relative displacements between adjacent grains and this phenomenon is referred to as grain boundary sliding. The theory behind grain boundary sliding is probably the least understood of all three low-rate creep mechanisms; however two types of grain boundary sliding mechanisms are usually described [16, 21]. The first one is called primary grain boundary sliding which occur at strain rates proportional to the square of the stress and inversely proportional to the square of the grain size. Primary grain boundary sliding occurs at boundaries located at 45° with respect to the stress axes where shear stress is highest [21]. The second type of grain boundary sliding occurs in conjunction with diffusional creep and is called “accommodation grain boundary sliding”, where additional diffusion occurs along the grain boundaries. The rate of diffusional creep is matched by the rate of accommodation grain boundary sliding in order to prevent cracks or voids from forming. This type of grain boundary sliding is most significant on grain boundaries parallel or perpendicular to the tensile stress axes. It is also important to note that accommodation grain boundary sliding creep would be inhibited by the presence of precipitate particles along the grain boundaries.

When sufficient time has passed, creep deformation will ultimately result in fracture. High temperature fracture can occur in three different modes – rupture, transgranular creep fracture, and intergranular creep fracture [16]. Rupture is accompanied by a high reduction in area (close to 100%) and happens at high stress and high temperature. It is believed that dynamic recovery and/or recrystallization takes place preventing the formation of internal voids which consequently allows the material to be capable of high reductions in area. Transgranular creep on the other hand is analogous to low temperature ductile fracture where internal cracks and voids form at highly stressed locations of the microstructure and coalesce. The fracture is ductile and the appearance of the fracture surface is very similar to ductile fracture at lower temperature. The third type of high temperature fracture is

intergranular creep which occurs at stress levels much less than those of rupture and transgranular creep fracture. In this fracture mode, cracks and voids forms along grains boundaries and coalesce to fracture in a brittle manner. Wedge-like cracks (or "w" voids) are believed to occur at higher stress levels than spherical shaped voids (or "r" voids). However, in some instances, wedge cracks are also thought to be the consequence of the accumulation of spherical voids [25]. Cracks and voids are usually associated with inclusions or precipitates. It is believed that the presence of these particles along the grain boundaries prevents the rate of accommodation grain boundary sliding from matching the deformation rate of diffusional creep thereby allowing cracks and voids to form at the grain boundaries [16, 21].

2.4 Brief Discussions on Void Growth Models

As mentioned in the previous section, it is believed that during high temperature creep, the presence of precipitate particles inhibits the rate of accommodation grain boundary sliding from matching the rate of diffusional creep, resulting in the formation of cracks or voids along the grain boundaries. This mechanism of void nucleation is still not well understood [25], nevertheless, the review papers by Goods and Brown [26], and [25] presented several void nucleation models. One major conclusion that was presented in the Goods and Brown [26] paper was that at high temperatures, the large amount of dislocation motion allows for plastic relaxation resulting in little local work hardening. As a consequence, nucleation of voids becomes difficult. It is believed that voids that eventually grow and cause failures in high temperature creep applications are formed at low temperature during material processing [26].

Void growth has been studied in some detail and a variety of models is available for treating the kinetics [27-31]. The void growth model presented by Raj and co-workers [27, 28] expands on the opinion that under the proper conditions, grain boundary voids nucleate and grow in size through diffusional motion of atoms and accumulation of vacancies [32]. These voids will then coalesce resulting in intergranular fracture. Their mathematical model is unique due to the fact that the model accounts not only for stress, temperature, and void density, but also the various interface energies resulting from different void configurations attributable to either microstructural locations of the voids or the configuration of the void-precipitate interface. This exceptional feature of the model

makes it most suitable for modeling creep void growth where the presence of precipitates along the grain boundary may be responsible for the formation of voids. The general equation of the void growth model given by Raj and co-workers is listed below (see [27, 28] for complete derivation of the equation):

Essentially, this equation accounts for the motion of atoms along the grain boundaries, the loading conditions experienced by the interface containing the voids, and finally the geometry of the voids at the grain boundary. A more detailed discussion of this equation will be given in Chapter 7.

$$\frac{dV}{dt} = 2\pi \frac{\Omega D_B \delta}{kT} \left(\sigma_\infty + p_v - \frac{2\gamma}{r_v} \right) \frac{\left(1 - \frac{r_B^2}{l^2} \right)}{\ln\left(\frac{l}{r_B} \right) - \frac{3}{4} + \frac{r_B^2}{l^2}\left(1 - \frac{r_B^2}{4l^2} \right)}$$

Other void growth models mentioned in the previous paragraph are also elegant but their application to experimentally obtained data can be rather complex. The differential equation model given by Cocks and Ashby [30] for instance, expands the work of Raj [27] and determines void growth via mechanisms of grain boundary diffusion, surface diffusion, or power-law creep, or via a combination of any two of these mechanisms. The model can also account for multiaxial stress states and the results are usually displayed on void growth maps. Several variations of the differential equation-based void growth model were also discussed in the review paper by Kassner [25]. Void growth models based on finite element modeling can also be found in the literature such in the ones presented in papers by Needleman and Rice [29] and Pardoen and Hutchinson [31].

2.5 Three-Dimensional Analysis of Materials

In materials science, it is often vital to study the microstructural features of a material in order to assess the constituents present and how they may interact with each other. Typically, a small representative sample of the material is obtained and prepared using standard metallographic methods, before being observed and photographed in an optical or scanning electron microscope. The characterization process then takes place from two-dimensional microscopic images and any information attained is extrapolated to the material bulk. This exercise is often adequate for homogeneous materials but in non

homogeneous materials, the full picture of the microstructure may be obscured. A common practice for non homogeneous material is then to acquire, prepare, and photograph samples from three orthogonal orientations of the bulk material and the resulting information are “combined” to provide a three-dimensional representation of the microstructure. This technique is usually sufficient for revealing general characteristics of a microstructure, but to fully show the size, shape, distribution, and connectivity of microstructural features requires proper three-dimensional observations.

The earliest known 3D analysis of microstructures was done in 1918 by Forsman [33] who employed the method of serial sectioning to study the 3D structure of pearlite. By making cardboard cutouts of features in each serial section layer and attaching these cutouts together, 3D representations of cementite lamellae were created. A later work in 1960s employed a combination of serial sectioning and motion pictures to show the structure of pearlite in three dimensions [34]. Early 3D microscopy research usually involved serial sectioning and some form of laborious physical or graphical reconstruction method, or the use of expensive motion picture techniques to represent microstructures in three dimensions. In order to reduce the time required for the serial sectioning processes, semi and fully automated apparatus have been introduced. Furthermore, in the 1990s, improvements in computer image processing and visualization capabilities allowed for better 3D observations of serial section images. For instance, Hull and co-workers [35] employed CAD/CAM software called CATIA to reconstruct several titanium prior-beta grains in three-dimensions.

The process of three-dimensional microscopy can be divided into three key segments: acquisition of a series of 2D images; processing of 2D images; and 3D reconstruction and visualization. Among the techniques used to obtain the 2D images, serial sectioning is possibly the least complicated and the most widely used method. In that method, a set of images (usually referred as the image stack) is obtained by consecutively imaging the same region of interest as a specific increment of depth of material is removed. Two important factors to consider during serial sectioning are the depth of each section and the placement of fiducial marks. The section depth is usually set to either between 0.05μm and 1.0μm for manual or semiautomated polishing methods or between 1.0μm and 20μm for micromilling methods [36]. The value chosen is dependent on the rate of material removal and the

microstructural features to be examined for the specific sample. Fiducial marks are typically microhardness indents, and they are used primarily in manual and semiautomated polishing cases. The purpose of these indents is threefold: mark out a region of interest; track the material removal rate; and align (register) the subsequent image set [36]. Further items to consider for the serial sectioning method are sample etching, image resolution, and the total number of serial section images to be obtained.

Other techniques used for obtaining 2D images are typically more complex and expensive. For example, focused ion beam (FIB) devices raster scan a beam of ions that sputters off a layer of material in each pass. This method allows for finer serial sectioning depth enabling high resolution observations and analyses of 3D features. A recent variation of the FIB device is the dual beam FIB-SEM instrument which has separate ion and electron columns. The separate electron column allows for the integration of other analysis tools such as the electron backscatter diffraction (EBSD) detector which enabled complex work such as the combined analysis of 3D morphology and crystallographic information for superaustenitic stainless steel [37]. Another technique used to generate series of 2D images for reconstruction is the x-ray microtomography technique. This method uses x-rays to non-destructively penetrate samples and obtain series of images at various positions within the sample. Various contrast mechanisms can be employed to generate the necessary image stack, and a general description of these mechanisms is available in ref [36].

For manual and semiautomated serial sectioning, an additional procedure of image alignment or registration is usually required before the image stack is ready for other forms of image processing. In this procedure, the first serial section image is used as the reference and the second image is then overlayed on top of the first image for comparison. By translation and rotation of the second image, the fiducial marks in the second image are made to coincide with the ones in the first image indicating that the second image is then registered to the first image. The same process is repeated for every subsequent image until the entire image stack has been registered. Some software packages or plugins perform the image registration procedure automatically (for example the StackReg plugin [38] inside NIH ImageJ [39]). Note that this image registration procedure is not required if

the series of 2D images were obtained at the same sample positions, which was inherent in more complex setups such as the dual-beam FIB-SEM.

Once a set of registered images is obtained, the next stage of 3D microscopy is the processing of these images. Processing of image stacks usually involves some method of highlighting the features of interest. Various public domain and commercial image processing software packages such as GIMP and Adobe Photoshop® are suitable for these purposes. In general, features of interest in each micrograph is usually "extracted" away from the surrounding and stored in its own image file. The same highlighting process (also called masking) is carried out for the entire series of images to generate a new image stack containing only the feature of interest.

The final stage of 3D microscopy is reconstruction and visualization of microstructural features. Again, a variety of public domain and commercial software are available for 3D reconstruction and visualization. In simple terms, 3D reconstructions are usually done by forming 3D surfaces from the outlines of the highlighted features. These outlines act as surface contours which are enclosed by the 3D surface. Some interpolation or smoothing between the layers is necessary to create a coherent image. Another method of 3D reconstruction is the ray-tracing method which produces very detailed and convincing images. A more detailed explanation on the various 3D reconstruction methods is given by Foley [40]. Finally, visualization of the 3D microstructure is usually done using the same software that generated the 3D reconstructions. The software usually includes some form of a viewing window complete with image manipulating tools such as zoom, pan, and rotate that allows the 3D reconstruction to be viewed from any perspective. Only then can the true shape, distribution, and connectivity of microstructural features be fully observed and studied.

The continued advancement in computer hardware and software has made the adaptation of 3D microscopy techniques easy and affordable for any metallurgy research facility. Essentially, in addition to normal sample preparation equipment and consumables, the only additional items required to begin doing basic 3D microscopy are a standard PC and image processing software.

Chapter 3

MATERIALS CHARACTERIZATION

A major portion of the experimental work was dedicated to the characterization of the reformer tube material which was critical in order to correctly determine all the microstructural features present. Once all the microstructural constituents were identified, the 3D reconstruction of the microstructure could then be properly performed. The characterization methods employed here include optical microscopy (OM), scanning electron microcopy (SEM), energy dispersive spectroscopy (EDS), electron backscattered diffraction (EBSD), transmission electron microscopy (TEM), selective area diffraction (SAD), and x-ray diffraction (XRD).

3.1 Reformer Tube Samples

The reformer tubes studied in this work were fabricated from Schmidt-Clemens Centralloy® CA4852-Micro centrifugal cast austenitic stainless steel tubes. This tube material is based on the standard heat resistant HP-type casting alloy containing 0.35-0.75 weight percent (wt%) C, 2.00 wt% (max) Si, 24-28 wt% Cr, 33-37 wt% Ni, and 2.00 wt% (max) Mn [6]. Chemical composition for Centralloy® CA4852-Micro is listed in Table I, showing that the material is within the specifications of an HP casting alloy and with small amounts of Nb and Ti. As discussed previously in Chapter 2, the additions of Nb and Ti in HP50-type alloy have been shown to improve the high temperature strength of the material and the presence of these elements was also shown to improve carburization resistance of this alloy during high temperature service [6, 9] (refer to Appendix I for typical properties of CA4852-Micro).

Table I: Main alloying elements (in wt%) present in Schmidt-Clemens Centralloy® CA4852-Micro. Remainder is Fe and other minor alloying elements [41].

%C	%Si	%Cr	%Ni	%Mn	%Nb	%Ti
0.45	1.50	25.0	35.0	1.00	1.50	additions

Each reformer tube in a typical steam-methane reformer has a diameter of approximately 125mm, wall thickness of 10mm, and an overall length of 13.5m, which is fabricated from three 4.5m segments that are welded together. The samples received for this work were obtained as 200mm long tube segments removed from various positions along several reformer tubes with known service histories. A segment of an as-cast tube that did not experience any high temperature exposure was also obtained for comparisons. A polished and etched cross-section of the reformer tube wall showing a typical macrostructure is shown in Figure 3.1 (Marble's reagent macroetch). The inner wall on the right-hand side of the image shows small equiaxed grains occupying approximately twenty percent of the wall thickness while the rest of the tube wall consists of large columnar grains that extend radially towards the outer wall.

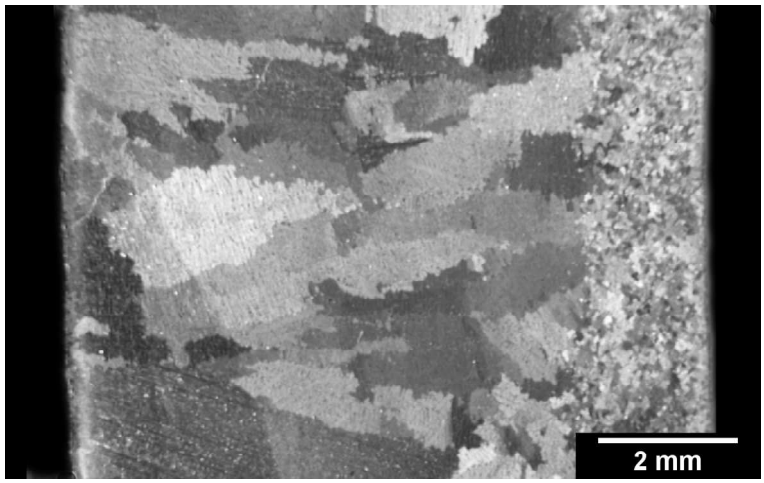

Figure 3.1: Cross-section of reformer tube wall showing the typical macrostructure consisting of fine equiaxed grains along the inner wall region and large columnar grains for the remaining wall thickness.

For HP-type 25Cr-35Ni centrifugal casting alloys containing Nb and Ti additions such as the CA4852-Micro, various precipitates have been reported for these alloys in the aged or ex-service conditions [11, 42-44]. In general, Cr-rich $M_{23}C_6$ precipitates are commonly observed as coarse intergranular precipitates along the grain and dendritic boundaries, and also as fine secondary intragranular precipitates. Another precipitate regularly reported in the literature is MC in the form of NbC, TiC or (Nb-Ti)C which may appear in the grain and cell boundaries or intragranularly. In alloys containing silicon, a silicide known as G-phase, may also develop from transformation of primary NbC at high temperatures [11, 42, 43]. During the characterization process, the various precipitates observed in the microstructure would be first assessed against the above mentioned candidates before being compared to other carbides or silicides which contain the same elements present in the observed precipitates. Various techniques would be utilized to ensure the proper identifications of all the precipitates observed.

3.2 Optical and Scanning Electron Microscopy of Precipitates

Curved sample blocks approximately 20×20×10-mm (arc-length × height × wall thickness) were removed from the as-received tube segments using a Buehler water-cooled abrasive cutter. Sample surfaces to be studied were next cut from these blocks using a Buehler Isomet® 11-1180 low-speed diamond saw (with oil as the lubricant). The low-speed diamond saw was used in order to minimize any surface deformation that might otherwise be introduced during the cutting process. The 10×10×10-mm samples were then mounted in Buehler Epomet® compound at 2000psi (13.8MPa), 180°C for 5 minutes in a Buehler manual mounting press. Using a Leco AP-60 automatic polisher, the 50mm diameter mounted samples (see Figure 3.2) then underwent grinding and polishing steps listed below (adapted from ref [45]):

1. Successive grinding steps using 240-grit and 400-grit SiC paper with water as the lubricant. A load of about 5lbf (4.4N) per sample was used with a turntable speed of 240rpm. Grinding time for 240-grit was approximately 10 minutes (or until the samples were planar) and 5 minutes for 400-grit.
2. Consecutive polishing steps using water-based Buehler MetaDi® 9, 3 and 1-μm diamond polishing compound and suspension on Buehler Trident® cloth. A load of 5lbf (4.4N) per sample and a speed of 120rpm were employed for each 5-minute polishing step.

3. Final polish step using Buehler MasterMet® 0.06µm colloidal silica suspension. The load, wheel speed, and polishing time were maintained at 5lbf (4.4N), 120rpm, and 5 minutes respectively for each step.

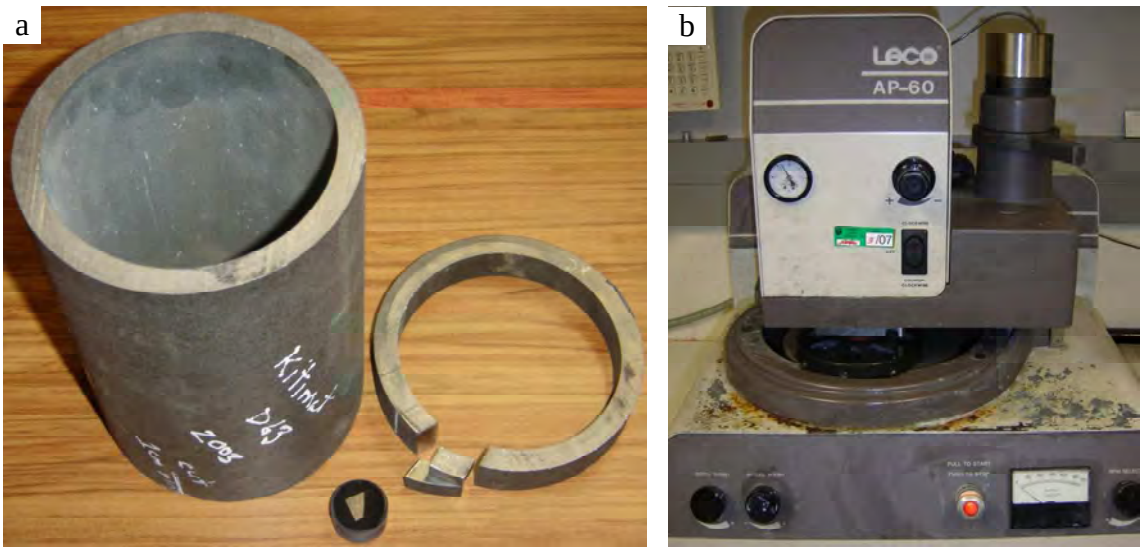

Figure 3.2: Preparation of metallography samples. (a) Removal of sample from the reformer tube segment to make a metallography mount; (b) Leco automatic polisher used for grinding and polishing of samples.

For optical microscopy examinations, samples were etched by a 60-75s immersion in freshly prepared glyceregia [46] (10ml glycerol + 15ml HCl + 5ml HNO_3). Several other etchants (Murakami's reagent, aqua regia, Kalling's reagent, among others), were also tested to reveal the reformer tube microstructure, but glyceregia was found to be the ideal etchant because it did not preferentially attack any of the phases present. In addition the etching results were easily reproducible from sample to sample provided a freshly prepared solution was used each time. On the contrary, Murakami's reagent was found to preferentially attack a particular precipitate (later found to be NbC) but otherwise produced an excellent color-etched microstructure. The other etchants tested were also found to attack particular features of the microstructure especially the fine precipitates. Optical microscopy observations were then done using a Leica DM-Inverted Research Microscope and brightfield images were captured with a Zeiss Axiocam digital camera connected to an Apple Power Macintosh G3 computer.

The optical micrograph in Figure 3.3a reveals the general microstructure of an ex-service tube consisting of a network of coarse grain and dendritic boundary precipitates and a scattering of fine intragranular precipitates. Several voids are also apparent in this image. The higher magnification image in Figure 3.3b shows three coarse precipitate types, tentatively labeled *A*, *B* and *C*, that would be identified later. Precipitates *A* and *B* appeared as light blue and grey respectively, and they were usually found along grain boundaries and dendritic positions. Precipitate *C* appeared as orange-brown and was usually observed intragranularly. The fine precipitates observed appeared as light blue in color. A small void appearing next to a type *A* precipitate is also highlighted in Figure 3.3b.

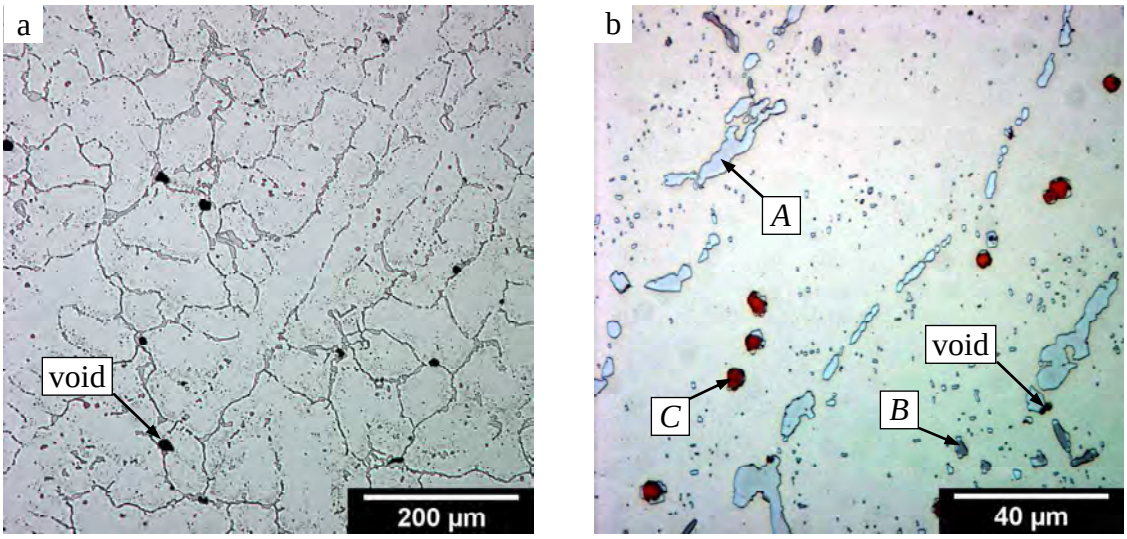

Figure 3.3: Microstructure of ex-service reformer tube. (a) Low magnification image of sample etched in glyceregia; (b) higher magnification image revealing three distinct precipitates *A*, *B*, and *C*.

The same area of the sample seen in Figure 3.3b was also observed in the SEM in backscatter electron (BSE) mode, as shown in Figure 3.4a. Precipitates were first characterized using the EDS technique. The equipment employed for SEM and EDS examinations are JEOL JSM-6100 Scanning Electron Microscope and Moran Scientific QXAS QUOLL Quantitative X-ray Analysis Unit. An accelerating voltage of 20kV and a working distance of 39mm were utilized for all observations. The same precipitates specified in Figure 3.3b are again indicated in Figure 3.4a and their corresponding EDS spectra are shown in Figures 3.4b-d. Based on the EDS spectra, precipitates *A*, *B*, and *C* were identified to be rich in Cr, Nb, and Ti respectively. Knowing the elements present in

the precipitates, a list of possible candidates was generated from various sources [47-64] listed in the Pearson's Handbook [65]. The list of possible precipitates is shown in Table II.

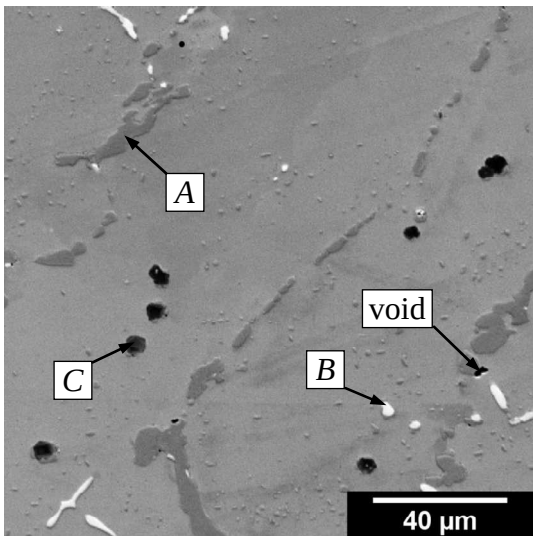

(a) BSE image of reformer tube;

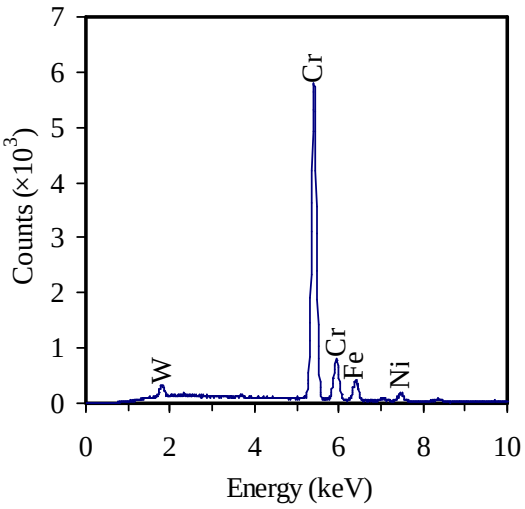

(b) EDS spectrum of precipitate *A*;

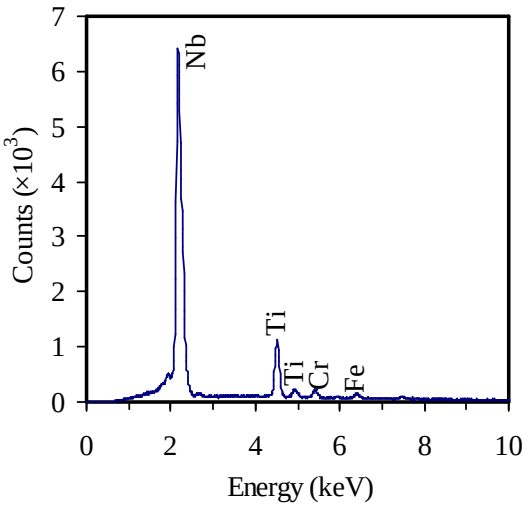

(c) EDS spectrum of precipitate *B*;

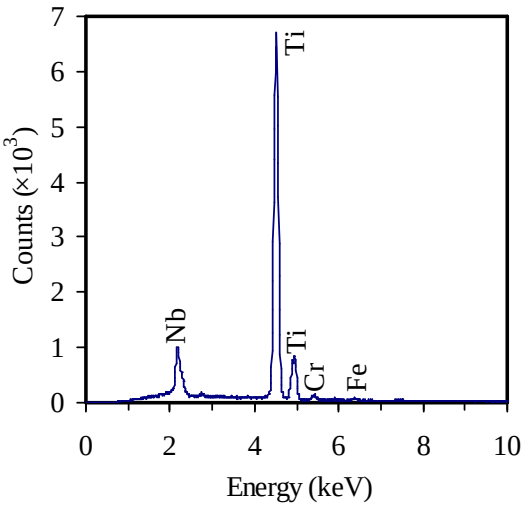

(d) EDS spectrum of precipitate *C*.

Figure 3.4: Backscatter electron (BSE) image of ex-service reformer tube and the corresponding EDS spectra of precipitates *A*, *B*, and *C*.

Table II: List of candidate compounds used to determine the unknown precipitates.

Compound	Space Group	Crystal System	Lattice Parameters – a_1, a_2, a_3 (nm)			α_1, α_2, α_3 (°)			Ref.
$Cr_2Fe_{14}C$	225	cubic	0.72004	0.72004	0.72004	90	90	90	[47]
Cr_3C	62	orthorhombic	0.512	0.680	4.580	90	90	90	[48]
Cr_3C_2	62	orthorhombic	0.55329	0.2829	1.1472	90	90	90	[49]
Cr_7C_3	62	orthorhombic	0.45265	0.70105	1.2142	90	90	90	[50]
$Cr_{23}C_6$	225	cubic	1.065	1.065	1.065	90	90	90	[51]
NbC	225	cubic	0.447	0.447	0.447	90	90	90	[52]
NbNiSi	62	orthorhombic	0.62232	0.36831	0.70882	90	90	90	[53]
$NbNiSi_2$	139	tetragonal	1.263	1.263	0.486	90	90	120	[54]
Nb_2C	194	hexagonal	0.3125	0.3125	0.4963	90	90	120	[55]
Nb_2Ni_3Si	194	hexagonal	0.480	0.480	0.780	90	90	120	[56]
Nb_3Ni_3C	227	cubic	1.1659	1.1659	1.1659	90	90	90	[57]
Nb_4C_3	221	cubic	0.44451	0.44451	0.44451	90	90	90	[58]
Nb_6C_5	144	trigonal	0.54641	0.54641	1.15422	90	90	120	[59]
$Nb_6Ni_{16}Si_7$	225	cubic	1.125	1.125	1.125	90	90	90	[60]
$Nb_9Ni_{20}Si$	194	hexagonal	0.4811	0.4811	0.8023	90	90	120	[61]
TiC	225	cubic	0.43271	0.43271	0.43271	90	90	90	[62]
Ti_2C	227	cubic	0.86	0.86	0.86	90	90	90	[63]
Ti_8C_5	166	trigonal	0.6115	0.6115	1.490	90	90	120	[64]

3.3 X-ray Diffraction of Precipitates

X-ray diffraction (XRD) method was used to confirm the identity of both the coarse and fine precipitates found in the samples. Rectangular slices approximately 10×10×1-mm were taken from the tubes and immersed in beaker containing 30ml glyceregia solution to dissolve away the austenite matrix. Since glyceregia becomes more dangerously reactive with time, the solution had to be replenished every two hours until all the austenite matrix had completely dissolved. The entire immersion time to dissolve the austenite matrix took approximately sixteen hours. Pouring out the final glyceregia solution, the remaining precipitate particles were then carefully retained in the beaker and rinsed - first with water and then with isopropyl alcohol, before being filtered out of the alcohol using a Whatman® GF/C glass microfibre[§] filter paper and left to dry.

The collected precipitates were then scanned in a Philips XRD system[**] consisting of a Philips PW1729 x-ray generator, PW1820 Goniometer, PW1710 Diffractometer Control and a PW2273/20 Copper x-ray tube. The x-ray tube operated at 50kV and 40mA (2kW power) producing Cu Kα radiation with a wavelength of 1.54178Å. The scan was performed at 0.01° steps between 10 and 100°. Identification of the precipitates was performed by comparing the obtained XRD spectrum against the simulated spectra of various candidate compounds previously listed in Table II. For each possible precipitate, the characteristic peaks of the simulated spectra were generated by Desktop Microscopist 2.2a software[††] using the data obtained from Pearson's Handbook [65].

Figure 3.5 shows the XRD spectrum of the powdered precipitates. The peaks were matched to characteristic peaks of $Cr_{23}C_6$, NbC and TiC. In addition, the lattice parameters for $Cr_{23}C_6$, NbC and TiC precipitates were calculated to be 1.062nm, 0.4425nm and 0.431nm respectively, which are in good agreement with values presented elsewhere [10, 43].

[§] 1.2μm particle retention in liquid at 98% particle retention rating
[**] Equipment located in the University of Canterbury Geology Department
[††] Lacuna Laboratories, Beaverton, Oregon, USA

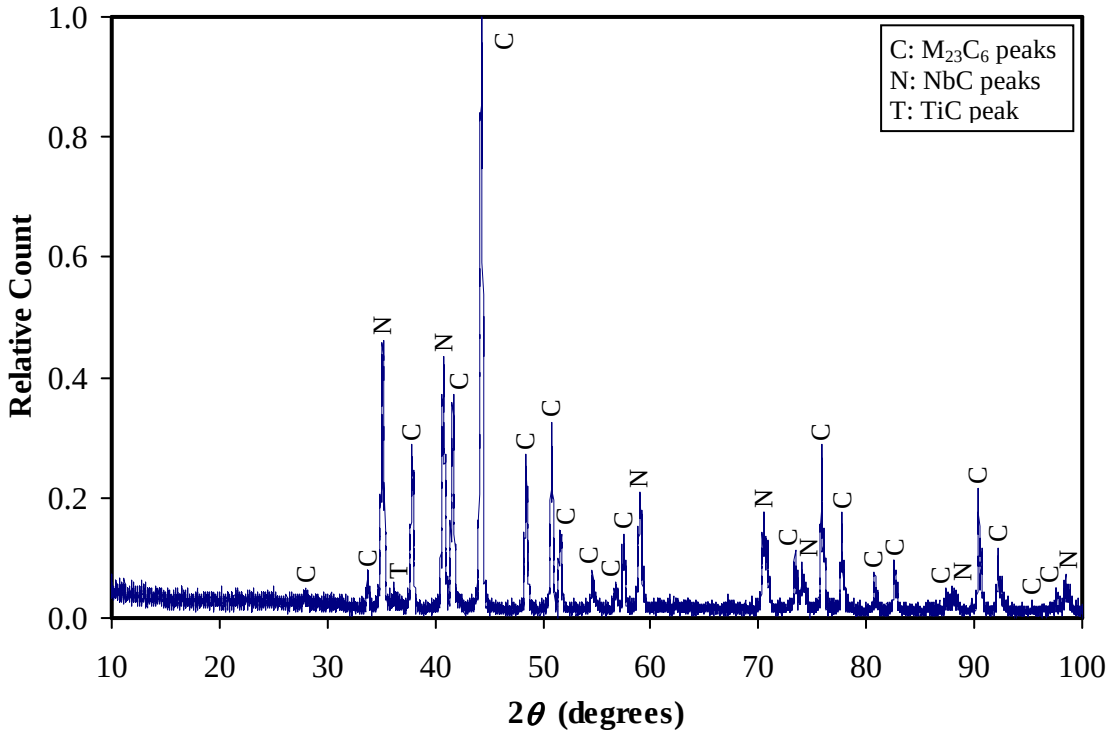

Figure 3.5: XRD spectrum of reformer tube precipitates. $M_{23}C_6$, NbC and TiC peaks are indicated.

3.4 Characterization of Precipitates Using EBSD

The next step of the identification of precipitates employed the EBSD technique, which was performed using the HKL Technology Nordlys II EBSD system attached to the JEOL JSM-6100 Scanning Electron Microscope. Samples were placed in the SEM sample holder tilted at 70° with respect to the electron beam, and viewed scanned an accelerating voltage of 20kV and a working distance of 30mm. The electron backscattered diffraction (EBSD) patterns or EBSPs from these precipitates were obtained and then compared against the list of possible compounds using HKL Technology's Flamenco software, and the best solutions are displayed in Figure 3.6. Referring back to Figure 3.4a, EBSD results indicated that the Cr-rich precipitate *A* is $Cr_{23}C_6$, the Nb-rich compound *B* is NbC, while the Ti-rich precipitate *C* is TiC, confirming the results obtained using the XRD technique. It must be noted that due to the presence of small amounts other elements observed in the EDS spectra of Figures 3.4b-d, the $Cr_{23}C_6$, NbC and TiC precipitates would be more accurately designated as $M_{23}C_6$ and MC respectively. In this thesis however, the terms $M_{23}C_6$, NbC and TiC will be used to classify these precipitates.

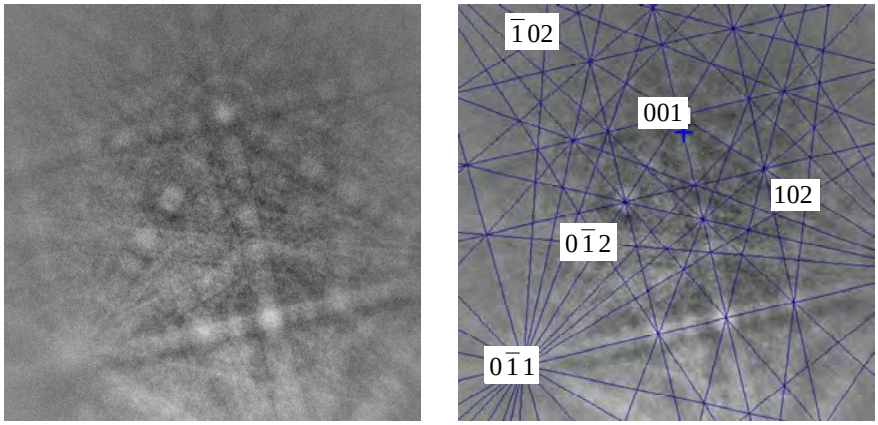

(a) EBSP of precipitate *A* and the simulated pattern of $M_{23}C_6$ structure;

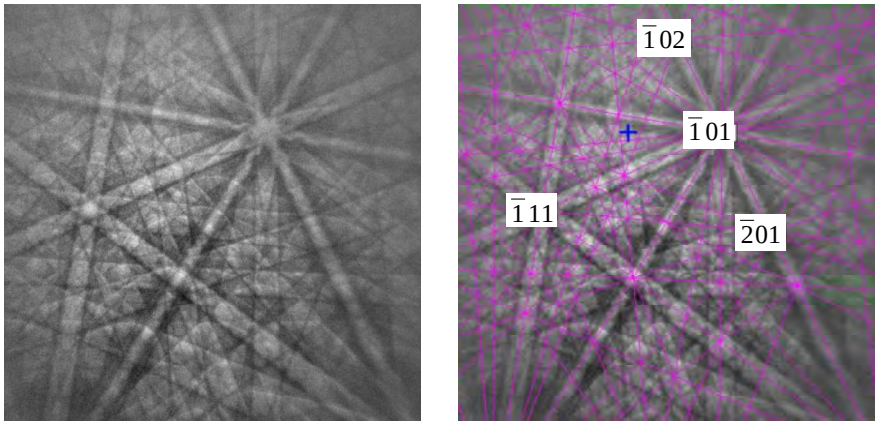

(b) EBSP of precipitate *B* and the simulated pattern of NbC structure;

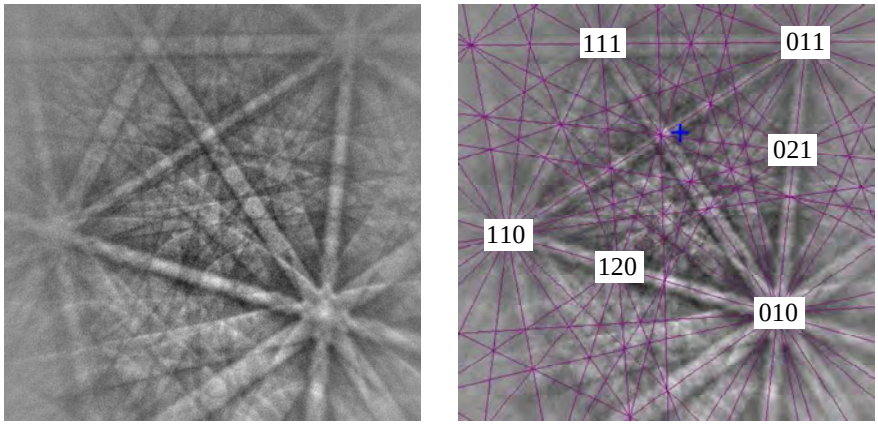

(c) EBSP of precipitate *C* and the simulated pattern of TiC structure.

Figure 3.6: Electron backscattered diffraction pattern of reformer tube precipitates.

3.5 Transmission Electron Microscopy of Fine Precipitates

Transmission electron microscopy (TEM) was used to characterize fine intragranular precipitates observed in the reformer tube microstructure. Samples of the tubes were obtained by cutting slices approximately 400µm thick using a Buehler Isomet® 11-1180 low-speed diamond saw. These slices were then placed in a punching jig to remove 3mm diameter disks. Each disk was then held and sanded in a jig which enabled the thickness of the disk to be further reduced to approximately 100µm. The disks were then thinned in an electrolyte solution of 35% (by volume) n-butyl alcohol, 6% perchloric acid, and 59% methanol at a temperature of -30ºC, voltage of 40V, and current of 25mA [66] using an E.A. Fischione automatic twin-jet electropolishing setup. The polishing temperature was obtained by immersing the electrolyte container in a methanol-liquid nitrogen bath. A light detector cuts off the power when it detects light transmitting through the small perforation made on the sample. Upon completion of the electropolishing step, the sample was cleaned in repeated immersions of methanol. Subsequent thinning was done by ion milling using a Gatan Precision Ion Polishing System[‡‡].

The TEM sample was then placed in a double-tilt sample holder before being loaded into the Hitachi H600 transmission electron microscope operating at 100kV with a filament current approximately 125µA. The perforation made during the electropolishing step was then located using the low magnification “SCAN” mode. Adjacent to the hole will be areas thin enough to be imaged by the TEM. Once located, the area of interest was then observed in “ZOOM” mode to obtain bright-field images. To obtain selective area diffraction (SAD) patterns, the sample must first be made eucentric by coinciding the tilt axes and the center of rotation of the viewed area. This meant that the area of interest remained centered during sample tilting. Using the smallest SAD aperture on the area of interest, SAD patterns were obtained in “DIFF” mode. All images were recorded on Kodak electron microscope film and processed in the darkroom accordingly. Images were obtained by scanning the negatives using an Epson flatbed scanner attached to an Apple Power Macintosh G3 computer.

[‡‡] Equipment located at Pacific Northwest National Laboratory (PNNL), Richland, Washington, USA.

Figure 3.7a shows the bright-field image of a fine intragranular precipitate observed in the reformer tube microstructure. The image shows a rectangular precipitate lying on the austenite matrix with several dislocations impeding on the precipitate. The SAD patterns, which show larger spots positioned at every three smaller spots, are characteristics of a cube-on-cube orientation relationship between the precipitate and the matrix, where the lattice parameter of the precipitates are approximately three times the lattice parameter of the matrix. Using methods outlined in Edington [67] the diffraction spots were indexed and the interplanar spacing was calculated (based on a camera constant of 296.1mm/nm) to be 0.360nm for the matrix and 1.08nm for the precipitate. These values are within less than 7 percent of reported values of 0.339nm for the matrix and 1.111nm for $M_{23}C_6$ precipitate [43]. All the fine intragranular precipitates observed in the TEM were identified as $M_{23}C_6$.

These fine intragranular precipitates were also characterized using a Philips CM30 transmission electron microscope[§§] operating at 300kV. Figure 3.8 shows an atomic resolution image of a Cr-rich fine intragranular precipitate. This image was obtained along a [100] zone axis and measurements of the lattice spacing yielded a lattice parameter value of 1.06nm which agreed with the previous measurements from indexed SAD patterns of $M_{23}C_6$ precipitates.

[§§] Equipment is located at US Naval Research Lab, Washington D.C. Philips CM30 TEM work was done by Associate Professor Milo V. Kral during a sabbatical leave in October 2003.

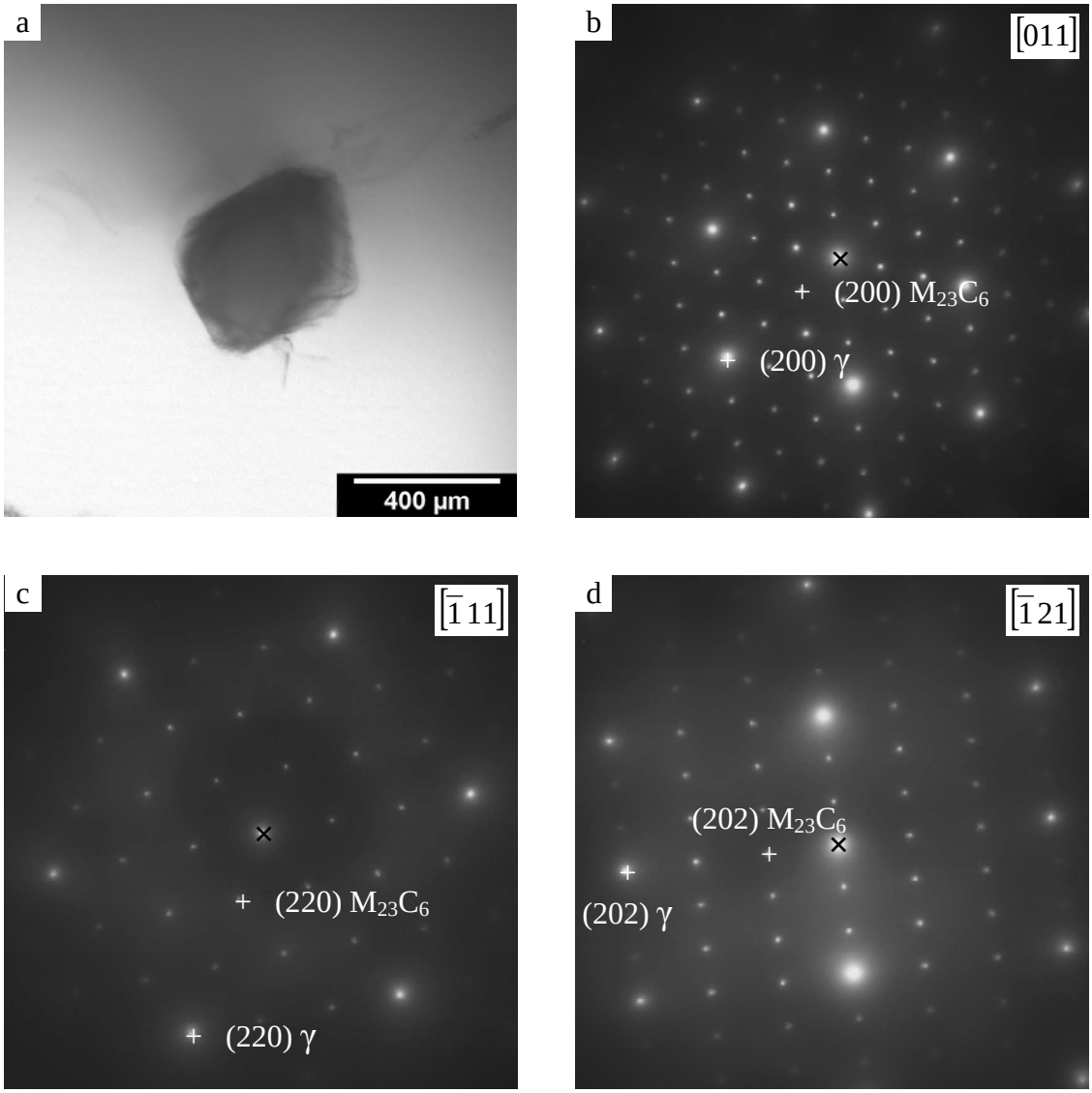

Figure 3.7: TEM bright field image and corresponding indexed SAD patterns of the fine intragranular precipitate identified as $M_{23}C_6$.

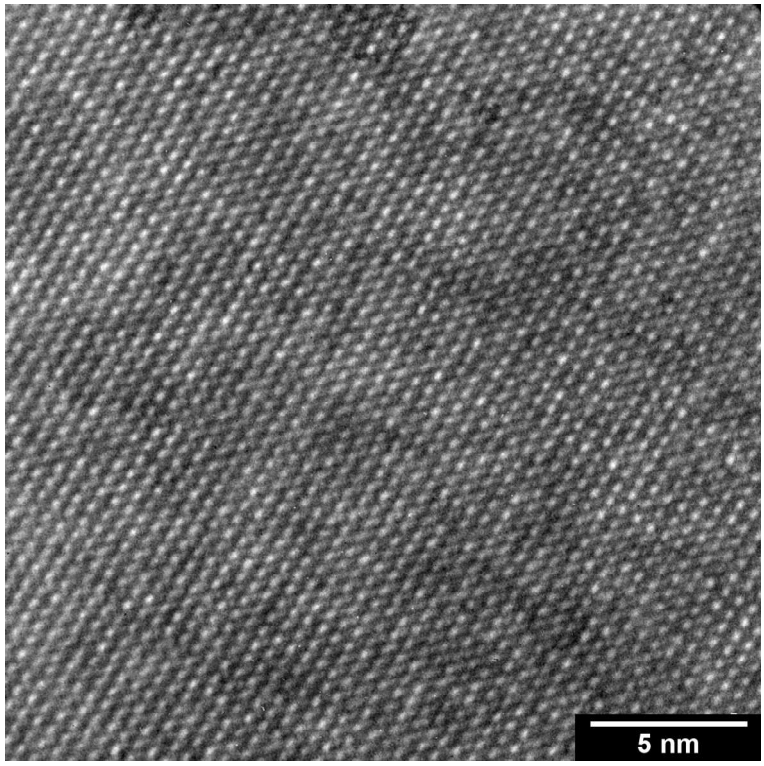

Figure 3.8: High resolution TEM image of a Cr-rich fine intragranular precipitate. Measurements of the lattice spacing indicated the precipitate is $M_{23}C_6$.

3.6 Summary of Precipitates in Ex-service Reformer Tube

Various characterization techniques were utilized to identify precipitates occurring in the ex-service steam-methane reformer tube. A summary of all precipitate types observed is listed in Table III.

Table III: Summary of precipitates characterized.

Precipitate	Crystal System	Measured Lattice Parameter, (nm)	Technique Used
$M_{23}C_6$	cubic	1.062	XRD, EBSD
NbC	cubic	0.4425	XRD, EBSD
TiC	cubic	0.431	XRD, EBSD
$M_{23}C_6$	cubic	1.06	SAD

Chapter 4

SERIAL SECTIONING AND 3D RECONSTRUCTION

This chapter describes in detail the serial sectioning and 3D reconstruction processes used in this research. The techniques for serial sectioning and 3D reconstruction employed in this work were adapted from methods described elsewhere [68]. A common difficulty faced in any 3D reconstruction work is the inability to recreate the visualization of 3D objects on 2D pages. A CDROM containing simple animated movies of serial section images and rotating 3D reconstructed volumes has been provided with this thesis to assist with the visualization of 3D reconstructions (see Appendix V). Figures which are accompanied by animated movies in the CDROM will be denoted by this icon  . All movies are in uncompressed audio-video interleave (AVI) format and compatible with Microsoft Media Player® and Apple Quicktime®.

4.1 Serial Sectioning Process

In materials studies, serial sectioning is a repetitive sequence of tasks which ultimately result in the compilation of a series of images that represents the microstructural volume of the material. A typical simplified sequence of tasks is as follows:

1. marking and imaging an area of interest,
2. removing a known thickness or depth of the material,
3. imaging the same area as in step 1,
4. repeating steps 2 and 3 until the total required volume of material have been removed.

The serial sectioning process was preceded by characterization of the precipitates present in the material, as previously discussed in Chapter 3. After the characterization process is completed, a major decision regarding the depth of material to be removed in each serial

section was necessary after considering the sizes of the grains, precipitates, and the voids within the material. During characterization, it was observed that equiaxed austenite grains along the inner wall of the tube were about 100µm in diameter while the columnar grain sizes were larger than 1mm. Furthermore, precipitate and void sizes ranged from submicron to tenths of micrometers. Due to the large disparity of these sizes, it would be impossible to reconstruct complete grains together with the associated precipitates and voids. Therefore, a compromise was made and for this work a serial section depth of 0.5µm was chosen. This decision also meant that the smallest feature to be reconstructed would be limited to 1µm (i.e. 2 serial sections), and features seen in only one serial section image will be ignored. The serial sectioning process commenced when the areas of interest were chosen and marked for imaging. Fiducial marks were made using a diamond pyramid indenter with 100g load in the Leco M-400-HI microhardness tester. The microhardness tester had a slightly modified sample stage which allowed for samples to be rotated in addition to the normal X-Y translation (see Figure 4.1) enabling the fiducial marks to be precisely placed on the samples. The indentations were arranged in a triangular pattern so that they surrounded an area with dimensions (length × width) as follows; for 200× magnification – 400×300µm, for 500× magnification – 160×120µm. These indentations served three purposes; identify areas to be imaged, indicate amount of material removed, and act as reference points during image registration (alignment). After etching in glyceregia, the first image of the serial section was then obtained using the Leica DM-Inverted Research Microscope and Zeiss Axiocam.

The ratio between the diagonal distance and the depth of the microhardness indentation is 7:1. Thus, in order to remove 0.5µm layer of material, the sample must be polished such that the diagonal dimension of the indentation marks was reduced by 3.5µm. Each sample was polished using either the Buehler Minimet® polisher or the Buehler Minimet® 1000 polisher (see Figure 4.2). A timer was used to control the amount of material removed while the applied load was kept constant at 5lbf (4.4N). Polishing speed was set at 50rpm.

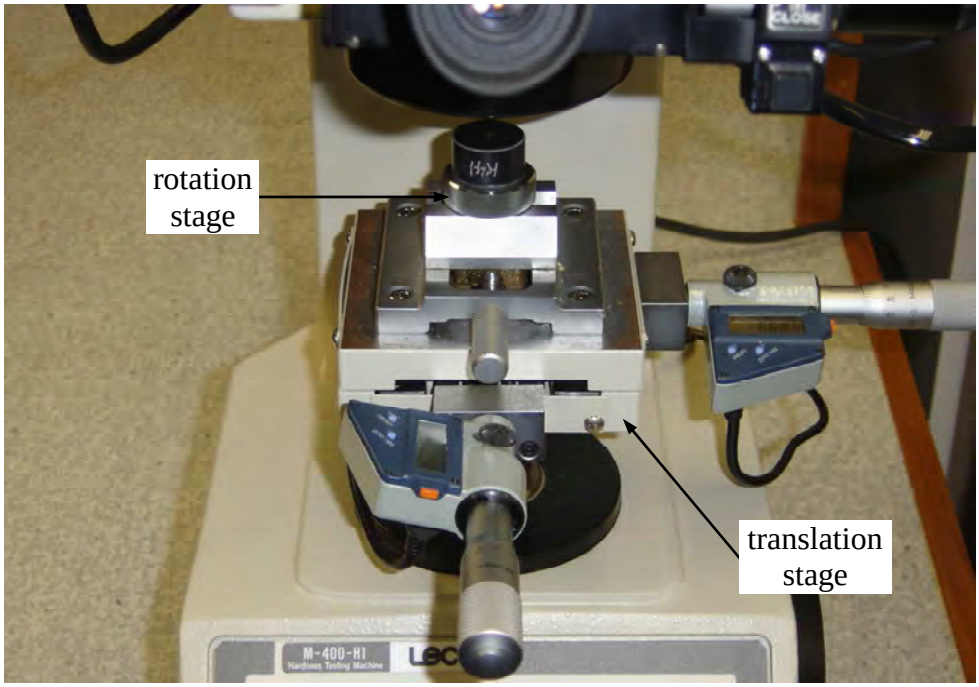

Figure 4.1: Microhardness tester used for placement of fiducial marks. The rotation and translation stages allowed for exact placement of indentation marks.

Initially, the sample was polished using Buehler MetaDi® 1µm diamond compound and suspension on Buehler Trident® cloth, followed by a final polish using Buehler MasterMet® 0.06µm colloidal silica suspension on Buehler Chemomet® pad. The diamond polish was used to reduce the indentation mark dimensions by 3µm and the colloidal silica polish reduced the dimension a further 0.5µm. This two-step process produced an excellent finish on the samples, however the process required at least two hours per serial section from the start of polishing to image capture. Furthermore, the colloidal silica suspension had a tendency to crystallize during the long polishing process, and these relatively large silica crystals (>0.06µm) caused scratches on the polished surface.

For subsequent samples, a one-step polishing stage using a fifty percent (by volume) water dilution of Buehler MasterPolish® suspension on Buehler Chemomet® pad was employed. Polishing load and speed settings on the Minimet® remained unchanged. The polishing results were not as impressive as colloidal silica polish, but the entire polish-etch-image process typically took less than one hour per serial section, dramatically reducing the total serial sectioning times for subsequent work. All serial section images were recorded as

1.3-megapixels (1280×1024), 24-bit RGB (red-green-blue) TIFF*** color images (file size approximately 3.9-megabytes per image).

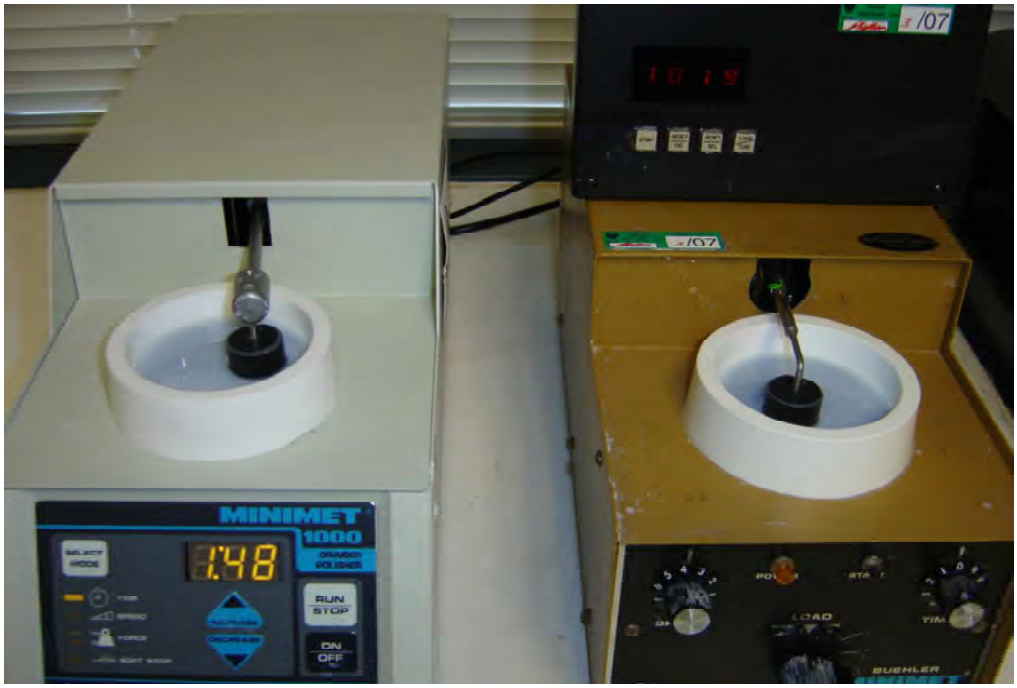

Figure 4.2: Buehler Minimet® 1000 polisher (left) and the older model Buehler Minimet® polisher (right) used for serial sectioning. The newer model has built-in electronic timer, load and speed setting. The older model employed an external "black box" (upper right) for timer and load controls.

For the reformer tube material studied in this work, a 100g indenter load normally produced an indentation with an initial diagonal dimension of about 30μm. After five serial sections, the diagonal dimension would be reduced to 12.5μm. At this point, a new set of fiducial marks would be placed around the area of interest at some distance away from the previous set of marks. This was done to preserve the continuity of the measurement of diagonal dimension, and also maintain the reference points for image registration. Figure 4.3 shows a sequence of nine serial section images of the same area. Note the reduction in sizes of the fiducial marks and the placement of new marks.

*** Tagged Image File Format

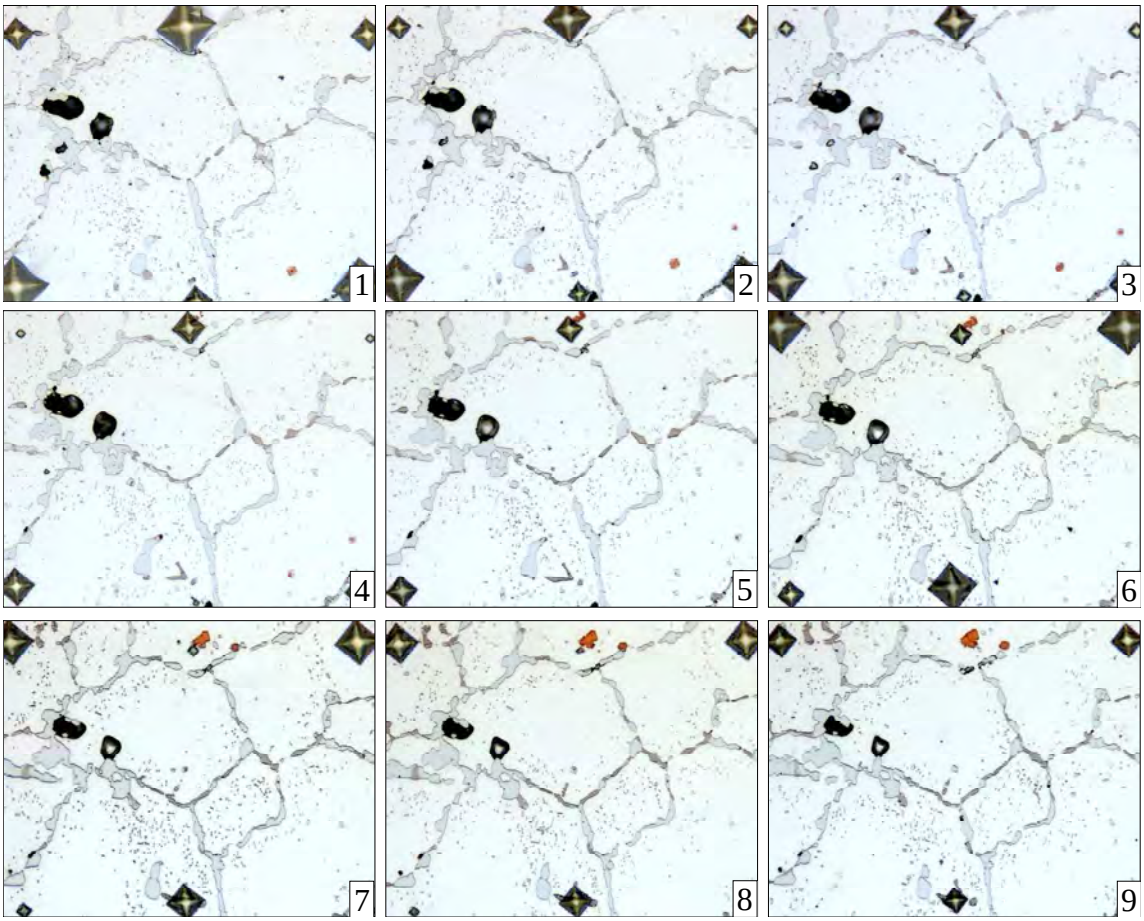

Figure 4.3: A sequence of nine serial section images showing the placement of fiducial marks and the reduction of their sizes due to polishing.

For this work, a decision was made to limit the number of serial sections to no more than 100 layers per sample. Several exploratory samples were serial sectioned and reconstructed in 3D and the decision to limit to 100 layers was made after considering these various factors. For reformer tube materials, typical grain sizes are about 80-120μm in diameter for equiaxed grains near the inside wall of the tube, and the grain sizes can be more than 2000μm in length for columnar grains which extend to the outside wall (refer to Figure 3.1). In contrast, void sizes were measured to be generally no larger than 50μm in diameter while the smallest voids to be reconstructed were limited to 1μm in diameter, based on the serial section thickness of 0.5μm and the decision made earlier to only reconstruct features appearing in at least two consecutive serial sections. Similarly, precipitate particle sizes range from less than 1μm for fine intragranular precipitates to more than 50μm for some grain boundary clusters. Ideally, it would be preferable to serial section and reconstruct at least a full grain depth, but this would not be practical for the case of reformer tubes. In terms of number of samples, between three to five reformer tube

segments were sourced for this work, and for each tube segment, samples were to be taken from two to four locations along the wall thickness. Assuming a total of four samples in each of five tube segments, the total time required for serial sectioning 100 layers per sample would amount to at least 2000 hours.

4.2 Image processing and 3D Reconstruction

The first procedure that must be performed prior to 3D reconstruction is the image registration process. During the serial sectioning process, the images were recorded from samples that were manually placed on the optical microscope, thus it would be almost impossible to place the sample at exactly the same position every time, which then resulted in an inherent displacement of the features from one serial section to the next. The collection of serial section images must therefore be aligned with respect to the first image recorded so that any features reconstructed later would represent the true attribute of the microstructure. In the early stages of this research, the image registration process was done manually by overlaying two consecutive images together using NIH ImageJ software [39]. The second image was then translated and rotated to align with the first image using the Align3_TP plugin [69] within ImageJ. This process is shown pictorially in Figure 4.4 which clearly shows the resulting superimposed indentations in the aligned images of Figure 4.4b. In the latter stages of this research, image registration was done automatically using the StackReg plugin [38] within ImageJ. Using ImageJ, the entire set of serial section images was first placed into an “image stack” and saved as a single TIFF image file. The StackReg plugin would then register this image using the first image as the reference and the resulting registered images were then be stored into another TIFF image stack for subsequent processes. Movies of the “before” and “after” process in Figure 4.4 are available in the accompanying CDROM.

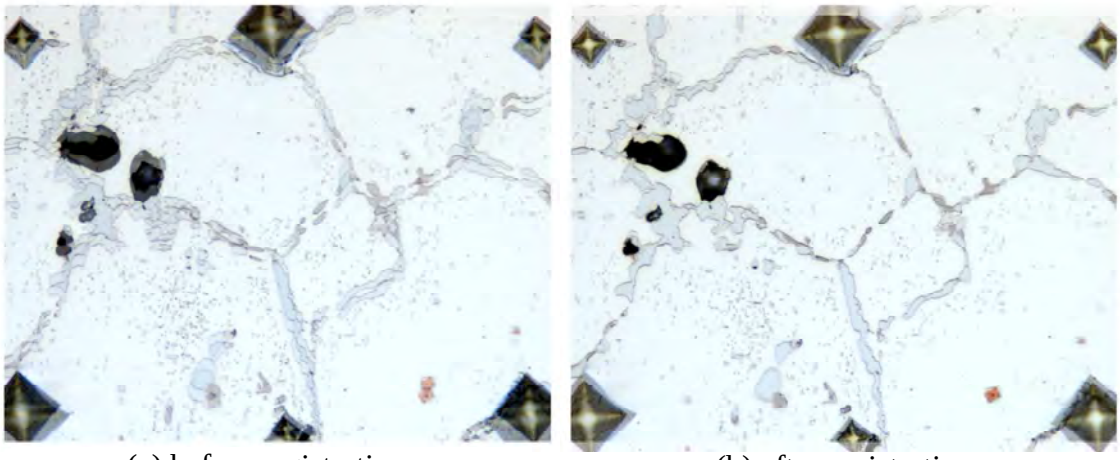

(a) before registration; (b) after registration

Figure 4.4: Overlayed pair of serial section images showing the manual image registration process; (a) image pair before registration showing offsetting features ⊙, (b) aligned image pair showing "convergence" of features ⊙.

Once the stack of registered images was obtained, the 24-bit RGB images were converted to 0.3-megapixels (640×512), 8-bit greyscale images and saved into another TIFF image file. This was done to reduce computer memory requirements during further image processing of the stack[†††]. A crude 3D reconstruction would then be performed on the greyscale image stack using the Volume Viewer plugin [70] in ImageJ to check the appearance of the 3D volume. A "transparent" view into a 3D volume could also be made using ImageJ. For the transparent view, the images were first inverted so that the background (matrix) became black and thus "removed", leaving the precipitates and voids. Based on this transparent view, a crude animation of the 3D volume rotating in space can also be performed within ImageJ; however this simple animation limits the rotation about either X or Y axis only. More detailed 3D reconstructions and manipulations required the use of more sophisticated software.

Figure 4.5a shows an isometric view of a sample 3D reconstruction consisting of 62 serial section layers at 0.5µm per layer, resulting in a 3D volume thickness of 31µm. The original set of serial section images were obtained for a rectangular area with dimensions of approximately 800×600µm (magnification of 100×) and then cropped to 790×539µm to

[†††] For example, the original 100-layer 1.3-megapixels, 24-bit RGB image stack will have a size of 393-megabytes while the size of 100-layer 0.3-megapixels, 8-bit grayscale image stack will only be 33-megabytes.

remove the fiducial marks. Figure 4.5b shows the "see-through" image of the same volume in (a) while Figure 4.5c shows a deep-etched image (glyceregia etch) of the same material reconstructed in (a) and (b) (different area, obviously). Note the appearance of the precipitate structure in the deep-etched image is similar to transparent view in (b); however the intragranular precipitates and voids are not observable since they have been removed by the deep etching process. As seen in Figures 4.5b and 4.5c, the serial sectioning technique coupled with a simple 3D reconstruction method have already demonstrated their usefulness to observe creep voids and adjoining microstructural features in 3D.

Detailed 3D reconstructions would also be done on selected regions of the volumes. An example of a 3D reconstruction process on a small serial section volume containing a few voids and various surrounding precipitates is shown in Figure 4.6. A serial section image of a single void and nearby precipitates is shown in Figure 4.6a. Prior to reconstruction, each serial section image was inverted and "cleaned up" to remove any features with thickness less than 1µm, as exemplified by Figure 4.6b. This step removed fine precipitates, dusts, scratches, or other anomalies captured in only one serial section image but did not appear in the preceding or succeeding images. Next, each void and precipitate type was marked by a different color, as shown in Figure 4.6c. This was the most time-consuming element of the 3D reconstruction process, but nevertheless a vital portion of the work. A separate image file would then be created for each feature observed (i.e. the voids and each precipitate type would have their own individual image stack).

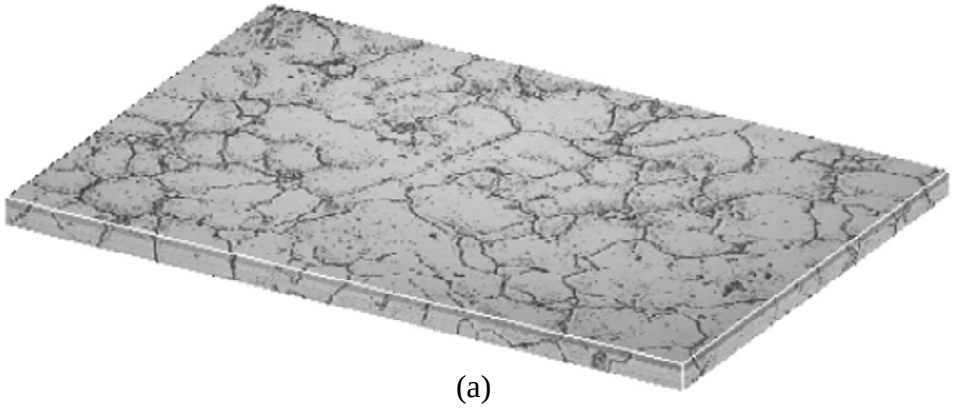

(a)

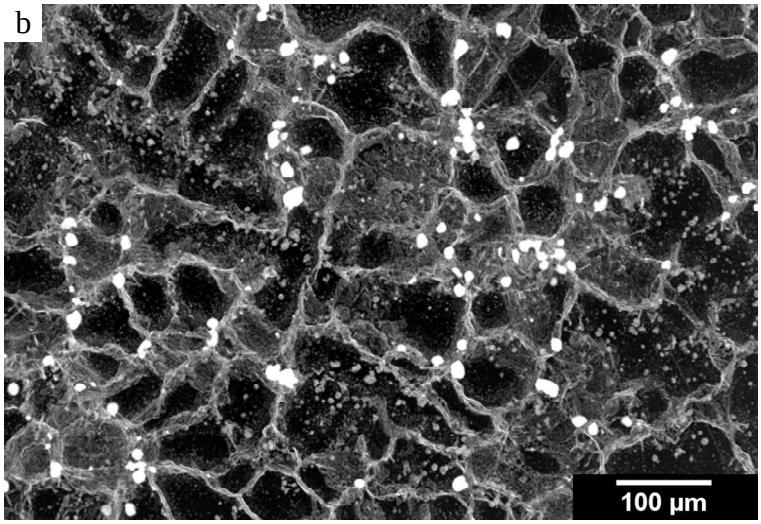

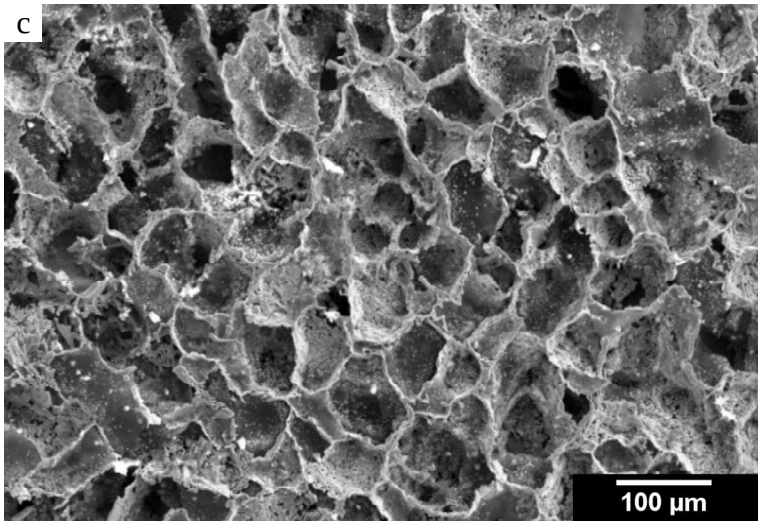

Figure 4.5: Example of a 3D view of ex-service reformer tube microstructure; (a) isometric view of a 790×539×31µm volume, (b) "transparent" view of the volume in (a) revealing voids as white areas, precipitates in grey, and austenite matrix as black, (c) deep-etch microstructure of the same material showing the network of precipitates, but all the fine precipitates and creep voids were "destroyed" by the deep-etching process.

Detailed 3D reconstruction was performed using a computer program written using RSI IDL software [71] which read the individual image stacks and reconstructed the microstructure accordingly. Edges of features highlighted (see Figure 4.6c) in consecutive serial section images were rendered into 3D surfaces to create a hollow 3D object. Similarly, the program could also build a solid 3D object from the serial section images; however the program execution is slower and more memory intensive for creation of solids as opposed to creation of surfaces. The separation of microstructural features done earlier allowed for these features to be independently reconstructed and they can then be revealed or hidden as required. Furthermore, employing the translation, rotation, and zoom tools in IDL, specific components of the reconstruction can be scrutinized in even greater detail. Figures 4.6d-g show the 3D reconstruction of creep voids and its surrounding features. By employing these 3D reconstructions, the interactions between creep voids and their surrounding precipitates can be properly studied.

It is also important to note the need of a moderately powerful computer system to adequately provide means of 3D reconstructions and observations. If the graphics capabilities are poor, 3D reconstruction time will be long and manipulation of the reconstructed image will also be time consuming. For the early part of this work (in 2003), all image processing, 3D reconstructions, and 3D observations were performed on an Apple Macintosh G4 computer with a 1GHz processor, 1GB of DDR RAM, and nVIDIA GeForce4 MX440 video card with 64MB of DDR RAM. Later graphics work (in 2006) was carried out on a generic PC with Intel Pentium IV 630 processor (3GHz), 1GB of DDR2 RAM, and ATI Radeon X1600 video card with 256MB of DDR2 RAM. Both computer setups would be considered as midrange setups during their initial lives but they performed adequately for all graphics work.

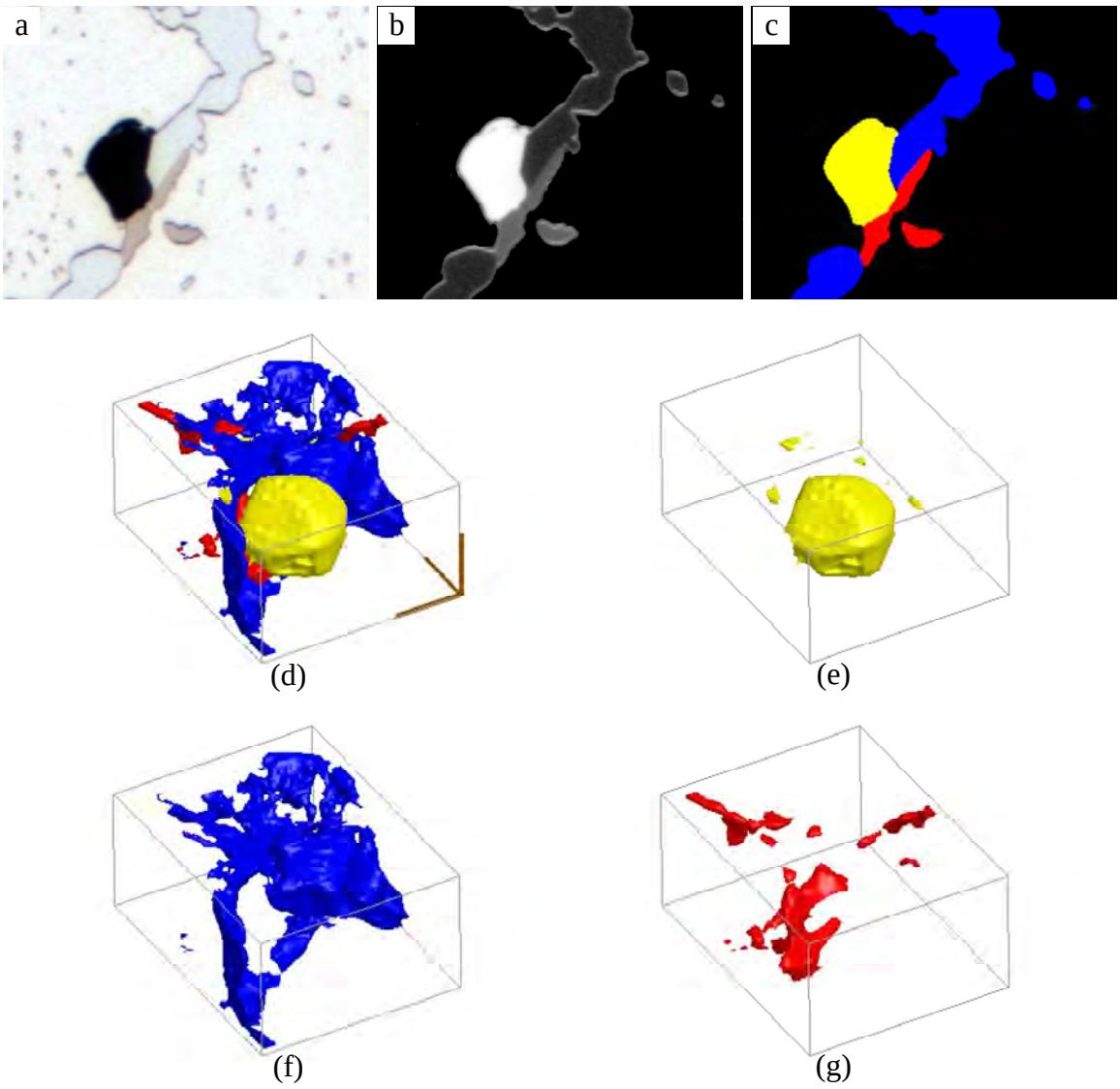

Figure 4.6: Detailed 3D reconstruction of a void and surrounding features; (a) a single serial section image showing a void, $M_{23}C_6$ precipitates (blue), and NbC precipitates (brown); (b) "cleaned" inverted image with fine precipitates removed; (c) image highlighting the various microstructural features – void is yellow, $M_{23}C_6$ is blue, NbC is red; (d) 3D reconstruction of a void and nearby precipitates ⊙; (e) void only ⊙; (f) $M_{23}C_6$ precipitates only ⊙; (g) NbC precipitates only ⊙.

4.3 3D Reconstruction of an As-Cast Reformer Tube Material

As mentioned in Chapter 3, the ex-service reformer tubes obtained for this research were Centralloy® CA4852-Micro centrifugal cast austenitic stainless steel tubes manufactured by Schmidt-Clemens. A tube segment in the as-cast condition was also obtained for the purpose of serial sectioning and 3D reconstruction. Prior to serial sectioning, the as-cast tube sample underwent the same procedures outlined previously, namely the processes of metallography sample preparation, grinding and polishing, and characterization of precipitates. Brightfield optical micrographs of the as-cast sample are shown in Figure 4.7. The most apparent difference between this as-cast microstructure and the ex-service microstructure of Figure 3.3 in Chapter 3 is the absence of fine intragranular precipitates. In addition, the as-cast grain boundary carbides have a more angular or faceted appearance and some of the precipitate colonies also appear lamellar, in contrast to the ex-service grain boundary carbides which have spheroidized and coarsened.

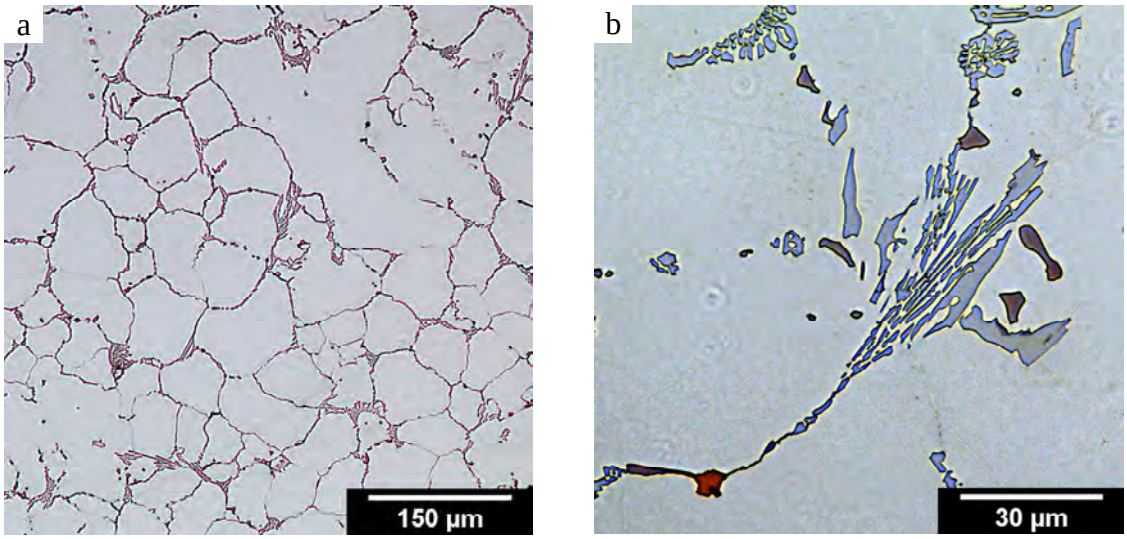

Figure 4.7: Microstructure of as-cast reformer tube. (a) Low magnification image of sample etched in glyceregia; (b) higher magnification image revealing three distinct precipitates.

Characterization of precipitates was performed using in the SEM using a combination of the EDS and EBSD techniques as described earlier in Chapter 3. A backscatter electron image of the as-cast tube sample is shown in Figure 4.8a with the associated EDS spectra for three distinct precipitates *A*, *B*, and *C* indicated. Other than minor differences in the relative heights of the peaks, the appearances of the EDS spectra of the as-cast tube were

very similar to the EDS spectra of the three precipitate types present in the ex-service tubes (refer to Figure 3.4 in Chapter 3); the main difference observed is the lack of Ti peak in the EDS spectrum of precipitate *B*. It is believed that strengthening of these reformer tube alloys may be partially due to formation of a more complex carbides such as (NbTi)C during high temperature exposure [10, 14, 15]. Nevertheless, using EBSD, the identity of the three precipitates *A*, *B*, and *C* in the as-cast microstructure was determined to be $M_{23}C_6$, NbC, and TiC respectively, which are the same precipitates present in the ex-service microstructure.

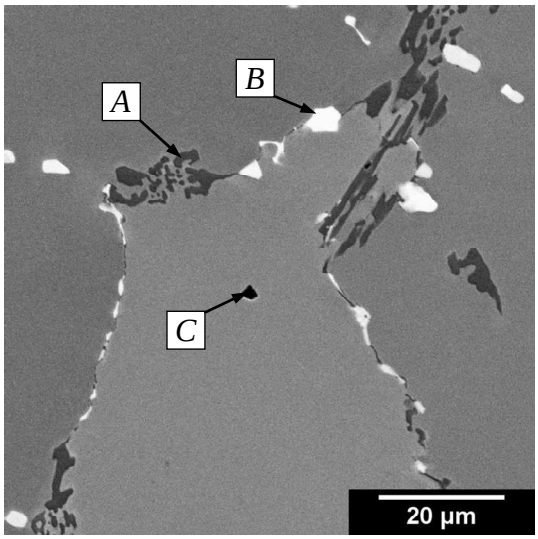

(a) BSE image of as-cast tube;

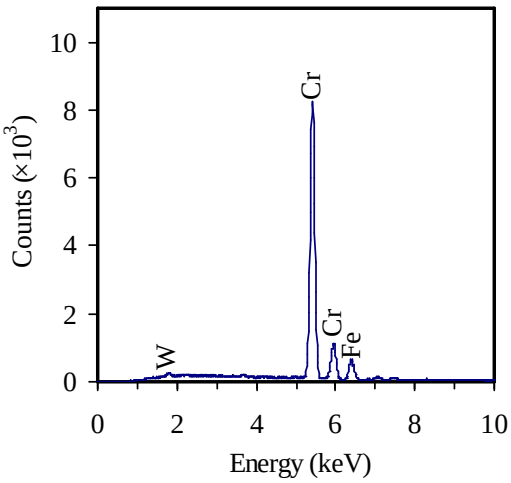

(b) EDS spectrum of precipitate *A*;

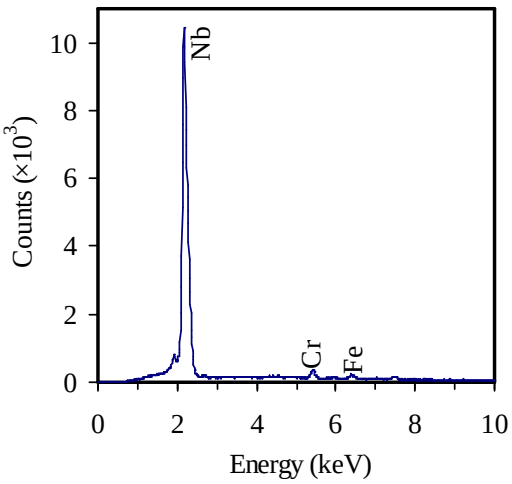

(c) EDS spectrum of precipitate *B*;

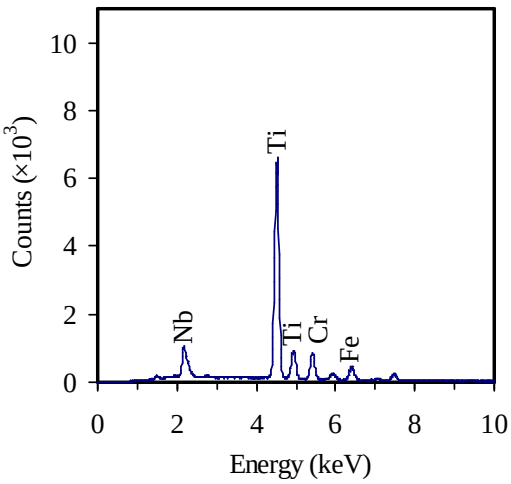

(d) EDS spectrum of precipitate *C*.

Figure 4.8: Backscatter electron (BSE) image of ex-service reformer tube and the corresponding EDS spectra of precipitates *A*, *B*, and *C*.

The serial sectioning methods used on the as-cast material were the same as the methods described in section 4.1, however only the one-step polishing stage using diluted Buehler MasterPolish® suspension on Buehler Chemomet® pad was employed. Serial sections were done at 0.5µm steps for one hundred layers (50µm). A total of four areas of the as-cast sample were selected for serial sectioning and 3D reconstruction; two 400×300µm areas in the equiaxed region of the inner wall of the tube, and one 400×300µm area each for the columnar regions of the mid-thickness and outer wall of the tube. The differences between the equiaxed and dendritic microstructures of the as-cast tube are evident in the simple 3D reconstructions shown in Figures 4.9 and 4.10. An EBSD map was superimposed on each of the isometric view of the 3D reconstructions (Figures 4.9a and 4.10b) to indicate the austenite grains. The maps clearly show the dissimilarities between the equiaxed and columnar structures of the reformer tube in terms of the austenite grain size and shape.

In Figure 4.9a, an isometric view of the equiaxed microstructure near the inner wall of the tube is shown, while Figure 4.9b represents the "transparent" view of the 3D reconstruction. The differences between the as-cast and the ex-service microstructures of the reformer tubes (compare Figure 4.9 to Figure 4.5) are also apparent from these reconstructions. The equiaxed structure is seen bounded by intergranular precipitates, some of which show the typically more angular and lamellar-like structure of the $M_{23}C_6$ precipitates, compared to the intergranular precipitates in Figure 4.5. There are also coarse intragranular precipitates observed in the as-cast structure similar to the ex-service microstructure; however the fine intragranular precipitates are not present in the as-cast tube.

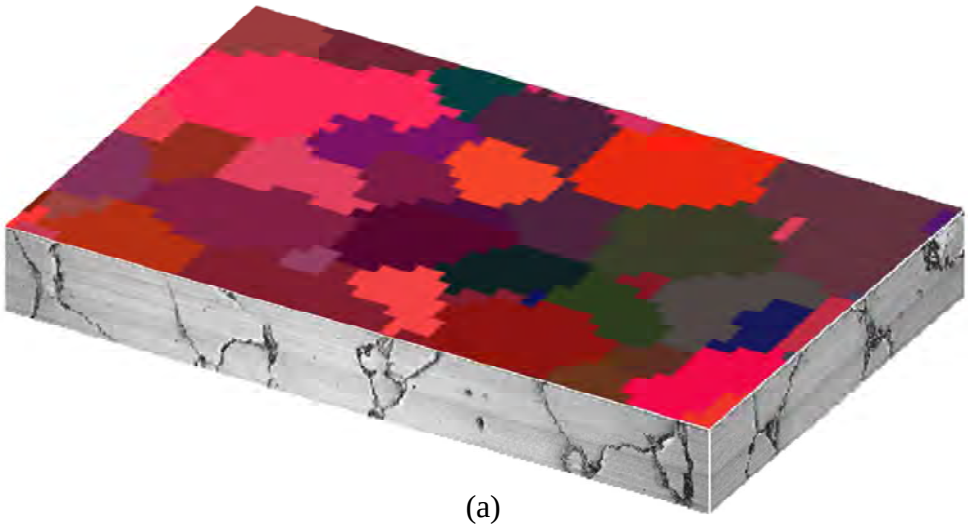

(a)

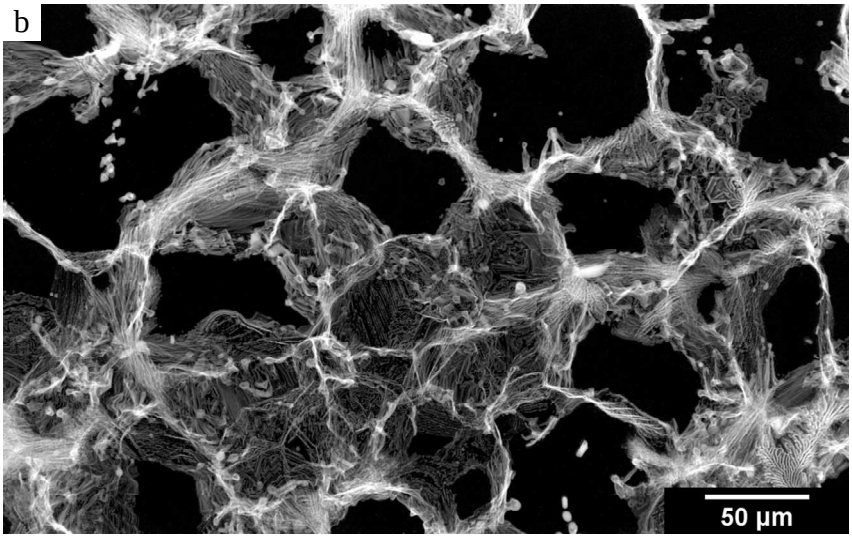

Figure 4.9: 3D reconstruction of an equiaxed region of the as-cast reformer tube. (a) isometric view of a 404×253×50µm volume obtained near the inner wall of the tube. An EBSD map is superimposed on the top layer to reveal the equiaxed austenite grains; (b) "transparent" view of the volume showing intergranular precipitates, coarse intragranular precipitates, and the absence of fine intragranular precipitates.

Figure 4.10 shows the typical 3D appearance of the columnar microstructure at the mid-thickness area of the reformer tube. Here, the precipitates surround the grain boundaries in addition to also bordering the "fingers" of the dendritic structure. Also observed are coarse intragranular precipitates appearing discretely between the dendritic and grain boundaries. Figure 4.10 also highlights the problem of 3D methods on complex materials with large disparities between the sizes of its features. The chosen serial sectioning parameters allowed for the precipitates to be faithfully reconstructed, however only a portion of the large grains was captured in the volume.

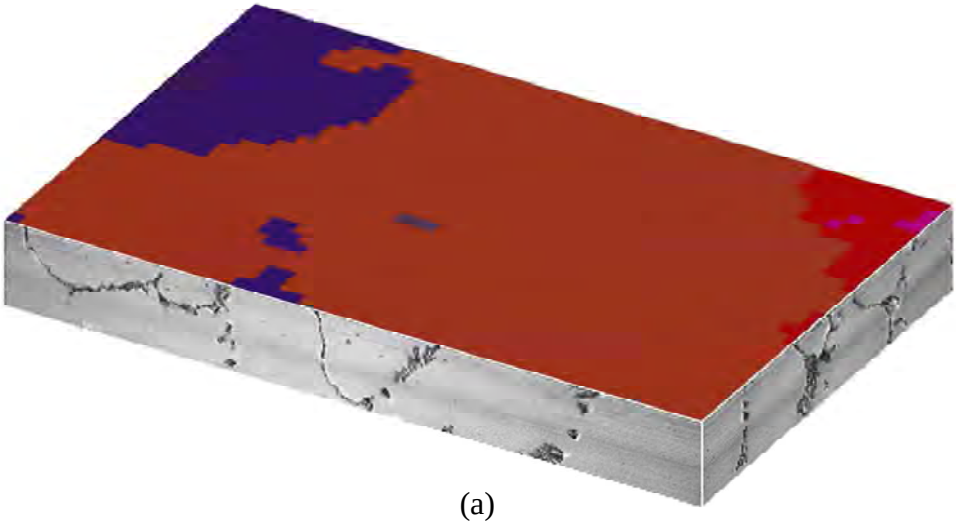

(a)

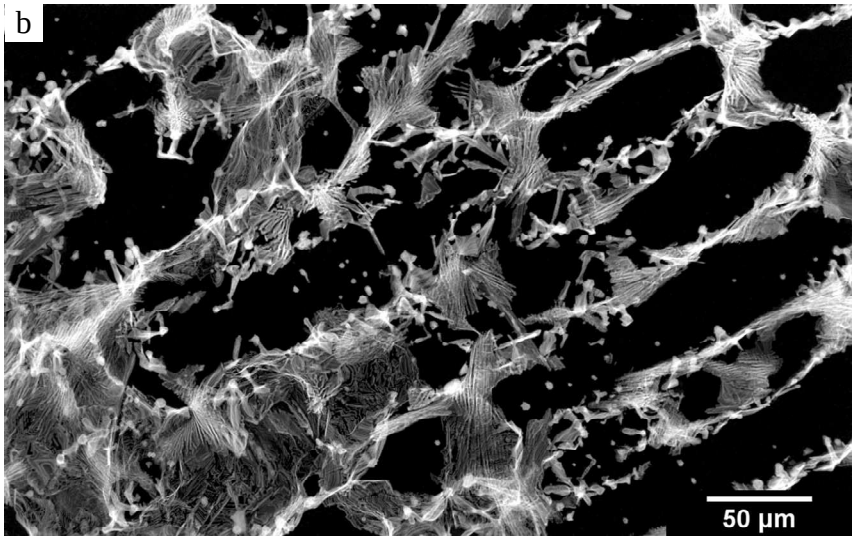

Figure 4.10: 3D reconstruction of a columnar region of the as-cast reformer tube. (a) isometric view of a 400×250×50µm volume obtained near the mid-thickness of the tube. An EBSD map is superimposed on the top layer to reveal the large columnar austenite grains; (b) "transparent" view of the volume showing precipitates at the grain and dentritic boundaries and also coarse intragranular precipitates.

A more detailed 3D reconstruction can also be performed on the volumes to show the various morphologies of the precipitates. Figure 4.11a shows an example of a detailed 3D reconstruction of a subvolume where different features are separated by colors. In this case, the $M_{23}C_6$, NbC, and TiC precipitates are blue, red, and green respectively. Additionally, the subvolume in Figure 4.11a can be further detached into two portions as shown in Figures 4.11b-c, to enable the viewer to have a less cluttered look into the microstructure. The various features can also be turned on or off for inspection, as shown

previously in Figure 4.6. Figures 4.11a-c show that the $M_{23}C_6$, NbC, and even TiC precipitates at the grain boundaries are intertwined, and this precipitate fragmentation attribute is believed to contribute significantly to the creep strength of this material [14, 15, 43]. The detailed 3D reconstruction also allowed for precipitate volume percent to be easily obtained. For the four volumes reconstructed for the as-cast tube, the volume percent was calculated to be 7.8% for $M_{23}C_6$, 3.1% for NbC, and 0.2% for TiC.

It also needs to be pointed out that detailed colored 3D reconstructions were usually not required for the analysis of the reformer tube microstructure. Simpler 3D reconstructions generally were able to show the microstructural features adequately in various shades of gray. Even when ambiguities occurred, the original colored serial section images were used to remove any uncertainties.

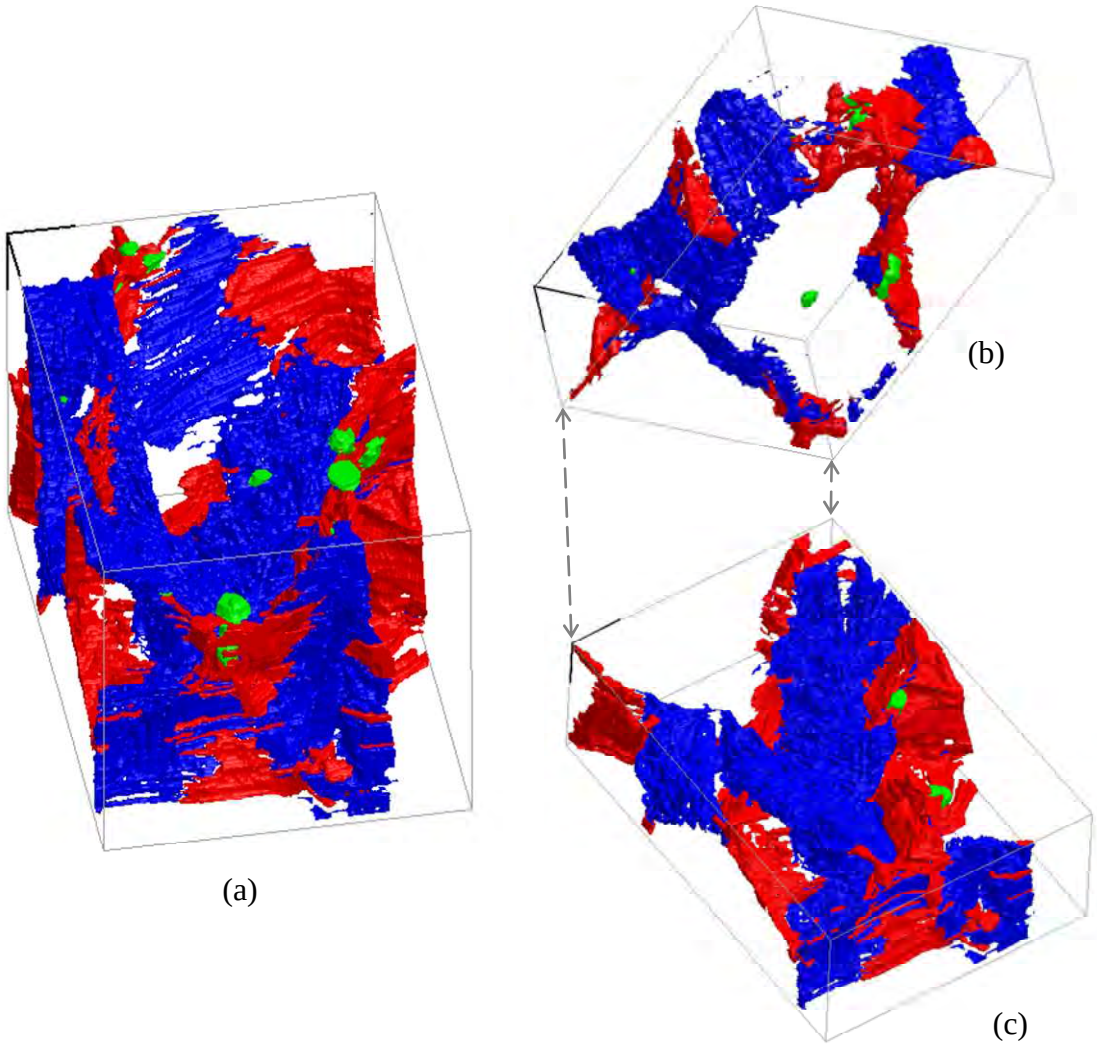

Figure 4.11: Detailed 3D reconstruction of a subvolume in the equiaxed region of the as-cast tube. (a) 53×79×50µm volume showing the $M_{23}C_6$, NbC, and TiC precipitates as blue, red, and green; (b) separated top half of the reconstruction in (a) showing a less cluttered appearance of the subvolume; (c) lower half of the reconstruction in (a) showing $M_{23}C_6$ precipitates lining up the base of the grain.

Chapter 5

ANALYSIS OF CREEP VOIDS IN A FAILED REFORMER TUBE

A sample which has undergone severe creep was selected for the initial study of creep voids. This sample was obtained from a reformer tube that had prematurely ruptured during service, and thus would contain numerous creep voids. Serial sectioning and 3D reconstruction techniques would then be employed to reveal the shapes, sizes, locations, and adjacent precipitates of the creep voids in 3D, information that cannot be obtained from two-dimensional micrographs alone. Additionally, crystallographic orientations of the phases adjacent to creep voids would be studied by electron backscatter diffraction (EBSD) to determine any crystallographic trends in creep void locations. A similar EBSD study on precipitates in the same material subjected to high temperature ageing (but with no creep deformation) would also be performed for comparison.

A major portion of this chapter has been published in "*3D analysis of creep voids in hydrogen reformer tubes*" by Azmi Abdul Wahab and Milo V. Kral, in Materials Science and Engineering A 412 (2005) 222-229.

5.1 Serial Sectioning and 3D Reconstruction Methods

The sample studied in this chapter was obtained from a ruptured reformer tube from the Methanex Kitimat plant in British Columbia, Canada. The tube had been in service for 60,000 hours (6.8 years) at approximately 2MPa internal pressure and a maximum service temperature of 940°C. Investigations into the cause of the premature creep failure discovered that there was excessive eccentricity of the bore of the tube resulting in a wall thickness less than the designed minimum sound wall thickness [72]. The tube material

was Schmidt-Clemens Centralloy® CA4852-Micro centrifugally cast austenitic stainless steel tubes similar to the one previously described in Chapter 3, but with a thirty percent equiaxed microstructure. This tube was selected for study in order to establish a "worst-case scenario" of a material which had undergone severe creep. The sample for study was obtained from a location adjacent to where rupture had occurred. The chosen location contained numerous creep voids but did not contain any cracks.

Prior to serial sectioning, precipitates in the ex-service sample were first characterized using the various techniques described earlier in Chapter 3, specifically optical microscopy, SEM/EDS, XRD, EBSD, and TEM. Once characterization of precipitates was completed, serial sectioning commenced on this sample using methods outlined in Chapter 4. Sectioning was performed at 0.5µm steps for sixty five layers for a total thickness of 32µm, and for this sample, the two-stage polishing process was employed. The Buehler MetaDi® 1µm diamond compound and suspension on Buehler Trident® cloth was used to remove approximately 0.4µm thick layer of the section, followed by a final polish using Buehler MasterMet® 0.06µm colloidal silica suspension on Buehler Chemomet® pad to remove the remaining 0.1µm of the serial section.

A total of four locations of the sample were selected for study; two 400×300µm areas and two 160×120µm areas were imaged at original magnifications of 200× and 500× respectively. All four areas were selected from the equiaxed region near the inner tube wall where most of the creep voids were located. Due to the relatively large size of some of the grains involved (in excess of 150µm), it was ascertained that only the two 400×300µm areas were suitable for 3D reconstruction and analysis.

Image processing and 3D reconstruction of the ex-service sample were also performed using methods described in detail in Section 4.2 of Chapter 4. The collection of images was first registered with respect to the first serial section by manually overlaying two consecutive images together, and manipulating the second image (rotating and translating) so that the fiducial marks of the second image line up with those of the first image. Separate image stacks were then created for each microstructural feature and specific colors were attributed to the various microconstituents and voids for enhanced visualization. Visualization of the 3D datasets allowed observation and quantification of

microstructural data that would have been impossible to study via other techniques. Information such as void volume or precipitate volume fraction can be determined by counting voxels which were then converted into units of volume. Furthermore, 3D reconstructions could be viewed and rotated about any axis and animated for further study of morphology and interconnectivity of features. By loading the specific image stacks, microstructural features can be revealed or hidden as needed (refer to Figure 4.6 in Chapter 4).

5.2 3D Characterization of Creep Voids

The precipitates characterized in this ex-service reformer tube were similar to the ones described earlier in Chapter 3. The coarse precipitates were identified as $M_{23}C_6$, NbC, and TiC, while the fine precipitates were established as $M_{23}C_6$. Figure 5.1 displays the isometric views of 3D reconstructions of one of the sectioned volumes. In Figure 5.1a, a total of 138 creep voids are reconstructed and highlighted in yellow and are superimposed on the 3D volume. Figures 5.1b shows only the creep voids while Figure 5.1c represents a smaller sub-volume showing the voids and grain-boundary precipitates in various colors. One observation that can immediately be made from this 3D reconstruction is that the creep voids are not uniformly distributed in the sample volume in terms of their size, shape, and location. This instant observation already highlights the effectiveness of 3D techniques in revealing the true microstructure of materials. On the other hand, Figure 5.1 also shows the problem of viewing 3D reconstructions on a two-dimensional medium such as the pages of this thesis. The inability to manipulate the appearance of the 3D reconstructions on paper reduces one's appreciation of the complexity of the microstructure and one's ability to fully study the reconstructed microstructure. Only via real time computer display enables the full comprehension of the generated 3D microstructure. The animated movies available in the accompanying CDROM allow for a limited amount of manipulation[‡‡‡] which to some extent would allow for better understanding of the microstructure in 3D.

[‡‡‡] Using the movie player scroll bar allows one to step through the movie frame by frame.

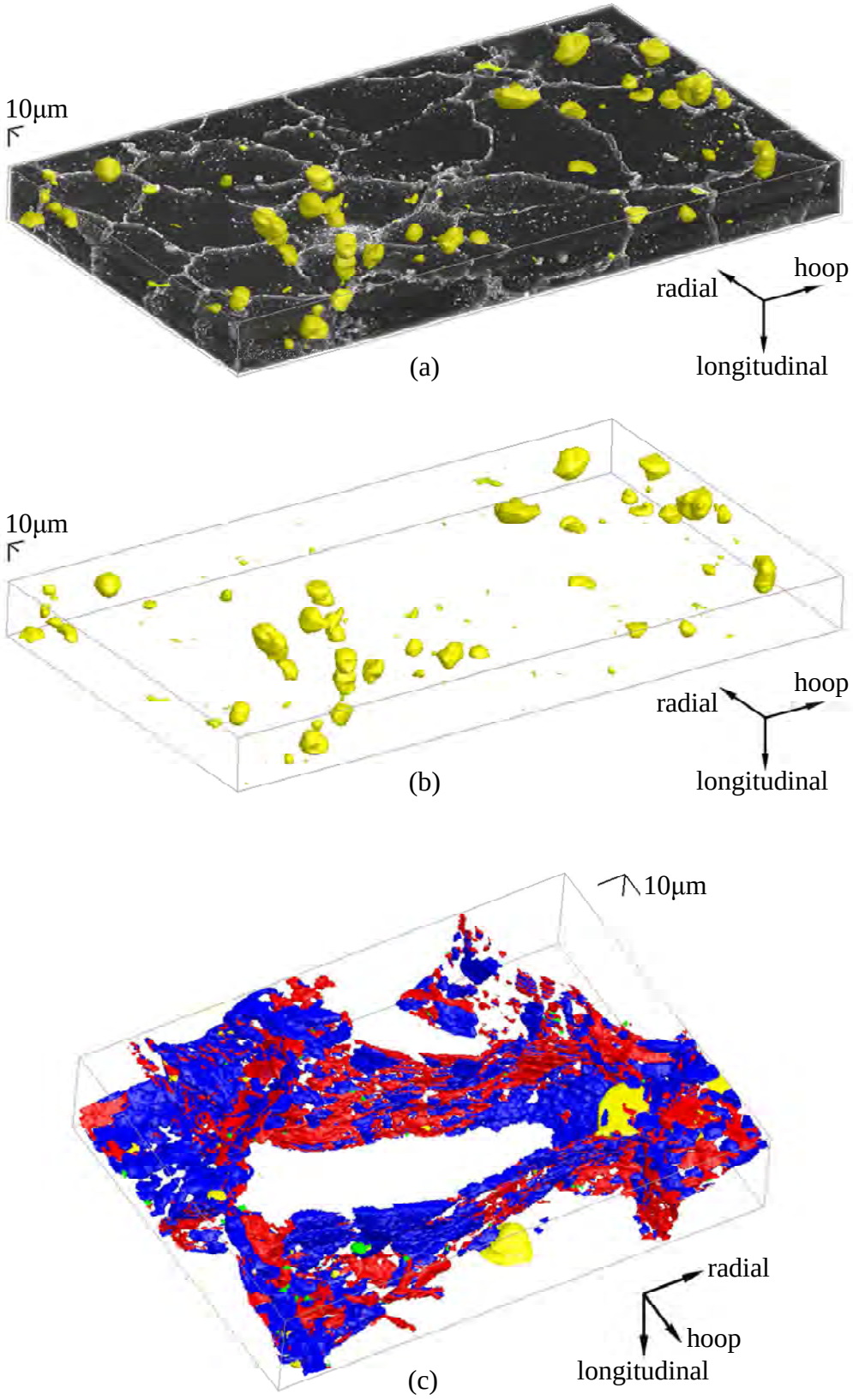

Figure 5.1: 3D reconstruction of a 403×204×32-µm volume; (a) reconstruction with austenite shown in black, voids in yellow, and precipitates shown in shades of grey; (b) reconstruction of 138 voids; (c) reconstruction a 130×179×32-µm sub-volume showing voids (yellow), $M_{23}C_6$ (blue), NbC (red) and TiC (green).

For this study, the 3D analysis outputs were void size, shape, location, and contact precipitate(s). Void sizes are represented by the equivalent sphere diameters of the void volumes. The volume of each void was first determined from voxel counts which were then converted to μm^3. By assuming that the voids are spheres, an equivalent diameter was calculated for each void. This was done to give a linear dimension value (i.e. µm) which conveniently represents the void size. For instance, it would be easier to visualize a 10µm diameter void than the same void with a volume of $524\mu m^3$. Void shape was then classified into three types – spherical, peanut, and ellipsoidal, as shown in Figure 5.2. Spherical voids are approximately equiaxed. Peanut-shape voids appear to be a coalescence of two or more spherical voids. Ellipsoidal voids are elongated-shaped voids without a distinct waist as seen in peanut-shaped voids. Void locations are shown schematically in Figure 5.3 and categorized as follows:

- facet – void located at interface between two austenite grains;
- edge – void located at intersecting edge of three austenite grains;
- corner – void located at the intersecting corner of four (or more) austenite grains.

"Contact precipitates" were determined by viewing the 3D reconstruction to determine which precipitates were in contact with the voids.

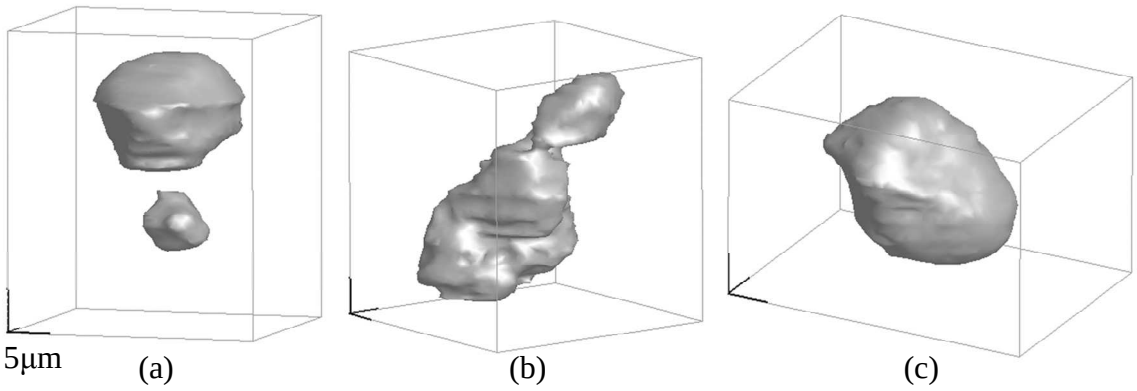

Figure 5.2: Classification of creep void shapes; (a) spherical voids; (b) peanut-shaped void which appear to be a joining together of two or more voids; (c) ellipsoidal void.

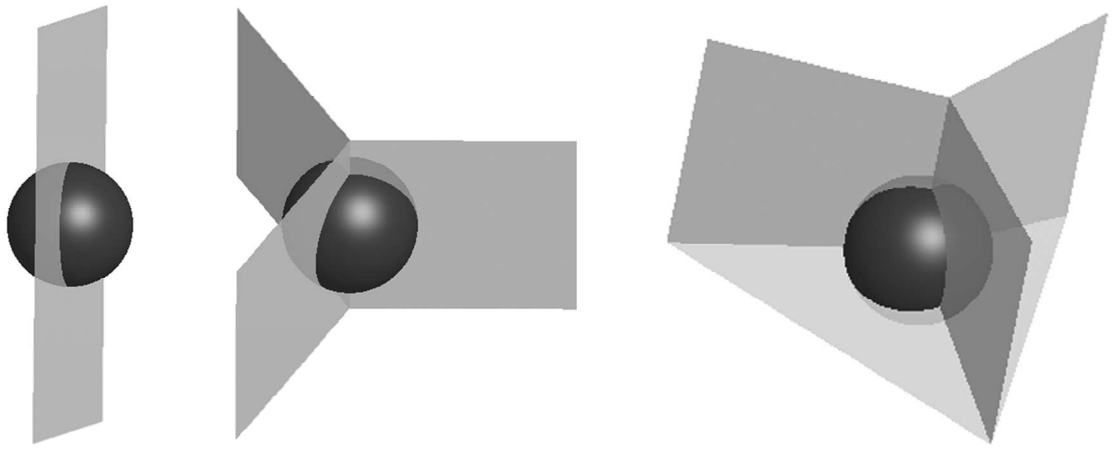

Figure 5.3: Schematic representations of void location classification; (a) void located on the facet between two grains; (b) void situated at the intersecting edge of three grains; (c) void located at the intersecting corner of four grains.

A total of 290 voids were reconstructed from the two larger serial-sectioned volumes (obtained at the original magnification of 200×), and their various characteristics observed from the 3D reconstruction are summarized in Figure 5.4. Figure 5.4a shows the overall void distribution represented by the equivalent void diameter. Total void volume for each diameter classification is indicated on the left axis while the number of voids in each class is indicated on the right axis. This graph simply points out that although there are a higher number of voids with diameters less than 4μm, the total volume occupied by these voids is small compared to the total volume occupied by voids that are larger than 12μm diameter.

Figure 5.4b shows a further breakdown of the void distribution in terms of their location within the grain structure. The larger voids appear predominantly along grain edges and corners (intersection of three and four grains respectively), while smaller voids are located primarily along facets (between two grains) and edges. There were a few instances of voids appearing intragranularly (within austenite grains) where they appear adjacent to Cr-rich $M_{23}C_6$ precipitates. These void locations are categorized as “Intragranular” on Figure 5.4b, and due to the low frequency of occurrence, their appearance on the graph is hardly visible.

Figure 5.4c displays the correlation between void location and void shape. Peanut-shaped voids account for most of the total void volume, perhaps unsurprisingly, since this void type appears to be a coalescence of two or more voids. Ellipsoidal voids occupy the least

amount of space, but it can be argued that these voids might also be a coalescence of two voids. In terms of numbers, there were more voids occurring at grain facets, however, the total volume of the voids at this location is less than as tenth of the volume taken up by voids at grain edges and corners. A possible explanation is as follows. In high temperature diffusional flow creep, deformation results when adjacent grains displace relative to each other in a process called "accommodation grain boundary sliding". Here, additional diffusion occurs along the grain boundaries to prevent cracks and voids from forming due to migration of atoms and vacancies during diffusional creep. However, in the presence of inclusions or precipitates, the rate of accommodation grain boundary sliding could not match deformation rate of diffusional creep, thus allowing voids to form [16, 21, 73]. In this material, the occurrence of larger voids at grain edges and corners coincide with the presence of large carbide clusters at these locations. These carbide clusters may have inhibited accommodation grain boundary sliding, hence causing large voids to grow, which lead to more severe creep damage at grain edges and corners.

Figure 5.4d displays the link between the precipitates in contact with the voids and their occurrences in terms of number of voids and fraction of total void volume. These results show that a higher number of voids was in contact with only $M_{23}C_6$ precipitate but a higher fraction of total void volume came in contact with both $M_{23}C_6$ and NbC precipitates. The most significant observation made from Figure 5.4d is that all the voids inspected came in contact with $M_{23}C_6$ somewhere along their perimeter. No voids were observed solely in contact with NbC and/or TiC precipitates. Correlation between creep void locations and $M_{23}C_6$ precipitates has been mentioned previously in the literature [73, 74]. From the present inspection of a single ex-service tube, it cannot be conclusively said that these voids nucleated only at $M_{23}C_6$ precipitates. However, it should be noted that for the material volume inspected, there was twice the amount of $M_{23}C_6$ compared to NbC (approximately 7% vs 3%, by volume), and thus the absence of voids solely adjacent to NbC precipitates is conspicuous. Another comment to follow these observations is that there were no other types of inclusions or impurities found to be associated with the voids. One work on bainitic CrMoV steel has indicated that creep voids nucleate exclusively on grain boundary sulfides [75]. It has also been proposed that creep voids nucleate only on "nonadherent grain boundary inclusions" [73]. However, in this work, no evidence was found to support this claim.

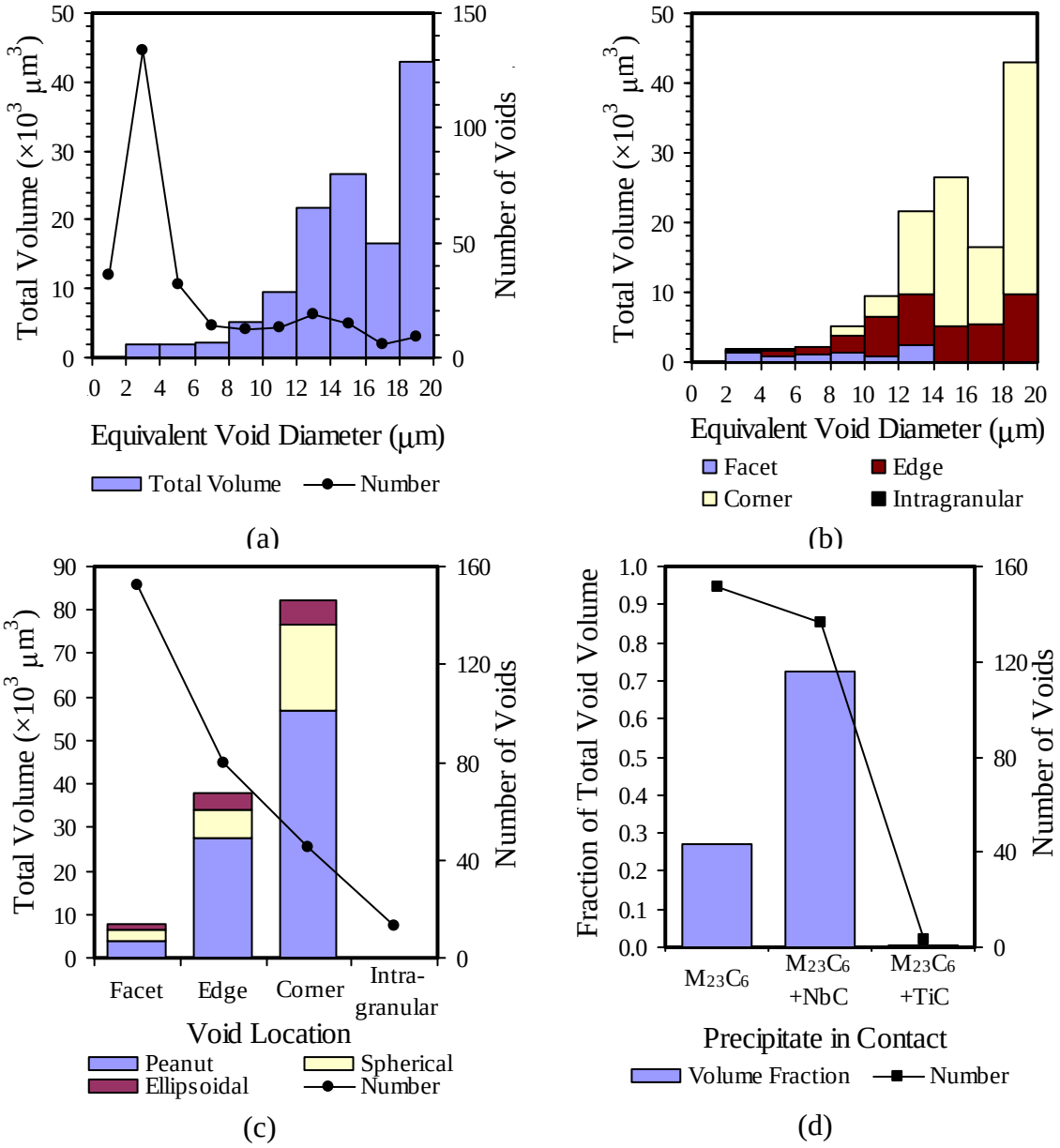

Figure 5.4: Characteristics of creep void obtained from 3D reconstruction of reformer tube material. Total number of voids analyzed is 290 obtained from two reconstructed volumes; (a) overall distribution of total void volume and number for various sizes of voids; (b) distribution in (a) is further categorized in terms of void location; (c) correlation between void location and void shape; (d) voids and contact precipitates listed as fraction of total void volume and void count.

5.3 EBSD of Creep Void Precipitates

It is important to restate here that all voids in the ex-service reformer tube were observed next to precipitates, and all of these voids came into contact with $M_{23}C_6$ somewhere along their perimeter. Previous studies [76-81] have shown that formation and growth of $M_{23}C_6$ precipitates in austenitic stainless steels is influenced by the orientation relationship (OR) between the precipitates and the adjacent austenite grains. Consequently, it was hypothesized that OR of the precipitate-austenite interface (i.e. between adjacent austenite grains, neighboring precipitates, or bordering austenite and precipitate particles), may also be responsible for the occurrence of $M_{23}C_6$ next to every void observed in the ex-service sample. Using EBSD, the crystallography of the $M_{23}C_6$-austenite interfaces of an ex-service sample was studied and compared to similar interfaces in an aged as-cast sample with no creep damage. This experiment was performed in order to establish any crystallographic trends that might be unique to $M_{23}C_6$ precipitates in tubes that were subjected to creep.

After sectioning layers 45[§§§], 55 and 65, all four areas of interests in the ex-service sample were subjected to EBSD scans to generate an overall orientation map. To expedite the EBSD and serial sectioning processes, scans were perform only after every tenth serial section layer, or every 5μm of material removed. Considering the fact that on average, the austenite grain size was about 80μm and void diameters were typically larger than 5μm, sufficient crystallographic information can still be obtained by scanning every tenth layer. An example of an EBSD map of the austenite grains is shown in Figure 5.5a (same location as Figure 5.1a). Here, the grains are represented by different colors according to their respective crystallographic orientations, which meant that grains shown in the same color have the same crystallographic orientation with respect to the reference axes. Furthermore, the output of EBSD mapping was also applied to the 3D reconstructions, as shown in Figure 5.5b (same location as Figure 5.1c). The reconstructions incorporated the crystallographic orientations to differentiate each austenite grain, while precipitates and voids were superimposed as areas of gray and white respectively. Following the EBSD mapping, all the voids and their immediate surroundings in all four areas were imaged using forescatter Z-contrast (FZ) and forescatter orientation (FO) detectors, in addition to

[§§§] EBSD system was installed in time only for layer 45 onwards.

the usual secondary electron (SE) image. The forescatter detector when coupled with an EBSD system generates the so-called forescatter image which reveals grain and subgrain structure of the samples. The forescatter Z-contrast detector revealed atomic number contrast of the different phases present while the forescatter orientation contrast detector exposed grains or subgrains and within the matrix and precipitates.

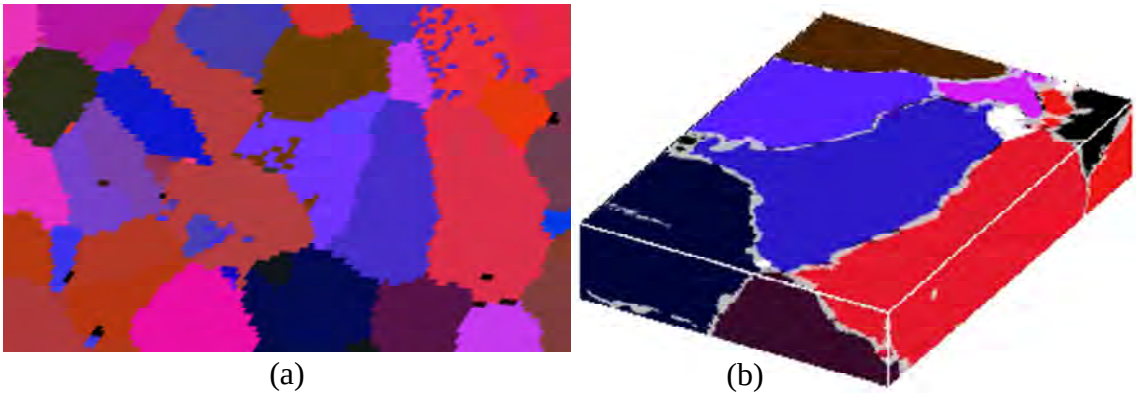

(a) (b)

Figure 5.5: EBSD mapping of reformer tube microstructure. (a) EBSD map obtained after layer 45 of the serial section process (same area as Figure 5.1a). (b) EBSD map superimposed on a 3D reconstruction to differentiate the austenite grains (same area as Figure 5.1c). Precipitates and voids are shown in gray and white, respectively.

A "control" sample was also prepared from an as-cast tube made from the same alloy as the ex-service tube. In order to replicate the service time and temperature, the control sample was aged at 1030°C for 500 hours in air resulting in a Larson-Miller parameter $(LMP)^{****}$ value of 33.4, compared to a value of 33.6 for the ex-service sample based on a temperature of 940°C for 60,000 hours. The control sample was used to determine the OR of the precipitate-austenite interface in an aged material and compare that to the OR of the precipitate-austenite interface in a material with creep deformation (ex-service sample).

The differences in microstructures between the ex-service and aged samples are very apparent in Figure 5.6. Although the *LMP* values were similar, the microstructural development of a sample that has undergone 6.8 years at a maximum temperature of 940°C (Figure 5.6a) is completely different from the aged sample that experienced 1030°C for only 500 hours (Figure 5.6b). The combined presence of applied stress, operating temperature, and perhaps a chemically active environment (of methane and hydrogen) for

**** Refer to Appendix I for Larson-Miller diagram for CA4852-Micro.

6.8 years resulted in the presence of numerous creep voids amongst the coarse precipitates lining up the grain boundaries. On the contrary, the grain boundary precipitates in the aged samples still show the lamellar-like appearance even though their form is much less angular or faceted as in the as-cast sample (refer to Figure 4.7 in Chapter 4). Furthermore, the intragranular precipitates appear slightly coarser and less in numbers in the ex-service tube, whereas in contrast, the aged sample contained denser and finer intragranular precipitates. The shorter time at high temperature, coupled with the lack of applied stress would have impeded the dynamics of the creep deformation processes, slowing the coarsening of the precipitates and the formation of voids. However, identity of precipitates in the aged sample was the same as in the ex-service tube.

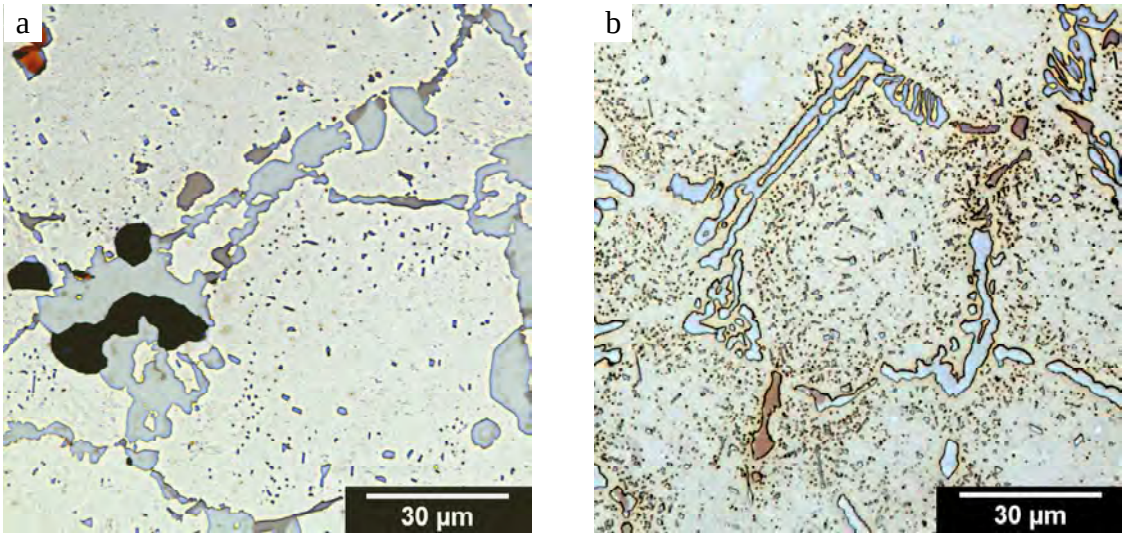

Figure 5.6: Differences in microstructure between the tube samples. (a) Ex-service reformer tube after 6.8 years at a maximum temperature of 940°C; (b) Aged tube sample after 500 hours at 1030°C. Larson Miller parameters for both tubes are similar.

EBSD patterns (or EBSPs) were then recorded in spot mode for specific locations of the matrix and precipitates surrounding the creep voids. For each precipitate grain in contact with a creep void, EBSPs were obtained from the precipitate as well as the austenite grains on both sides of the grain boundary. In instances where the precipitate grain contained subgrains, EBSPs were obtained from each subgrain if its size was larger than the size of the electron beam. The occurrence of these subgrains within large precipitate colonies would certainly influence the orientation relationships (OR) data obtained if the electron beam size is larger than the subgrain size. This would be due to the fact that the largest

subgrain within the electron beam spot would dominate the EBSD pattern and obscure the pattern from any smaller subgrains. EBSD scans were also carried out on the "control" sample. Since the control sample did not contain any creep voids, grain boundary precipitates were selected at random and EBSPs were obtained for these precipitates and the adjacent austenite matrices.

An example of the EBSD procedure is demonstrated in Figure 5.7. Figures 5.7a, 5.7b, and 5.7c are examples of SE, FZ, and FO images of a creep void and its vicinity. The locations where EBSPs were obtained are identified in Figure 5.7c. Examples of typical EBSPs are shown in Figures 5.7d through 5.7j. A combination of EDS and EBSD was used to positively identify the various precipitates observed.

HKL Technology's Flamenco software was used to analyse the EBSPs which then automatically calculated a 3×3 orientation matrix for each EBSP. The misorientation $\boldsymbol{M}$ between any two phases (*A* and *B*) can then be obtained from the matrix operation:

$$[\boldsymbol{A}][\boldsymbol{B}]^{-1} = [\boldsymbol{M}]$$

where $[\boldsymbol{A}]$ and $[\boldsymbol{B}]$ are orientation matrices of locations within phases *A* and *B* with respect to an arbitrary reference axis system. Assuming that:

$$[\boldsymbol{M}] = \begin{bmatrix} m_{11} & m_{12} & m_{13} \\ m_{21} & m_{22} & m_{23} \\ m_{31} & m_{32} & m_{33} \end{bmatrix}$$

the orientation relationship (OR) between location *A* and *B* is then:

$$\begin{bmatrix} m_{11} & m_{21} & m_{31} \end{bmatrix}_A // \begin{bmatrix} 1 & 0 & 0 \end{bmatrix}_B$$
$$\begin{bmatrix} m_{12} & m_{22} & m_{23} \end{bmatrix}_A // \begin{bmatrix} 0 & 1 & 0 \end{bmatrix}_B$$
$$\begin{bmatrix} m_{31} & m_{32} & m_{33} \end{bmatrix}_A // \begin{bmatrix} 0 & 0 & 1 \end{bmatrix}_B$$

The misorientation angle θ_M and axis $[u\ v\ w]$ between *A* and *B* can also be calculated from misorientation matrix $[\boldsymbol{M}]$ by the following equations:

$$\theta_M = \cos^{-1}\left(\frac{m_{11} + m_{22} + m_{33} - 1}{2}\right) \qquad \begin{bmatrix} u & v & w \end{bmatrix} = \begin{bmatrix} m_{23} - m_{32} & m_{31} - m_{13} & m_{12} - m_{21} \end{bmatrix}$$

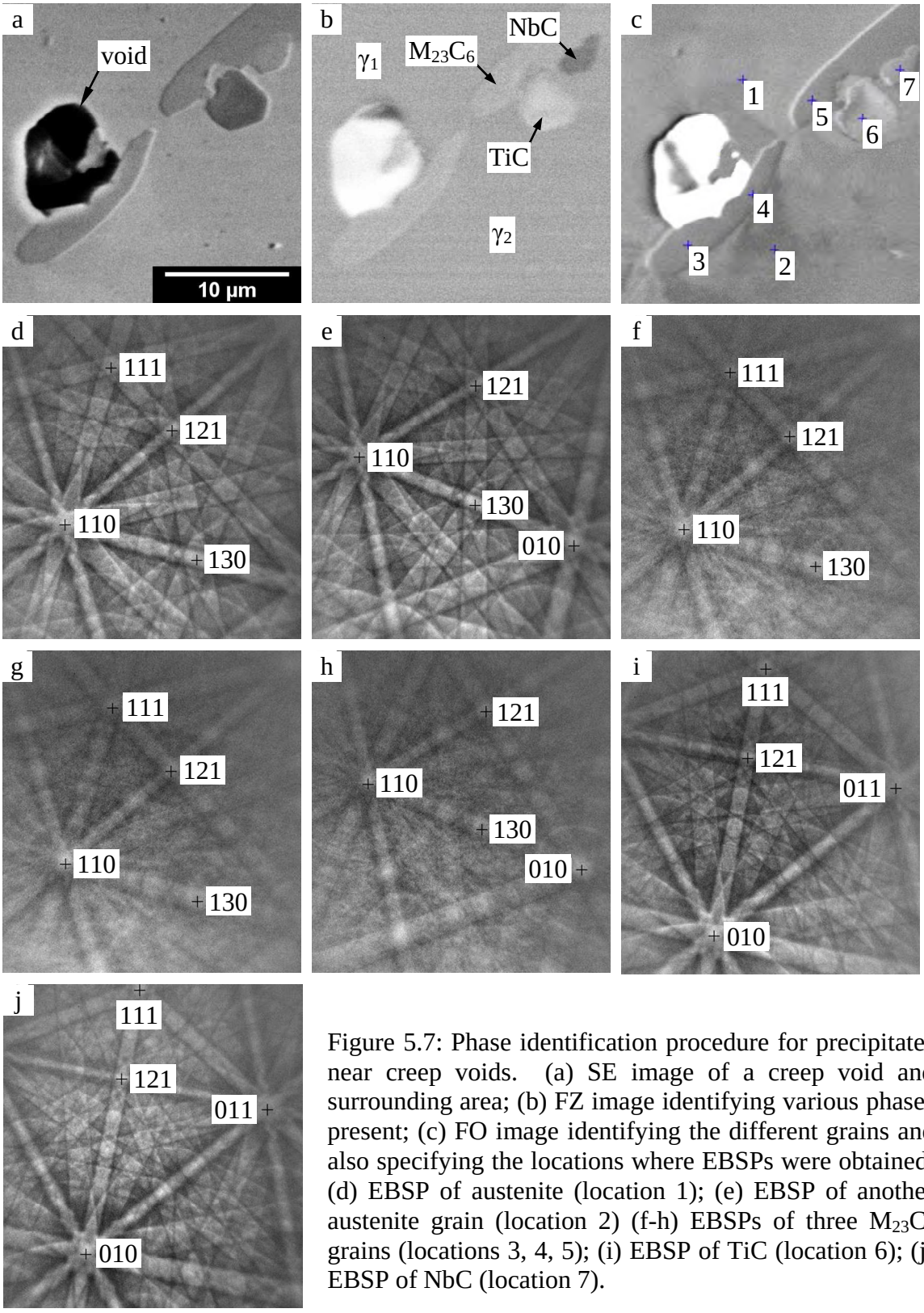

Figure 5.7: Phase identification procedure for precipitates near creep voids. (a) SE image of a creep void and surrounding area; (b) FZ image identifying various phases present; (c) FO image identifying the different grains and also specifying the locations where EBSPs were obtained; (d) EBSP of austenite (location 1); (e) EBSP of another austenite grain (location 2) (f-h) EBSPs of three $M_{23}C_6$ grains (locations 3, 4, 5); (i) EBSP of TiC (location 6); (j) EBSP of NbC (location 7).

Figure 5.8a shows the OR between $M_{23}C_6$ precipitates adjacent to creep voids and each adjacent austenite matrix grain in the form of a [100] stereographic triangle. A total of 442 points was plotted. Data represented by filled squares are $M_{23}C_6$ precipitates with a near cube-cube OR (high coherency) with an adjacent austenite grain while data represented by open squares are for $M_{23}C_6$ precipitates with a random OR (low coherency). Typically an angular difference between grains of 10-15° is taken as low angle grain boundary, where dislocation arrays are able to compensate for the interface mismatch [82]. For this work, near cube-cube OR is determined by a misorientation angle of 10° or less. Figure 5.8b shows the distribution of misorientation angles for $M_{23}C_6$ precipitates and austenite grains in the vicinity of the creep voids. The distribution showed that approximately twenty percent of the $M_{23}C_6$ precipitates adjacent to voids show a near cube-cube OR, while the remaining eighty percent of these precipitates occurred on low coherency interfaces.

Previous work by King and Bell [83] stated that grain boundary precipitates should obtain rational OR with one of the adjacent grains. Specifically, works by Lewis and Hattersley [77] and Beckitt and Clark [76] on $M_{23}C_6$ precipitates in austenitic stainless steels indicate that grain boundary $M_{23}C_6$ precipitates should display a cube-cube OR with at least one of the adjacent austenite grains. Furthermore, long term ageing such as the service condition experienced by the ex-service reformer tube would typically result in “realignment” of the grain boundary carbides towards a near cube-cube OR so that the total interface energy is lowered [77]. This would imply that the occurrence of cube-cube OR between $M_{23}C_6$ precipitates and the adjacent austenite grains should be fifty percent. Interestingly, this hypothesis was demonstrated by the “control” sample which underwent high temperature ageing without any loading. As mentioned earlier, the “control” sample was aged in air at 1030°C for 500 hours. Although the ex-service alloy experienced service at 940°C for 60,000 hours, both Larson-Miller parameters were similar (33.4 for control sample, 33.6 for the ex-service). The OR data for the control sample (total of 272 points) showed a higher degree of clustering around the 100 pole, as indicated in Figure 5.8c. The misorientation angle distribution in Figure 5.8d established that cube-cube OR between $M_{23}C_6$ precipitates and austenite occurred forty seven percent of the time.

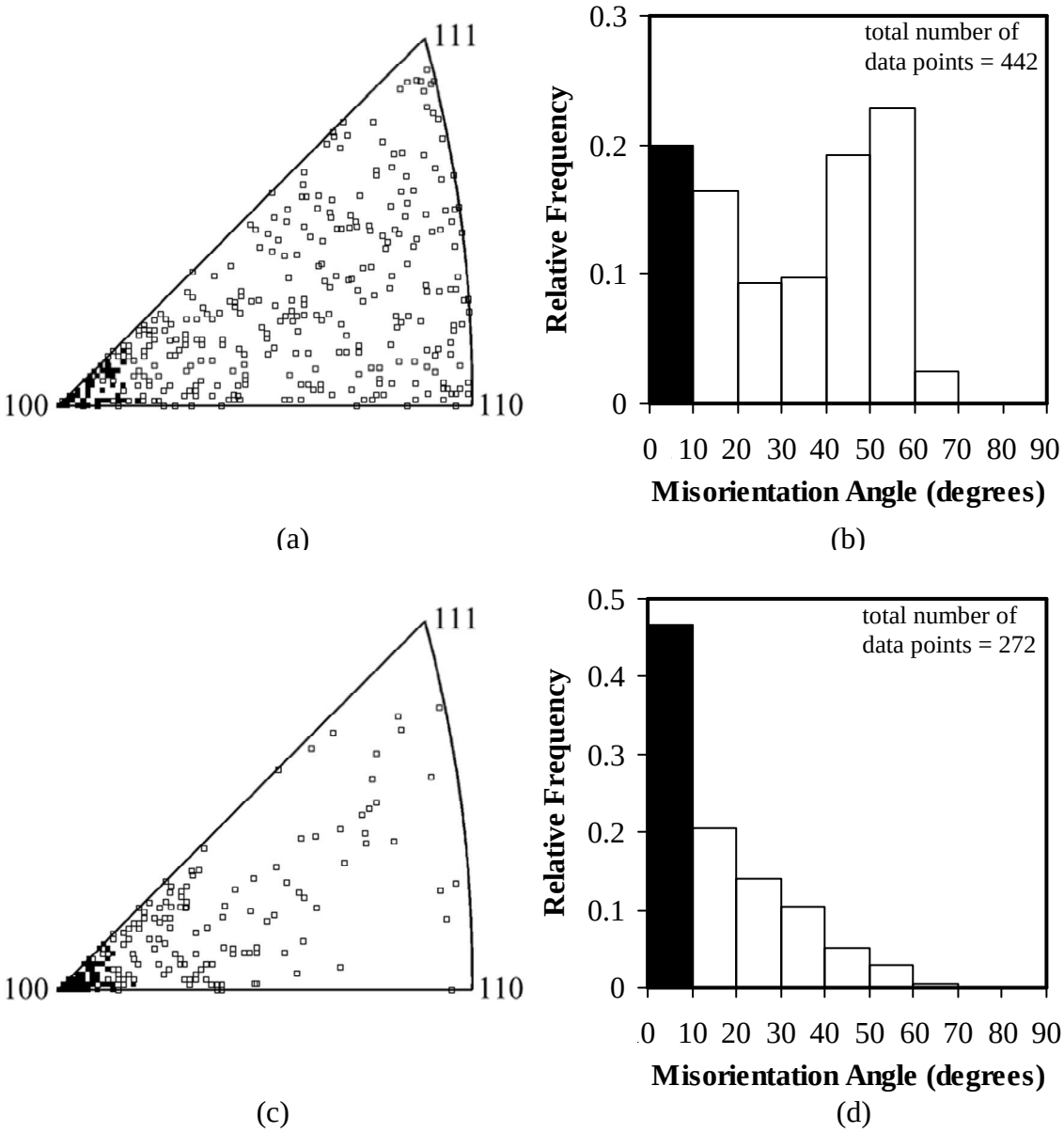

Figure 5.8: Comparison of orientation relationships and misorientation angles between ex-service material and laboratory-aged sample. (a) OR between $M_{23}C_6$ and austenite grains in ex-service tube sample, closed squares indicate $M_{23}C_6$ precipitates with near cube-cube OR with austenite; (b) misorientation angle distribution of OR data shown in (a), black histogram bar correspond to near cube-cube data ; (c) OR between $M_{23}C_6$ and austenite grains in laboratory-aged sample; (d) misorientation angle distribution of OR data shown in (c).

Based on the above observations, it is believed the preferred sites for creep voids are low coherency boundaries (random OR) between $M_{23}C_6$ precipitates and austenite. One possible explanation for this phenomena is the low coherency boundaries contained more vacancies due to lattice mismatch. As mentioned in Chapter 2, diffusional flow creep occurs at low stress and high temperature, and this mechanism requires the motion of

atoms and vacancies. Perhaps, this makes low coherency interfaces ideal locations for voids to initially form. The applied stress and high temperature would then result in continuous motion of atoms and vacancies which would cause permanent deformation of the grains. However, the presence of precipitates at the grain boundaries is believed to inhibit the rate of accommodation grain boundary sliding from matching the rate of diffusional creep, resulting in the formation of these voids along precipitates at the grain boundaries [21].

5.4 Conclusions

Creep voids in an ex-service hydrogen reformer tube have been studied via serial sectioning and 3D reconstruction. Creep voids are not uniformly distributed through the volume in terms of their size, shape, and location. The largest voids were formed by coalescence of two or more voids resulting in a peanut shape. Almost all of the voids appeared near grain boundary carbides and the larger of these voids were located at grain edges and corners. This is possibly due to the presence of large carbides acting as obstruction to accommodation grain boundary sliding, and also as large sources of vacancies for the atom-vacancy migrations of the diffusional flow creep. All voids appeared next to precipitates and all of these voids made contact with $M_{23}C_6$ precipitates. No voids were observed in sole contact with TiC or NbC precipitates. EBSD observation of the $M_{23}C_6$ precipitates surrounding these voids showed that 80% of the voids were found adjacent to precipitates with a random OR with the surrounding austenite matrix, rather than being distributed equally (50%) at precipitates with either cube-cube or random OR with the austenite matrix.

Chapter 6

CREEP VOIDS AT VARIOUS STAGES OF CREEP

In this portion of the research, samples were taken from three locations along the length of a single reformer tube to investigate the effects of service conditions on the characteristics of creep voids. In addition, samples were obtained from various positions along the wall thickness where there are also differences in temperature, stress, and microstructure. The characteristics of these voids were studied with the idea of applying the findings to a classic void growth model presented by Raj and Ashby [27]. The application of data obtained from 3D observations to a growth model is anticipated to bring new insights and the Raj and Ashby model will be discussed further in the next chapter.

A portion of this chapter has been published in a paper entitled "*A Three-Dimensional Characterization of Creep Void Formation in Hydrogen Reformer Tubes*" by Azmi Abdul Wahab, Christopher R. Hutchinson and Milo V. Kral, in Scripta Materialia 55 (2006) 69-73.

6.1 Experimental Details

The samples studied in this chapter were taken from a single reformer tube that was retired after 90,000 hours of service at Methanex Kitimat plant in British Columbia, Canada. The tube was retired due to excessive diametral strain (based on an in-house deformation criterion) but was otherwise structurally sound with no cracks or ruptures. As previously described in Chapter 3, the tube material is Schmidt-Clemens Centralloy® CA4852-Micro centrifugally cast austenitic stainless steel. The microstructure of this tube consists of small equiaxed grains along 20% of the inner cross-section of the tube, while the remaining outer cross-section contains large columnar grains. Various precipitates outline the grain and cell boundaries of the equiaxed and columnar structures and these

precipitates are responsible for the high temperature characteristics of the reformer tube (refer to Section 2.2 in Chapter 2).

The locations along the reformer tube where the samples were obtained were at distances of 12.5m, 9.9m, and 2.4m from the top inlet flange and these samples were identified as K1, K2, and K3 respectively. Profiles for the inner and outer wall temperatures and the internal pressure for this ex-service tube are shown in Figure 6.1, with the respective sample locations indicated. Additionally, the diametral strains for the tube and the corresponding sample locations are shown in Figure 6.2. The strain measurements were determined from LOTIS™ inspections†††† performed on the tube. Note that samples K1 and K2 were taken from the same tube segment while K3 is from an adjoining tube segment‡‡‡‡. A summary of the operating conditions for all three samples is given in Table IV.

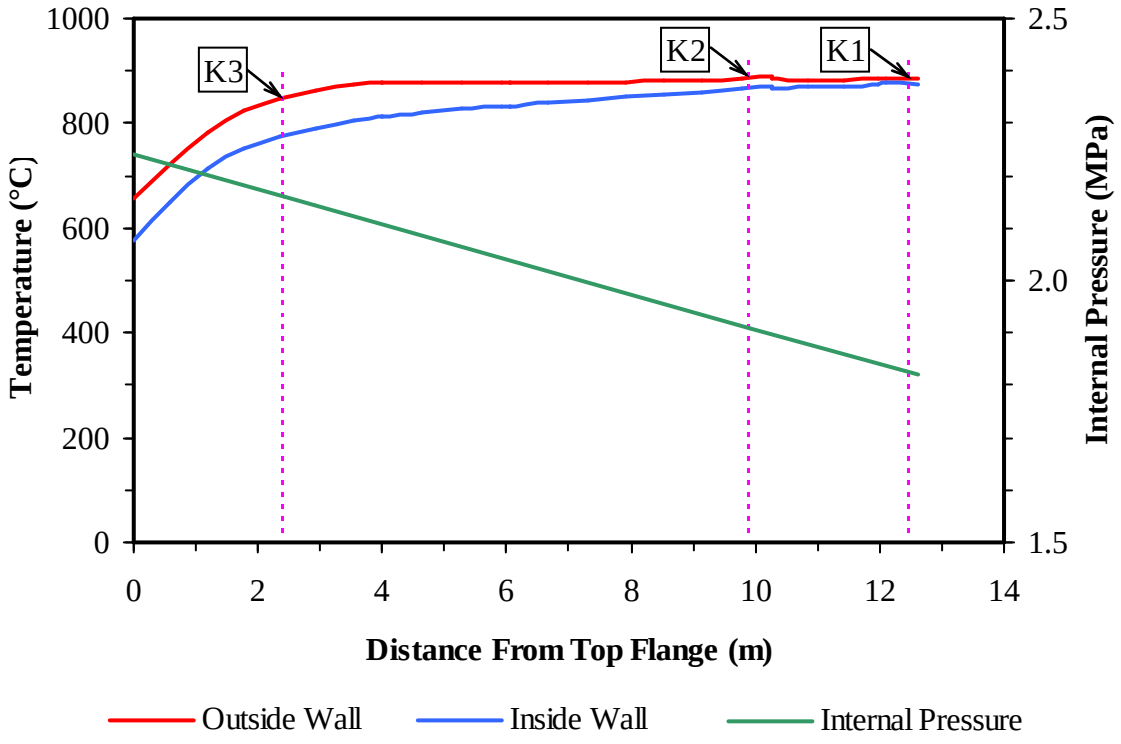

Figure 6.1: Temperature and pressure profiles of the Kitimat ex-service reformer tube. Locations where samples were obtained (K1, K2, K3) are indicated on the graph.

†††† LOTIS™ (Laser Optic Tube Inspection System) is a non-destructive measurement system developed by QUEST Integrated, Inc., Washington, USA..

‡‡‡‡ Reformer tubes are fabricated by welding three 4.5m segments.

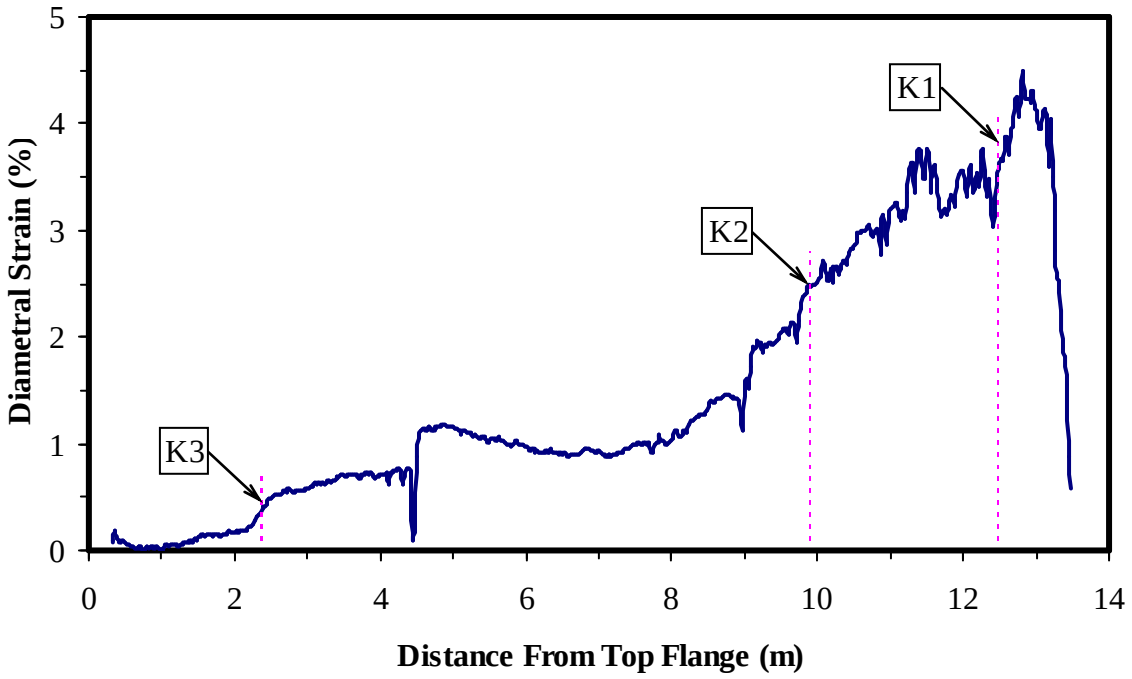

Figure 6.2: Diametral strain of the Kitimat ex-service reformer tube. Locations of samples K1, K2, and K3 are shown on the graph.

Table IV: Summary of operating conditions for the obtained samples.

Sample	Life, hours	Distance from top flange, m	Diametral Strain, %	Temperature, °C	Internal Pressure, MPa
K1	90000	12.5	3.7	878-888	1.82
K2	90000	9.9	2.5	867-886	1.91
K3	90000	2.4	0.4	775-848	2.16

In general, the methods employed for characterization of precipitates, serial sectioning, and 3D reconstruction on these samples are similar to those described earlier in Chapters 3 and 4. Characterization of the precipitates was performed using a combination of EDS and EBSD techniques. The serial sectioning process was carried out via the one-step polishing method using a fifty percent (by volume) water dilution of Buehler MasterPolish® suspension on Buehler Chemomet® pad. For each sample location, four 400×300×50 µm volumes of material were obtained, each from 100 serial sections at a 0.5 µm sectioning increment. Two volumes were taken in the equiaxed-grain region near the inside wall of

the tube and the other two volumes were taken from different locations containing large columnar grains, one from mid-thickness and another from an outer wall area. These approximate areas are shown graphically in Figure 6.3. EBSD scans of the samples were done on five serial sections layers; for K1 sample, EBSD scans were made every tenth section starting at layer 15 and ending at layer 55; for samples K2 and K3, EBSD scans were performed at every twenty layers from layer 10 to layer 90[§§§§].

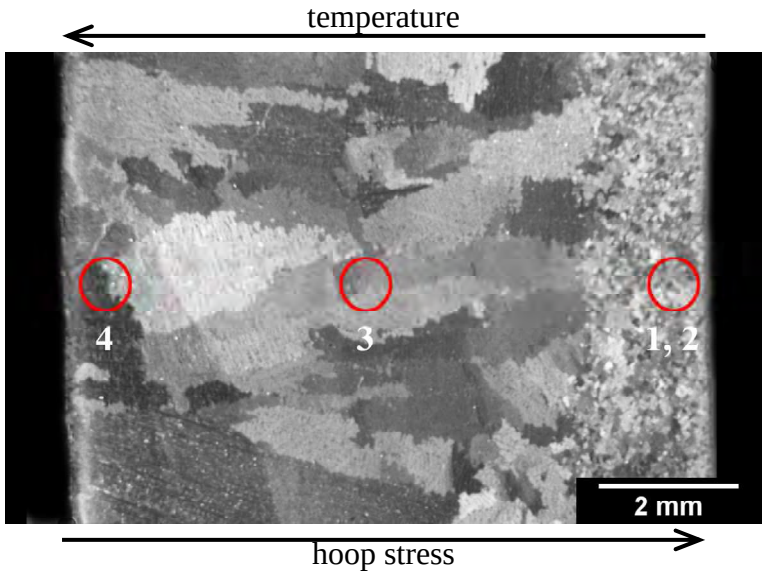

Figure 6.3: Macrostructure of the reformer tube wall showing the approximate locations of where the volumes were obtained for 3D reconstructions. The inner wall of the tube is on the right hand side of the image and the increase in temperature and hoop stress relative to the wall thickness is indicated by the arrows.

Registration of serial section images was carried out using NIH ImageJ software [39] and the "StackReg" plug-in [38], while 3D reconstructions of the volume were performed using RSI's IDL [71]. Void measurements such as volume, inter-void distance and grain boundary angle were achieved using various tools available in ImageJ, while void characteristics such as shape, type, location, and precipitate in contact were visualized using a combination of ImageJ and IDL.

[§§§§] Due to the large austenite grain sizes, EBSD scans were reduced from every tenth serial section to every twentieth serial section (every 10μm).

6.2 3D Reconstructions and Characterization of Voids

Characterization of precipitates via EDS and EBSD techniques revealed that three types of precipitates were present in the tube samples. Coarse chromium-rich $M_{23}C_6$ precipitates were present in the cell and grain boundaries and were also present as fine intragranular precipitates. Other precipitates present were of the MC-type carbides that appeared as either NbC in the cell and grain boundaries, or as TiC that appeared predominantly within the grains.

Twelve hundred serial sections were obtained to generate twelve reconstructed volumes for the three reformer tube samples. Four volumes were reconstructed for each sample, and examples of 3D reconstructions of the equiaxed and columnar microstructures are shown in the isometric views of Figures 6.4 and 6.5, respectively, with the corresponding EBSD maps superimposed on the top layers to show the austenite grains. Creep voids appear as the irregular dark shapes whereas the various precipitates appear in varying shades of grey. The differences between the equiaxed structure and the columnar structure are clearly evident, as revealed by the EBSD maps, and the carbide distribution generally marks the grain boundaries in the equiaxed microstructures of Figure 6.4, and dendrite arm boundaries in the columnar microstructures of Figure 6.5.

The precipitate morphologies and the distribution of creep voids of the same volumes shown in Figures 6.4 and 6.5 are further illustrated in the “transparent” views of Figures 6.6 and 6.7. The higher service temperature experienced by K1 samples resulted in larger creep void volumes and coarser precipitates as clearly shown in Figures 6.6a and 6.7a, compared to the K3 samples shown in Figures 6.6c and 6.7c. The differences in precipitate morphologies due to the temperature variations are also apparent in Figures 6.6a and 6.7a compared to Figures 6.6c and 6.7c. In the higher temperature samples of Figures 6.6a and 6.7a, the grain and cell boundary precipitates appear rounder and coarser measuring around 6μm wide in grain facets and up to 15μm wide in grain edges and corners. In contrast, the precipitates are thinner and more angular in the lower temperature samples in Figures 6.6c and 6.7c and measured approximately 3μm wide and rarely exceeded 5μm in width. Furthermore, intragranular precipitates are also much finer and appear in abundance near the grain and cell boundaries in the lower temperature samples. All data in this chapter were obtained from these “transparent” greyscale 3D reconstructions.

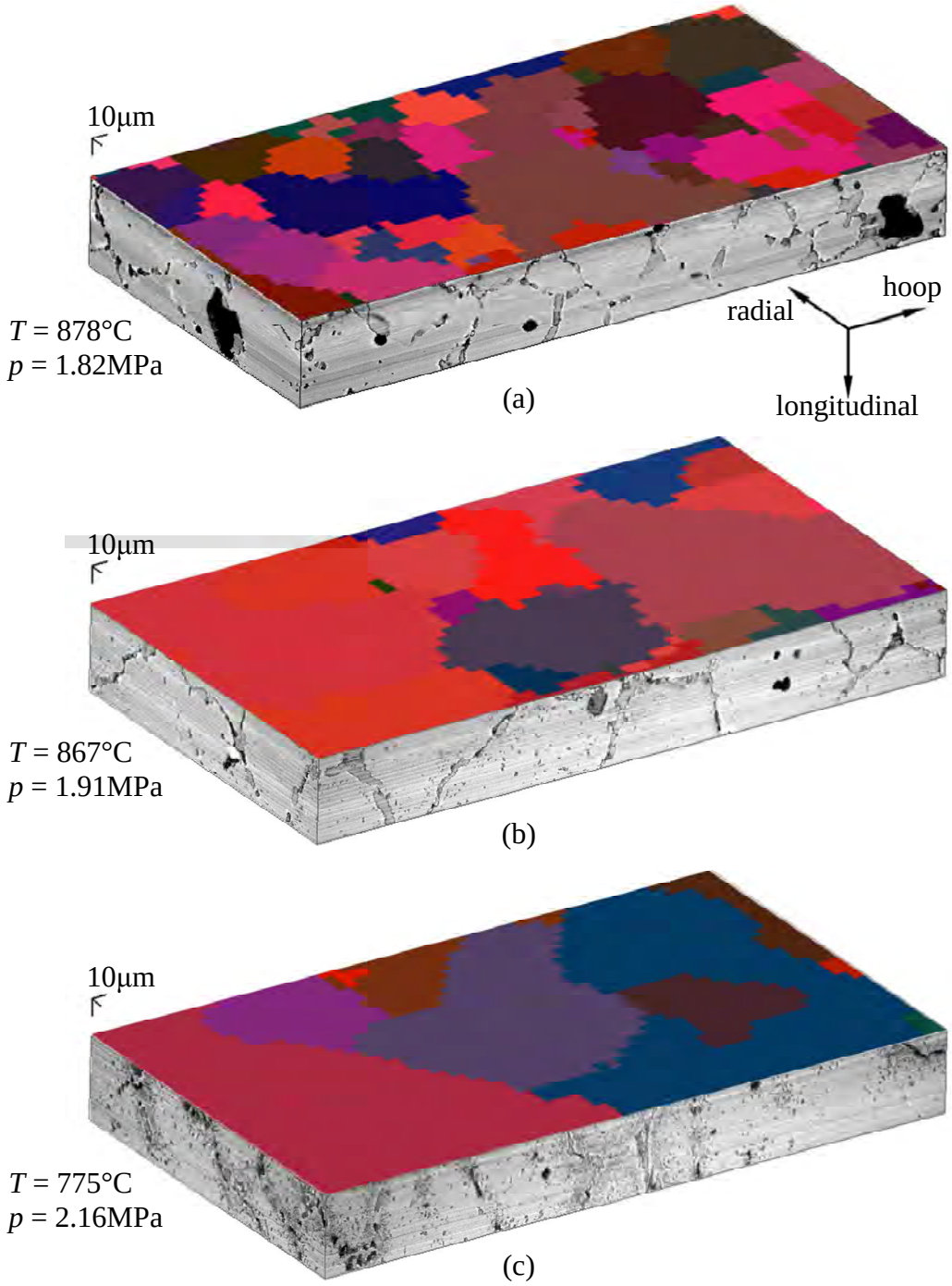

Figure 6.4: 3D reconstructions of the equiaxed microstructure at the inner wall of the tube. (a) Sample K1; (b) sample K2; (c) sample K3. Note that diametral strain and temperature decreases from the sample in (a) to the sample in (c), but the internal pressure increases. The orientation of the volumes with respect to the tube axes is indicated. EBSD maps are superimposed on the top layer.

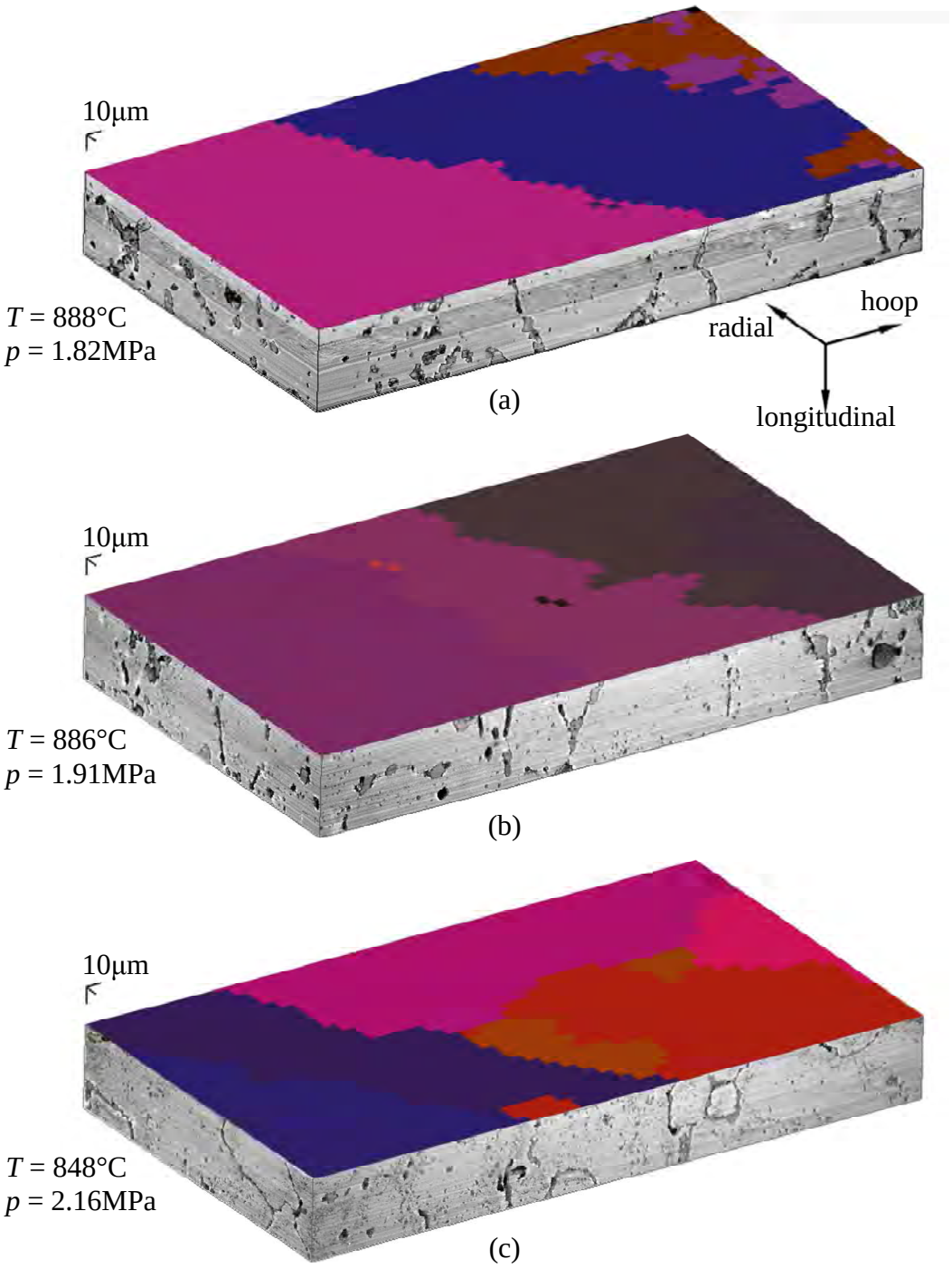

Figure 6.5: 3D reconstructions of the columnar microstructure at the outer wall of the tube. (a) Sample K1; (b) sample K2; (c) sample K3. Note that diametral strain and temperature decreases from the sample in (a) to the sample in (c), but the internal pressure increases. The orientation of the volumes with respect to the tube axes is indicated. EBSD maps are superimposed on the top layer.

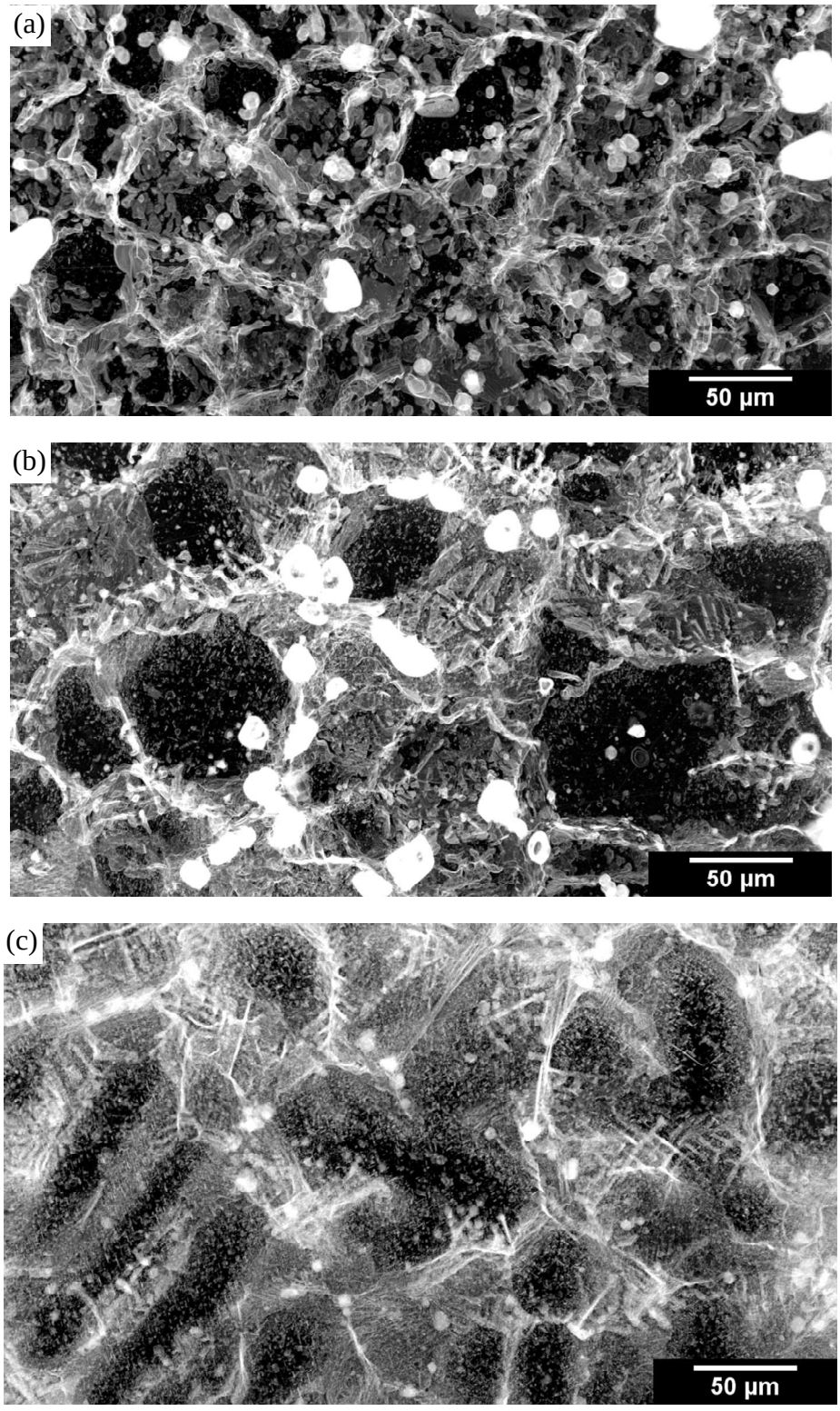

Figure 6.6: Transparent views of the 3D reconstructions of the equiaxed microstructure. (a) Sample K1; (b) sample K2; (c) sample K3. Creep voids appear as white colored globules. Precipitates are coarser and voids are larger in (a) where the service temperature is highest. The respective hoop, radial, and longitudinal stress directions are horizontal, vertical, and perpendicular to the page.

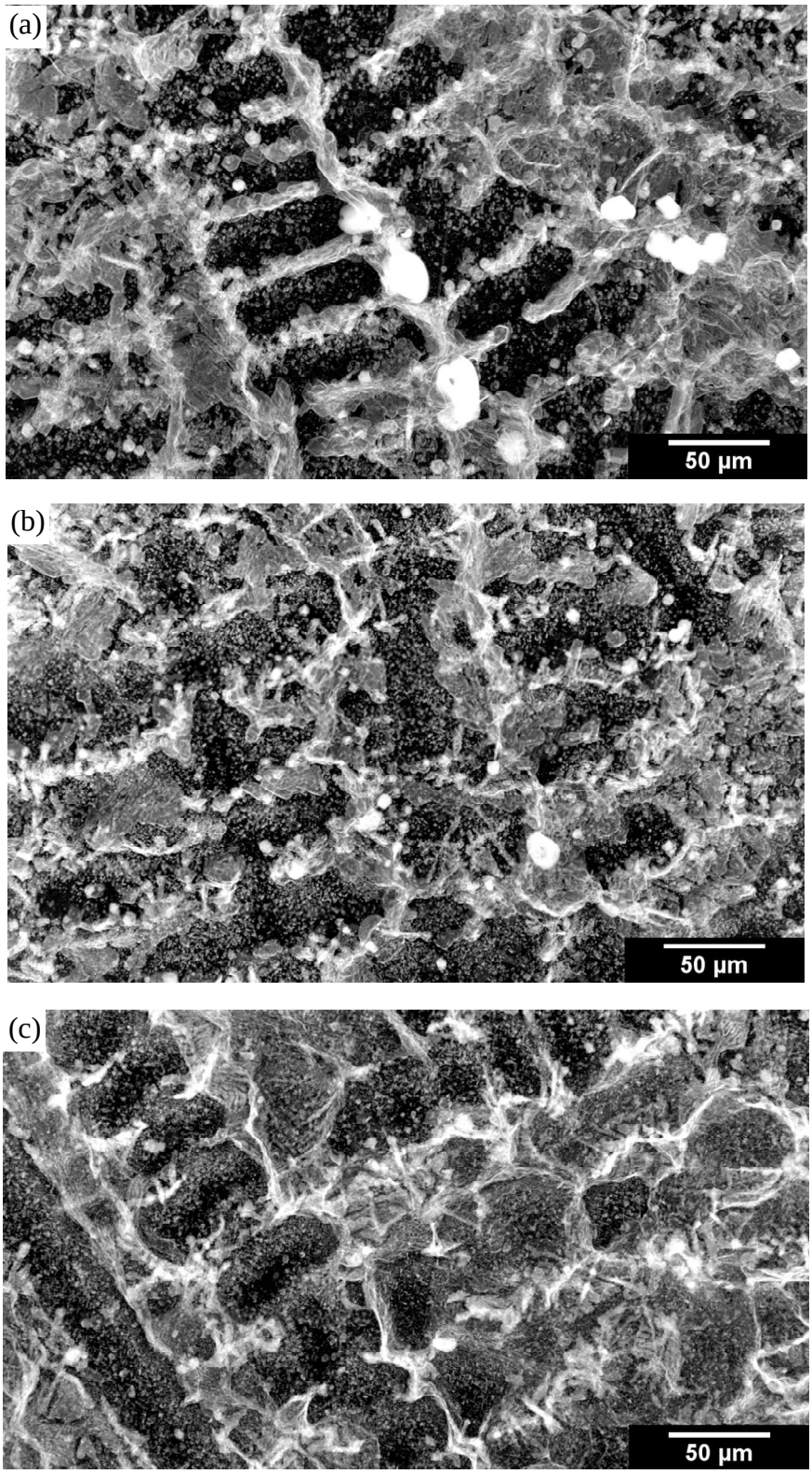

Figure 6.7: Transparent views of the 3D reconstructions of the columnar microstructure. (a) Sample K1; (b) sample K2; (c) sample K3. The respective hoop, radial, and longitudinal stress directions are horizontal, vertical, and perpendicular to the page.

Table V lists the various details relating to the twelve reconstructed volumes. Temperatures for locations 1 and 2 in each sample were taken as the respective inner wall temperatures (see Figure 6.1) whereas temperatures for location 4 were set as the outer wall temperatures. Mid-thickness temperatures for location 3 were simply approximated as the middle value between the inner and outer wall temperatures. Effective stresses, referred here as "Tresca" stresses, were calculated (using the equations listed in Appendix II) to represent the combined effect of stresses due to temperature, internal pressure, and tube weight. The volume size of each reconstruction is simply the area of the cropped image multiplied by the total sectioning depth (50μm in each case). From EBSD scans, the number of grains captured in each reconstructed volume can be determined. However, in most cases only a portion of a grain is contained in the volume. The number of grains listed in column six of Table V represents both full and partial grains that were sectioned. Creep is strongly affected by grain boundaries and thus it is useful to present the value for the total grain boundary area contained within the reconstructed volumes, as well as the number of grains. Using data from EBSD scans, the grain boundary area for each volume was determined by calculating the total length of boundaries per serial section and multiplying by the volume thicknesses.

Table V: Particulars of reconstructed volumes.

Sample-Volume	Micro-structure	Calculated Temperature, °C	Tresca Stress, MPa	Volume Size, $\times 10^{-3}$ mm^3	Number of Grains Sectioned (full & partial)	Grain Boundary Area, mm^2
K1-1	equiaxed	878	20.5	3.9	82	0.190
K1-2	equiaxed	878	19.4	4.4	36	0.133
K1-3	columnar	883	15.1	5.0	3	0.026
K1-4	columnar	888	4.77	4.6	4	0.024
K2-1	equiaxed	867	30.0	4.5	35	0.106
K2-2	equiaxed	867	29.6	4.3	30	0.114
K2-3	columnar	876	7.69	4.4	19	0.054
K2-4	columnar	886	11.4	4.6	8	0.038
K3-1	equiaxed	775	116	4.7	14	0.069
K3-2	equiaxed	775	107	4.5	16	0.051
K3-3	columnar	812	13.8	4.4	16	0.078
K3-4	columnar	848	55.2	4.4	16	0.076

Various 3D measurements were acquired from the 3D reconstructions. Information such as void size, count, shape, location, and contact precipitates were obtained in similar manner as was done previously in Chapter 5, i.e. void sizes were represented by equivalent void diameters to account for non-spherical voids, and classifications of void shapes and locations follow the classifications given in Figures 5.2 and 5.3. Additional information was also obtained from the 3D reconstructions specifically the void types, void-to-void distance, and grain boundary angles. Void types occurring on the grain boundaries follow the classification suggested by Raj and Ashby [27] as indicated in Figure 6.8. Type A voids occur on the precipitate-matrix interface in one of the matrix grains whereas type B voids span two or more matrix grains. A third void classification was also made here as intragranular voids or type C, which refer to voids appearing at intragranular $M_{23}C_6$ precipitates. Void-to-void distance was obtained by determining the distance to the closest neighboring void. From 3D reconstructions performed using NIH ImageJ, the centroids of all the voids within the reconstructed volume can be obtained and exported to a spreadsheet. By applying the Pythagorean Theorem to the coordinates of these centroids, the distance from one void to the closest neighboring void can then be established. For measurement of GB angles, the angle of a grain boundary adjacent to a void is measured with respect to the hoop stress axis. For voids occurring at grain edges, three angles were measured, whilst for voids at corners, four angles were recorded. The results of these measurements will be presented in the next section.

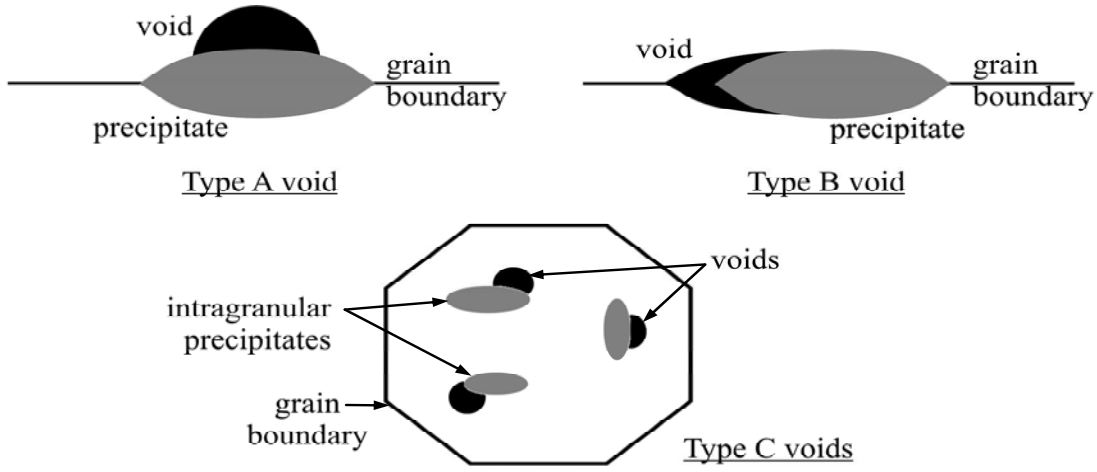

Figure 6.8: Type A, B and C classification of void types.

6.3 Results and Observations

From the twelve 3D reconstructions, a total of 1268 voids were reconstructed and characterized. Figure 6.9a-c shows the total volume, mean diameter, and void density for creep voids occurring at the inner wall, mid-thickness, and outer wall of the tube. For each 3D reconstruction, the total void volume was determined by summing the volumes of all grain boundary voids contained within the reconstruction. The mean diameter values were determined by first calculating the mean volume of voids and then determining the equivalent mean diameter by assuming that all voids are spherical. Meanwhile, the void density for each reconstruction was obtained by dividing the number of grain boundary voids by the grain boundary area. This action resulted in a void density value that is independent of the reconstructed volume size or the number of grains sectioned.

In essence, the two plots in Figure 6.9a and 6.9b show that larger voids tend to occur at the bottom of the reformer tube (sample K1) where temperature is generally higher than the top of the tube (sample K3). However, in each sample location, there is a decrease in both the total void volume and the size of the voids from the inner wall regions to the outer wall regions of the tube even though the temperature is higher on the outer wall. It is important to note that the inner wall of the tube consisted of equiaxed microstructure, which in general contained more grain boundary areas for voids to nucleate and grow. Referring back to Table V to compare the grain boundary areas, it appeared that for instances where there were large differences in grain boundary areas between the inner and outer wall (samples K1 and K2), the observed differences for total void volume and mean void diameter between the inner and outer wall were significant. Conversely, in the case of the K3 sample, the grain boundary areas at the inner and outer wall were quite similar, and the respective differences for total void volume and mean void diameter were not as dramatic.

In terms of the density of grain boundary voids shown in Figure 6.9c, the general trend for samples K1 and K2 indicated an increasing in the number of voids per grain boundary area from the inner to the outer wall. It needs to be noted that at the inner wall, the microstructure is equiaxed and the grain boundary area is larger than at the outer wall, while the temperature is lower than at the outer wall. In contrast, sample K3 appears to indicate a different deformation mechanism considering that the effective stresses were much higher for K3 due to the higher difference in temperature between the inner and

outer wall (refer to Table V). Nevertheless, the obtained measurements of mean diameter and void density will be applied to the void growth model to be presented in Chapter 7, and the effects of temperature, stress, and microstructure will be further analyzed.

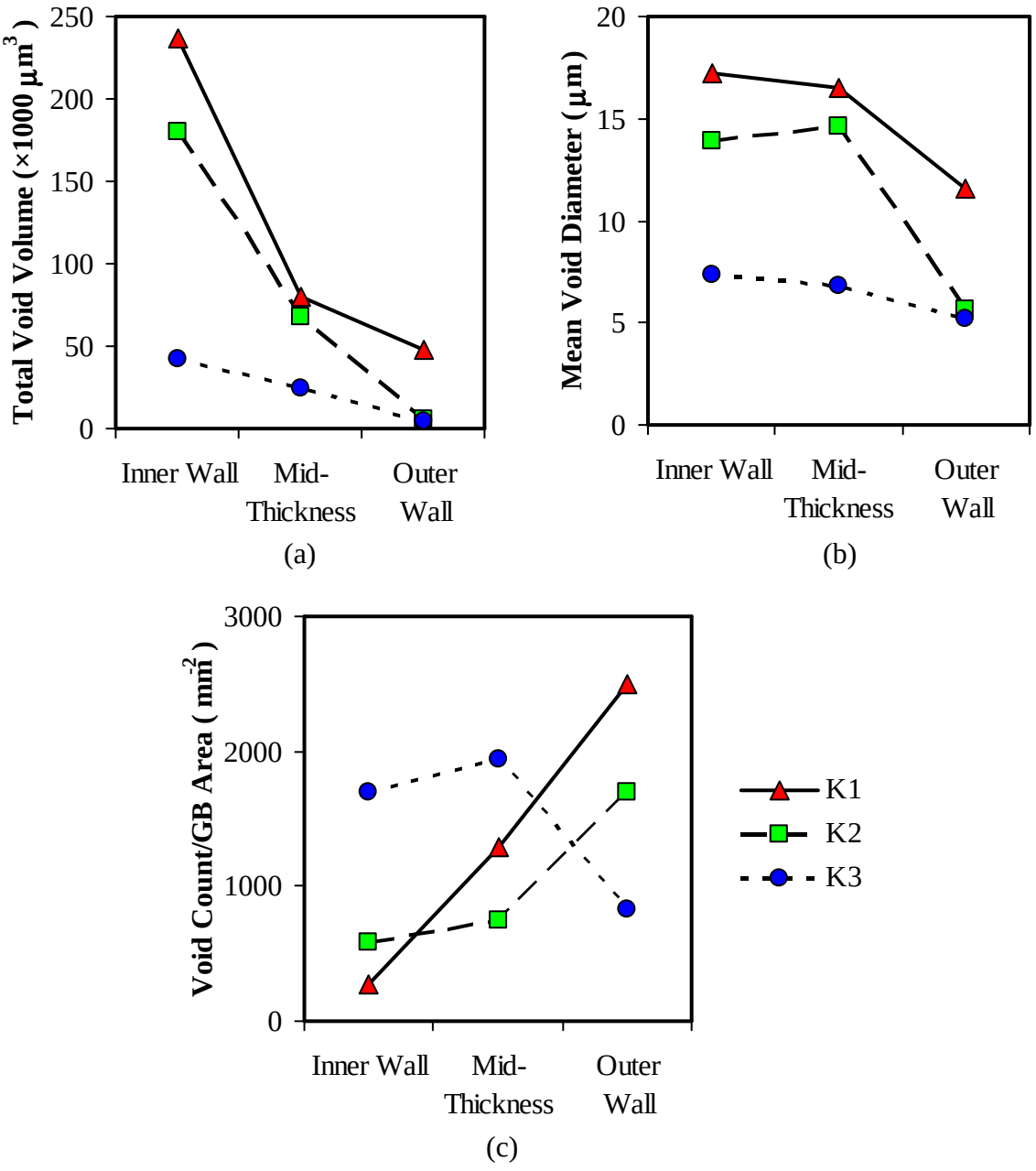

Figure 6.9: Comparison of characteristics of grain boundary voids between the three samples taken at various positions along the reformer tube and at three wall positions. (a) Total void volume; (b) mean void diameter; (c) void density.

The mean void diameter and the void density data presented in Figure 6.9b and 6.9c are further broken down to see the how various microstructural features affect the size and density of these voids. Void size can be thought of as a representation of void growth whereas void density can be assumed to represent nucleation. Void size and void density information obtained were separated in terms of void locations, adjoining precipitates(s), void type, and their shape. These trends are discussed further in the following paragraphs and their outcome will also be applied into the model in Chapter 7.

Figure 6.10a shows the influence of void location on the size and density of creep voids in the samples obtained. Generally, most of the larger voids are located at grain edges and corners. However, this information is somewhat misleading for the mid-thickness and outer wall regions of the tube samples where data were not available for comparisons due to the predominance of large columnar grains (i.e. very few corners and edges were actually observed). This is evident for sample K1 where mid-thickness and outer wall reconstructed volumes did not contain any grain edges or corners. Thus, these large columnar grains may be inadequately represented in the 3D reconstructions. Nevertheless, in comparing only the inner wall regions, samples K1 and K2 show a similar behavior where voids are largest at the grain corners (four-grain junctions) and smallest at grain facets (two-grain junctions). In contrast, sample K3, which experienced the lowest temperature but highest stress, shows a different behavior where its largest voids occur at the grain edges (three-grain junctions) and the smallest voids were at the grain corners.

If we regard void size as the representation of void growth, the results in Figure 6.10a imply that voids grow more readily at grain edges and corners. It has long been advocated that void growth is the result of diffusion occurring across the void surface and subsequent migration of atoms along the grain boundaries [25]. The highly disordered nature of the interfaces at grain edges and corners (due to presence of more lattice mismatch from three or four grain boundaries) would thus make corners and edges the ideal locations for diffusion to occur, thereby enhancing the creep deformation process. However, the presence of precipitates at these locations would impede the process of accommodation grain boundary sliding from matching the process of diffusional creep, resulting ultimately in the growth of voids

The main observation to be made from Figure 6.10b is that a much higher number of voids was found at grain facets than at grain edges and corners. Considering void density as representing nucleation, the higher number of voids at grain facets may not be too surprising, since in a typical microstructure there will always be more grain facets present than grain edges and corners. It is conceivable that simply because of the higher numbers of grain facets than edges or corners, there would likely be more sites at facets for voids to nucleate. Furthermore, comparing inner and outer wall of samples K1 and K2, void density numbers also shows an increase from the inner wall than the outer wall. This may be either due to the higher temperature at the outer tube wall, or due to the fact that the voids at the inner wall have coalesced and thus reduced in number. Sample K3 again shows an opposite behavior, presumably due to a different creep mechanism resulting from the lower temperature but higher stress present at the inner wall of this location of the tube.

Nucleation of creep voids is still not a well-understood field. In his review paper, Kassner [25] summarized three theories of void nucleation:

- nucleation from grain boundary ledges or at triple point caused by grain boundary sliding;
- nucleation due to vacancy condensation at high stress regions;
- nucleation due to dislocation pile-ups.

The presence of precipitates at grain boundaries (such as the reformer tubes studied here) may require a combination of all three mechanisms for void nucleation to occur [25]. In the reformer tube material, samples taken from the lower portion of the tube (hotter region) most probably have undergone void nucleation either from grain boundary sliding at or vacancy condensation since the stresses were relatively lower than in the upper region of the tube. At the upper region of the tube, the higher stresses present may have resulted in voids nucleating due to dislocation pile-ups. Nevertheless, both the void size and density information gathered here will be used in the model in Chapter 7.

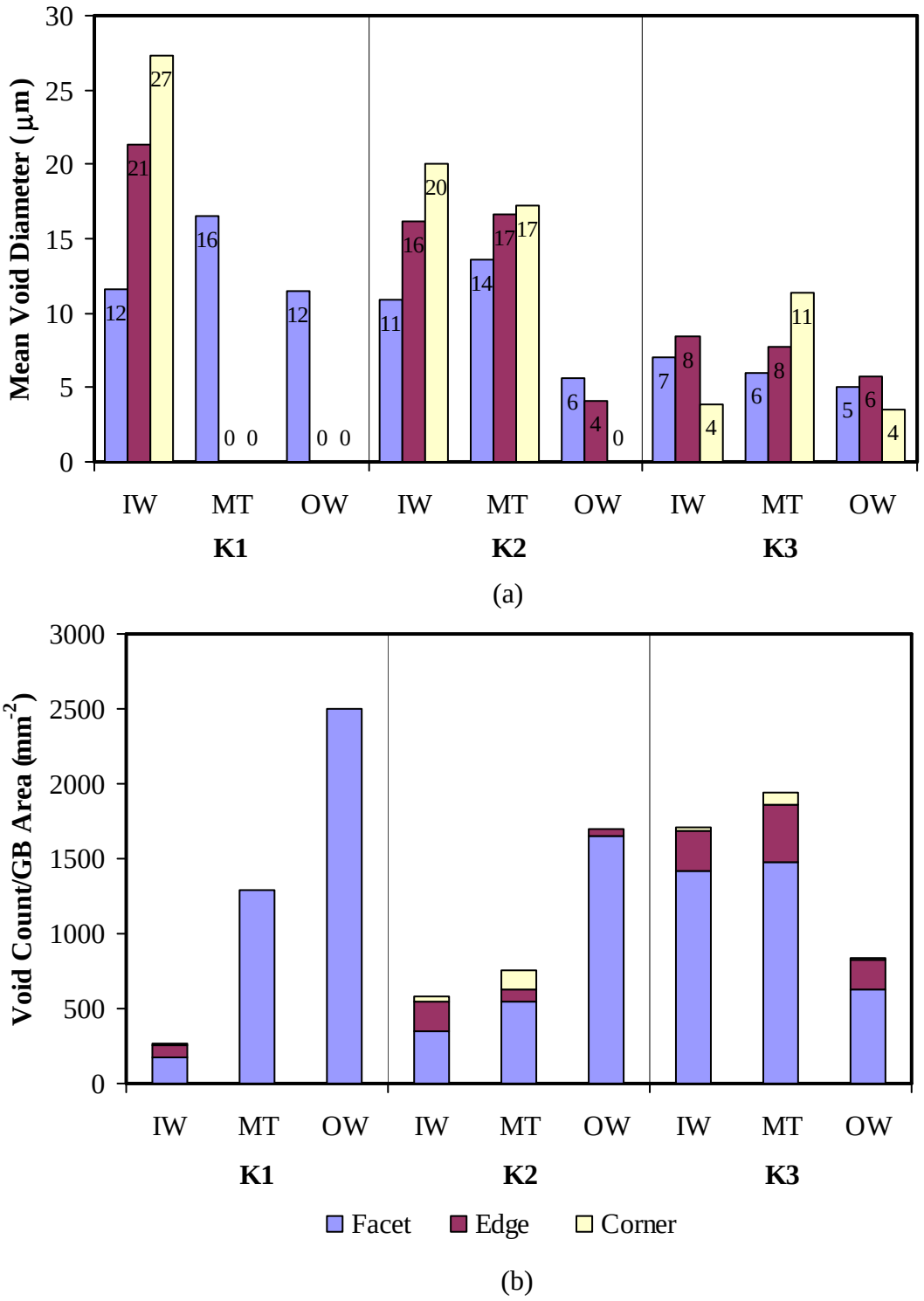

Figure 6.10: Correlation of void location with: (a) void size, and (b) void density. Samples were obtained at various positions along the reformer tube and at three wall positions. (Note: IW=inner wall, MT=mid-thickness, OW=outer wall).

Figures 6.11a-b show the breakdown of void size and density of contact precipitates. The most important information obtained from these two figures is that all observed voids encountered $M_{23}C_6$ precipitates somewhere along their perimeter. No voids were observed solely in contact with either NbC or TiC, or with both of these precipitates together. Additionally, no voids were observed not in contact with any precipitate at all. This outcome further confirmed the same observations made earlier in Chapter 5 on a different reformer tube sample where all the voids were also observed in contact with $M_{23}C_6$ precipitates.

Figure 6.11a also shows that the larger voids tend to appear next to a combination of $M_{23}C_6$ and NbC or a combination of $M_{23}C_6$, NbC, and TiC precipitates. Initially, it was thought that this may simply be due to the fact that when the voids grew large enough, they will encounter more precipitates and precipitate types other than just $M_{23}C_6$. However, looking at the smaller voids at the outer wall of sample K2 and at all locations of sample K3, precipitates other than $M_{23}C_6$ were present even though these voids were less than 10μm in diameter. Thus, void size may not matter and it must mean that although the presence of $M_{23}C_6$ is required for voids to form, the additional presence either NbC or TiC or both precipitates may induce the growth of these voids further. Yet, inspecting the mean diameter of voids appearing next to only $M_{23}C_6$ and TiC precipitates uncover that they are the smallest with a mean void diameter no larger than 5μm. This eliminated TiC as a factor affecting void growth, leaving $M_{23}C_6$ and NbC precipitates as probable factors influencing the growth of these voids.

Figure 6.11b illustrates that most of the voids appeared either next to $M_{23}C_6$ precipitates exclusively or next to both $M_{23}C_6$ and NbC precipitates. Very few voids were located next to all three precipitates together, and voids appearing next to both $M_{23}C_6$ and TiC precipitates are almost nonexistent. Moreover, the overall number of voids in contact with either $M_{23}C_6$ or both $M_{23}C_6$ and NbC is similar. However, since no voids appeared next to NbC precipitates exclusively, the appearance of $M_{23}C_6$ precipitates in all cases of Figure 6.11 implies that perhaps $M_{23}C_6$ precipitates are solely responsible for overall void nucleation. Nonetheless the combined presence of $M_{23}C_6$ and NbC may still induce the voids to grow largest. This fact will be taken into consideration in the modeling of void growth in Chapter 7.

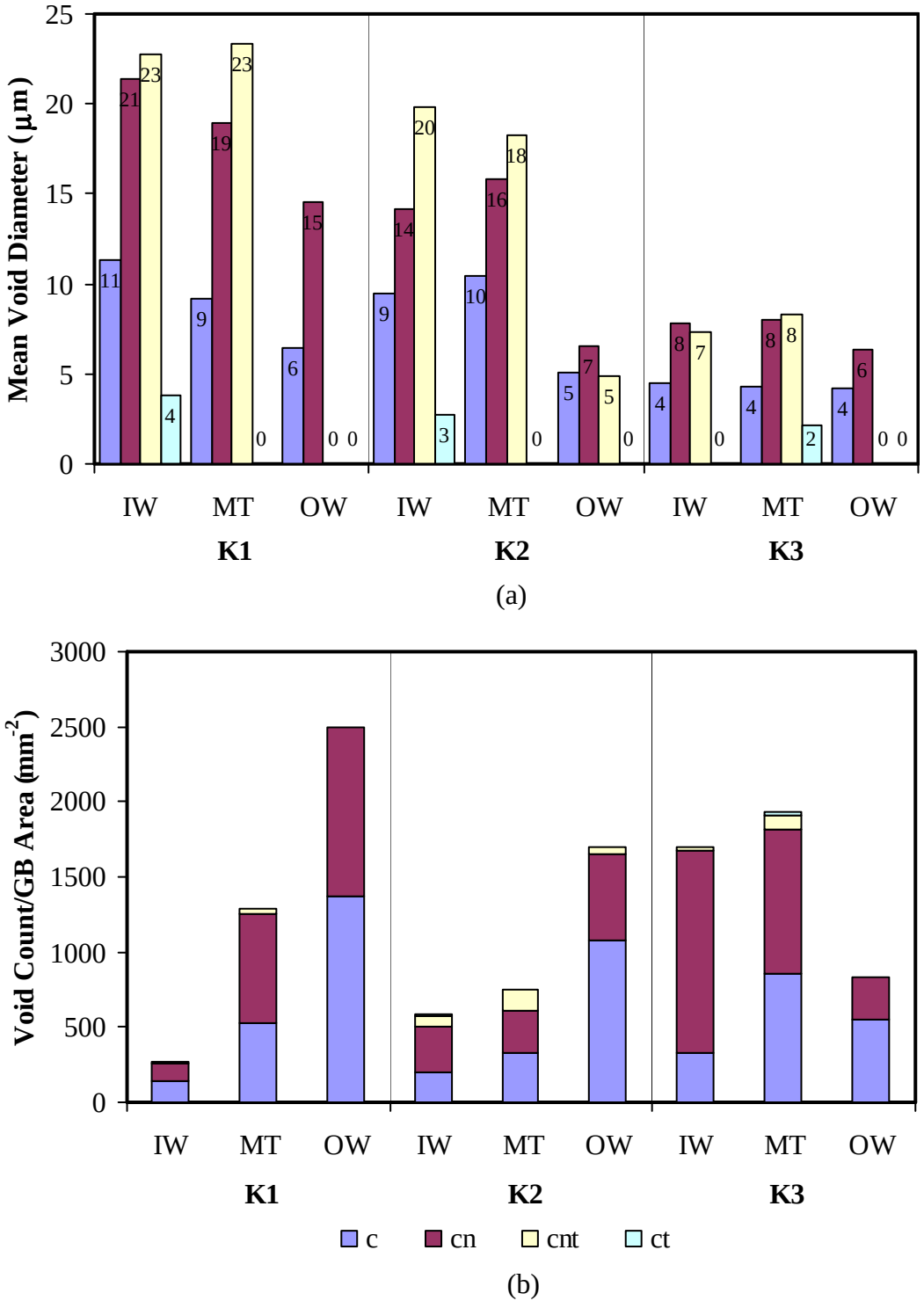

Figure 6.11: Correlation of contact precipitates with: (a) void size, and (b) void density. Note: c = $M_{23}C_6$, cn = $M_{23}C_6$+NbC, cnt = $M_{23}C_6$+NbC+TiC, ct = $M_{23}C_6$+TiC.

The classification of void size and density into void types (as defined earlier in Figure 6.8) are presented in Figures 6.12a-b. Figure 6.12a indicates that at lower temperatures, void sizes for type A and type B voids are approximately equal. At higher temperatures, type B voids are essentially the larger void type, and the extent to which they are larger than type A voids are even more obvious towards the lower portion of the reformer tube (sample K1). Referring to Figure 6.8, a type B void extends across the boundaries of two grains and thus it would be expected that the larger voids are the ones extending into other grains.

Alternatively, Figure 6.12b show that there were a higher number of type A than type B voids at higher temperatures, even though their number were quite similar at lower temperatures. It is possible that voids are equally likely to have nucleated as type A or type B voids, especially in the equiaxed structure. The higher void count for the mid-thickness and outer wall locations of sample K1 may be due to the reconstructed volume containing only grain facets and no edges or corners. The overall picture gained from Figures 6.12a-b reveal that type A voids were slightly more predominantly occurring. However, since type B voids span across grain boundaries, the availability of vacancies from these boundaries may stimulate the growth of type B voids further, as evident in the larger mean void diameters of the higher temperature samples (K1 and K2). Nevertheless, both types of voids will be considered in the void growth model.

A final categorization of void size and density was made for void shapes according to Figure 5.2 in Chapter 5. Figure 6.13a reveals that the largest voids are peanut shaped. This may imply void coalescence since that shape may be due to two or more interconnected spherical voids. Most of the voids are spherical, as indicated in Figure 6.13b. This would imply that voids nucleate and grow initially as spherical voids and only change into peanut shape voids when two or more voids coalesce. A category for ellipsoidal void was also made, but the ellipsoidal void could be a peanut shape void without a distinct “waist”. In future work, void shapes should be taken into consideration when ex-service samples are modelled. For instance, ten large peanut-shaped voids with the equivalent diameter of 30μm may be misleading in the model calculations (as opposed to for instance, twenty 15μm diameter voids). It may be necessary to actually determine the probable number of voids contained within the peanut-shaped during 3D observations.

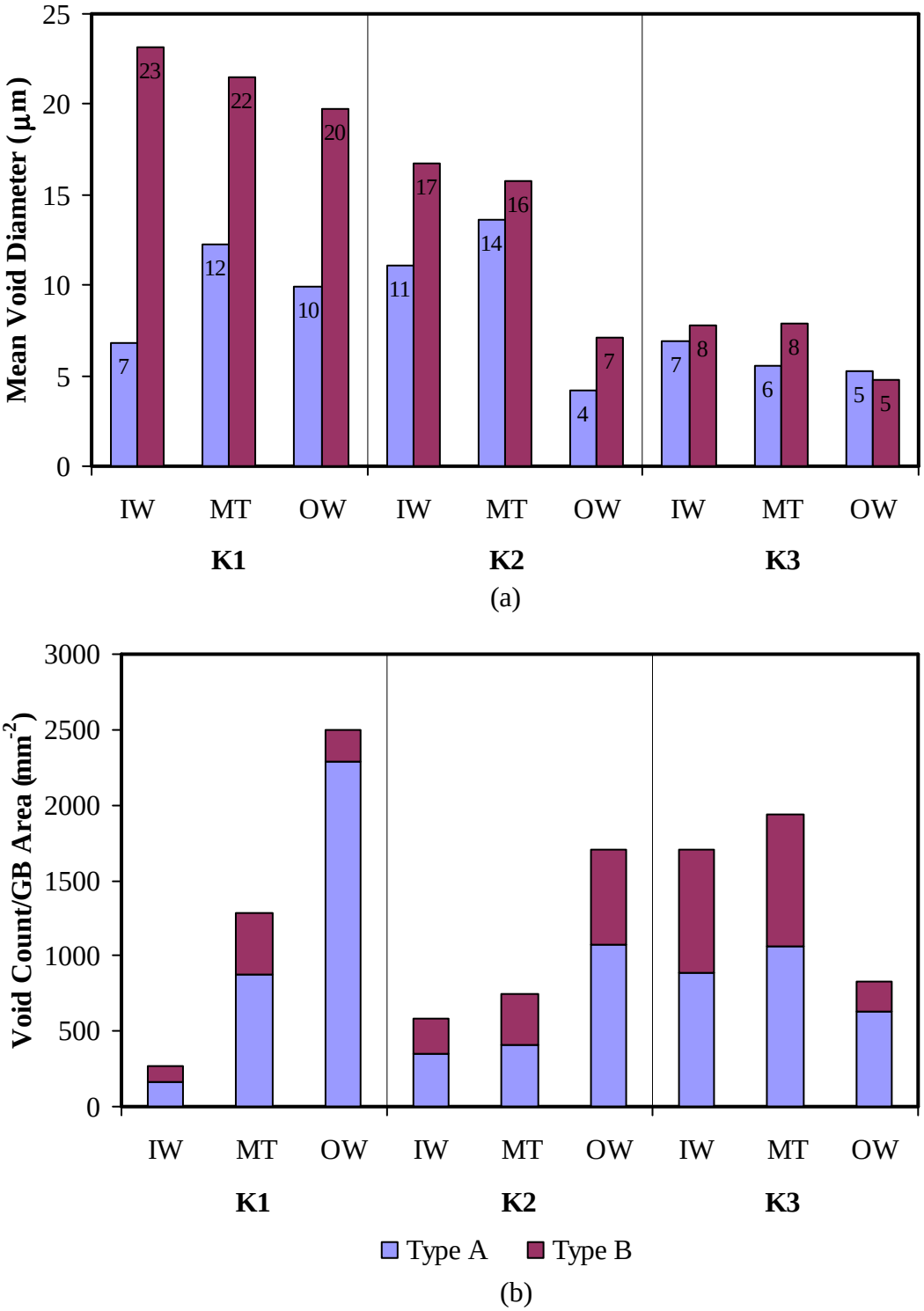

Figure 6.12: Correlation of void type with: (a) void size, and (b) void density. Void types were classified according to Figure 6.8 (intragranular voids are not shown).

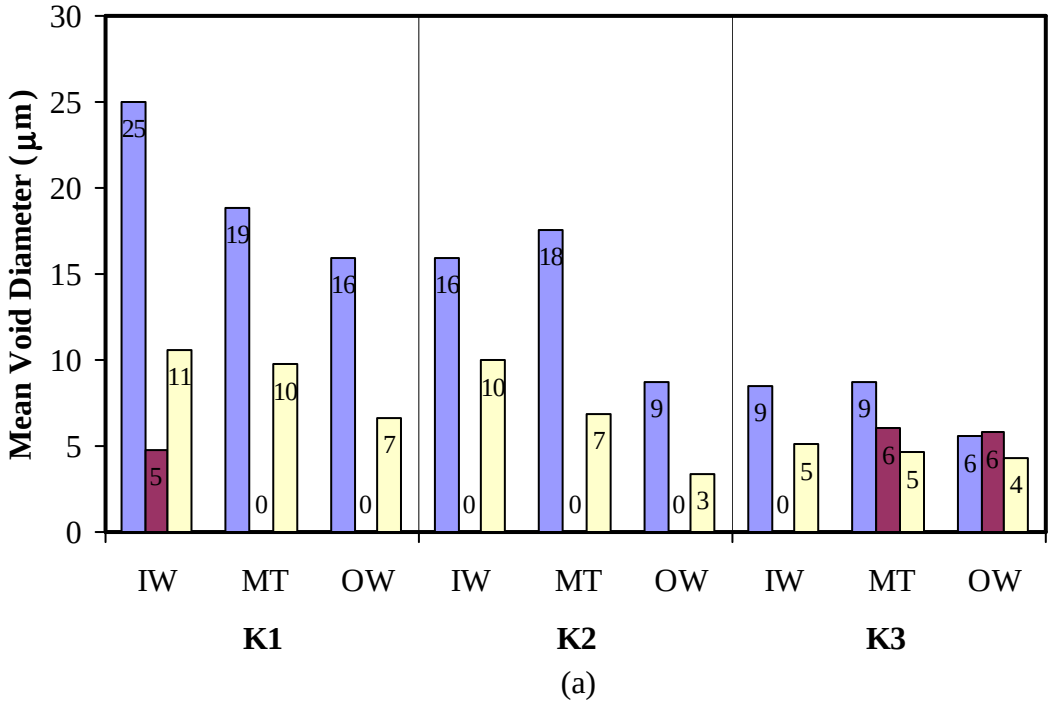

(a)

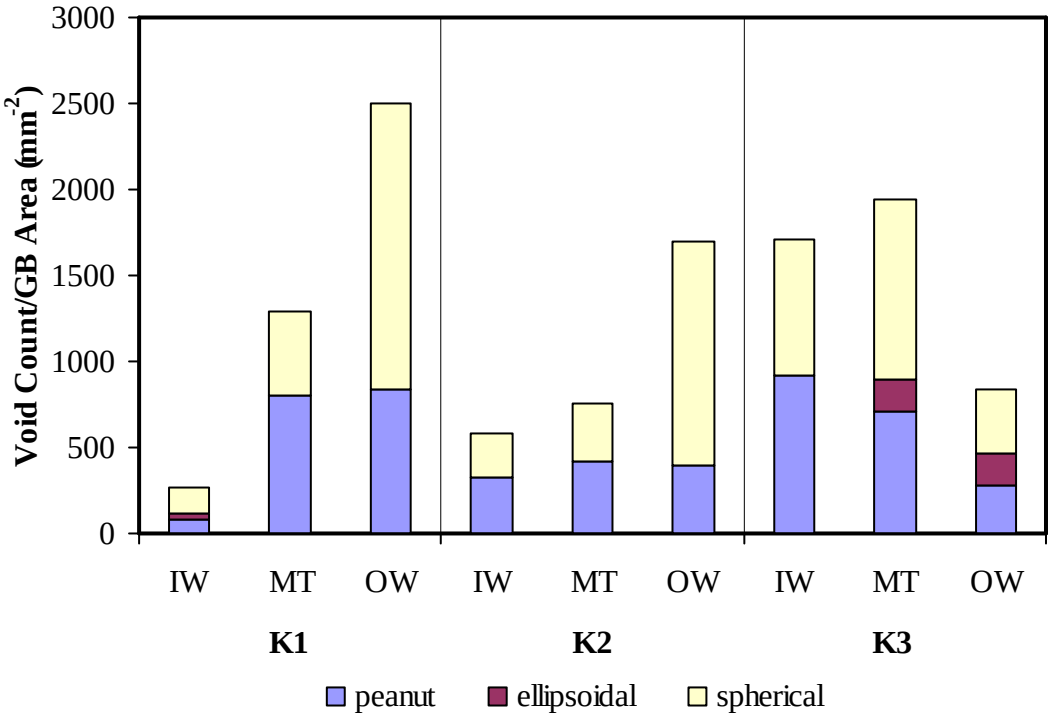

(b)

Figure 6.13: Correlation of void shape with: (a) void size, and (b) void density. Categorization of void shape is done according to Figure 5.2.

The next measurement made from the 3D reconstructions is the void-to-void distance. Two types of void-to-void distances were obtained. The first method measures the distances from the centroid of one void to the centroid of the closest neighboring void. The second method calculates the void-to-void distances using the equation $2l = 1/\sqrt{\rho}$ where $2l$ is the void-to-void distance and ρ is the void density per grain boundary area [27] shown in Figure 6.9c. The first method produced a "minimum" void-to-void distance whereas the second method resulted in a "mean" void-to-void distance, and these two results are shown graphically in Figure 6.14a-b. The resulting plot shows that the minimum void-to-void distances have a narrower range for all three regions of the tube (between 10 and 25 μm). On the other hand, the mean void-to-void distances are approximately 2 to 2.5 times greater than the "minimum" value. It was observed from the 3D reconstructions that for especially for the equiaxed microstructure, voids tend to cluster at grain edges (three-grain junctions) and corners (four-grain junctions) resulting in the small "minimum" void-to-void distance but large "mean" void-to-void distances are due to the higher distances between these void clusters. The larger distances between void clusters in an equiaxed microstructure would presumably make linking or coalescence more difficult than in an array of voids that lined up along columnar grain boundaries. This observation supports the belief that the presence of equiaxed grain structure along the inside wall region of a reformer tube impedes creep crack propagation [9].

Another measurement obtained from the 3D reconstructions is the orientation of grain boundaries containing creep voids. The angles of these grain boundaries were measured with respect to the hoop direction of the tube to determine any correlation between the appearance of voids and the orientation of the grain boundaries. Note that for voids that occurred at grain edges, three angles were measured while four angles were recorded for voids that were found at corners. The resulting distributions of these measurements are shown in Figure 6.15. In general, the grain boundaries where voids were found averaged around 45 degrees regardless of sample location. This agrees well with the orientation of the maximum shear stress, which will occur at 45 degrees with respect to the maximum and minimum principal stress directions (the hoop and radial directions, respectively).

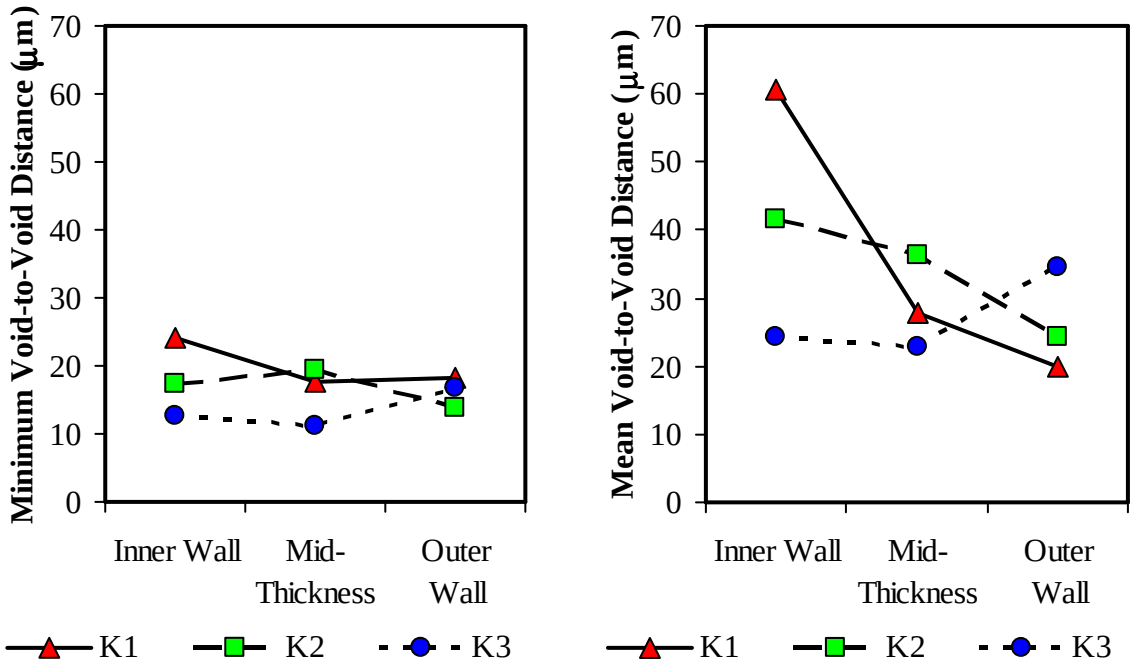

Figure 6.14: Comparison of "minimum" and "mean" void-to-void distances. The larger "mean" distance indicate the effect of void clustering.

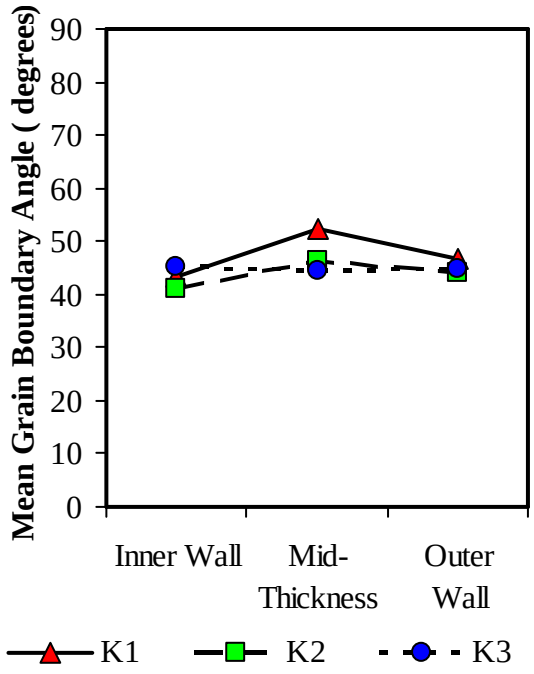

Figure 6.15: Mean angle of grain boundaries containing voids. Measurements were taken with respect to the hoop stress axis.

6.4 Summary

Three-dimensional techniques have been applied to reconstruct and analyze creep voids appearing at various positions along an ex-service reformer tube. A number of significant creep void parameters were obtained, including:

- characteristics of void sizes, shapes and locations;
- void density and separation statistics;
- the geometry of neighboring grain boundaries;
- void-precipitate configuration;
- the identity of neighboring precipitates.

General trends that have not been identified in any previous work can be gleaned from 3D observations. For example, there appear to be two separate mechanisms for void formation and growth. For sample K3, the difference in temperature between the inner and outer wall would result in a larger effective stress acting on the tube. Consequently, the creep mechanism at work is believed to be either Harper-Dorn or grain boundary sliding, both of which are a combination of diffusional flow and dislocation creep mechanisms. At the cooler end of the tube, the highest void density occurred at the inner wall of the tube where the temperature is lowest, effective stress is highest, and the microstructure consists of equiaxed grains.

On the other hand, for samples K1 and K2, the effective stresses should be relatively low compared to K3, and thus, the probable creep mechanism is Coble creep, which is a diffusional flow creep mechanism caused by motion of vacancies along the grain boundaries. At the hot end of the tube, the highest void density occurs at the outer wall where temperature is highest, and the microstructure consists of large columnar grains. In general, void size increases towards the hotter end of the tube. A higher number of voids were found at grain facets (two-grain junctions). However, larger voids were located at grain edges (three-grain junctions) and grain corners (four-grain junctions). All voids were also observed to be in contact with $M_{23}C_6$ precipitates with the larger voids also encountering NbC and TiC precipitates. It is thought that $M_{23}C_6$ may be solely responsible for void nucleation, however the combined presence of $M_{23}C_6$ and NbC resulted the largest voids in the material. In addition, from 3D observations and analyses, it appeared that at lower temperatures, type A and type B voids were almost equal in size and numbers. At

higher temperatures, type B voids grew larger than type A voids, possibly assisted by the supply of vacancies from the grain boundaries in which type B voids reside. Overall, spherical voids were more common at all temperatures, but at higher temperatures, larger voids were peanut shaped, indicating coalescence of voids have occurred. Measurements of void separation also show a small range in the minimum void-to-void distances whereas the mean distances are 2 to 2.5 times greater than the minimum distances. This agreed with the 3D observations that showed clustering of voids especially at the grain edges and corners of the equiaxed microstructure. Finally, the grain boundaries containing voids were oriented at 45 degrees with respect to the hoop stress direction, coinciding with the direction of maximum shear stress.

It is important to emphasize that only by means of the 3D techniques employed in this work that void characteristics such as shape, location, clustering, and various void-matrix-precipitate configurations (void type, grain boundary angle, etc), can be determined and observed. Information such as voids being situated next to $M_{23}C_6$ precipitates have been speculated before [74] but 3D observations now confirmed this information. It still has to be identified which of the observed parameters are most influential upon the formation, growth, and coalescence of creep voids that leads to material failure. Tube manufacturing process can influence directly or indirectly some of these parameters. For instance, controlling the temperature of the casting mould will influence the solidification process and thus the grain structure of the tube wall [9]. Grain shapes and sizes may be manipulated to enhance the service life of these tubes. It is anticipated that using the information gathered from these 3D analyses in the void growth model would shed new insights on which microstructural feature having most significant effect on tube life.

Chapter 7

MODELING THE GROWTH OF CREEP VOIDS

To realize further efficiencies in the creep performance of reformer tube alloys requires an understanding of the damage accumulation processes that leads to unacceptable strains and ultimately to material failure. The ductile failure of metallic materials loaded under creep conditions typically proceeds by the nucleation, growth and coalescence of creep voids followed by macroscopic crack propagation [25, 84]. In this chapter, the creep void data collected from 3D reconstructions generated in Chapters 5 and 6 will be applied to a well-known creep void growth model by Raj and others [27, 28]. Various permutations of the parameters obtained from this work will be applied to the model to simulate conditions that may be beneficial to extending the service lives of reformer tubes.

7.1 Void Growth Model

As discussed briefly in Chapter 2, when given sufficient time, high temperature creep deformation will ultimately result in fracture. Three possible modes of fracture are listed as follows [16]:

- rupture, which occurs at high temperature and high stress levels;
- transgranular fracture, which occurs at low temperature and high stress levels;
- intergranular creep fracture, which occurs at high temperature and low stress levels.

In the intergranular creep fracture mode, cracks or voids form along grain boundaries and coalesce leading to brittle fracture. Spherical shaped voids usually form at lower stress levels than wedge-like voids, and both of these void types are often associated with inclusions and precipitates at the grain boundaries [16, 21]. The creep voids observed in the reformer tube samples in Chapters 5 and 6 were generally spherical in nature, appeared mainly next to grain boundary precipitates, and formed in components experiencing low-

stress high temperature deformation. Thus the fracture mode in the reformer tubes studied in this work can be described as intergranular creep fracture due to coalescence of spherical voids forming at grain boundary precipitates.

Given the very long service lifetimes expected of the steam-methane reformer tubes, it would be very useful to develop a simplified computational description of the damage accumulation processes so that some guidance on the expected effects of any designed microstructural changes could be obtained before performing time-consuming and costly long-term creep experiments. It is intended that this initial model will apply the data obtained from 3D reconstructions and analyses, and the calculation process itself will be rather uncomplicated and will be done using common computational software. As mentioned in Chapter 2, the void growth model presented by Raj and co-workers [27, 28] accounts for stress, temperature, void density, and various void-precipitate-matrix configurations such as void size, type and locations. This special trait of the model makes it suitable for modeling creep void growth in reformer tubes where all voids were observed next to precipitates. On the other hand, finite element models proposed by Needleman and Rice [29] and Pardoen and Hutchinson [31], are deemed to be too difficult for application to the reformer tubes studied in this work. The finite element modeling of the void-precipitate interfaces in the microstructure would be too complicated and beyond the scope of this work. The finite element modeling of void-precipitate interfaces in itself would however make an interesting future study.

The differential equation for the void growth model given by Raj and co-workers is listed below (see [27, 28] for derivation of the equation):

$$\frac{dV}{dt} = 2\pi \; \frac{\Omega D_B \delta}{kT} \left(\sigma_\infty + p_v - \frac{2\gamma}{r_v} \right) \frac{\left(1 - \frac{r_B^2}{l^2} \right)}{\ln\left(\frac{l}{r_B} \right) - \frac{3}{4} + \frac{r_B^2}{l^2}\left(1 - \frac{r_B^2}{4l^2} \right)} \qquad \text{- equation (1).}$$

I II III

The equation is divided into three segments as defined below:

I. motion of atoms along the grain boundary:

Ω = atomic volume= $\dfrac{\text{atomic mass}}{(\text{atomic density})(6.022\times10^{23})}$;

$D_B\delta$ = grain boundary diffusivity = $\delta(D_B)_0 \exp\left(\dfrac{-Q_B}{RT}\right)$;

δ = grain boundary thickness;

$(D_B)_0$ = grain boundary diffusion coefficient;

Q_B = grain boundary activation energy;

R = universal gas constant = 8.314 J mol^{-1} K^{-1};

k = Boltzman's constant = 1.381×10^{-23} J K^{-1};

T = absolute temperature.

II. loading conditions:

σ_∞ = remote applied stress = effective stress from multiaxial loading condition;

p_v = internal gas pressure inside the void;

γ = surface free energy of the void;

r_v = radius of void surface.

III. void size and spacing effects:

r_B = radius of curvature of void projection on the grain boundary;

l = ½ the average void-to-void spacing.

A time-dependent parameter representing the area-fraction of voids in a grain boundary, A was then defined in ref. [27] as:

$$A=\frac{r_B^2}{l^2}\text{, with } \frac{dA}{dt}=\frac{1}{2\pi r_B l^2}\frac{dV}{dt}.$$

Using the substitutions $2\gamma = r_c(\sigma_\infty + p_v)$ and $r_v = r_B\sqrt{\dfrac{\pi}{F_B}}$, equation (1) can be rewritten as:

$$\frac{dA}{dt} = \frac{\Omega D_B \delta}{kT} \frac{(\sigma_\infty + p_v)}{l^3} \frac{\left(1 - \frac{r_c}{r_B}\sqrt{\frac{F_B}{\pi}}\right)(1-A)}{\sqrt{A}\left[\frac{1}{2}\ln\left(\frac{1}{A}\right) - \frac{3}{4} + A\left(1 - \frac{A}{4}\right)\right]}$$

- equation (2).

where:

F_B = geometry factor of void configuration on the grain boundary;

r_c = critical radius for void nucleation.

Using $r_B = l\sqrt{A}$, equation (2) is then rearranged to calculate a time-to-rupture value t_r by:

$$t_r = \frac{kT}{\Omega D_B \delta} \frac{l^3}{(\sigma_\infty + p_v)} \int_{A\min}^{A\max} \frac{1}{f(A)} dA$$

- equation (3).

where $\frac{1}{f(A)} = \frac{\sqrt{A}\left[\frac{1}{2}\ln\left(\frac{1}{A}\right) - \frac{3}{4} + A\left(1 - \frac{A}{4}\right)\right]}{\left(1 - \frac{r_c}{l}\sqrt{\frac{F_B}{\pi A}}\right)(1-A)}$

A simple Visual Basic program was written in Microsoft Excel® as a macro to numerically evaluate the integral in equation (3) and the results was subsequently used to calculate the time-to-rupture, t_r. Microsoft Excel was chosen due to its ability to easily accept and modify different input datasets and produce the various respective graphical outputs (refer to Appendix III for program codes and spreadsheet layout). The main problem in running this model was the determination of the proper material constants to be used. It was shown in Chapter 5 and 6 that all creep voids encountered $M_{23}C_6$ precipitates somewhere along their perimeter. Thus, material constants for an $M_{23}C_6$-Fe interface were obtained. Data for austenitic Fe-Fe interfaces will also be used for comparisons. Material constants to be used in the calculations are listed in Table VI for both $M_{23}C_6$-Fe and austenitic Fe-Fe type interfaces.

Table VI: Material constants for Fe (as the diffusing atom) at a grain boundary interface [85].

Ω = atomic volume $= \frac{\text{atomic mass}}{(\text{atomic density})(6.022\times10^{23})}$ • For Fe atom: atomic volume = 55.85 g/mole atomic density = 7.87×10^{6} g/m^3
$D_B\delta$ = grain boundary diffusivity $= \delta(D_B)_0 \exp\left(\frac{-Q}{RT}\right)$ $\delta(D_B)_0$ = grain boundary diffusivity constant Q_B = grain boundary activation energy • Data for $M_{23}C_6$-Fe interface: Fe-16%Cr–14%Ni–0.2%C austenitic stainless steel [86] $\delta(D_B)_0 = 2.00\times10^{-14}$ m^3/s $Q_B = 1.695\times10^{5}$ J/mol • Data for Fe-Fe interface (alternate): Fe-20%Cr–25%Ni–0.2%C Nb-stabilized austenitic stainless steel [87] $\delta(D_B)_0 = 8.30\times10^{-13}$ m^3/s $Q_B = 1.799\times10^{5}$ Joule/mole

In the initial run of the model, data obtained from 3D reconstructions in Chapters 5 and 6 will be applied to the simulation. A time-to-rupture value t_r will be calculated for each sample based on their respective service parameters and current damage levels (i.e. existing ex-service void sizes, void densities etc.). This t_r value will represent the "remaining life" for each sample location. Next, the model will then be generalized to cater for any generic reformer tube and its time-to-rupture will be calculated for a typical reformer application. Various tube characteristics will be tested with the model to observe their effects on extending the life of these tubes.

Parameters to be used in equation (3) such as temperature and applied stress were either obtained or calculated from service conditions. Temperature values were obtained from service temperature profiles such as the one shown in Figure 6.1. The remote applied stress σ_∞ was taken as the effective stress (or Tresca stress) resulting from the internal pressure, weight of the tube, and temperature gradient across the tube wall, and was calculated using the methods shown in Appendix II. Tresca criterion was chosen instead of the von Mises criterion as the method for calculating the effective stresses merely because it provided the more conservative values (for the reformer tubes, Tresca effective stresses are no more than 15 percent larger than von Mises effective stresses). In Chapter 6, it was shown that on average, voids were found at grain boundaries oriented at 45° to the hoop stress direction, and this corresponds to the planes of maximum shear in which the Tresca stress is the normal stress. Furthermore, for simplicity, the effective stress calculations accounted only for elastic conditions and the effect of plastic deformation in relieving thermal stresses in the reformer tube was not accounted for. Finally, the internal gas pressure p inside the voids is assumed to be zero.

The integral term $1/f(A)$ of equation (3) will be evaluated from A_{min} to A_{max}. The value of A_{min} will be calculated from the equation $A = r_B^2 / l^2$ where r_B is the starting void radius and l is one-half the void-to-void spacing $2l$ as defined in Figure 7.1. In the initial run of the model for ex-service samples, the value r_B was set as the mean radius of the voids and the value of l would be based on either l_{mean} or l_{min} measurements obtained from 3D reconstructions (recall that l_{mean} was calculated from void density at the grain boundaries while l_{min} was measured as the mean distance from one void to the closest neighboring void). The integral upper limit A_{max} will be set to 0.5 to represent (arbitrarily) the final area fraction of the grain boundary occupied by voids at rupture. This value implies that when the square of the ratio between the projected void radius on the grain boundary and half the void-to-void spacing is 0.5, the material is assumed to be no longer usable (as opposed to A_{max} = 1 when the voids are already interconnected). The value for the critical radius for void nucleation r_c will be set as 2.5nm, and varied between 1 and 10nm to monitor the consequence of variations in this parameter (r_c value is not well established, values of 2-5nm are commonly used [25], the value of 2.5nm was used in ref. [28], the value of 1nm is approximately the lattice parameter of $M_{23}C_6$).

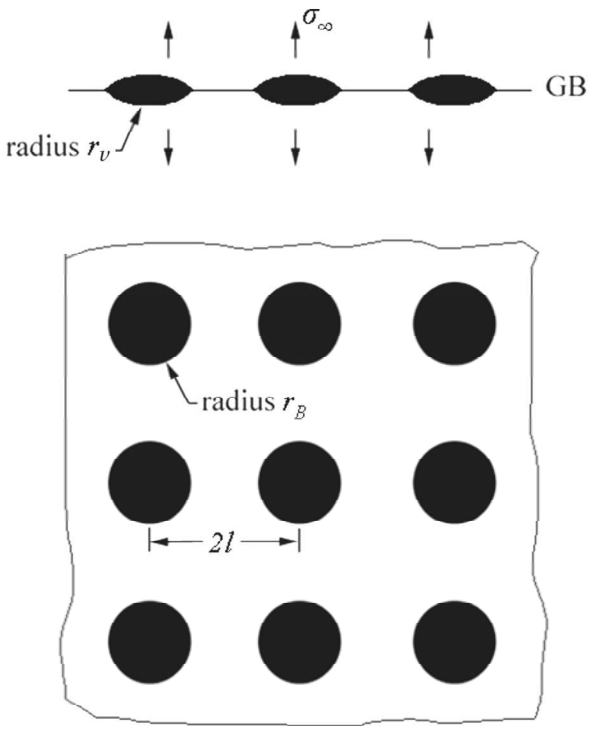

Figure 7.1: Schematic of void array on a grain boundary and the associated parameters.

Equations for the geometry factor of void configuration on the grain boundary F_B are listed in Figure 7.2 for the five possible void configurations. Angular values of α, β, or θ for these geometry factors will be initially set at the midpoint of their respective ranges and varied from the respective lower and upper bounds to observe the effects on the results of the model (the upper bound of $\pi/2$ represents a spherical void). The choice of which void configuration to employ in the model would be established on the results of 3D reconstructions of Chapters 5 and 6. It was discovered that based on void counts, most of the voids characterized in Chapter 6 would be described either as type 2 or type A, i.e. the voids were found mostly on the grain facets (two-grain junctions) and the void-precipitate configurations were primarily type A (refer to Figures 6.10b and 6.12b). The geometry factors for these two void configurations are the same and thus the angles α or β can be assigned the same value. The summary of all the ex-service sample parameters used in the model is listed in Table VII.

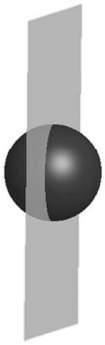

a) void at grain facet (2-grain junction):

$$F_B = \pi \sin^2 \alpha_F$$

(α_F = angle at the void-grain boundary junction)

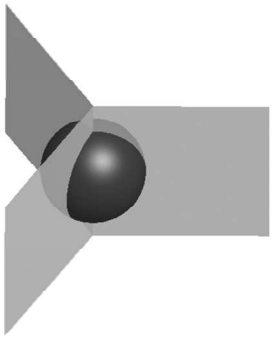

b) void at grain edge (3-grain junction):

$$F_B = -\frac{\pi}{\cos\alpha_F} - 2\pi + \frac{6\sin^{-1}(\frac{1}{2}\csc\alpha_F)}{\cos\alpha_F} - \cos\alpha_F\sqrt{4\sin^2\alpha_F - 1} + 3\cos^{-1}\left(\frac{\cot\alpha_F}{\sqrt{3}}\right)\left(3-\cos^2\alpha_F\right)$$

c) void at grain corner (4-grain junction):

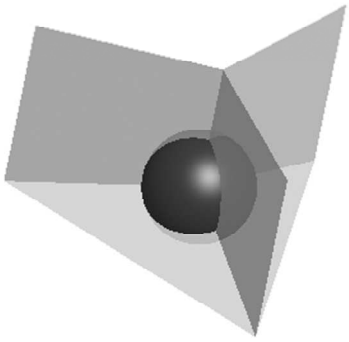

$$F_B = -\frac{2\pi}{\cos\alpha_F} - 2\pi + \frac{12}{\cos\alpha_F}\cos^{-1}\left[\frac{\sqrt{2}-\cos\alpha_F\sqrt{3-A^2}}{A\sin\alpha_F}\right] - \frac{3}{2}A\left[\sqrt{4\sin^2\alpha_F - A^2} - \frac{A^2}{\sqrt{2}}\right] + 6\left(3-\cos^2\alpha_F\right)\sin^{-1}\left(\frac{A}{2\sin\alpha_F}\right)$$

where $A = \frac{2}{3}\left[\sqrt{2\left(4\sin^2\alpha_F - 1\right)} - \cos\alpha_F\right]$

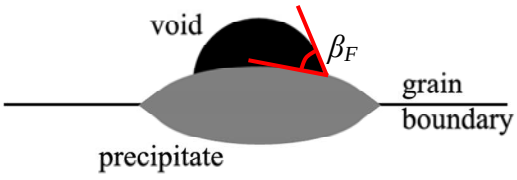

d) type A void:

$$F_B = \pi \sin^2 \beta_F$$

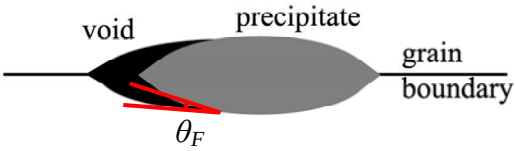

e) type B void:

$$F_B = \pi \sin^2 \theta_F$$

Figure 7.2: Geometry factor of void configuration on the grain boundary F_B. For (a), (d), and (e), the respective angles α_F, β_F, and θ_F range from 0 to $\pi/4$. For (b) and (c), the angle α_F ranges from $\pi/6$ to $\pi/4$.

Table VII: Summary of ex-service sample parameters used in the model. Note: letters I, M, and O in the sample ID represents "inner wall", "mid-thickness", and "outer wall" respectively.

Sample ID	Micro-structure	T, K	σ_∞, $\times 10^6$Pa	l_{min}, $\times 10^{-6}$m	l_{mean}, $\times 10^{-6}$m	r_B, $\times 10^{-6}$m	Dominant GB void types (based on void count)
K1-I	equiaxed	1151	19.9	12	30	8.6	2, A
K1-M	columnar	1156	15.1	8.8	14	8.3	2, A
K1-O	columnar	1161	4.77	9.1	10	5.8	2, A
K2-I	equiaxed	1140	29.8	8.6	21	7.0	2, A
K2-M	columnar	1149	7.69	9.7	18	7.3	2, A
K2-O	columnar	1159	11.4	7.0	12	2.8	2, A
K3-I	equiaxed	1048	111	6.3	12	3.7	2, A
K3-M	columnar	1085	13.8	5.6	11	3.4	2, A
K3-O	columnar	1121	55.2	8.3	17	2.6	2, A
X1-I	equiaxed	1213	30.2	7.7	15	4.8	2, A

7.2 Results and Discussions

The initial run of the model was carried out using data from Tables VI and VII as the starting point. The resulting plot of time-to-rupture versus the reciprocal of absolute temperature for all the samples from Chapters 5 and 6 is shown in Figure 7.3, with a straight line fitted through the data points. Essentially the plot represents the estimate of the remaining life for the current level of creep damage; for instance for sample X1, the time to rupture was calculated at 7.6×10^6 seconds or about 88 days (refer to Appendix III for a sample calculation for sample X1). Since this particular sample came from an adjoining segment of an already failed reformer tube, the remaining life value obtained seems reasonable.

Of the ten points plotted in Figure 7.3, data points for samples K1-I, K2-M, and K3-I deviated from the fitted line by almost an order of magnitude. The model used here is highly sensitive to void density numbers, and for samples K1-I and K2-M, the volumes reconstructed did not contain a high enough number of voids per grain boundary area, which can be due to coalescence of the voids affecting the void density numbers (i.e. two or more voids being counted as one). On the other hand, sample K3-I had a higher void density than expected, and even though these voids were small, the model calculated a

short time-to-rupture value based on the high void density. It is important to note that of all ten samples, sample K3-I experienced the lowest temperature (1048K) but the highest effective stress (111MPa), and it is possible that this sample experienced a different creep deformation regime [30, 88] (perhaps power-law creep or coupled diffusion and power-law creep), whereas the model used here was based on creep deformation due to diffusional motion [27].

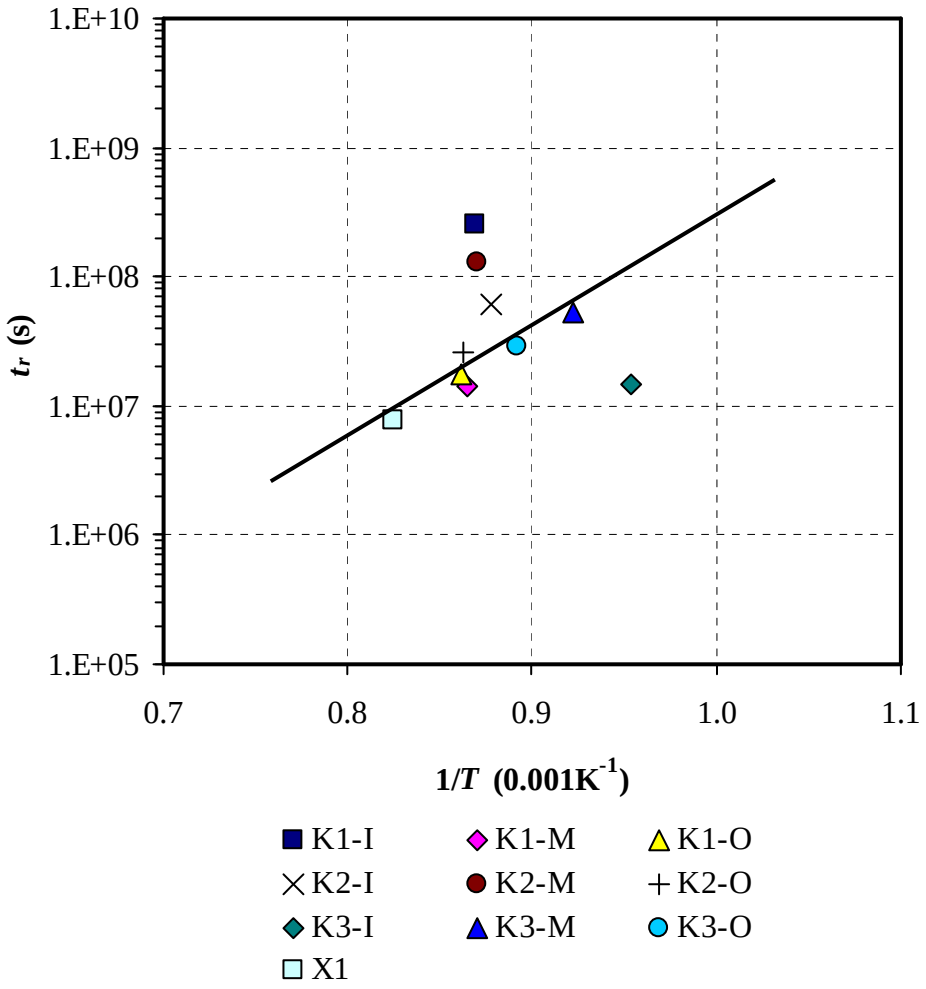

Figure 7.3: Plot of time-to-rupture versus the reciprocal of absolute temperature for the ex-service samples with their existing level of creep damage.

The accuracy of the simulation of time-to-rupture is also highly dependent on the material constants. For the plot in Figure 7.3, the grain boundary diffusivity constant and activation energy values were obtained from a $M_{23}C_6$-austenite interface where Fe is the diffusant atom and the Fe-Cr-Ni alloy matrix consists of 16wt% Cr, 14wt% Ni, and 0.2wt% C. This

was the only available data found for the $M_{23}C_6$-austenite interface. In contrast, if the data for an austenite Fe-Fe interface was used (refer to Table VI), the resulting fitted line in the plot of time-to-rupture in Figure 7.3 would be shifted down by more than one order of magnitude (t_r value for sample X1 is now 5.1×10^5 seconds or 6 days). Since all the creep voids were found adjacent to $M_{23}C_6$ precipitates, the former data would be used for all subsequent calculations. It was discussed in Chapter 6 that NbC precipitates in the presence of $M_{23}C_6$ may enhance the growth of voids. However no grain boundary data were available to test this hypothesis.

Additionally, the time-to-rupture calculations for the ex-service samples used l_{mean} values, based on 3D void density measurements, as l (one-half the void-to-void spacing), while r_B values were set as the mean radii of existing voids. It was discovered that the l_{min} values (based on the distance from each void to its closest neighboring void) would invalidate the computations because l_{min} values for some ex-service samples would result in the lower bound of the integral A_{min} to be larger than the upper bound A_{max}, implying that the sample would have already failed. Thus all the time-to-rupture estimates in Figure 7.3 used l_{mean} values based on 3D void density measurements.

The next stage of the modeling process was carried out on an idealized reformer tube with an external diameter of 125mm and a wall thickness of 10mm. For modeling purposes, five locations along the length of the tube were selected at 2.5m intervals (labeled N1 through N5), and at each of these locations, calculations were performed at the inner wall, the outer wall, and at the location where the effective stress is minimum, resulting in a total of fifteen modeling positions. Stresses for this tube were calculated based on to the service temperature and pressure distributions shown previously in Figure 6.1. The Tresca stress distributions for locations N1 through N5 are shown graphically in Figure 7.4, while the modeling locations selected and their corresponding service parameters are listed in Table VIII. Note that in Figure 7.4, the locations for minimum effective stresses do not coincide with the mid-thickness positions. Also, as done previously, the calculated Tresca stress will be used as the remotely applied stress σ_∞ in the calculations. Material constants for $M_{23}C_6$-austenite interface (Table VI) were used in the computations, while geometry factors used were for type A voids with $\beta = 45°$.

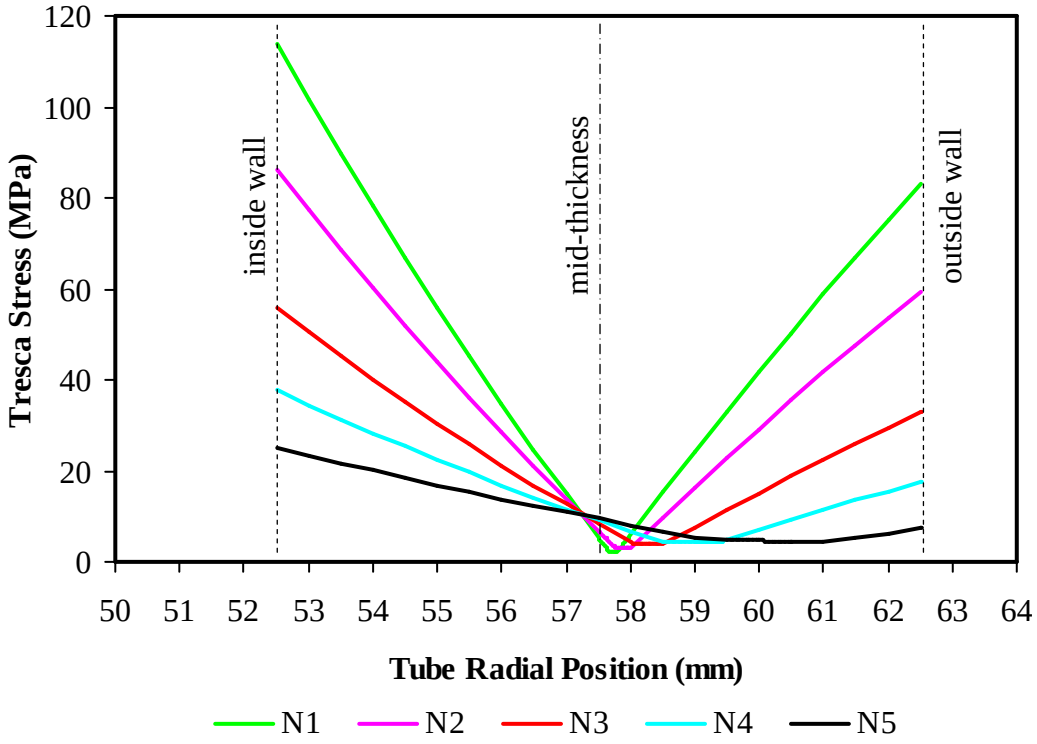

Figure 7.4: Comparison of Tresca stress distributions for various positions along the length of the idealized reformer tube. Samples N1 through N5 represent locations at 2.5m intervals starting at 2.5m to 12.5m from the top inlet flange.

Table VIII: Summary of modeling parameters for the idealized tube. (Note: I, O, and 'min' represent 'inner wall', 'outer wall', and 'minimum stress' locations respectively).

Sample ID	Distance from Top Flange, m	p, MPa	T, K	σ_∞, $\times 10^6$Pa
N1-I N1-min N1-O	2.5	2.16	1048 1087 1121	114 2.09 83.1
N2-I N2-min N2-O	5.0	2.07	1097 1126 1151	86.4 2.98 59.5
N3-I N3-min N3-O	7.5	1.99	1119 1138 1151	55.7 3.98 32.9
N4-I N4-min N3-O	10.0	1.91	1141 1154 1159	37.7 4.43 17.7
N5-I N5-min N5-O	12.5	1.82	1151 1159 1161	25.2 4.59 7.31

The lower bound A_{min} of the integral term $1/f(A)$ in equation (3) was based on a starting void radius r_B which was set equal to the critical radius for void nucleation r_c of 2.5nm (approximately 2.5 times the lattice parameter of $M_{23}C_6$ precipitate). The void-to-void spacing $2l$ was taken as 80μm (l = 40μm), which is the approximate grain diameter of the equiaxed microstructure, and in addition, the assumption was also made that the number of void nuclei is fixed (i.e. $2l$ value is constant). In reality, the number of nucleation sites varies with time and their rate of formation would be dependent on various factors such as temperature, stress, and microstructural characteristics [27]. In this work, 3D void data was obtained from ex-service samples only, thus the nucleation growth behavior of these voids in the material during early high temperature service was not studied. Meanwhile, the upper bound A_{max} of the integral was set to 0.5, and for these calculations, the largest void size at "rupture" would be about 56μm based on the fixed void-to-void distance of 80μm.

Figure 7.5 represents the time-to-rupture for the various locations on the idealized reformer tube, showing a somewhat distinctive C-shape for the distribution. Note that for clarity, the coloring scheme of the data points followed the stress distribution plot of Figure 7.4. In addition, data for inside wall, outside wall, and minimum stress locations were represented by diamonds, squares, and triangles respectively. Upon closer inspection, the graph can be noticeably divided into two parts. The upper portion of the curve consisted of triangular markers representing minimum stress locations and thus tube failures would be unlikely to occur at these locations. The lower section of the curves contained data from the inside and outside wall of the tube where stresses were higher. From this plot, it was initially quite surprising to see that the location of the tube with the shortest time-to-rupture is at the outside wall of the tube 5m from the top inlet flange. However, it must be reminded that this simulation assumed a reformer tube with a uniform microstructure and with an equal density of void nuclei throughout the thickness, and hence the time-to-rupture would only be dependent on the Tresca stresses, which combined the effects of pressure, temperature, and weight of the tube.

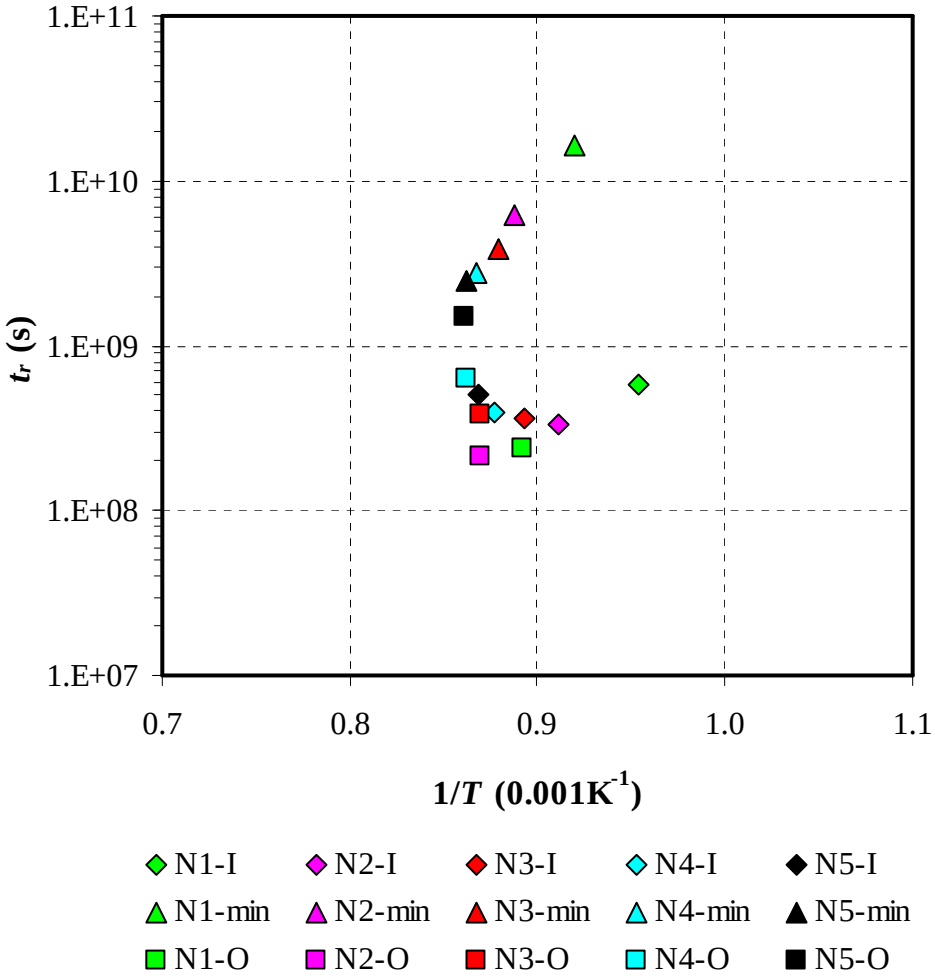

Figure 7.5: Time-to-rupture behavior for various sample locations on the idealized reformer tube.

A slight modification to the model was made by considering that a typical reformer tube would contain equiaxed grains at the inner wall region and columnar grains elsewhere. It was observed from 3D reconstructions that the secondary dendrite arm spacings of the equiaxed structure averaged about 60μm. In the high temperature samples, large voids were viewed to occur at every two dendrite arms resulting in a void spacing of $2l$ = 120μm. Employing only this slight adjustment, the simulation produced another time-to-rupture curve shown in Figure 7.6. In this plot, all the data points representing the doubled void-to-void distances were shifted upwards near and above the 10^9 seconds level. Data for the inner wall regions (equiaxed) were still based on $2l$ = 80 μm and they exhibit a shallow U-shape with time-to-rupture ranging from 3.4×10^8 to 5.8×10^8 seconds (10.8 to 18.4 years).

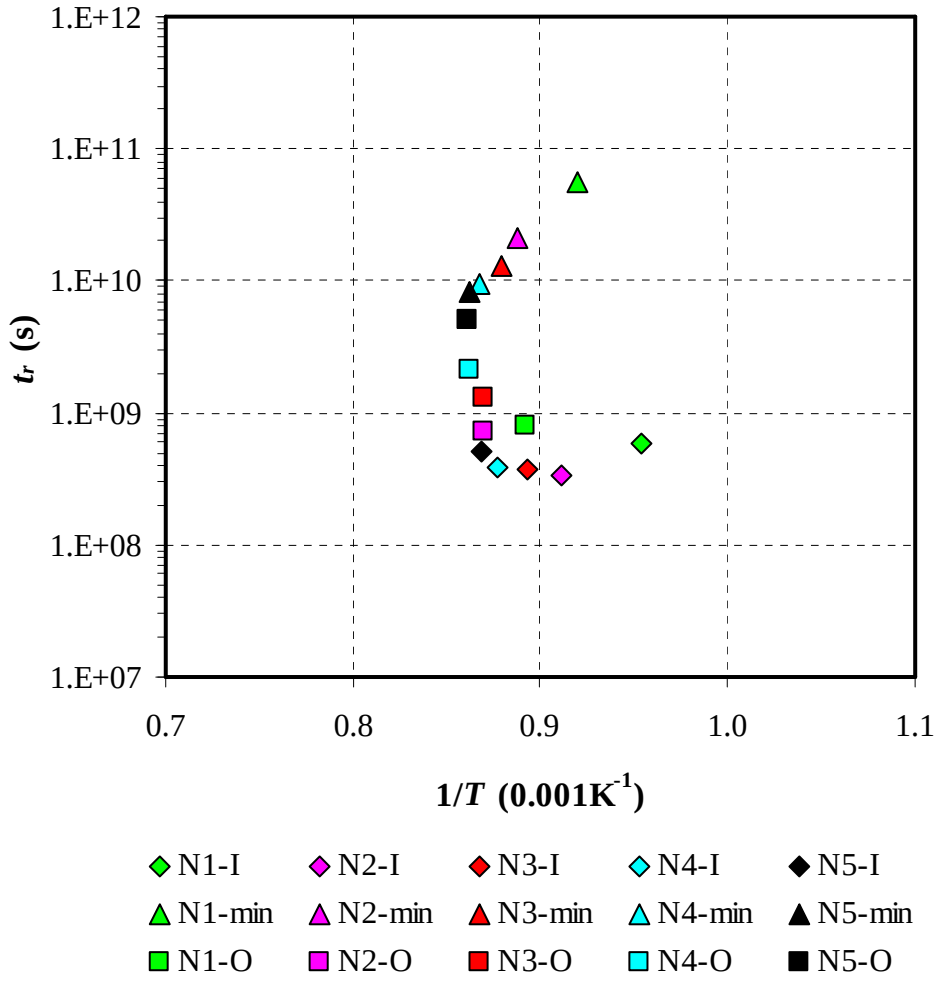

Figure 7.6: Adjusted time-to-rupture behavior for various sample locations on the idealized reformer tube. Calculations for inner wall samples used $2l$ = 80μm, while computations for other locations used $2l$ = 120μm.

The final stage of the modeling process was determining the effects of variations of the parameters used. As previously discovered, the material constants had a significant influence on the outcome of the computations. Changing constants from $M_{23}C_6$-Fe to Fe-Fe interface resulted in a more than one order of magnitude variation in the time-to-rupture value. It was also implied by the plots in Figures 7.5 and 7.6 that variations in the void-to-void distance would substantially affect the resulting calculations. Varying the void-to-void distance from 60 to 117nm yielded the plot shown in Figure 7.7 for time-to-rupture for inner wall locations of the tube. The lower value of 60μm were chosen since that was approximately the mean void-to-void distance for sample K1, while the higher value of 117μm was obtained by averaging the distance between grain edges in sample K1

(measurements were performed from 3D reconstructions). In Figure 7.7, the upper line represented $2l$ = 117μm, while the lower limit corresponded to $2l$ = 60μm. For reference, distance between grain corners in sample K1 averaged at about 130μm. Using this number for the upper limit would certainly raise the upper curve of Figure 7.7 even higher.

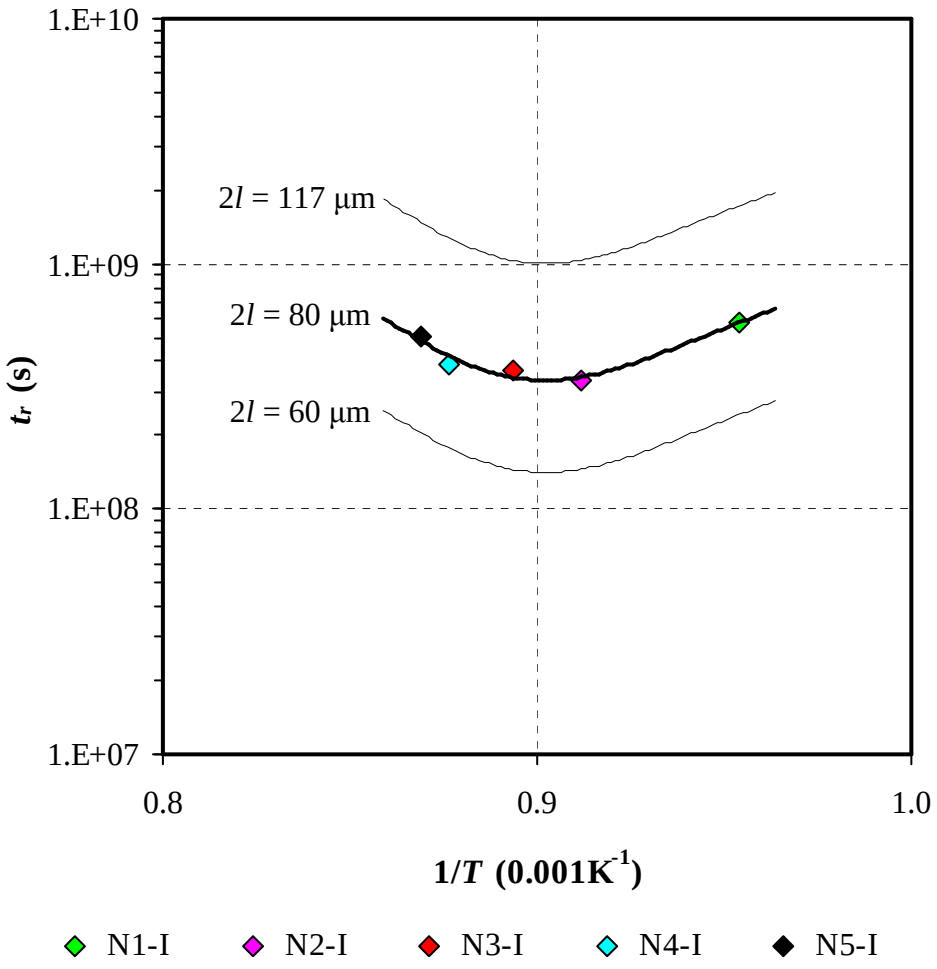

Figure 7.7: Effect of variations in void-to-void distance on the time-to-rupture computations for samples at the inner wall of the idealized reformer tube. Lower bound is for $2l$ = 60μm, upper bound is for $2l$ = 117μm.

Other parameters found to appreciably affect the time-to-rupture computations were the inner and outer wall temperatures. Variations in either or both of these parameters which caused change in ΔT would noticeably alter the time-to-rupture curve. Figure 7.8a shows the effect on t_r when the outer wall temperature was increased by 1% (lower bound) and decreased by 1% (upper bound). On the other hand, Figure 7.8b shows the effect of a 1% increase and decrease in inner wall temperature. The lower bounds on the graph were due

to the inner wall temperature being increased by 1%. Although the 3D work done here have no bearing on the temperature, the temperature effects are presented here just for completeness.

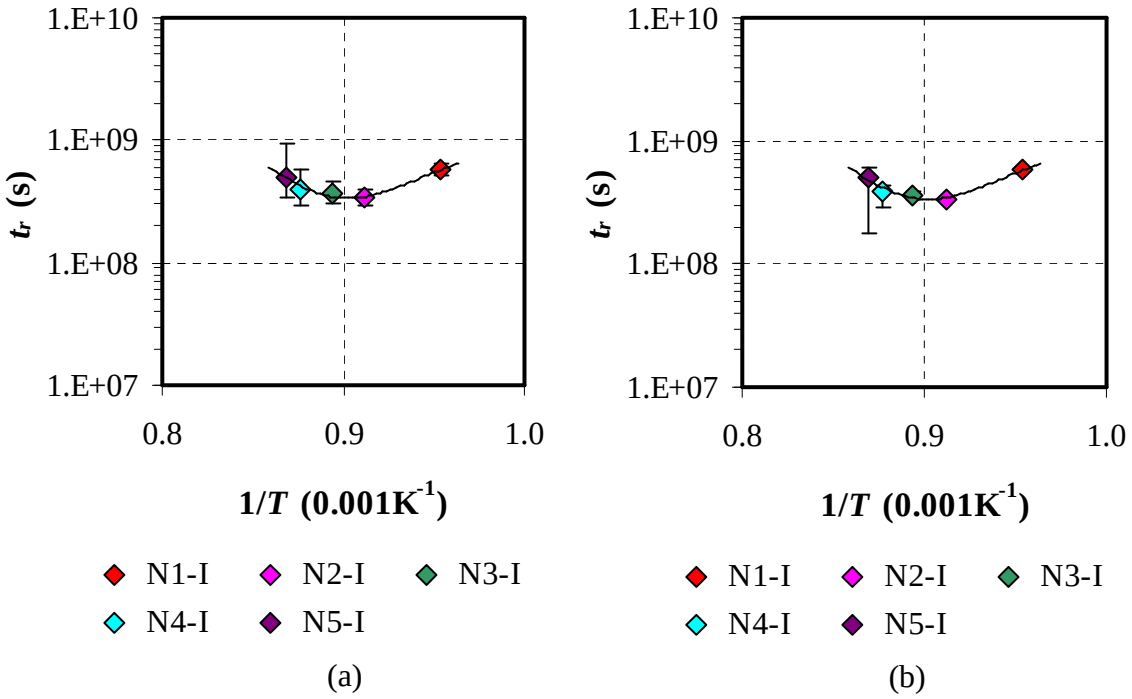

Figure 7.8: Effect of tube wall temperature variations on the time-to-rupture computations. (a) Outside wall temperature variation of ±1%; (b) inside wall temperature variation of ±1%. Lower bound is due to increase in temperature.

Variations in other modeling parameters did not significantly affect the time-to-rupture calculations. In most cases, these variations were too small to be visible on the logarithmic vertical scale of the plot. These influences of the various computational factors are summarized in Table IX.

Table IX: Percent change (average) in time-to-rupture t_r due to variations in various modeling parameters. (Note: α and E are temperature dependent, and their respective values are given in Appendix I).

Parameter	Starting value	Variations	Percent Change
void radii, r_B, r_c	2.5nm	1nm, 10nm	0.0086, 0.043
void types	Type A β = 45°	Type 2, A or B: α, β, θ = 0°, 90° Type 3 α = 30°, 90° Type 4 α = 30°, 90°	-0.014, +0.44 -0.0097, +0.0022 -0.010, +0.0097
wall thickness, t	10mm	9mm, 11mm	-2.3, +1.9
coeff. of thermal expansion, α	$\alpha = \alpha(T)$	0.95 $\alpha(T)$, 1.05 $\alpha(T)$	-3.6 +3.9
modulus of elasticity, E	$E = E(T)$	0.95 $E(T)$, 1.05 $E(T)$	-3.5 +3.8
integral upper limit, A_{max}	0.5	0.3, 0.7	-24.4, +10.3
void-to-void distance, $2l$	80μm	60μm, 117μm	-57.8, +213
outside wall temperature, T_o	$T_o = T_o(y)$	0.99 $T_o(y)$, 1.01 $T_o(y)$	-37.5, +18.9
inside wall temperature, T_i	$T_i = T_i(y)$	0.99 $T_i(y)$, 1.01 $T_i(y)$	-6.8, +19.6

7.3 Final Thoughts

Data from 3D reconstructions of voids in a steam-methane reformer tube was used to refine a simplified void growth model developed by Raj and co-workers [27, 28]. Void data from ex-service reformer tubes were used to test the applicability of the model to determine time-to-rupture for the ex-service samples based on their existing level of creep

damage. A generalized model was then created to determine time-to-rupture for an idealized reformer tube which experience typical steam-methane reformer conditions.

Although the computations were rather crude, they demonstrated the utility of 3D data in developing a simple void growth model. Note that creep failures typically progress by the nucleation, growth and coalescence of creep voids, but the model shown in this work only catered to the growth of the voids. Additional research would be required to obtain three dimensional information of void nucleation, which would then complement the simple void growth model presented here. The combined model could then be refined further to accommodate coalescence of voids.

It was also demonstrated here that the accuracy of the void growth model was highly dependent on a few factors. Firstly, material constants for grain boundary diffusion behavior had a substantial effect on the results. Constants used in the modeling process must be adapted from the same type of material. The model would be improved if the grain boundary diffusion data were actually obtained for the same material. The other critical component of the model is the void density factors, which in this work were given in terms of void-to-void distance. Here, it was assumed that the void-to-void distance is based on a predetermined grain size and hence the number of void nuclei is also constant. Changing this value based on 3D measurements greatly affect the results. For instance, by using the mean void-to-void distance of $2l = 60\mu m$, which was measured from and ex-service tube, reduced the time-to-rupture by approximately 50%. On the other hand using a higher value based on a measured distance between grain edges yielded a longer time-to-rupture.

Although further improvements to the model are needed to increase the accuracy of the predictions, the following general conclusions can be made based on the 3D observations and the application of the void growth model:

- Tube material with a matrix-precipitate system of higher grain boundary activation energy would yield a higher time-to-rupture life. Perhaps improvements in the matrix-precipitate interface by variation in alloy content may result in formation of precipitates with higher grain boundary activation energies..

- Larger equiaxed grains in the inner wall of the reformer tubes may lead to longer distances between grain edges and corners hence longer void cluster-to-void cluster distances.
- Larger secondary dendrite arm spacing may further enhance the service life of the reformer tube.

Chapter 8

SUMMARY AND CONCLUDING REMARKS

When bringing this work to a closure, the author was frequently reminded that research of this nature must extend the boundaries of knowledge in order to be of use. It is certainly hoped that this thesis had presented a novel way of studying material deformation or failure by viewing the defects and associated microstructural features in 3D, and from these unique observations, it is anticipated that the knowledge of the high temperature creep deformation and void formation in steam-methane reformer tubes is further enhanced. At the very least, this work should serve as the initiator to various future research projects.

8.1 Summary

Steam methane reformers contain hundreds of centrifugally cast austenitic stainless steel tubes operating at temperatures up to 950°C and internal pressures of 2.5MPa. The typical material used for the tubes is based on an HP-type casting alloy. The failure of the tubes is by nucleation, growth and coalescence of creep voids culminating in rupture. Failure by rupture is preferably pre-empted by retirement from service according to a schedule or to predetermined deformation limits.

In this research, ex-service reformer tubes were obtained from a Methanex plant in British Columbia, Canada. The tubes were fabricated from Schmidt-Clemens Centralloy® CA4852-Micro centrifugally cast tubes. In the ex-service condition, the microstructure of the tube consists of a network of grain boundary and dendritic precipitates in austenite matrix. Fine intragranular precipitates were also present. Various techniques were applied to characterize the microstructural features present, and it was discovered that the coarse precipitates lining the grain and dentritic boundaries were usually either Cr-rich $M_{23}C_6$ or

NbC precipitates. Coarse TiC precipitates were also found along the boundaries or at intragranular positions. The fine intragranular precipitates are exclusively $M_{23}C_6$. An as-cast tube sample was also obtained for comparison. The microstructure of the as-cast tube is clearly different than the ex-service tube due to the absence of fine intragranular precipitates. Furthermore, the grain boundary and dendritic precipitates appeared more faceted and lamellar-like. Characterization of the precipitates revealed the same types as in ex-service tubes; Cr-rich $M_{23}C_6$, NbC, and TiC precipitates.

Three-dimensional techniques of serial sectioning and 3D reconstruction have been applied to study creep voids in the reformer tubes. Samples were obtained from a failed reformer tube and also from three positions along an ex-service reformer tube which was retired from service due to excessive deformation. A number of significant observations and characteristics were obtained from viewing creep voids in three dimensions, including:

- characteristics of voids - sizes, shapes and locations;
- void density and separation statistics;
- the geometry of neighboring grain boundaries;
- void-precipitate configuration;
- the identity of neighboring precipitates.

Creep voids are not uniformly distributed through the volume in terms of their size, shape, and location. In general, void size increased towards the hotter end of the tube. The largest voids were formed by coalescence of two or more spherical voids resulting in a peanut shape. Most the voids observed show rounded surfaces, characteristic of low-stress high temperature void formation as opposed to wedge-like cracks which occur at higher stress levels.

It needs to be added here that laboratory creep tests were initially planned on as-cast reformer tube samples. However, preliminary work revealed that these interrupted test samples and conditions could not faithfully replicate the ex-service material. Due to the curvature of the tube, it was impossible to obtain a uniaxial creep test piece from the reformer tube that can be tested such that the same microstructural orientation and features aligned with the principal stress direction of the reformer tube in service. Attempts at performing a pressurized tube test in the presence of hydrogen gas were also not yet

successful. Moreover it was observed that the creep voids and surrounding microstructure of the accelerated test samples were completely different from the ex-service samples even though their Larson-Miller parameters were identical. The sample from the accelerated creep test revealed voids that were wedge-like (Figure 8.1a) while the ex-service sample showed more spherical voids (Figure 8.1b). Furthermore the density of fine secondary precipitates was higher in the accelerated test sample compared to the ex-service sample, as evident in Figure 8.1. Based on these issues, laboratory creep tests were not performed in this work.

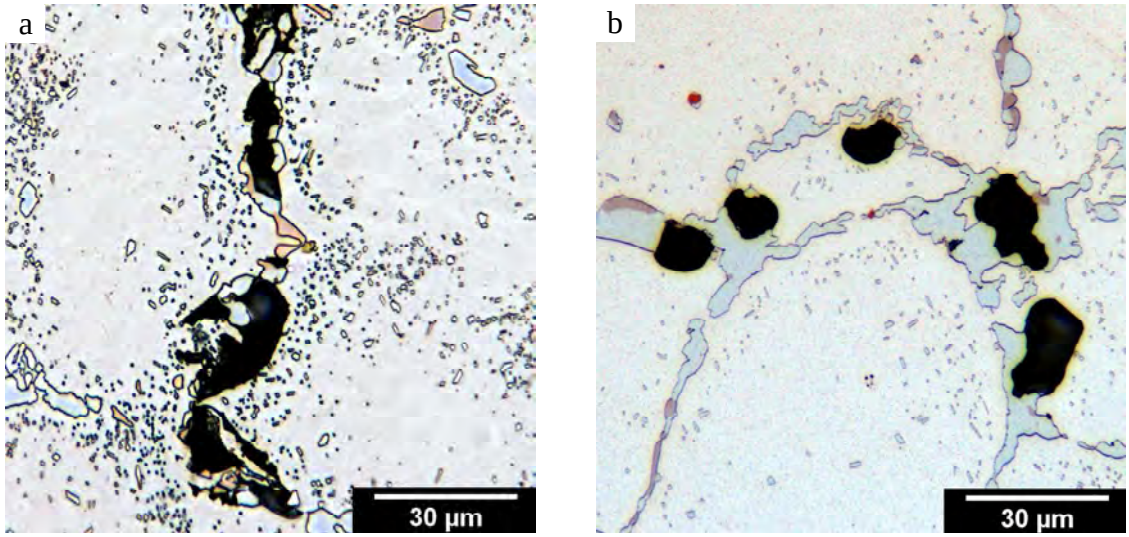

Figure 8.1: Void shapes and microstructures of tube material subjected to creep. (a) Accelerated creep test sample; (b) ex-service sample. Note: LMP for both samples are similar.

Almost all of the voids appeared near grain boundary carbides and most of these voids appeared at precipitates located at grain facets (two-grain junctions). However, the larger of these voids were located next to precipitates at grain edges (three-grain junctions) and corners (four-grain junctions). There were also a small number of voids that were observed away from grain boundaries, and these voids appeared at precipitates located either at dendrite arm boundaries or intragranular positions. As expected, no voids were observed away from precipitates either at grain boundaries or intragranularly.

Two different measures of void separation were obtained from 3D observations. Void density values were acquired by counting the number of voids per grain boundary area, and the "mean" void-to-void distance can be determined from this number. On the other hand,

by measuring the distance from each void to its closest neighbor, the “minimum” void separation distance can be established. It was shown that the mean void-to-void distances were about 2.5 times greater than the minimum distances. This agreed with the 3D observations that showed clustering of voids especially at the grain edges and corners of the equiaxed microstructure.

Next, the grain boundaries containing voids were found to have an average orientation of 45 degrees with respect to the hoop stress direction. The reformer tube experiences a three-dimensional state of stress, however the larger stresses are parallel to the hoop and axial directions (radial stresses are comparatively smaller). As a result, the direction of maximum shearing stress will also be located at 45 degrees with respect to the hoop direction, and the stress normal to this maximum shear stress plane will be the highest effective stress, which in this work was referred to as Tresca stress.

Void-precipitate configurations can be classified as type A or type B voids. Type A voids appear next to a precipitate and only lie in one grain, whereas type B voids extend into two or more grains. From 3D observations and analyses, it appeared that voids may equally nucleate as type A or type B voids. However, the positioning of type B voids, which spans the grain boundary, assisted greatly with the growth of these voids, possibly due to the increased mobility of atoms along the grain boundaries. Additionally, voids appear to nucleate as spherical voids, and as creep progressed, these voids may link up to form peanut-shaped voids.

All voids made contact with $M_{23}C_6$ precipitates somewhere along their perimeter, whereas no voids were observed in sole contact with TiC or NbC precipitates, or appearing “alone”. EBSD observation of the $M_{23}C_6$ precipitates surrounding these voids showed that eighty percent of the voids were found adjacent to precipitates with a low coherency (random OR) with the surrounding austenite matrix. Interestingly, material defects associated with precipitates having a random OR with the surrounding matrix have been previously reported. Kinzel [89] showed that corrosion on $M_{23}C_6$ interfaces with an irrational OR with the austenite matrix was more pronounced. More recently, Kim and co-workers demonstrated that higher coherency of grain boundary $M_{23}C_6$ carbides resulted in better

resistance to cavity nucleation for austenitic stainless steels under creep-fatigue conditions [90].

From 3D reconstructions, various measured parameters were used in the void growth model developed by Raj and co-workers [27, 28]. The most important information obtained was that the void density measurements had a significant effect on the growth model. Other parameters obtained did not show considerable influence on the calculations. Based on the 3D observations and the application of the void growth model, the following general conclusions can be made:

- Tube material with a matrix-precipitate system of higher grain boundary activation energy would yield a higher time-to-rupture life. Perhaps improvements in the matrix-precipitate interface can be achieved by variations in alloying content and elements to produce changes in terms of precipitate types, size, or fragmentation.
- Larger equiaxed grains in the inner wall of the reformer tubes may lead to longer distances between grain edges and corners hence longer void cluster-to-void cluster distances.
- Larger secondary dendrite arm spacing may further enhance the service life of the reformer tube.

8.2 Future Work

As with most research endeavors, the outcomes of this research probably raise more questions than provide answers. One of the limitations of this work is the relatively small volume of material and relatively small number of samples that were serial sectioned and consequently reconstructed. For the reformer tube samples, the need to reconstruct large 3D volumes to cater for the large grain sizes on the order of hundreds of micrometers wide was hampered by the requirements to also reconstruct small voids that were on the order of only a few micrometers in diameter. In this work, of the five tube samples obtained (X1, K1, K2, K3, as-cast), a total of twenty 3D volumes were reconstructed from approximately two thousand serial section images. However it is quite surprising to know that the total volume of all twenty reconstructed 3D volumes is a mere $0.08mm^3$. Automated 3D serial sectioning devices such as Robo-Met.3D [91] or dual-beam FIB systems [92] can, in theory, automatically serial section large sets of data for analyses. Continual

improvements on these types of system may in the near future allow for collection of 3D data to be more efficient and less time consuming.

In terms of materials, this work studied ex-service reformer tubes manufactured from only one type of alloy. Tubes made of different alloy content could certainly be studied in the future for comparisons. Furthermore, differences in microstructural configurations of the tube such as different grain sizes or ratio between equiaxed and columnar structures can also be considered. It would also be interesting to investigate in detail the formation, evolution, and characteristics of various precipitates in the reformer tube alloy, and how these precipitates affect the high temperature behavior of these materials. Another item of interest is the generation of precise deformation maps for these materials. These deformation maps would allow for accelerated laboratory creep tests to more accurately simulate long term high temperature deformation. High temperature pressurized tube tests would also be expected to shed new insights on the creep behavior of these materials.

With regards to modeling of void growth, the inclusion of void nucleation factors is crucial for better prediction of creep damage. A 3D study of nucleation behavior either in laboratory tested samples or early ex-service tubes would be required to complement the void growth aspects learned in this work. Accommodating the factor of void coalescence should enhance the combined model further.

REFERENCES

1. Worden, S., *Microstructural Analysis of Creep Damage in Methanol Reformer Tubes,* in *Final Year Project, supervised by Kral, M.V.* 2000, Mechanical Engineering Department, University of Canterbury: Christchurch.

2. *Global Environmental Excellence Report 2002,* Methanex Corporation: Vancouver, Canada.

3. *Global Environmental Excellence Report 2005,* Methanex Corporation: Vancouver, Canada.

4. Kew, R. *History of tube failures in a large top-fired reformer*. in *IMTOF 97*. 1997. San Diego: ICI Katalco.

5. Wen-Tai, H. and Honeycombe, R.W.K., *Structure of centrifugally cast austenitic stainless steels: Part 1 HK 40 as-cast and after creep between 750 and 1000^{o}C.* Materials Science and Technology, 1985. **1**: p. 385-389.

6. Davis, J.R., ed. *Heat-Resistant Materials*. ASM Specialty Handbook. 1997, ASM International: Materials Park, Ohio.

7. Jones, J. and Huber, J. *Improved reformer furnace efficiency (An update on reformer tube metallurgy).* in *IMTOF 97*. 1997. San Diego: ICI Katalco.

8. Shaw, S.W.K. and Quarrell, A.G., Journal of the Iron and Steel Institute, 1957. **185**: p. 10.

9. Kirchheiner, R. and Woelpert, P. *Niobium in centrifugally cast tubes for petrochemical applications*. in *Proceedings of the International Symposium Niobium*. 2001. Orlando, USA.

10. Sourmail, T., *Precipitation in creep resistant austenitic stainless steels.* Materials Science and Technology, 2001. **17**: p. 1-14.

11. Barbabela, G.D., de Almeida, L.H., da Silveira, T.L., and Le May, I., *Role of Nb in modifying the microstructure of heat-resistant cast HP steel.* Materials Characterization, 1991. **26**(3): p. 193-197.

12. de Almeida Soares, G.D., de Almeida, L.H., da Silveira, T.L., and Le May, I., *Niobium additions in HP heat-resistant cast stainless steels.* Materials Characterization, 1992. **29**(3): p. 387-396.

13. Barbabela, G.D., de Almeida, L.H., da Silveira, T.L., and Le May, I., *Phase characterization in two centrifugally cast HK stainless steel tubes.* Materials Characterization, 1991. **26**(1): p. 1-7.

14. Wen-Tai, H. and Honeycombe, R.W.K., *Structure of centrifugally cast austenitic stainless steels: Part 2 effects of Nb, Ti, and Zr.* Materials Science and Technology, 1985. **1**: p. 390-397.

15. Shinoda, T., Zaghloul, M.B., Kondo, Y., and Tanaka, R., *The effect of single and combined additions of Ti and Nb on the structure and strength of the centrifugally cast HK40 steel.* Transactions ISIJ, 1978. **18**: p. 139-148.

16. Courtney, T.H., *Mechanical Behavior of Materials*. 2000, New York: McGraw-Hill.

17. Dowling, N.E., *Mechanical Behavior of Materials: Engineering Methods for Deformation, Fracture, and Fatigue*. 2nd ed. 1999, Upper Saddle River, NJ: Prentice Hall.

18. Nabarro, F.R.N., *Creep in commercially pure metals.* Acta Materialia, 2006. **54**(2): p. 263-295.

19. Abdul Wahab, A. and Bowles, C.Q., *Creep of Pb-Sn, Bi-Sn, and Bi-Pb solder alloys (unpublished work).* 1989, University of Missouri - Kansas City.

20. Langdon, T.G., *Creep at low stresses: An evaluation of diffusion creep and Harper-Dorn creep as viable creep mechanisms.* Metallurgical and Material Transactions, 2002. **33A**(2): p. 249-259.

21. Nabarro, F.R.N., *Creep at very low rates.* Metallurgical and Material Transactions, 2002. **33A**(2): p. 213-218.

22. Gifkins, R.C., *Grain-boundary participation in high-temperature deformation: An historical review.* Materials Characterization, 1994. **32**(2): p. 59-77.

23. Blum, W. and Maier, W., *Harper-Dorn Creep - a Myth?* Physica Status Solidi (a), 1999. **171**(2): p. 467-474.

24. Nabarro, F.R.N., *Harper-Dorn Creep - A Legend Attenuated?* Physica Status Solidi (a), 2000. **182**(2): p. 627-629.

25. Kassner, M.E. and Hayes, T.A., *Creep cavitation in metals.* International Journal of Plasticity, 2003. **19**(10): p. 1715-1748.

26. Goods, S.H. and Brown, L.M., *Overview No. 1 : The nucleation of cavities by plastic deformation.* Acta Metallurgica, 1979. **27**(1): p. 1-15.

27. Raj, R. and Ashby, M.F., *Intergranular fracture at elevated temperature.* Acta Metallurgica, 1975. **23**: p. 653-666.

28. Raj, R., Shih, H.M., and Johnson, H.H., *Correction to: "Intergranular fracture at elevated temperature".* Scripta Metallurgica, 1977. **11**(10): p. 839-842.

29. Needleman, A. and Rice, J.R., *Plastic creep flow effects in the diffusive cavitation of grain boundaries.* Acta Metallurgica, 1980. **28**: p. 1315-1332.

30. Cocks, A.C.F. and Ashby, M.F., *On creep fracture by void growth.* Progress in Materials Science, 1982. **27**(3-4): p. 189-244.

31. Pardoen, T. and Hutchinson, J.W., *An extended model for void growth and coalescence.* Journal of the Mechanics and Physics of Solids, 2000. **48**: p. 2467-2512.

32. Ratcliffe, R.T. and Greenwood, G.W., *Mechanism of Cavitation in Magnesium During Creep.* Philosophical Magazine, 1965. **12**(115): p. 59-69.

33. Forsman, O., *Undersokning av rymdstrukturen hos ett kolstal av hypereutektoid sammansattning.* Jernkontor-ets Ann, 1918. **102**: p. 1-30.

34. Hillert, M., *The formation of pearlite,* in *The Decomposition of Austenite by Diffusional Processes*, Zackay, V.F. and Aaronson, H.I., Editors. 1962, Interscience: New York. p. 197-237.

35. Hull, D.A., McCammond, D., Hoeppner, D.W., and Hellier, W.G., *Titanium prior-beta grain volume distribution by quantitative serial sectioning techniques.* Materials Characterization, 1991. **26**(2): p. 63-71.

36. Kral, M.V., Ice, G., Miller, M.K., Uchic, M.D., and Rosenberg, R.O., *Three-Dimensional Microscopy*, in *ASM International Metallography and Microstructures Handbook (Volume 9)*, Voort, G.V., Editor. 2004, ASM International: Materials Park, Ohio. p. 448-467.

37. Lewis, A.C., Bingert, J.F., Rowenhorst, D.J., Gupta, A., Geltmacher, A.B., and Spanos, G., *Two- and three-dimensional microstructural characterization of a super-*

austenitic stainless steel. Materials Science and Engineering: A, 2006. **418**(1-2): p. 11-18.

38. Thévenaz, P., *StackReg*, available from http://bigwww.epfl.ch/thevenaz/stackreg/.

39. NIH, *ImageJ*, available from http://rsb.info.nih.gov/ij/.

40. Foley, J.D., *Computer Graphics: Principles and Practice*. 2nd ed. 1990, Reading, Massachusetts: Addison-Wesley.

41. Schmidt+Clemens, *Centralloy CA4852-Micro material data sheet*. 2001, Schmidt+Clemens Group: Lindlar-Kaiserau, Germany.

42. Soares, G.D.d.A., de Almeida, L.H., da Silveira, T.L., and Le May, I., *Niobium additions in HP heat resistant cast stainless steels.* Materials Characterization, 1992. **29**: p. 387-396.

43. de Almeida, L.H., Ribeiro, A.F., and Le May, I., *Microstructural characterization of modified 25Cr-35Ni centrifugally cast steel furnace tubes.* Materials Characterization, 2002. **49**(3): p. 219-229.

44. Kenik, E.A., Maziasz, P.J., Swindeman, R.W., Cervenka, J., and May, D., *Structure and phase stability in a cast modified-HP austenite after long-term ageing.* Scripta Materialia, 2003. **49**(2): p. 117-122.

45. Vander Voort, G.F., *Buehler's Guide to Materials Preparation*. 2002, Lake Bluff, Illinois: Buehler Ltd.

46. Vander Voort, G.F., *Metallography, Principles and Practice*. 1984, New York: McGraw-Hill.

47. Arbuzov, M.P., Golub, S.Y., and Karpets, M.V., *Ordering structure of austenite of chromium steel.* Physics of Metals and Metallography, 1986. **62**(1): p. 95-99.

48. Fruchart, D., Chaudonet, P., Fruchart, R., Rouault, A., and Senateur, J.P., *Etudes structurales de composes de type cementite: Effet de l'hydrogene sur Fe3C suivi par diffraction neutronique. Spectrometrie Mossbauer sur FeCo2B et Co3B dopes au 57 Fe.* Journal of Solid State Chemistry, 1984. **51**: p. 246-252.

49. Rundqvist, S. and Runnsjo, G., *Crystal structure refinement of Cr3C2.* Acta Chemica Scandinavica, 1969. **23**: p. 1191-1199.

50. Rouault, M.A., Herpin, P., and Fruchart, M.K., *Etude cristallographique des carbures Cr7C3 ET Mn7C3.* Annales De Chimie, Paris, 1970. **5**(461-470).

51. Bowman, A.L., Arnold, G.P., Storms, E.K., and Nereson, N.G., *The crystal structure of Cr23C6.* Acta Crystallographica B, 1972. **28B**: p. 3102-3103.

52. Stuart, H. and Ridley, N., *Thermal expansion of some carbides and tessellated stresses in steel.* Journal of The Iron and Steel Institute, London, 1970. **208**: p. 1087-1092.

53. Jeitschko, W., Jordan, A.G., and Beck, P.A., *V and E phases in ternary systems with transition metals and silicon or germanium.* Transactions of the Metallurgical Society of AIME, 1969. **245**: p. 335-339.

54. Markiv, V.Y., Hladyshevsky, E.I., Skolozdra, R.V., and Kryyakevich, P.I., *Ternary compounds RX'X'' in the systems Ti-V(Fe,Co,Ni)-Si and some related systems.* Dopovidi Akademi Nauk Ukrans'koi RSR, Seriya A: Fiziko-Teknichni Ta Matematichni Nauki, 1967. **3**: p. 266-269.

55. Rudy, E., Windisch, S., and Brukl, C.E., *Revision of the vanadium-carbon and niobium-carbon systems.* Planseeberichte Fuer Pulvermetallurgie, 1968. **16**: p. 3-33.

56. Bardos, D.I., Gupta, K.P., and Beck, P.A., *Ternary laves phase with transition elements and silicon.* Transactions of the Metallurgical Society of AIME, 1961. **221**: p. 1087-1088.

57. Stadelmaier, H.H. and Fiedler, M.L., *The ternary system nickel-niobium-carbon.* Zeitschrift Fuer Metallkunde, 1975. **66**: p. 224-225.

58. Zubkov, V.G., Dubrovskaya, L.B., Gel'd, P.V., Ckhaj, V.A., and Dorofeev, Y.A., *The crystal structure of C3Nb4.* Doklady Akademi Nauk SSSR, 1969. **184**(4): p. 874-876.

59. Landesman, J.P., Christensen, A.N., de Novion, C.H., Lorenzelli, N., and Convert, P., *Order-disorder transition and structure of the ordered vacancy compound Nb6C5: powder neutron diffraction studies.* Journal of Physics C, Solid State Physics, 1985. **18**: p. 809-823.

60. Matteo, A., Llanes, L., Anglada, M., Redjaimia, A., and Metauer, G., *Characterization of the intermetallic G-phase in an AISI 329 duplex stainless steel.* Journal of Materials Science, 1997. **32**: p. 4533-4540.

61. Blazina, v. and Trojko, R., *Structural investigations of the Nb(1-x)SixT2 and Nb(1-x)AlxT2 (T=Cr,Mn,Fe,Co,Ni) systems.* Journal of the Less Common Metals, 1986. **119**(2): p. 297-305.

62. Capkova, P., Karen, P., and Dobiasova, L., *Determination of molar ration in AB(1-x) rocksalt-type compounds by x-ray powder diffraction method. Application to TiC(1-x).* Crystal Research and Technology, 1986. **21**(6): p. 735-740.

63. Goretzki, H., *Neutron diffraction studies on titanium-carbon and zirconium-carbon alloys.* Physica Status Solidi, 1967. **20**(K141-K143).

64. Khaenko, B.V., Golub, S.Y., and Arbuzov, M.P., *The order structure of titanium carbide.* Soviet Physics-Crystallography, 1980. **25**(1): p. 63-67.

65. Villars, P. and Calvert, L.D., *Pearson's Handbook of Crystallographic Data for Intermetallic Phases*. second ed. 1991, Materials Park, Ohio: ASM International.

66. Kestel, B.J., *Polishing Methods for Metallic and Ceramic Transmission Electron Microscopy Specimens*. 1986, Springfield, Virginia: US National Technical Information Service.

67. Edington, J.W., *Electron Diffraction in the Electron Microscope*. Monographs in Practical Electron Microscopy in Materials Science; : Monograph 2. 1975, London: Macmillan.

68. Kral, M.V. and Spanos, G., *Three-dimensional analysis of proeutectoid cementite precipitates.* Acta Materialia, 1999. **47**(2): p. 711-724.

69. Parker, J.A., *Align3_TP*, available from http://www.med.harvard.edu/JPNM/ij/plugins/Align3TP.html.

70. Barthel, K.U., *Volume Viewer*, available from http://www.f4.fhtw-berlin.de/~barthel/ImageJ/ImageJ.htm.

71. RSI, *IDL*, available from http://www.rsinc.com/.

72. Jimenez, J.L. and Cristobal, I., *Investigation report: Reformer tube failure analysis - Methanex Corporation*. 2000, Centracero.

73. Sklenicka, V., Kucharova, K., Svoboda, M., Kloc, L., Bursik, J., and Kroupa, A., *Long-term creep behavior of 9-12%Cr power plant steels.* Materials Characterization, 2003. **51**: p. 35-48.

74. Muralidharan, G., Maziasz, P.J., Evans, N.D., Santella, M.L., Liu, K.C., Hemrick, J.G., Sikka, V.K., and Pankiw, R.I. *Effect of precipitation on creep properties of certain cast H-series austenitic stainless steels*. in *MS&T*. 2004. New Orleans, Lousiana.

75. Cane, B.J. and Middleton, C.J., *Intergranular creep-cavity formation in low-alloy bainstic steel.* Metal Science, 1981. **15**: p. 295.

76. Beckitt, F.R. and Clark, B.R., *The shape and mechanism of formation of M23C6 carbide in austenite.* Acta Metallurgica, 1967. **15**(1): p. 113-129.

77. Lewis, M.H. and Hattersley, B., *Precipitation of M23C6 in austenitic steels.* Acta Metallurgica, 1965. **13**: p. 1159-1168.

78. Pumphrey, P.H. and Edington, J.W., *The structure of the semicoherent interface between grain boundary nucleated M23C6 and austenitic stainless steels.* Acta Metallurgica, 1974. **22**: p. 89-94.

79. Singhal, L.K. and Martin, J.W., *The growth of M23C6 carbide on grain boundaries in an austenitic stainless steel.* Transactions of the Metallurgical Society of AIME, 1968. **242**: p. 814-819.

80. Singhal, L.K. and Martin, J.W., *The growth of M23C6 carbide on incoherent twin boundaries in austenite.* Acta Metallurgica, 1967. **15**: p. 1603-1610.

81. Wolff, U.E., *Orientation and morphology of M23C6 precipitated in high nickel austenite.* Transactions of the Metallurgical Society of AIME, 1966. **236**: p. 19-27.

82. Randle, V., *The Measurement of Grain Boundary Geometry*. Electron Microscopy in Materials Science Series, ed. Cantor, B. and Goringe, M.J. 1993, Bristol: Institute of Physics Publishing.

83. King, A.D. and Bell, T., *Crystallography of grain boundary proeutectoid ferrite.* Metallurgical Transactions, 1975. **6A**: p. 1419-1429.

84. Embury, J.D. *Ductile fracture*. in *6th International Conference on Strength of Metals and Alloys (ICSMA 6)*. 1982. Melbourne, Australia: Pergamon.

85. Kaur, I. and Gust, W., *Handbook of Grain and Interphase Boundary Diffusion Data*. Vol. 1-2. 1989, Stuttgart: Ziegler Press.

86. Assassa, W. and Guiraldenq, P., *Influence of C on the Kinetics of Diffusion in Bulk and at Grain Boundaries of the Base Elements of an Fe-Cr-Ni Austenitic Stainless Steel.* Metaux-Corrosion-Industrie, 1977. **621**: p. 170-181.

87. Smith, A.F. and Gibbs, G.B., *The volume and grain-boundary diffusion of iron in 20 per cent Chromium-25 per cent Nickel Niobium-stabilized stainless steel.* Metal Science Journal, 1968. **2**(3): p. 47-50.

88. Frost, H.J. and Ashby, M.F., *Deformation-Mechanism Maps: The Plasticity and Creep of Metals and Ceramics*. 1982, Oxford: Pergamon Press. 175.

89. Kinzel, A.B., *Chromium carbide in stainless steel.* Transactions AIME, 1952. **194**: p. 469-488.

90. Kim, K.J., Hong, H.U., Min, K.S., and Nam, S.W., *Correlation between the carbide morphology and cavity nucleation in an austenitic stainless steels under creep-fatigue.* Materials Science and Engineering A, 2004. **387-389**: p. 531-535.

91. Spowart, J.E., Mullens, H.M., and Puchala, B.T., *Collecting and analyzing microstructures in three dimensions: A fully automated approach.* JOM, 2003. **55**(10): p. 35.

92. Uchic, M.D., *Three-Dimensional Microscopy - Focused Ion Beam Tomography*, in *ASM International Metallography and Microstructures Handbook (Volume 9)*, Voort, G.V., Editor. 2004, ASM International: Materials Park, Ohio. p. 458-459.

93. Morozov, E.M. and Fridman, I.B., *Thermal stresses and their calculation*, in *Strength and deformation in nonuniform temperature fields; a collection of scientific papers*, Fridman, I.B., Editor. 1964, Consultants Bureau: New York.

94. Muvdi, B.B. and McNabb, J.W., *Engineering mechanics of materials*. 3rd ed. 1991, New York: Springer-Verlag.

95. Beyer, W.H., ed. *CRC Standard Mathematical Tables and Formulae*. 29 ed. 1991, CRC Press: Boca Raton.

Appendix I

SELECTED PROPERTIES OF CENTRALLOY CA4852-MICRO

The figures in the following pages represent typical mechanical properties of Schmidt-Clemens Centralloy CA4852-Micro centrifugal cast tubes. Data for CA4852-Micro were taken from ref [41]. In addition, other physical and mechanical properties are as follows:

Density, ρ_t = 8.0g/cm^3

Thermal Conductivity, k_T = 14.6W/mK

Poisson's ratio, ν = 0.3

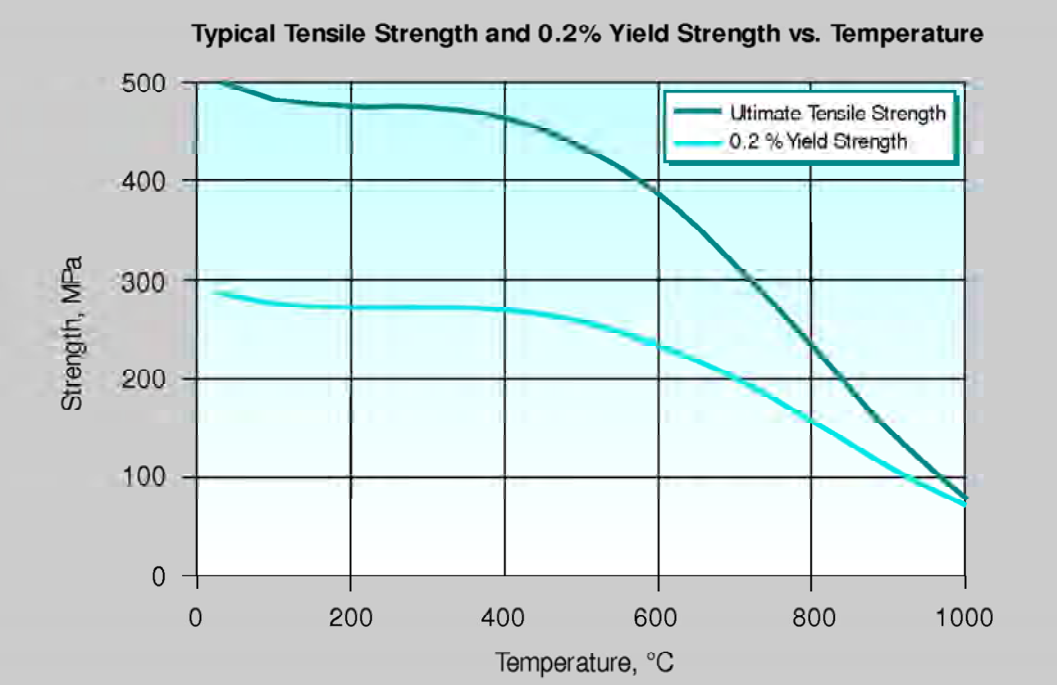

a) yield and tensile strength;

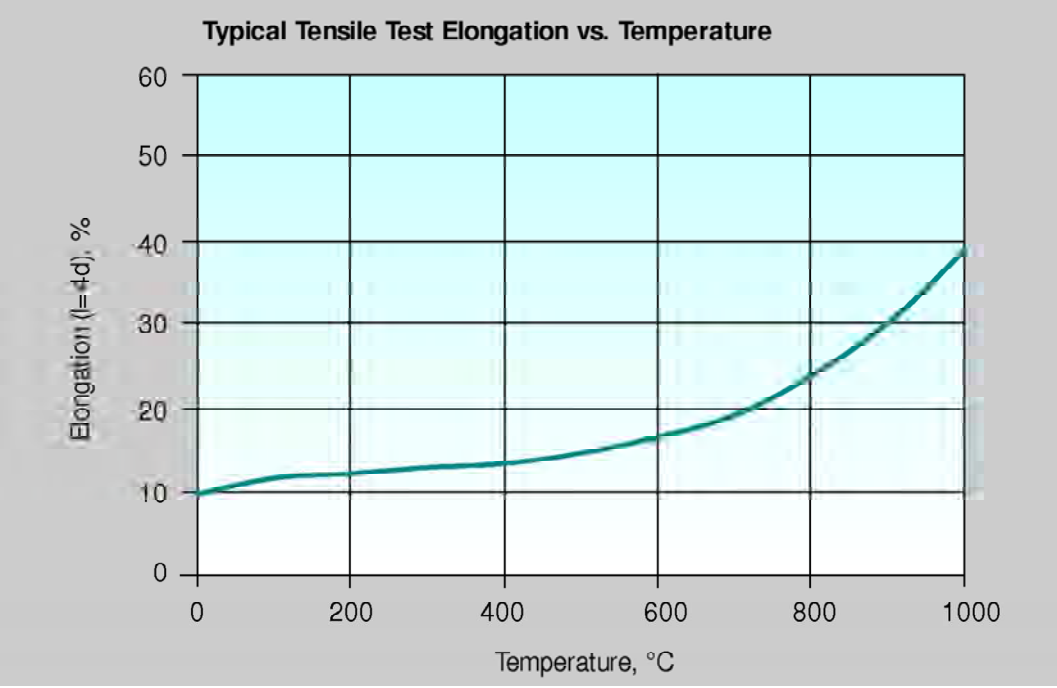

b) percent elongation

Figure I.1: Tensile properties for Schmidt-Clemens Centralloy CA4852-Micro. (a) Yield and tensile strength; (b) percent elongation.

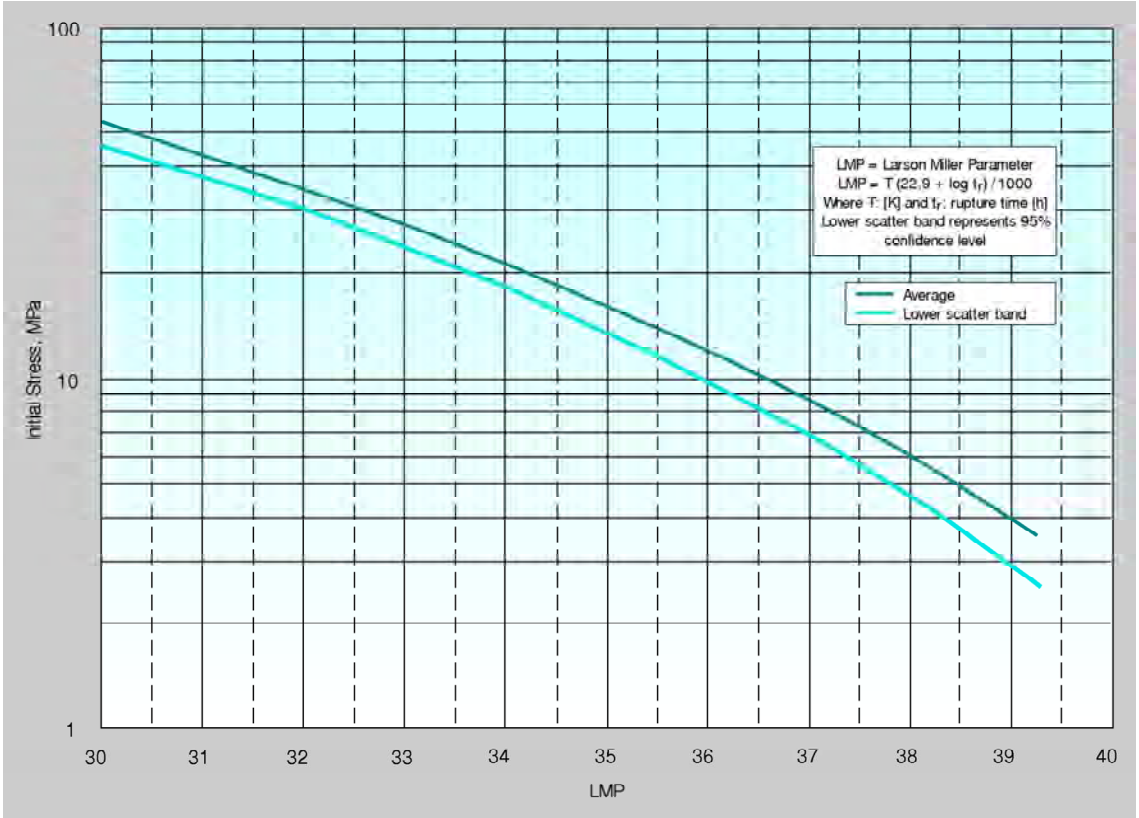

Figure I.2: Parametric stress rupture strength for Schmidt-Clemens Centralloy CA4852-Micro.

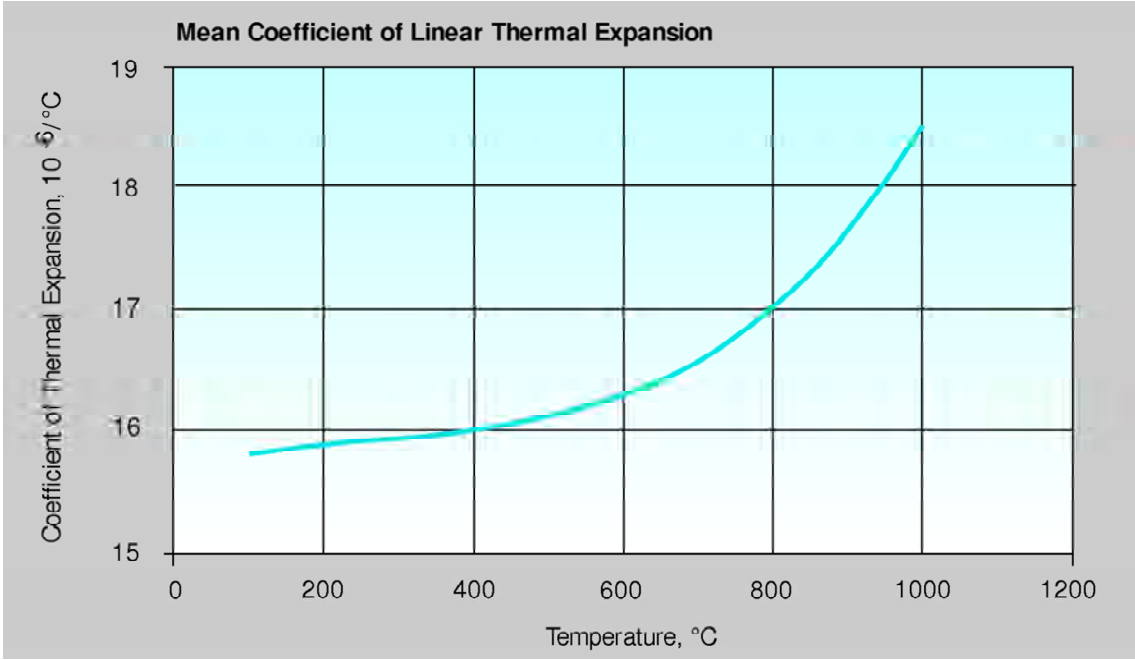

Figure I.3: Coefficient of linear thermal expansion for Schmidt-Clemens Centralloy CA4852-Micro.

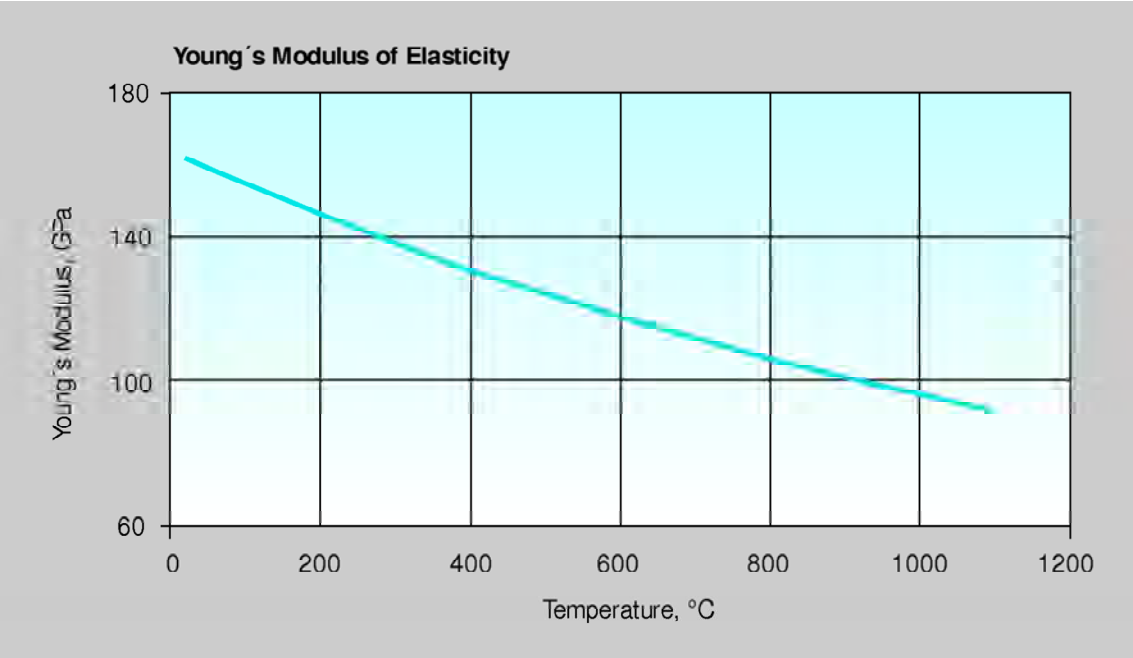

Figure I.4: Modulus of Elasticity for Schmidt-Clemens Centralloy CA4852-Micro.

Appendix II

CALCULATION OF STRESSES IN THE REFORMER TUBE

II.1 Thermal Stresses

Consider a long thick-walled cylinder symmetric about the tube axis as shown in Figure II.1 with a tube wall temperature distribution of $T = T(r)$.

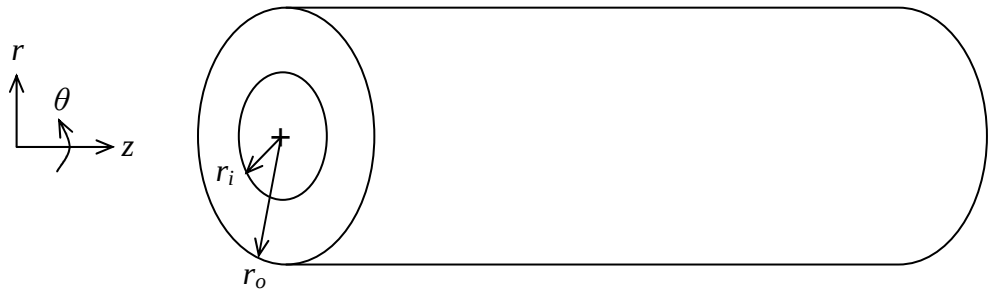

Figure II.1: Schematic of a long thick-walled cylinder and its reference axes.

The hoop, radial, and axial thermal stresses are given by the following equations [93]:

$$\sigma_{hT} = \frac{\alpha_T E}{1-\nu}\left[\left(1+\frac{r_i^2}{r^2}\right)\left(\frac{1}{r_o^2-r_i^2}\right)\int_{r_i}^{r_o} Tr\,dr + \frac{1}{r^2}\int_{r_i}^{r} Tr\,dr - T\right]$$

$$\sigma_{rT} = \frac{\alpha_T E}{1-\nu}\left[\left(1-\frac{r_i^2}{r^2}\right)\left(\frac{1}{r_o^2-r_i^2}\right)\int_{r_i}^{r_o} Tr\,dr - \frac{1}{r^2}\int_{r_i}^{r} Tr\,dr\right]$$

$$\sigma_{aT} = \frac{\alpha_T E}{1-\nu}\left[\left(\frac{2}{r_o^2-r_i^2}\right)\int_{r_i}^{r_o} Tr\,dr - T\right]$$

where: α_T = coefficient of thermal expansion (see Appendix I)

E = modulus of elasticity (see Appendix I)

$T = T(r)$ = temperature distribution

v = Poisson's ratio = 0.3 (assumed constant)

r_i = tube internal radius

r_o = tube external radius.

Assuming a steady heat flux through the wall, with α_T, E, and v also being constant across the wall, the hoop, radial, and axial thermal stresses can be approximated by [93]:

$$\text{hoop stress}: \quad \sigma_{hT} = \frac{\alpha_T E(T_i - T_o)}{2(1-\nu)} \left[\frac{1 - \ln\left(\frac{r_o}{r}\right)}{\ln\left(\frac{r_o}{r_i}\right)} - \frac{\left(\frac{r_o}{r}\right)^2 + 1}{\left(\frac{r_o}{r_i}\right)^2 - 1} \right]$$

$$\text{radial stress}: \quad \sigma_{rT} = \frac{\alpha_T E(T_i - T_o)}{2(1-\nu)} \left[\frac{-\ln\left(\frac{r_o}{r}\right)}{\ln\left(\frac{r_o}{r_i}\right)} + \frac{\left(\frac{r_o}{r}\right)^2 - 1}{\left(\frac{r_o}{r_i}\right)^2 - 1} \right]$$

$$\text{axial stress}: \quad \sigma_{aT} = \frac{\alpha_T E(T_i - T_o)}{2(1-\nu)} \left[\frac{1 - 2\ln\left(\frac{r_o}{r}\right)}{\ln\left(\frac{r_o}{r_i}\right)} - \frac{2}{\left(\frac{r_o}{r_i}\right)^2 - 1} \right]$$

where: T_i = inside wall temperature

T_o = outside wall temperature

r = radial distance to point of interest.

(other variables as defined earlier)

II.2 Stresses Due to Internal Pressure

Lame's Equations: hoop, radial, and axial stresses due to internal pressure p in a long thick-walled cylinder [94]:

$$\text{hoop stress}: \quad \sigma_{hp} = \frac{pr_i^2}{r_o^2 - r_i^2}\left(1 + \frac{r_o^2}{r^2}\right)$$

$$\text{radial stress}: \quad \sigma_{rp} = \frac{pr_i^2}{r_o^2 - r_i^2}\left(1 - \frac{r_o^2}{r^2}\right)$$

$$\text{axial stress}: \quad \sigma_{ap} = \frac{pr_i^2}{r_o^2 - r_i^2}$$

where: p = internal pressure.
(other variables as defined earlier)

II.3 Stresses Due to Tube Weight

Tube hangar system supports seventy five percent of tube weight. The axial stress due to tube weight is:

$$\text{axial stress}: \quad \sigma_{aW} = 0.25 \times \frac{W_t}{A_t} = 0.25 \times \frac{\rho_t g A_t l_t}{A_t} = 0.25 \times \rho_t g l_t$$

$$\text{axial stress per length of tube}: \quad \frac{\sigma_{aW}}{l_t} = -19.62 \times 10^{-3}\ \text{MPa/m}$$

where: W_t = weight of tube
A_t = cross sectional area of tube
ρ_t = density of reformer tube = 8000kg/m^3 (from ref [41])
g = gravitational acceleration = 9.81m/s^2
l_t = vertical distance from top flange to point of interest.

Negative sign indicates compressive stress.

II.4 Calculation of Effective Stress

Effective stress (to be referred in this thesis as Tresca stress) was calculated using the Tresca criterion as follows [17]:

$$\sigma_{TS} = \mathrm{MAX}\left\{|\sigma_1 - \sigma_2|,\ |\sigma_1 - \sigma_3|, |\sigma_2 - \sigma_3|\right\}$$

where $\sigma_1 = \sigma_{hT} + \sigma_{hp}$

$\sigma_2 = \sigma_{rT} + \sigma_{rp}$

$\sigma_3 = \sigma_{aT} + \sigma_{ap} + \sigma_{aW}$.

(principal stresses from combined hoop, radial, and axial stresses)

Appendix III

CALCULATION OF TIME-TO-RUPTURE

Microsoft Excel® was used to calculate time-to-rupture t_r for the void growth model. A simple Visual Basic program was written as a macro to numerically evaluate the integral in equation (3) of Chapter 7. The Extended Simpson's Rule [95] was used as the method for numerical integration. A separate macro program was also written to calculate the void geometry factors shown in Figure 7.2. The results of these two programs were then used in conjunction with other standard Excel spreadsheet functions to calculate and plot the time-to-rupture, t_r. The layout of the Excel spreadsheet used for these calculations will also be presented in this Appendix.

III.1 Code for Void Geometry Factors

Three short program functions were written to calculate the void geometry factors. Function Fb_2AB was used for either two-grain junction, type A, or type B voids. Functions Fb_3 and Fb_4 were used for three-grain junction and four-grain junction voids respectively. The single input variable for all three functions is as defined below:

angle : void interface angle (in degrees).

```
'-----------------------------------------------------------------------------------------------------------------------
Function Fb_2AB(angle)
   Const Pi = 3.141592654
   alpha = angle * Pi / 180
   Fb_2AB = Pi * Sin(alpha) ^ 2
End Function
'-----------------------------------------------------------------------------------------------------------------------
Function Fb_3(angle)
   Const Pi = 3.141592654
```

```
    alpha = angle * Pi / 180
    Fb3part1 = (Pi / Cos(alpha)) + 2 * Pi
    asinterm = 1 / (2 * Sin(alpha))
    Fb3part2 = 6 / (Cos(alpha)) * Atn(asinterm / Sqr(-asinterm ^ 2 + 1))
    Fb3part3 = Cos(alpha) * Sqr(4 * Sin(alpha) ^ 2 - 1)
    acosterm = 1 / (Sqr(3#) * Tan(alpha))
    Fb3part4 = 3 * (Atn(-acosterm / Sqr(-acosterm ^ 2 + 1)) + 2 * Atn(1)) * (3 - Cos(alpha) ^ 2)
    Fb_3 = -Fb3part1 + Fb3part2 - Fb3part3 + Fb3part4
End Function
'-------------------------------------------------------------------------------------------------------------------
Function Fb_4(angle)
    Const Pi = 3.141592654
    alpha = angle * Pi / 180
    Aterm = 2 / 3 * (Sqr(2 * (4 * Sin(alpha) ^ 2 - 1)) - Cos(alpha))
    Fb4part1 = (2 * Pi / Cos(alpha)) + 2 * Pi
    acosterm = (Sqr(2) - Cos(alpha) * Sqr(3 - Aterm ^ 2)) / (Aterm * Sin(alpha))
    Fb4part2 = 12 / (Cos(alpha)) * (Atn(-acosterm / Sqr(-acosterm ^ 2 + 1)) + 2 * Atn(1))
    Fb4part3 = 1.5 * Aterm * (Sqr(4 * Sin(alpha) ^ 2 - Aterm ^ 2) - Aterm ^ 2 / Sqr(2))
    asinterm = Aterm / (2 * Sin(alpha))
    Fb4part4 = 6 * (Atn(asinterm / Sqr(-asinterm ^ 2 + 1))) * (3 - Cos(alpha) ^ 2)
    Fb_4 = -Fb4part1 + Fb4part2 - Fb4part3 + Fb4part4
End Function
'-------------------------------------------------------------------------------------------------------------------
```

III.2 Code for Integrating the Term 1/*f*(*A*)

The two Visual Basic functions below, inverse_fA and integrate_inverse_fA were used to numerically integrate the term 1/*f*(*A*) in equation (3) of Chapter 7. Input variables to these functions are as defined below:

- A : transfer variable from functions inverse_fA to integrate_inverse_fA
- rc : critical radius for void nucleation
- l : ½ of void-to-void spacing
- Fb : geometry function of void configuration on the grain boundary
- Amax : upper integration limit
- Amin : lower integration limit
- n : number of integration steps

Note: '&' indicates a line continued from the previous line of code ('&' is not used in the actual Visual Basic code).

```
'-----------------------------------------------------------------------------------------------------------------------
Function inverse_fA(A, rc, l, Fb)
        Const e = 2.718281828
        Const Pi = 3.141592654
        inverse_fA = A ^ 0.5 * (0.5 * Log(1 / A) / Log(e) - 0.75 + A * (1 - A / 4))
&                       / ((1 - rc / l * (Fb / Pi / A) ^ 0.5) * (1 - A))
End Function
'-----------------------------------------------------------------------------------------------------------------------
Function integrate_inverse_fA(Amax, Amin, n, l, Fb, rc)
        h = (Amax - Amin) / n
        sum_odds = 0
        sum_evens = 0
        A_odds = A_min + h
        For i = 1 To n - 1 Step 2
                sum_odds = sum_odds + inverse_fA(A_odds, rc, l, Fb)
                A_odds = A_odds + 2 * h
        Next i
        A_evens = A_min + 2 * h
        For j = 2 To n - 2 Step 2
                sum_evens = sum_evens + inverse_fA(A_evens, rc, l, Fb)
                A_evens = A_evens + 2 * h
        Next j
        integrate_inverse_fA = h / 3 * (inverse_fA(Amin, rc, l, Fb) + 4 * sum_odds
&                       + 2 * sum_evens + inverse_fA(Amax, rc, l, Fb))
End Function
'-----------------------------------------------------------------------------------------------------------------------
```

III.3 Spreadsheet Layout to Calculate Time-to-Rupture

The Excel spreadsheet used in calculating time-to-rupture is shown in Table X. All the data used for computations were placed in column A. The grayed cells indicate cells containing formulas (listed in the notes following the Table X). A sample calculation using data for X1 tube sample is shown the table.

Table X: Layout of Microsoft Excel spreadsheet used in calculating time-to-rupture for the void growth model.

	A	B	C	D	E
1	**INPUT DATA & PRELIMINARY CALCULATIONS**				
2	Data	Description	REMARKS		
3	X1	sample ID			
4	55.85	amu	atomic mass, g mole^{-1}		
5	7.87E+06	density	atomic density, g m^{-3}		
6	6.02E+23	η	Avogadro's number		
7	1.18E-29	Ω	atomic volume, m^3 (see note 1)		
8	1.38E-23	k	Boltzmann's constant, J K^{-1}		
9	8.314	R	gas constant, J mol^{-1} K^{-1}		
10	1213.0	T	absolute temperature, K		
11	2.00E-14	$(\delta D_b)_0$	GB diffusivity constant, m^3 s^{-1}		
12	1.70E+05	Q_b	GB activation energy, J mol^{-1}		
13	3.02E+07	σ_∞	remote applied stress, N m^{-2} (Tresca stress)		
14	0	p	pressure inside of voids, N m^{-2}		
15	A	void type	void geometry parameter - choices:		
16	45	α_2 (deg)	2 (0<α_2<90 is active);		
17	60	α_3 (deg)	3 (30<α_3<90 is active);		
18	60	α_4 (deg)	4 (30<α_4<90 is active);		
19	45	β (deg)	A (0<β<90 is active);		
20	45	θ (deg)	B (0<θ<90 is active)		
21	1.5708	F_b	(see note 2)		
22	1.45E-05	l	void-to-void distance, m		
23	4.8E-06	r_B	projected radius on GB, m		
24	2.5E-09	r_c	critical void radius, m		
25	1.10E-01	A_{min}	$A_{min}=(r_B/l)^2$ (see note 3)		
26	5.00E-01	A_{max}	arbitrarily set at 0.5		
27	1000	n	integral steps		
28	**RESULTS**				
29	7.61E+06	t_r	time to rupture, s (see note 4)		
30	8.24E-01	1000x1/T	0.001K^{-1} (see note 5)		
31	940.0	T	temperature, ℃ (see note 6)		
32	1213.0	T	temperature, K		
33	X1	sample ID			

Notes:

1. $\Omega = \dfrac{\text{atomic mass}}{(\text{atomic density})\left(6.022\times10^{23}\right)}$ = A4/A5/A6.

2. F_B is calculated using one of the functions listed in section III.1 depending on the void type entry in cell A15. The equation used in cell A21 is:

=IF(A15="A",Fb_2AB(A19),IF(A15="B",Fb_2AB(A20),IF(A15=2,Fb_2AB(A18),

& IF(A15=3,Fb_3(A18),IF(A15=4,Fb_4(A18),"error"))))).

3. $A_{\min} = \frac{r_B^2}{l^2}$ = (A23/A22)^2.

4. Calculation of t_r using the functions listed in section III.2. Equation used is:

   =(A8*A32*A22^3)/(A7*(A11*EXP(-A12/(A9*A32)))*A13)

   & *integrate_inverse_fA(A26,A25,A27,A22,A21,A24).

5. $1000 \times 1/T$ = 1000/A10.

6. T in degrees Celcius = A10-273.

Appendix IV

PUBLICATIONS

The following journal papers were published during the course of this research and are attached in the following pages of this Appendix.

Azmi Abdul Wahab, Milo V. Kral, "*3D Analysis of creep voids in hydrogen reformer tubes*", Materials Science and Engineering A 412 (2005) 222-229.

Azmi Abdul Wahab, Christopher R. Hutchinson, Milo V. Kral, "*A three-dimensional characterization of creep void formation in hydrogen reformer tubes*", Scripta Materialia 55 (2006) 69-73.

ELSEVIER

Materials Science and Engineering A 412 (2005) 222–229

MATERIALS SCIENCE & ENGINEERING A

www.elsevier.com/locate/msea

3D analysis of creep voids in hydrogen reformer tubes

Azmi Abdul Wahab, Milo V. Kral *

Department of Mechanical Engineering, University of Canterbury, Private Bag 4800, Christchurch, New Zealand

Accepted 18 August 2005

Abstract

An ex-service hydrogen reformer tube composed of Fe–0.45% C–25% Cr–35% Ni–1.0% Si–1.5% Nb–1.0% Mn (approximate wt.%) was examined via serial sectioning and 3D reconstruction to characterize creep voids in terms of their size, location, and surrounding precipitates. In addition, electron backscatter diffraction (EBSD) technique was used to investigate any crystallographic influence on the location of these voids. Observations in 3D show that void distribution is not uniform in terms of size, shape, and location. Most of the voids are oblong and occur at grain edges and corners. In addition, all observed voids were in contact with the Cr-rich $M_{23}C_6$ precipitates. EBSD results showed that 80% of the $M_{23}C_6$ precipitates surrounding these voids have an irrational crystallographic orientation relationship (OR) with the austenite matrix, contrary to the expectation that grain boundary precipitates nearly always obtain rational OR with respect to one adjacent grain.

Keywords: 3D reconstruction; Creep voids; Reformer tube; EBSD; Orientation relationship

1. Introduction

In petrochemical plants, the production of hydrogen from natural gas is carried out in hydrogen reformers where the following reactions occur in the presence of a nickel catalyst:

$$CH_4 + H_2O \rightarrow CO + 3H_2$$

$$CO + H_2O \rightarrow CO_2 + H_2$$

Hydrogen reformers consist of hundreds of vertically oriented catalyst-filled tubes operating at a temperature of more than 900 °C and an internal pressure of approximately 2 MPa. These tubes have an internal diameter and wall thickness of about 125 and 10 mm, respectively, and are typically expected to sustain service for 100,000 h (11.4 years) with diametral strain not exceeding 3%. These service requirements result in high temperature deformation in a regime of relatively low stresses (less than 20 MPa), and low creep rates ($8 \times 10^{-11}\ s^{-1}$) where the reported creep mechanisms are diffusional creep, Harper-Dorn (H-D) creep, and grain boundary sliding [1,2].

Centrifugally cast austenitic stainless steel alloys containing high amounts of carbon (0.4 wt.%), chromium (25 wt.%) and nickel (20–35 wt.%) were developed for these purposes. The additions of Cr and Ni are well known for improving corrosion resistance and strength at elevated temperatures, while the high amount of C inhibits σ-phase formation [3]. Creep strengthening is achieved via the formation of Cr-rich $M_{23}C_6$ carbides in the reformer tube microstructure. Primary carbides, which form a grain boundary network during casting, are suspected to play an important role in restraining grain boundary sliding [4]. The secondary carbides, which appear as fine intragranular precipitates during service, are believed to hinder dislocation motion [4]. With increasing service time, the primary and secondary Cr-rich $M_{23}C_6$ carbide particles have a tendency to coarsening, which in turn reduces creep strength [5]. Additions of Nb and Ti lead to "fragmentation" and refinement of the grain boundary carbide network, as well as creating a finer and more stable dispersion of intergranular carbides, which would all result in added creep resistance [6–8].

It is well known from previous work on austenitic stainless steels [9–14] that $M_{23}C_6$ nucleation site has an influence on the crystallography of these precipitates. For instance, $M_{23}C_6$ precipitation in the grain interior results in the best lattice match (cube-cube OR), while grain boundary carbides obtain a near-rational OR with at least one adjacent austenite grain [10]. This is significant because material behaviour appeared to be linked to crystallographic relationship between the precipitate and the adjacent matrix. Corrosion studies on austenitic stainless steels by Kinzel [15] indicated that corrosion was more pronounced

* Corresponding author. Tel.: +64 3 3642987x7392; fax: +64 3 3642078.
E-mail address: milo.kral@canterbury.ac.nz (M.V. Kral).

0921-5093/$ – see front matter © 2005 Elsevier B.V. All rights reserved.
doi:10.1016/j.msea.2005.08.223

Table 1
Main alloying elements (in wt.%) present in the reformer tube sample

C	0.49
Cr	23.5
Ni	32.1
Si	1.07
Nb	1.14
Ti	0.13
Mn	0.91
W	0.46
Fe + others	Bal

Remainder is Fe and other minor alloying elements.

on $M_{23}C_6$ interfaces having a low registry with the austenite matrix. More recent work on austenitic stainless steels under creep-fatigue conditions show that higher coherency of grain boundary $M_{23}C_6$ carbides result in better resistance to cavity nucleation [16].

Three-dimensional analysis of microstructures is often very useful in understanding true microstructural features of materials [17,18]. Earlier attempts in 3D analysis usually involved a serial sectioning technique and motion pictures [19] or some form of physical reconstruction method [20] to provide a representation of the features in 3D. With the advent of superior image processing and visualization software and the corresponding computer hardware, 3D analysis of microstructures have been successfully employed in understanding microstructural characteristics in materials such as alloy steels [21] and particle reinforced metal matrix composites [22].

In the present work, an ex-service hydrogen reformer tube was examined via serial sectioning and computer-aided 3D reconstruction. The serial sectioning and 3D reconstruction techniques revealed the shapes, sizes, locations, and adjacent precipitates of the creep voids in 3D, information that cannot be obtained from two-dimensional micrographs alone. Additionally, crystallographic orientations of the phases adjacent to creep voids were obtained by electron backscatter diffraction (EBSD) to determine any crystallographic trends in creep void locations. It is anticipated that 3D data obtained from this and additional work will be applied to various available creep failure models [23,24].

2. Experimental details

The ex-service hydrogen reformer tube obtained for this work has been in service at approximately 940 °C and 2 MPa internal pressure for 60,000 h (6.8 years). Chemical composition for this tube is listed in Table 1. A sample from the reformer tube was mounted in Buehler Epomet epoxy, and underwent grinding and polishing steps of 240 and 400 grit silicon carbide papers, 9 and 3 μm diamond paste, culminating with a final polish of 0.06 μm colloidal silica. A "control" sample was also prepared from an as-cast tube made from the same alloy as the ex-service tube. This sample was aged at 1030 °C for 500 h in air, and will be used to compare the crystallography of the precipitates. For reference, the Larson-Miller parameter for the control sample is 33.4 compared to a value of 33.6 for the ex-service sample.

For optical microscopy (OM) examinations, the samples were etched in glyceregia (10 ml glycerol + 15 ml HCl + 5 ml HNO_3) prior to observation using a Leica DM-IRM Microscope with Zeiss Axiocam digital camera. For scanning electron microscopy (SEM), energy dispersive spectroscopy (EDS), and electron backscatter diffraction (EBSD), the samples were examined after an extended polish in colloidal silica. The equipment employed for SEM, EDS and EBSD examinations are JEOL JSM-6100 scanning electron microscope, Oxford eXL energy dispersive analyzer with a Be window, and HKL Technology EBSD system. An accelerating voltage of 20 kV was utilized for these observations.

X-ray diffraction (XRD) was also used to confirm the precipitates present in the material. A small sample of the tube was immersed in glyceregia for up to 8 h (successive immersions of two hours per fresh solution) to dissolve the austenite matrix. The remaining precipitate was powdered and scanned in a Philips PW1729 XRD system at 50 kV and 40 mA Cu Kα radiation. Identification of peaks was performed by matching simulated patterns of various compounds generated from Pearson's Handbook [25].

Transmission electron microscopy (TEM) was used to characterize fine intragranular precipitates present in the material. TEM samples were initially thinned in a solution of 35% *n*-butyl alcohol, 6% perchloric acid, and 59% methanol at −30 °C, 40 V, and 25 mA using an E.A. Fischione twin-jet electropolishing setup followed by ion milling using a Gatan Precision Ion Polishing System. TEM examination was performed using a Hitachi H600 transmission electron microscope at 100 kV.

In general, the serial sectioning technique employed here is similar to previous work [21]. Serial sectioning was performed only on the ex-service tube, which was done by successive polishing of the sample using 1 μm diamond compound and 0.06 μm colloidal silica suspension. Prior to the serial sectioning process, reference fiducial marks were placed on the sample using a Leco microhardness tester in order to identify areas of interest and also to align the image stacks for later 3D reconstruction. Furthermore, size reduction of the fiducial marks indicated the amount of material removed with each section. Before the marks were completely polished off, new marks were made so that continuity was preserved for the next polishing steps. Serial sections were done at 0.5 μm steps for sixty five layers (32 μm). Prior to imaging, the sample was lightly etched in glyceregia. A total of four areas of the sample were selected for study; two 400 μm × 300 μm areas and two 160 μm × 120 μm areas were imaged at original magnifications of 200× and 500×, respectively. Due to the relatively large size of the grains involved (in excess of 150 μm), it was ascertained that only the two 400 μm × 300 μm areas were suitable for 3D reconstruction and analysis.

After layers 45, 55 and 65, all four areas of interests in the sample were subjected to EBSD scans to generate an overall orientation map. Following the EBSD mapping, the voids and their immediate surroundings were imaged using forescatter Z-contrast (FZ) and forescatter orientation (FO) detectors, in addition to the usual secondary electron (SE) image. The forescatter Z-contrast detector revealed atomic number contrast

of the different phases present while the forescatter orientation contrast detector exposed grains or subgrains within the matrix and precipitates.

EBSD patterns (or EBSPs) were then recorded in spot mode for specific locations of the matrix and precipitates surrounding the creep voids. For each carbide grain in contact with a creep void, EBSPs were obtained from the carbide as well as the austenite grains on both sides of the grain boundary. In instances where the carbide grain contains subgrains, EBSPs were obtained from each subgrain if its size is larger than the size of the electron beam. The occurrence of these subgrains within larger carbide colonies would certainly influence the OR data obtained if the electron beam size is larger than the subgrain size. EBSD scans were also carried out on the "control" sample. Since the control sample did not contain any creep voids, grain boundary precipitates were selected at random and EBSPs were obtained for these precipitates and the adjacent austenite matrices. HKL Technology's Flamenco software was used to analyse the EBSPs, which then automatically calculated a 3×3 orientation matrix for each EBSP. The misorientation M between any two phases (A and B) can then be obtained from the matrix operation:

$$[A][B] - 1 = [M]$$

where [A] and [B] are orientation matrices of locations within phases A and B with respect to an arbitrary reference axis system. Assuming that:

$$[M] = \begin{bmatrix} m_{11} & m_{12} & m_{13} \\ m_{21} & m_{22} & m_{23} \\ m_{31} & m_{32} & m_{33} \end{bmatrix}$$

the orientation relationship (OR) between location A and B is then:

$$[m_{11} \quad m_{21} \quad m_{31}]_A // [1 \quad 0 \quad 0]_B$$
$$[m_{12} \quad m_{22} \quad m_{23}]_A // [0 \quad 1 \quad 0]_B$$
$$[m_{31} \quad m_{32} \quad m_{33}]_A // [0 \quad 0 \quad 1]_B$$

The misorientation angle θ and axis $[u\ v\ w]$ between A and B can also be calculated from misorientation matrix [M] by the following equations:

$$\theta = \cos^{-1}\left(\frac{m_{11} + m_{22} + m_{33} - 1}{2}\right)$$

$$[u \quad v \quad w] = [m_{23} - m_{32} \quad m_{31} - m_{13} \quad m_{12} - m_{21}]$$

Micrographs of serial sections were first aligned based on the fiducial marks. For this purpose, the public-domain NIH ImageJ 1.3 [26] software was employed. This software has available software "plug-ins" specific for aligning image stacks from serial sections as well as the ability to generate crude 3D renditions and animations for quick checking of the sectioned volume to reveal creep voids and their surroundings. After image alignment, specific features in individual serial section images were identified and a separate image stack was created for the series of images containing similar features. For instance, all creep voids were highlighted (with other areas blacked out) in each serial section image and an image stack containing only voids were created. The same treatment was performed to highlight different precipitates present and then each of these features was stored in their respective image stack. From the individual image stacks, information such as void volume or carbide volume fraction can be determined by counting voxels (volume picture elements), which were then converted into units of volume. For 3D reconstruction, a computer program was written using RSI's IDL 6.0 [27] to read the image stacks, and interpolate between image layers to produce a three-dimensional representation of the volume. This 3D representation can be rotated about any axis and animated for further study. By loading the specific image stacks, microstructural features can be revealed or hidden as needed. Specific colors were attributed to various microstructural features for enhanced visualization.

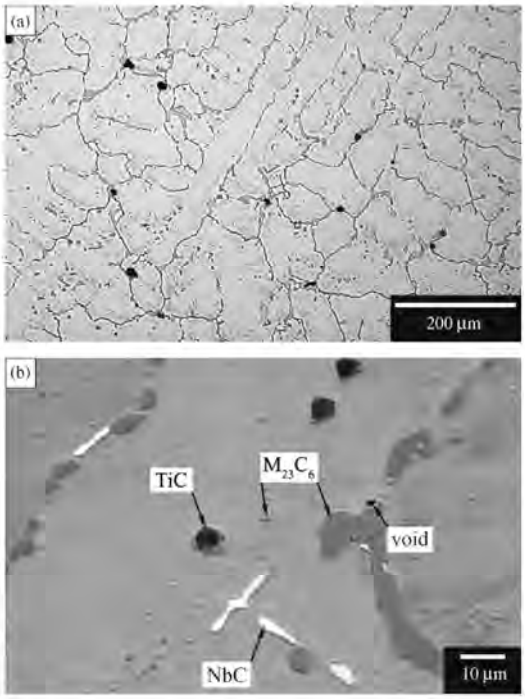

Fig. 1. Microstructure of ex-service reformer tube; (a) optical microscope image of sample etched in glyceregia; (b) backscatter electron (BSE) image identifying three precipitate types $M_{23}C_6$, NbC, and TiC.

3. Results and discussion

Fig. 1a shows the general appearance of the microstructure of the ex-service tube, while Fig. 1b is a backscatter electron (BSE) image of the tube with the various types of precipitates labelled. Identification of coarse precipitates was performed by a combination of EDS, EBSD and XRD, as described previously. Identification of fine precipitates was achieved via TEM and SAD. There were three types of precipitates present in the material:

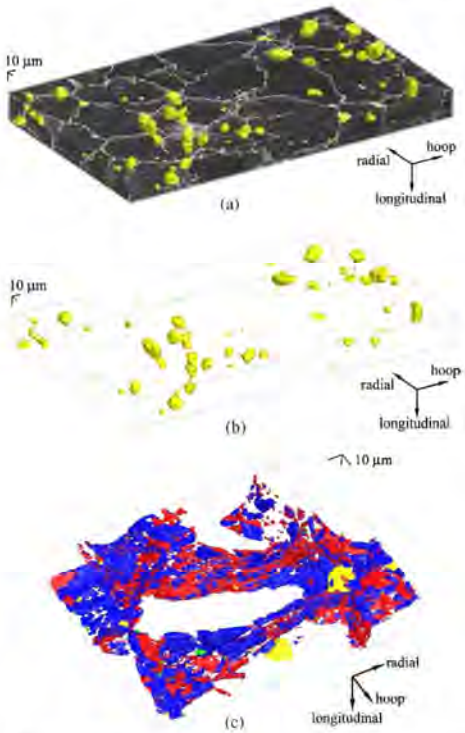

Fig. 2. 3D reconstruction of a 403 μm × 204 μm × 32 μm volume: (a) reconstruction with austenite shown in black, voids in yellow, and precipitates shown in shades of grey; (b) reconstruction of 138 voids; (c) reconstruction a 130 μm × 179 μm × 32 μm sub-volume showing voids (yellow), $M_{23}C_6$ (blue), NbC (red) and TiC (green).

- Cr-rich $M_{23}C_6$—appeared both intragranularly as fine precipitates and along the grain boundaries as coarse intergranular precipitates;
- NbC—found along the grain boundaries;
- TiC—predominantly occurred intragranularly.

Characterization of the "control" sample revealed that the same three precipitate types were also present.

Fig. 2 displays the isometric views of 3D reconstructions of one of the sectioned volume. In Fig. 2a, a total of 138 creep voids are reconstructed and highlighted in yellow and are superimposed on the 3D volume. Fig. 2b and c show only the voids and grain-boundary precipitates, respectively. The first observation made from these 3D reconstructions is that the creep voids are not uniformly distributed in the sample volume in terms of size, shape, and location. This observation highlights the importance of 3D techniques to reveal the true microstructure of materials. For this study, the 3D analysis outputs were void size, shape, location, and contact precipitate(s). Void sizes are represented by the equivalent sphere diameters of the void volumes. This was done to give a linear dimension value (i.e. μm), which conveniently represents the void size. For instance, it would be easier to visualize a 10 μm diameter void than the same void with a volume of 524 μm^3. Void shape was classified into three types—spherical, peanut, and ellipsoidal, as shown in Fig. 3. Spherical voids are approximately equiaxed, peanut-shape voids appear to be a coalescence of two or more spherical voids, and ellipsoidal voids are elongated-shaped voids without a distinct waist as seen in peanut-shaped voids. Void locations are shown schematically in Fig. 4 and categorized as follows:

- boundary—void located at boundary plane between two austenite grains;
- edge—void located at intersecting edge of three austenite grains;
- corner—void located at the intersecting corner of four (or more) austenite grains.

"Contact precipitates" were determined by viewing the 3D reconstruction to determine which precipitates are in contact with the voids.

A total of 290 voids were reconstructed from two serial-sectioned volumes, and their various characteristics observed from the 3D reconstruction are summarized in Fig. 5. Fig. 5a shows the overall void distribution represented by the equivalent void diameter. Total void volume for each diameter classification is indicated on the left axis while the number of voids in each class is indicated on the right axis. This graph simply points out that although there are a higher number of voids with diameters less than 4 μm, the total volume occupied by these voids is small compared to the total volume occupied by voids that are larger than 12 μm diameter. Fig. 5b shows a further breakdown of the void distribution in terms of their location within the grain structure. The larger voids appear predominantly along

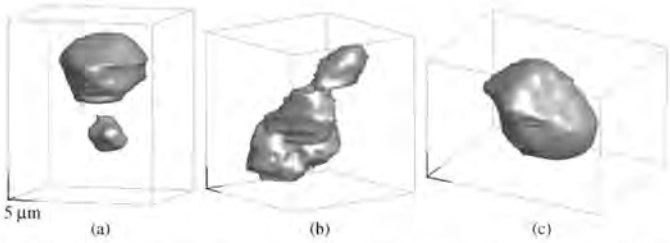

Fig. 3. Classification of creep void shapes: (a) spherical voids; (b) peanut-shaped void which appear to be a joining together of two or more voids; (c) ellipsoidal void.

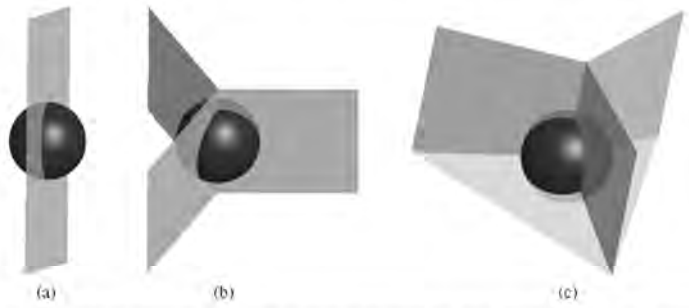

Fig. 4. Schematic representations of void location classification: (a) void located on the boundary plane between two grains; (b) void situated at the intersecting edge of three grains; (c) void located at the intersecting corner of four grains.

grain edges and corners (intersection of three and four grains, respectively), while smaller voids are located primarily along boundaries (between two grains) and edges. There were a few instances of voids appearing intragranularly (within austenite grains) where they appear adjacent to Cr-rich $M_{23}C_6$ precipitates. These void locations are categorized as "Intragranular" on Fig. 5b, and due to the low frequency of occurrence, their appearance on the graph is hardly visible.

Fig. 5c displays the correlation between void location and void shape. Peanut-shaped voids account for most of the total void volume, perhaps unsurprisingly, since this void type appears to be a coalescence of two or more voids. Ellipsoidal voids occupy the least amount of space, but it can be argued that these voids might also be a coalescence of two voids. In terms of numbers, there were more voids occurring at boundaries between two grains, however, the total volume of the voids at this location is less than as tenth of the volume taken up by voids at grain edges and corners. A possible explanation would be that creep voids are most likely to nucleate first at grain edges and corners where there would be more vacancies due to lattice mismatch between carbide and austenite. Moreover, the occurrence of large voids at these locations are consistent with the

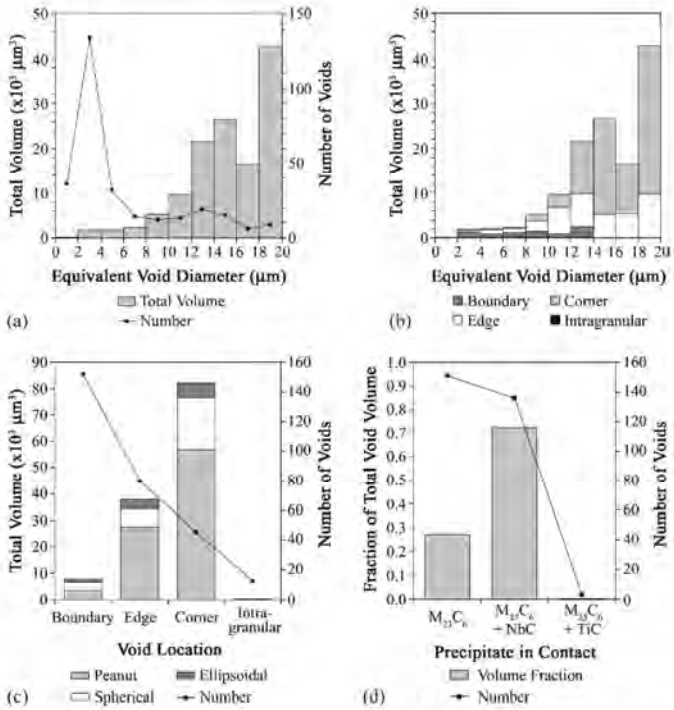

Fig. 5. Characteristics of creep void obtained from 3D reconstruction of reformer tube material. Total number of voids analyzed is 290 obtained from two reconstructed volumes; (a) overall distribution of total void volume and number for various sizes of voids; (b) distribution in (a) is further categorized in terms of void location; (c) correlation between void location and void shape; (d) voids and contact precipitates listed as fraction of total void volume and void count.

current belief that void nucleation and growth transpires due to grain boundary sliding along geometrical irregularities at grain boundaries where stress concentration is high [28]. This would lead to more severe creep damage at grain edges and corners.

Fig. 5d displays the link between the precipitates in contact with the voids and their occurrences in terms number of voids and fraction of total void volume. Results show that a higher number of voids were in contact with only $M_{23}C_6$ precipitate but a higher fraction of total void volume came in contact with both $M_{23}C_6$ and NbC precipitates. The most significant observation made from Fig. 5d is that all the voids inspected came in contact with $M_{23}C_6$ somewhere along their perime-

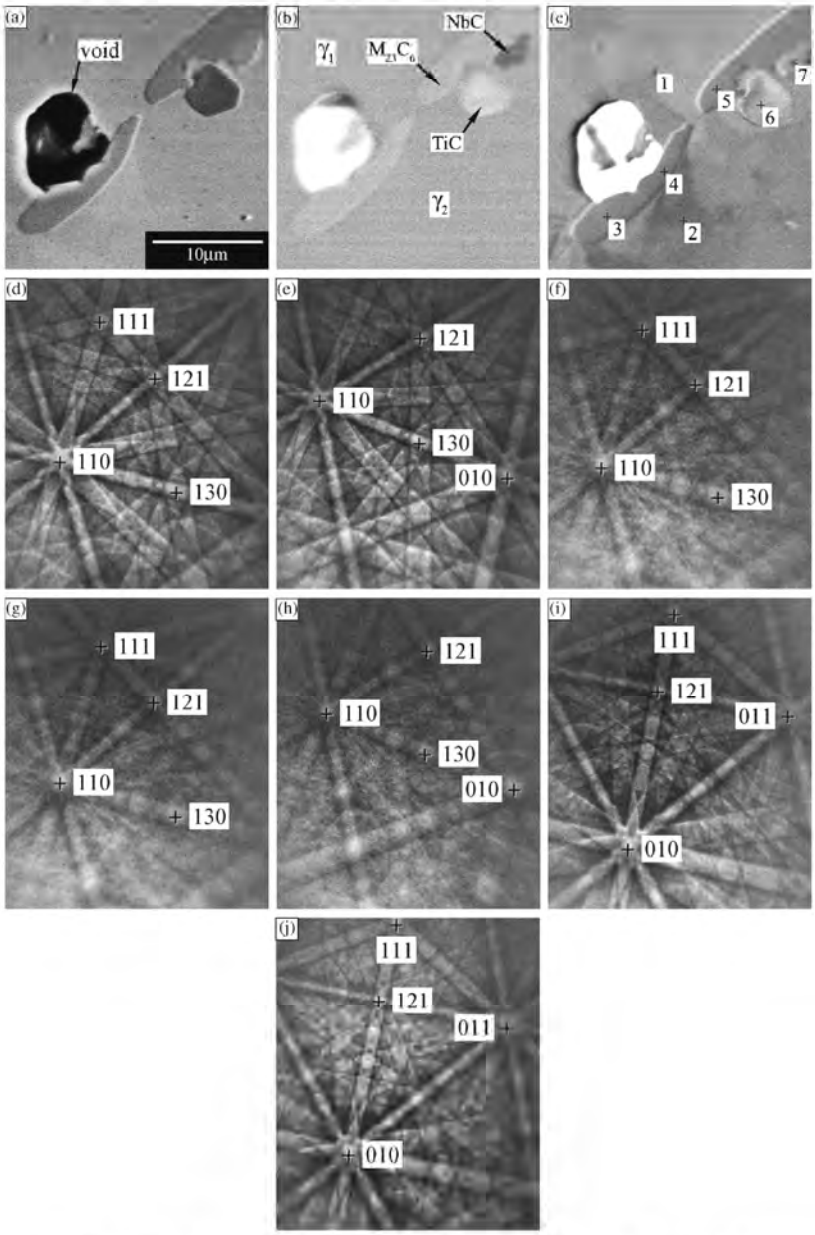

Fig. 6. (a) SE image of a creep void and surrounding area; (b) FZ image identifying various phases present; (c) FO image identifying the different grains and also specifying the locations where EBSPs were obtained; (d) EBSP of austenite (location 1); (e) EBSP of another austenite grain (location 2) (f–h) EBSPs of three $M_{23}C_6$ grains (locations 3, 4, 5); (i) EBSP of TiC (location 6); (j) EBSP of NbC (location 7).

ter. No voids were observed solely in contact with NbC and/or TiC precipitates. Correlation between creep void locations and $M_{23}C_6$ precipitates have been previously mentioned [28,29]. From the present inspection of a single ex-service tube, it cannot be conclusively said that these voids nucleated only at $M_{23}C_6$ precipitates. However, it should be noted that for the material volume inspected, there was twice the amount of $M_{23}C_6$ compared to NbC (approximately 7% versus 3%, by volume), and thus the absence of voids solely adjacent to NbC precipitates is conspicuous. Another comment to follow these observations is that there were no other types of inclusions or impurities found to be associated with the voids. One work on bainitic CrMoV steel has indicated that creep voids nucleate exclusively on grain boundary sulfides [30]. It has also been proposed that creep voids nucleate only on "nonadherent grain boundary inclusions" [28].

An example of the phase identification procedure is shown in Fig. 6. Fig. 6a–c are examples of SE, FZ, and FO images of a creep void and its vicinity. The locations where EBSPs were obtained are identified in Fig. 6c. Examples of typical EBSP's are shown in Fig. 6d–j. A combination of EDS and EBSD was used to identify the various precipitates observed.

Fig. 7a shows the OR between $M_{23}C_6$ precipitates adjacent to creep voids and each adjacent austenite matrix grain in the form of a [1 0 0] stereographic triangle. A total of 442 points was plotted. Data represented by filled squares are $M_{23}C_6$ precipitates with a near cube-cube OR (high registry) with an adjacent austenite grain while data represented by open squares are for $M_{23}C_6$ precipitates with a random OR. Typically an angular difference between grains of 10–15° is taken as low angle grain boundary, where dislocation arrays are able to compensate for the interface mismatch [31]. For this work, near cube-cube OR is based on a misorientation angle of 10° or less. Fig. 7b shows the distribution of misorientation angles for $M_{23}C_6$ precipitates and austenite grains in the vicinity of the creep voids. The distribution showed that approximately twenty percent of the $M_{23}C_6$ precipitates adjacent to voids show a near cube-cube OR.

Previous work by King and Bell [32] stated that grain boundary precipitates should obtain rational OR with one of the adjacent grains. Additionally, works by Lewis and Hattersley [9] and Beckitt and Clark [11] on $M_{23}C_6$ precipitates in austenitic stainless steels have also indicated that grain boundary $M_{23}C_6$ precipitates should display a cube-cube OR with at least one of the adjacent austenite grains. Furthermore, long term ageing such as the service condition experienced by the ex-service reformer tube would typically result in coalescing of the grain boundary carbides towards a near cube-cube OR so that the total surface energy is lowered [9]. This would imply that the occurrence of cube-cube OR between $M_{23}C_6$ precipitates and the adjacent austenite grains should be 50%. Interestingly, this hypothesis was demonstrated by the "control" sample, which underwent high temperature ageing. The OR data for the control sample (total of 272 points) showed a less random appearance,

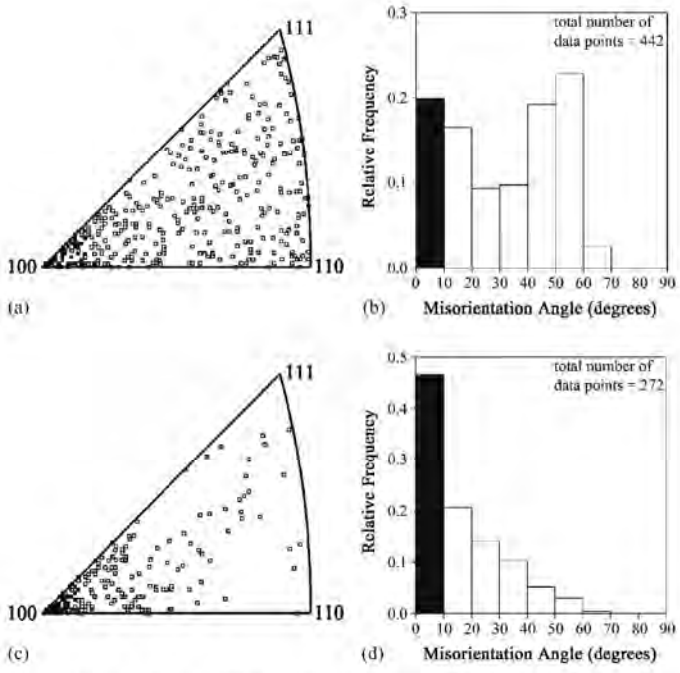

Fig. 7. Comparison of orientation relationships and misorientation angles between ex-service material and laboratory-aged sample: (a) OR between $M_{23}C_6$ and austenite grains in ex-service tube sample, closed squares indicate $M_{23}C_6$ precipitates with near cube-cube OR with austenite; (b) misorientation angle distribution of OR data shown in (a), black histogram bar correspond to near cube-cube data; (c) OR between $M_{23}C_6$ and austenite grains in laboratory-aged sample; (d) misorientation angle distribution of OR data shown in (c).

as indicated in Fig. 7c, while the misorientation angle distribution in Fig. 7d established that cube-cube OR between $M_{23}C_6$ precipitates and austenite occurred forty seven percent of the time. It is important to recall that the Larson-Miller parameters for both the ex-service sample and the "control" sample are similar (33.6 and 33.4, respectively). Based on these observations, it is believed that the twenty percent occurrence of $M_{23}C_6$ with cube-cube OR near creep voids occurs because the preferred sites for creep voids are low registry boundaries between $M_{23}C_6$ precipitates and austenite.

4. Conclusions

Creep voids in an ex-service hydrogen reformer tube have been studied via serial sectioning and 3D reconstruction. Creep voids are not uniformly distributed through the volume in terms of their size, shape, and location. The largest voids were formed by coalescence of two or more voids resulting in a peanut shape. Almost all of the voids appeared near grain boundary carbides and the larger of these voids were located at grain edges and corners. All voids made contact with $M_{23}C_6$ precipitates, whereas no voids were observed in sole contact with TiC or NbC precipitates. EBSD observation of the $M_{23}C_6$ precipitates surrounding these voids showed that most of the voids are adjacent to precipitates with a random OR with the surrounding austenite matrix.

Acknowledgements

The authors would like to thank Methanex (NZ) Ltd. and Schmidt & Clemens (Spain) for funding of this work.

References

[1] T.G. Langdon, Metall. Mater. Trans. 33A (2002) 249–259.
[2] F.R.N. Nabarro, Metall. Mater. Trans. 33A (2002) 213–218.
[3] T. Sourmail, Mater. Sci. Technol. 17 (2001) 1–14.
[4] G.D. Barbabela, L.H. de Almeida, T.L. da Silveira, I. Le May, Mater. Characterization 26 (1991) 1–7.
[5] G.D. Barbabela, L.H. de Almeida, T.L. da Silveira, I. Le May, Mater. Characterization 26 (1991) 193–197.
[6] L.H. de Almeida, A.F. Ribeiro, I. Le May, Mater. Characterization 49 (2003) 219–229.
[7] T. Shinoda, M.B. Zaghloul, Y. Kondo, R. Tanaka, Trans. ISIJ 18 (1978) 139–148.
[8] H. Wen-Tai, R.W.K. Honeycombe, Mater. Sci. Technol. 1 (1985) 390–397.
[9] M.H. Lewis, B. Hattersley, Acta Metall. 13 (1965) 1159–1168.
[10] U.E. Wolff, Trans. Metall. Soc. AIME 236 (1966) 19–27.
[11] F.R. Beckitt, B.R. Clarck, Acta Metall. 15 (1967) 113–129.
[12] L.K. Singhal, J.W. Martin, Trans Metall Soc AIME 242 (1967) 814–819.
[13] L.K. Singhal, J.W. Martin, Acta Metall. 15 (1967) 1603–1610.
[14] P.H. Pumphrey, J.W. Edington, Acta Metall. 22 (1974) 89–94.
[15] A.B. Kinzel, Trans. AIME 194 (1952) 469–488.
[16] K.J. Kim, H.U. Hong, K.S. Min, S.W. Nam, Mater. Sci. Eng. A387–389 (2004) 531–535.
[17] M.V. Kral, M.A. Mangan, G. Spanos, R.O. Rosenberg, Mater. Characterization 45 (2000) 17–23.
[18] M.V. Kral, G. Ice, M.K. Miller, M.D. Uchic, R.O. Rosenberg, in: G.V. Voort (Ed.), ASM International Metallography and Microstructures Handbook, Vol. 9, ASM International, Materials Park, Ohio, 2004, pp. 448–467.
[19] M. Hillert, in: V.F. Zackay, H.I. Aaronson (Eds.), The Decomposition of Austenite by Diffusional Processes, Interscience, New York, 1962, pp. 197–237.
[20] O. Forsman, Jernkontor-ets Ann. 102 (1918) 1–30.
[21] M.V. Kral, G. Spanos, Acta Mater. 47 (1999) 711–724.
[22] M. Li, S. Ghosh, T.N. Rouns, H. Weiland, O. Richmond, W. Hunt, Mater. Characterization 41 (1998) 81–95.
[23] R. Raj, M.F. Ashby, Acta Metall. 23 (1975) 653–666.
[24] M.E. Kessner, T.A. Hayes, Int. J. Plasticity 19 (2003) 1715–1748.
[25] P. Villars, L.D. Calvert, Pearson's Handbook of Crystallographic Data for Intermetallic Phases, Second ed., ASM International, Materials Park, Ohio, 1991.
[26] NIH, http://rsb.info.nih.gov/ij/.
[27] RSI, http://www.rsinc.com/.
[28] V. Sklenicka, K. Kucharova, M. Svoboda, L. Kloc, J. Bursik, A. Kroupa, Mater. Characterization 51 (2003) 35–48.
[29] G. Muralidharan, P.J. Maziasz, N.D. Evans, M.L. Santella, K.C. Liu, J.G. Hemrick, V.K. Sikka, R.I. Pankiw, in MS&T 2004, New Orleans, Lousiana.
[30] B.J. Cane, C.J. Middleton, Metal Sci. 15 (1981) 295.
[31] V. Randle, The Measurement of Grain Boundary Geometry, Electron Microscopy, in: B. Cantor, M.J. Goringe (Eds.), Materials Science Series, Institute of Physics Publishing, Bristol, 1993.
[32] A.D. King, T. Bell, Metall. Trans. 6 (1975) 1419–1429.

Available online at www.sciencedirect.com
SCIENCE DIRECT
ELSEVIER
Scripta Materialia 55 (2006) 69–73
Scripta MATERIALIA
www.actamat-journals.com

Viewpoint Paper

A three-dimensional characterization of creep void formation in hydrogen reformer tubes

Azmi Abdul Wahab,[a] Christopher R. Hutchinson[b] and Milo V. Kral[a,*]

[a] *Department of Mechanical Engineering, University of Canterbury, Private Bag 4800, Christchurch, New Zealand*
[b] *Department of Materials Engineering, Monash University, Clayton 3800, Australia*

Received 21 October 2005; revised 23 February 2006; accepted 27 February 2006
Available online 12 April 2006

Abstract—The techniques of serial sectioning and three-dimensional reconstruction were used to characterize creep voids occurring in an ex-service hydrogen reformer tube. The influence of variations in temperature, stress and microstructure types on the characteristics of creep voids are considered in the study. The results revealed that the highest void density per grain boundary area occurred at the outer wall of the tube where the temperature is highest and the microstructure consists of large columnar grains, compared to the inner wall of the tube consisting of smaller equiaxed grains.

Keywords: Creep; Austenitic steels; 3D

1. Introduction

Hydrogen reformers are typically fabricated from hundreds of centrifugally cast Fe–Cr–Ni–C austenitic stainless steel tubes. These tubes are expected to operate at temperatures around 900 °C and internal pressures between 2 and 3 MPa for 100,000 h (11.4 years). To achieve these requirements, the tubes contain high amounts of C (0.4 wt.%), Cr (25 wt.%) and Ni (35 wt.%), as well as small additions of Nb and Ti. The creep resistance of the material is largely attributed to the presence of primary intergranular Cr-rich $M_{23}C_6$ carbides that inhibit grain boundary sliding and secondary intragranular $M_{23}C_6$ carbides that restrain dislocation motion [1]. Fragmentation of $M_{23}C_6$ grain boundary carbides by NbC and TiC is believed to further enhance creep properties [2–4].

To realize further efficiencies in the creep performance of these alloys requires an understanding of the damage accumulation processes that lead to unacceptable strains and ultimately to material failure. The ductile failure of metallic materials loaded under creep conditions typically proceeds by the nucleation, growth and coalescence of creep voids followed by macroscopic crack propagation [5]. Given the very long lifetimes expected of the hydrogen reformer tubes, it would be very useful to develop a simplified computational description of the damage accumulation processes so that some guidance on the expected effects of any designed microstructural changes could be obtained before performing time-consuming and costly long-term creep experiments. Void growth has been studied in some detail and a variety of models is available for treating the kinetics [6–9]. Void nucleation probably remains the least well understood of the processes [7,10] and an understanding at least of the preferred sites for nucleation and the resulting spatial distribution is required for even a first-order treatment of the damage accumulation process [7]. Three-dimensional (3D) microstructure reconstruction techniques now provide an effective means of obtaining this important information on void formation, distribution and evolution and we report here some of our 3D observations of creep void formation in hydrogen reformer tubes.

Three-dimensional characterization techniques have recently been applied to creep voids in an ex-service hydrogen reformer tube to determine void shapes, sizes, locations, and to identify precipitates adjacent to voids [11]. It was revealed that larger creep voids tend to be "peanut-shaped", suggesting a coalescence of two (or more) voids, and these voids occurred predominantly at grain edges and corners. Furthermore, all the voids were found adjacent to $M_{23}C_6$ precipitates. Electron

* Corresponding author. Tel.: +64 3 3642987x7392; fax: +64 3 3642078; e-mail: milo.kral@canterbury.ac.nz

1359-6462/$ - see front matter © 2006 Acta Materialia Inc. Published by Elsevier Ltd. All rights reserved.
doi:10.1016/j.scriptamat.2006.02.045

backscatter diffraction (EBSD) showed that 80% of the adjacent precipitates have an irrational orientation relationship with the austenite matrix. This result is consistent with other work in austenitic stainless steels, which show that low registry $M_{23}C_6$–austenite interfaces are more prone to material failures such as corrosion [12] and creep-fatigue [13].

In the present work, four 3D volumes were reconstructed from an ex-service reformer tube to determine the influence of variations in temperature, stress and microstructure on the characteristics of creep voids. These operational parameters have been related to geometrical aspects of creep voids, e.g. shape, size, inter-void distance and hoop stress axis–grain boundary angle, as well as to microstructural features such as void type, void location, and neighboring precipitates.

2. Materials and methods

The sample used in this study was taken from a tube which was retired from service after 90,000 h due to excessive diametral strain, but was otherwise structurally sound with no cracks or ruptures. The diametral strain was determined to be 3.7% for a sample obtained from a location experiencing an internal pressure of 2.65 MPa and service temperatures ranging from 875 °C on the inner wall to 895 °C on the outer wall. The tube material is a centrifugally cast austenitic stainless steel composed of Fe–0.45% C–25% Cr–35% Ni–1.5% Si–1.5% Nb–1.0% Mn (approximate weight per cent). The microstructure of this tube consists of small equiaxed grains along 20% of the inner cross-section of the tube, while the remaining outer cross-section contains large columnar grains.

In general, characterization, serial sectioning, and 3D reconstruction methods used on this sample have been reported elsewhere [11]. Four $400 \times 300 \times 50$ μm volumes of material were obtained from 100 serial sections at a 0.5 μm sectioning increment. Two volumes were taken in the equiaxed-grain region near the inside wall of the tube. Two volumes were taken from different locations containing large columnar grains, one from mid-thickness and another from an outer wall area. EBSD scans of the samples were taken at every tenth section starting with layer 15 and ending at layer 55. Registration of serial section images was carried out using NIH ImageJ 1.33 software [14] and the "StackReg" plug-in [15]. Three-dimensional reconstructions of the volume were performed using RSI's IDL 6.1 [16]. Void measurements such as volume, inter-void distance and grain boundary angle were achieved using various tools available in ImageJ, while void characteristics such as shape, type, location, and precipitate in contact were visualized using a combination of ImageJ and IDL.

3. Results and discussion

The macrostructure of the tube indicating the approximate locations of the four reconstructed volumes is shown in Figure 1a. The equiaxed structure of volumes I and II, and the columnar structure of volumes

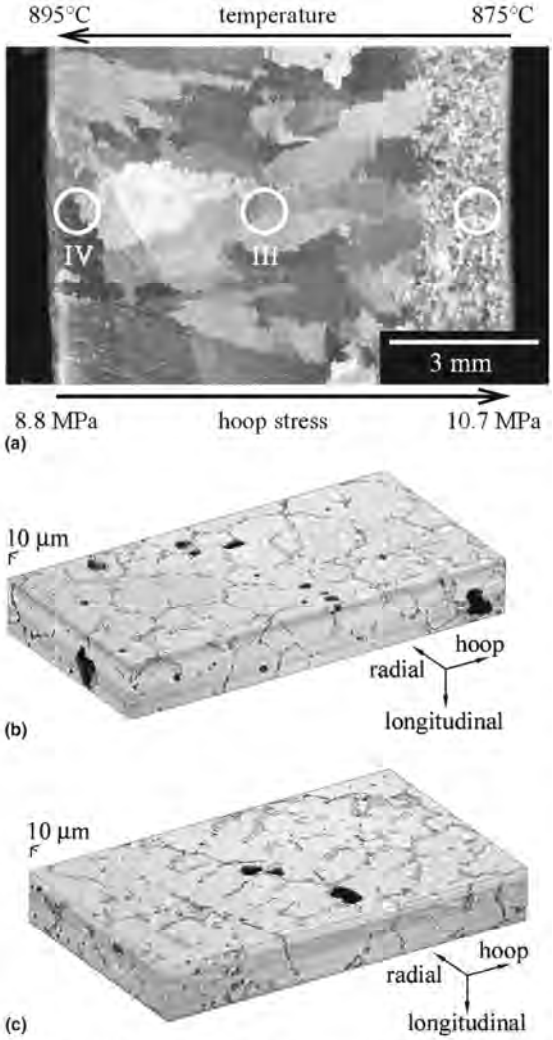

Figure 1. (a) Cross-section of reformer tube showing fine equiaxed grains along 20% of the inner wall region and large columnar grains for the remaining areas, approximate location of reconstructed volumes are indicated. (b) 3D reconstruction of volume I (equiaxed) and (c) 3D reconstruction of volume IV (columnar).

III and IV are clearly evident. Service parameters and 3D reconstruction details related to each reconstructed volume are summarized in Table 1. Note that hoop stress values are calculated based on internal pressure at the location of the sample. Radial and longitudinal stresses were determined to be compressive and thus ignored.

The equiaxed microstructure of volumes I and II allowed reconstruction of many grains, while the relatively coarse, columnar microstructure of volumes III and IV restricted study to portions of only a few grains. Examples of 3D reconstructions of the volumes I (equiaxed) and IV (columnar) are illustrated in Figure 1b and c, respectively. Creep voids appear as the irregular dark

Table 1. Particulars of reconstructed volumes

Volume	Microstructure	Temperature (°C)	Hoop stress (MPa)	Volume size ($\times 10^{-3}$ mm^3)	Number of grains sectioned (full/partial)	Grain size (mm)	Grain boundary area (mm^2)
I	Equiaxed	875	15.2	3.9	80	0.047	0.190
II	Equiaxed	875	15.1	4.4	36	0.068	0.133
III	Columnar	885	14.7	5.0	3	0.444	0.026
IV	Columnar	895	13.7	4.6	4	0.409	0.024

shapes. The carbide distribution in volume IV (Fig. 1c) marks dendrite arm boundaries, since true grain boundaries could only be reliably revealed using EBSD. Grain count and grain sizes were obtained from EBSD scans, while grain boundary areas were estimated by calculating the average boundary length from the EBSD scans and multiplying by the volume thicknesses.

Figure 2a shows the number of voids per grain boundary area as a function of void size for the inner wall, mid-thickness and outer wall of the tube. The void size distribution is represented by the equivalent diameters in order to account for non-spherical voids. The corresponding void volume per grain boundary area is shown in Figure 2b. Since creep is strongly affected by grain boundaries, void count and void volume values were normalized by grain boundary area, and therefore only voids occurring at grain boundaries are included in the plots.[1] The two charts in Figure 2a and b simply indicate that although there were a large number of voids less than 8 μm in size, the total accumulated volume for these voids is small compared to voids between 20 and 36 μm. An interesting observation can be made from Figure 2c where the average void densities and volumes are plotted for the inner wall, mid-thickness and outer wall regions. The results show that void density and accumulated volume is lowest at the inner wall even though grain sizes are smaller and the hoop stress is higher at this location. The highest void density occurred at the outer wall. However, in terms of accumulated void volume, the largest voids occurred at the center of the tube wall. Note that while the highest temperature occurred at the outer wall, the highest stress occurred at the inner wall of the tube. These competing parameters may result in creating the optimum conditions for creep void nucleation and growth at the mid thickness area. Nevertheless, the results show that void densities in the grain boundaries are lower at the inner wall.

Figure 3 shows the "average" and "minimum" void-to-void distance for all three regions of the tube. The "minimum" void-to-void distance was obtained by averaging the closest neighboring void distance for each void observed, while the "average" void-to-void distance was determined from the void densities of Figure 2c using the equation $2l = 1/\sqrt{\rho}$ where $2l$ is the void-to-void distance and ρ is the void density per unit grain boundary area [7]. The resulting plot shows that the minimum void-to-void distances are similar for all three regions of the tube (approximately 20 μm). On the other hand, the average void-to-void distances for mid-thickness and outer wall are approximately ten times greater than the "minimum" value, whereas the average void-to-void distance for the equiaxed inner wall region is almost thirty times greater. It was observed from the 3D reconstructions that for the equiaxed microstructure, voids tend to cluster at grain edges (three-grain junctions) and corners (four-grain junctions) resulting in the small "minimum" void-to-void distance but large "average" void-to-void distances are due to the higher distances between these void clusters. The larger distances between void clusters in an equiaxed microstructure would presumably make linking or coalescence of voids more difficult.

The effect on void formation of the angle of grain boundary orientation with respect to the hoop stress axis was also examined. For voids occurring at grain edges, three angles were measured, whilst for voids at corners, four angles were recorded. The resulting distributions of these measurements are shown in Figure 4. In general, most of the voids occurred at grain boundaries that are non-perpendicular and non-parallel with respect to the hoop stress. The results for mid-thickness region appear to show a preference for grain boundary angles between 50° and 70°; however, this may be the effect of the small number of grains sectioned for the volume.

Voids are further characterized by their types and locations as shown by the charts in Figures 5 and 6. Grain boundary void types follow the classification given by Raj and Ashby [7] (Fig. 5a). Type A voids occur on the precipitate–matrix interface in one of the matrix grains, whereas type B voids span multiple matrix grains. A third void type is classified here as intragranular voids, which refer to voids appearing at intragranular $M_{23}C_6$ precipitates. Figure 5b shows a breakdown of void types at the inner wall, mid-thickness, and outer wall of the tube given as a fraction of total void volume. There appears to be a shift from mainly type B voids at the inner wall to mainly type A voids at the outer wall. In regions with columnar grains (mid-thickness and outer wall regions), voids predominantly appear at columnar grain boundaries (two-grain junctions). This apparent tendency must be considered with caution, since the present volume reconstruction technique prevents a large number of grain edges and corners being reconstructed due to the relatively large size of the columnar grains. An effort is currently underway to acquire a much larger volume reconstruction from the columnar regions. In regions with equiaxed grains (the inner wall), the most prevalent void locations are grain edges (three-grain junctions), although significant fractions of total void volume are located at grain boundaries and corners. There also appears to be a 5% occurrence of intragranular voids at the outer wall, whereas the occurrence of these voids at mid thickness and inner wall is minimal.

[1] Earlier work showed that intragranular voids account for only 2% of total void volume [11].

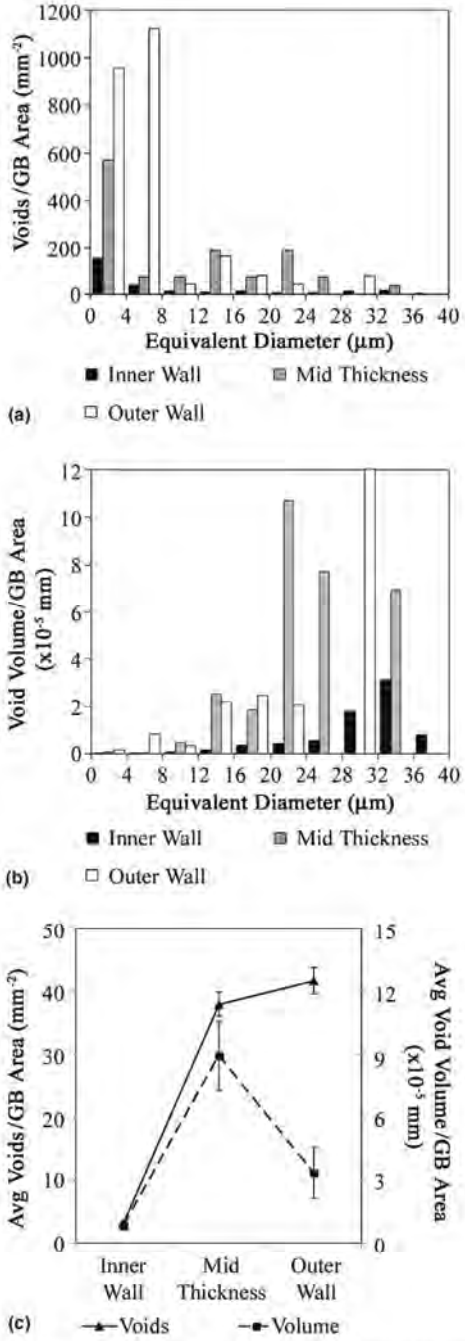

Figure 2. Void count and volume for grain boundary voids, (a) void density distribution, (b) void volume distribution and (c) comparisons of void density and void volume for inner wall, mid-thickness, and outer wall regions of the tube.

Void shapes and the identity of the neighboring precipitates were also characterized. There appears to be no influence of position within the tube wall on either the void shape or identity of the neighboring precipitates.

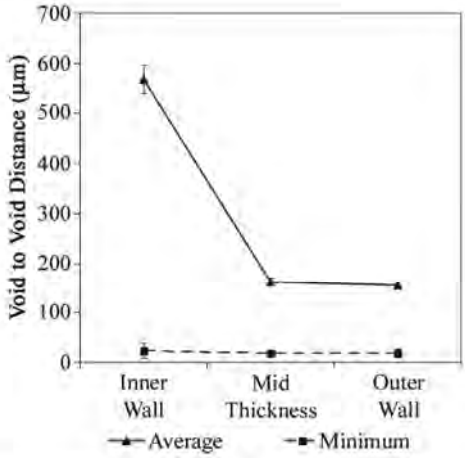

Figure 3. Comparison of "average" and "minimum" void-to-void distance for three locations of the reformer tube wall.

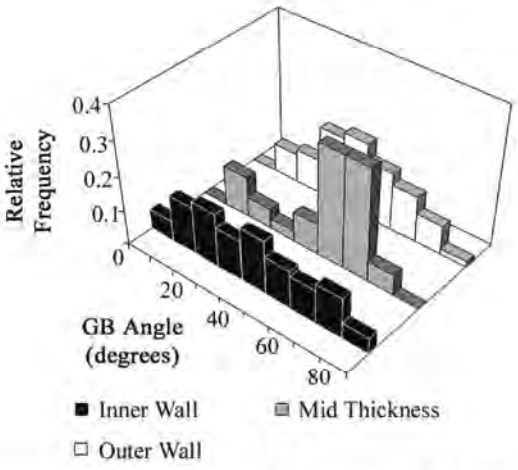

Figure 4. Angle of grain boundaries containing creep voids. Measurements are taken with respect to the hoop stress axis.

Approximately 85% of the total void volume consisted of peanut-shaped voids, which suggests that voids have coalesced. It was also found that all voids encounter at least one $M_{23}C_6$ precipitate somewhere along their perimeter. These two observations are consistent with results reported earlier [11].

4. Summary

Three-dimensional analysis has been applied to determine a number of significant creep void parameters, including:

- void sizes, shapes and locations,
- void density and separation statistics,
- the geometry of neighboring grain boundaries,
- void–precipitate configuration and
- the identity of neighboring precipitates.

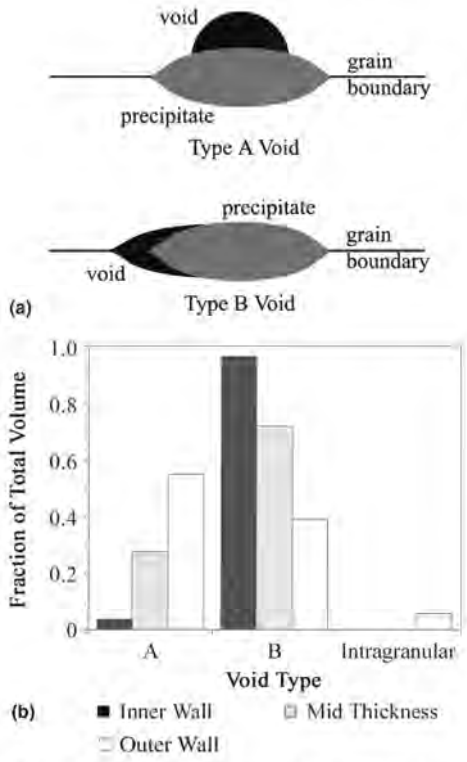

Figure 5. (a) Type A and B classification of void types and (b) analysis of void types at various locations of the tube.

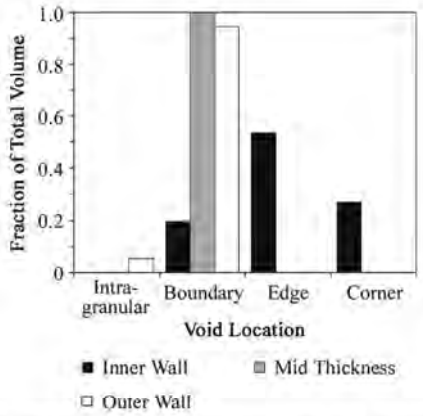

Figure 6. Breakdown of void locations for inner wall, mid-thickness, and outer wall of the tube.

This type of three-dimensional microstructure analysis will be used in the refinement of damage accumulation models [6–10]. General trends that have not been identified in any previous work can be gleaned from 3D observations. For example, the highest void density occurred at outer wall of the tube where the temperature is highest and the microstructure consists of large columnar grains. Although the actual void counts are higher for the inner wall of the tube that consist of smaller equiaxed grains, normalizing the void counts over the grain boundary area yields a significantly lower void density for the equiaxed microstructure of the inner wall. It still has to be identified whether a lower void density per grain boundary area that yields a higher void-to-void distance would delay the coalescence of creep voids that leads to material failure.

Acknowledgements

The authors gratefully acknowledge the support of Methanex (NZ) Ltd. and Schmidt & Clemens (Spain) for funding of this work.

References

[1] G.D. Barbabela, L.H. de Almeida, T.L. da Silveira, I. Le May, Mater. Charact. 26 (1991) 1–7.
[2] L.H. de Almeida, A.F. Ribeiro, I. Le May, Mater. Charact. 49 (2003) 219–229.
[3] T. Shinoda, M.B. Zaghloul, Y. Kondo, R. Tanaka, Trans. ISIJ 18 (1978) 139–148.
[4] H. Wen-Tai, R.W.K. Honeycombe, Mater. Sci. Technol. 1 (1985) 390–397.
[5] J.D. Embury, in: R.C. Gifkins (Ed.), 6th International Conference on Strength of Metals and Alloys, Pergamon Press, Melbourne, Oxford, Australia, 1982.
[6] A.C.F. Cocks, M.F. Ashby, Prog. Mater. Sci. 27 (1982) 189–244.
[7] R. Raj, M.F. Ashby, Acta Metall. 23 (1975) 653–666.
[8] A. Needleman, J.R. Rice, Acta Metall. 28 (1980) 1315–1332.
[9] T. Pardoen, J.W. Hutchinson, J. Mech. Phys. Solids 48 (2000) 2467–2512.
[10] S.H. Goods, L.M. Brown, Acta Metall. 27 (1979) 1–15.
[11] A.A. Wahab, M.V. Kral, Mater. Sci. Eng. A 412 (2005) 222–229.
[12] A.B. Kinzel, Trans. AIME 194 (1952) 469–488.
[13] K.J. Kim, H.U. Hong, K.S. Min, S.W. Nam, Mater. Sci. Eng. A387–A389 (2004) 531–535.
[14] NIH. ImageJ 1.33. Available from: <http://rsb.info.nih.gov/ij/>.
[15] P. Thévenaz, StackReg. Available from: <http://bigwww.epfl.ch/thevenaz/stackreg/>.
[16] RSI. IDL 6.1. Available from: <http://www.rsinc.com/>.

Appendix V

ANIMATED 3D MOVIES

A CDROM containing simple animated movies of serial section images and rotating 3D reconstructed volumes is attached in this Appendix to assist with the visualization of 3D reconstructions. Figures in the thesis which are accompanied by animated movies in this CDROM will be denoted by this icon  . All movies are in uncompressed audio-video interleave (AVI) format and compatible with Microsoft Media Player® and Apple Quicktime®. Movie files are named according to the corresponding figure numbers in the thesis. Movies of several 3D reconstructions not shown in this thesis are also included in the CDROM for additional reference.